MODELING OF INTERSONIC DELAMINATION IN CURVED-THICK
COMPOSITE LAMINATES UNDER QUASI-STATIC LOADING

A THESIS SUBMITTED TO
THE GRADUATE SCHOOL OF NATURAL AND APPLIED SCIENCES
OF
MIDDLE EAST TECHNICAL UNIVERSITY

BY

BURAK GÖZLÜKLÜ

IN PARTIAL FULFILLMENT OF THE REQUIREMENTS
FOR
THE DEGREE OF DOCTOR OF PHILOSOPHY
IN
AEROSPACE ENGINEERING

MARCH 2014

MODELING OF INTERSONIC DELAMINATION IN CURVED-THICK
COMPOSITE LAMINATES UNDER QUASI-STATIC LOADING

submitted by **BURAK GÖZLÜKLÜ** in partial fulfillment of the requirements for the degree of **Doctor of Philosophy in Aerospace Engineering Department, Middle East Tachnical University** by,

Prof. Dr. Canan Özgen   _____
Dean, Graduate School of **Natural and Applied Sciences**

Prof. Dr. Ozan Tekinalp   _____
Head of Department, **Aerospace Engineering**

Assoc. Prof. Dr. Demirkan Çöker   _____
Supervisor, **Aerospace Engineering**

Examining Committee Members

Prof. Dr. Altan Kayran   _____
Aerospace Engineering Dept., METU

Assoc. Prof. Dr. Demirkan Çöker   _____
Aerospace Engineering Dept., METU

Assist. Prof. Dr. İlker Temizer   _____
Mechanical Engineering Dept., Bilkent Uni.

Assoc. Prof. Dr. Uğur Polat   _____
Civil Engineering Dept., METU

Assist. Prof. Dr. Ercan Gürses   _____
Aerospace Engineering Dept., METU

Date: 06.03.2014

I hereby declare that all information in this document has been obtained and presented in accordance with academic rules and ethical conduct. I also declare that, as required by these rules and conduct, I have fully cited and referenced all material and results that are not original to this work.

Name, Last name: Burak Gözlüklü

Signature :

ABSTRACT

MODELING OF INTERSONIC DELAMINATION IN CURVED AND THICK
COMPOSITE LAMINATES UNDER QUASI-STATIC LOADING

Gözlüklü, Burak

PhD, Department of Aerospace Engineering

Supervisor: Assoc. Prof. Dr. Demirkan Çöker

March 2014, 327 pages

One of the widely used geometrically complex parts in advanced commercial aircraft is L-shaped composite laminates in which mixed-mode delamination failure is reported. Dynamic delamination under quasi-static loading is studied using explicit finite element method in conjunction with Cohesive Zone Modeling (CZM). A 4-noded interface element working with Bilinear (BL), Xu-Needleman (XN) and rate-dependent bilinear (RD) CZMs are implemented in ABAQUS/Explicit. The interface elements are validated with benchmark tests from literature for each fracture mode subjected to static and dynamic loading. A 12-ply woven-fabric Graphite/Epoxy L-shaped composite laminate is modeled with BL cohesive layers placed in all interfaces. Macromechanical and micromechanical behaviors are compared to experiments and are found to be in good agreement. Single delamination initiates in mode-I and smoothly transitions to mode-II during propagation at intersonic crack tip speeds reaching 3500 m/s. Shear Mach waves fronts, follower reflecting waves, train of pulses in normal stresses and vortex like particle velocity patterns are observed. The analysis is repeated using XN and RD CZMs. XN CZM exhibited early slippage of plies due to low initial stiffness, whereas RD CZM provided the best agreement with experiments. This thesis reports the intersonic crack propagation in engineering parts for the first time, which was previously observed in earthquakes.

Keywords**:** Intersonic fracture, delamination, composite materials, fracture mechanics, cohesive zone method.

ÖZ

BÜKÜMLÜ VE KALIN KOMPOZİT LAMİNATLARDAKİ INTERSONİK DELAMİNASYONUN SANKİ-STATİK YÜK ALTINDA MODELLENMESİ

Gözlüklü, Burak

Doktora, Havacılık ve Uzay Mühendisliği

Tez Yöneticisi: Doç. Dr. Demirkan Çöker

Mart 2014, 327 sayfa

İlerli ticari uçaklarda en çok kullanılan karmaşık şekilli parçalardan biri olan L-şekilli kompozit laminatlarda karmaşık-modlu delaminasyon raporlanmaktadır. Belirli sonlu eleman metodu ile Kohezif Alan Metodu (KAM) kullanılarak dinamik delaminasyon sanki-statik yük altında modellenmiştir. Çift-Doğrusal (ÇD), Xu-Needleman (XN) ve hıza bağlı çift-doğrusal (HB) KAM'lar 4-düğümlü arayüz elemanı üzerinden ABAQUS-Explicit'e uygulanmıştır. Arayüz elemanları literatürden alınan ölçüt testleriyle her kırılma modu için statik ve dinamik yük altında doğrulanmıştır. Her arayüzde ÇD kohezif elemanlar konularak 12-katmanlı bir Grafit/Epoksi L-şekilli kompozit laminat modellenmiştir. Makromekanik ve mikromekanik davranışlar deneylerle karşılaştırılmış ve iyi sonuçlar elde edilmiştir. Tek bir delaminasyon mod-I altında oluşmuş ve yavaşça mod-II durumunda 3500 m/s intersonik çatlak ucu hızlarında ilerlemiştir. Kesme Mak dalga önleri, takipçi yansıyan dalgalar, normal gerilim puls treni, girdap benzeri parçaçık hız vektör desenleri gözlemlenmiştir. Aynı analiz XN ve HB KAM'larla tekrarlanmıştır. XN KAM düşük ilk sertliği sebebiyle kaymalar göstermiş, HB KAM ise deneylerle en yakın sonuçları vermiştir. Bu tez daha önce depremlerde görülen intersonik kırılmayı mühendislik yapılarında da gözlendiğini ilk kez göstermiştir.

Anahtar Kelimeler**:** Intersonik kırılma, delaminasyon, kompozit malzemeler, çatlak mekaniği, Kohezif Alan Metodu

I would like to dedicate my thesis to my mother Gülçin,

my father Mehmet, my brother Burçin

and

my love Burcu

ACKNOWLEDGEMENTS

TABLE OF CONTENTS

LIST OF TABLES

TABLES

LIST OF FIGURES

xiv

LIST OF SYMBOLS

SYMBOLS

A	Area
a	Half-crack length
A(t)	Loading acceleration
$\bar{A}$	Reduced area
B	Thickness of specimen
$\widetilde{B}$	Matrix relating strain to displacement
c	Ratio of inner to outer radiuses
$C, \widetilde{C}, \widetilde{C}^{\mathbf{Strn}}$	Compliance, compliance matrix in plane stress, compliance matrix in plane strain, respectively
C_d	Dilatational wave speed
C_R	Rayleigh wave speed
C_s	Shear wave speed
d	Damage
$d_{0.6}$	Definition of crack tip with partially (60%)damaged cohesive interface
$d_{1.0}$	Definition of crack tip with fully (%100) damaged cohesive interface
E, E'	Modulus of elasticity, modulus of elasticity for plane strain isotropic material
$\bar{E}$	Damaged loading/unloading stiffness of interface
E_0	Penalty stiffness value
E_{11}, E_1	Longitudinal modulus of elasticity in chord (fiber) direction
E_{22}, E_2	Modulus of elasticity in transverse (perpendicular to the fiber) direction
E_{33}, E_3	Modulus of elasticity in the thickness direction
E_r	Modulus of elasticity in radial (normal) direction
E_θ	Modulus of elasticity in hoop direction
F	Force

f_c	Stitching density
G, G_i	Energy Release Rate in mixed-mode, in mode- i (i = I,II,III), respectively
G_c, G_{ic}	Fracture Toughness in mixed-mode, in mode- i (i = I,II,III), respectively
$G_{ic,\infty}$	Limit fracture toughness under infinite loading speed for mode-i (i = I,II,III)
$G_{io,0}$	Static fracture toughness under quasi-static loading for mode-i (i = I,II,III)
h_i	Thickness of arm, i
H_n	Constants of Newton-Cotes integration for node set, n (n = 1,2)
i	Node number, mode index
J	J-integral, Jacobian
j	Iteration number
k	Ratio of rate-dependency
K, K_i	Stress Intensity Factor in mixed-mode, in mode- i (i = I,II,III), respectively
$\widetilde{K}$	Tangent stiffness matrix
K_c, K_{ic}	Critical Stress Intensity Factor in mixed-mode, in mode- i (i = I,II,III), respectively
L	Length of arm, Left crack tip (fully damaged, experimentally observable, mode-I)
ℓ	Left crack tip (Partially damaged, mode-II)
l_{CZ}, $l_{CZ\text{-}i}$	Length of cohesive zone, length of cohesive zone under mode-i (i = I,II,III), respectively
L_e	Length of the smallest element dimension in mesh
M	Moment load
$\widehat{M}$	Mass matrix
M_s	Acting moment on a section location
n	Node set
$\widetilde{N}$	Matrix of shape functions
N_e	Number of elements per ply thickness

N_n	Shape functions for node set, n (n = 1,2)
h_e	Height of element
P	Axial load
$\hat{P}$	External load vector
$\hat{P}_{r,ch}$	Internal load vector due to cohesive traction
$\hat{P}_r$	Internal load vector
q	Flexural distributed loading, ratio of works of separation of mode-II to mode-I conditions for Xu-Needleman Cohesive Zone Model
$\tilde{Q}$	Matrix relating separation to displacement
$\tilde{Q}'$	Matrix relating displacement to separation
R	Right crack tip (fully damaged, experimentally observable, mode-I), Resistance curve
r	Right crack tip (Partially damaged, mode-II)
r	Radius, dimensionless parameter in Xu-Needleman Model.
$\hat{R}$	Transformation (rotation) matrix
R_i, R_m, R_o	Inner, mean and outer radiuses, respectively
S	Surface Area
S_{ij},	Components of stiffness matrix (i,j = 1,2,.,6), stiffness matrix in plane stress, respectively
S_L	Distance between left crack tip (L) and the initiation point
S_R	Distance between right crack tip (R) and the initiation point
t	Time
t_L	Loading duration
T, T_i	(Cohesive) multi-axial traction, traction vector, traction under mode-i loading (i = I,II,II), respectively
$\hat{T}_{ext}$	External traction vector
t_{elp}	Elapsed time to damp kinetic energy triggered by loading
$t_{in,BL}$	Time of initiation for the simulation using Bilinear Cohesive Zone Model
$t_{in,RD}$	Time of initiation for the simulation using Rate-Dependent Cohesive Zone Model

$t_{in,XN}$	Time of initiation for the simulation using Xu-Needleman Cohesive Zone Model
t_{in,XN_1}	Time of initiation for the simulation using Xu-Needleman Cohesive Zone Model with single interface
$T_{io,0}$	Static interfacial strength under quasi-static loading for mode-i ($i =$ I,II,III)
$T_{io,\infty}$	Limit interfacial strength under infinite loading speed for mode-i ($i =$ I,II,III)
T_o, $T_{o,i}$	Maximum traction/interfacial strength in mixed-mode condition, maximum traction/interfacial strength under mode-i ($i =$ I,II,III), respectively
u, $\hat{u}$	Displacement, displacement vector, respectively
U,U_i	Displacement loading, displacement loading in direction, i ($i =$ x,y,z), respectively
U_L	Total displacement of loading
$\hat{u}_e$	Nodal displacement vector with respect to global coordinate system
V	Shear load, crack tip speed, volume
$V(t)$	Loading speed
V_c	Critical speed
w	Width of the specimen
w_e	Length of cohesive element, width of elements
α	Total angle of curved region
β	Ratio of mode-II separation to mode-I separation
γ	Engineering shear strain, dimensionless factor for bi-material interface cracks
γ_p	Phenomenological surface energy density
γ_s	Surface energy density
$\dot{\delta}$	Separation velocity
δ, δ_i	Mixed-mode separation (relative displacement of crack surfaces), separation due mode-i loading ($i =$ I,II,III), respectively
$\dot{\delta}_c$	Reference critical separation velocity

δ_c, $\delta_{c,i}$	Critical separation in mixed-mode condition, critical separation under mode-i (i = I,II,III), respectively
δ_I^*	Separation in normal direction for a total failure of interface due to mode-II loading without a mode-I load for Xu-Needleman Cohesive Zone Model
$\delta_{ic,0}$	Static critical separation under quasi-static loading for mode-i (i = I,II,III)
$\delta_{ic,\infty}$	Limit critical separation under infinite loading speed for mode-i (i = I,II,III)
$\delta_{io,0}$	Static onset separation under quasi-static loading for mode-i (i = I,II,III)
$\delta_{io,\infty}$	Limit onset separation under infinite loading speed for mode-i (i = I,II,III)
$\dot{\delta}_o$	Reference onset separation velocity
δ_o, $\delta_{o,i}$	Onset separation in mixed-mode condition, onset separation under mode-i (i = I,II,III), respectively
ε_{xx}, ε_{xy}, ε_{xz}	Normal strain in x-axis, shear strain in y-axis, shear strain in z-axis on yz-plane, respectively
ε_{yy}, ε_{yx}, ε_{yz}	Normal strain in y-axis, shear strain in x-axis, shear strain in z-axis on xz-plane, respectively
ε_{zz}, ε_{zy}, ε_{zx}	Normal strain in z-axis (generally to the page direction), shear strain in y-axis, shear strain in x-axis on xy-plane, respectively
$\widehat{\Delta}$	Separation vector in global coordinate system
Δt	Stable time incrementation
Δt_{BL}	Time after initiation for the simulation using Bilinear Cohesive Zone Model
Δt_{RD}	Time after initiation for the simulation using Rate-Dependent Cohesive Zone Model
Δt_{XN}	Time after initiation for the simulation using Xu-Needleman Cohesive Zone Model
δx	Virtual parameter of x
Δx	Change (delta) of x

ζ, k_L	Dimensionless material parameters
η	Non-dimensional constant, curve-fitting constant for B-K criterion
θ	Angular location in curved region, Angle of shear Mach wave front
θ_c	Total angle of crack
θ_e	Orientation of interface element
κ	Constant for lengths of cohesive zone
λ	Non-dimensional constant, Lame's constant
μ	Shear modulus of elasticity for isotropic materials, Lame's constant
μ_{ij}, G_{ij}	Shear modulus of elasticity in ij-plane ($i,j = 1,2,3$ or $i,j = $ x,y,z)
μ_{ss}	Coefficient of friction for Coulomb model.
ν_{ij}	Poisson's ratio ($i,j = 1,2,3$ or $i,j = $ x,y,z)
ξ	Non-dimensional longitudinal axis of interface element
Π	Strain energy
Π_e	External work done
Π_{KE}	Kinetic energy
ρ	Density
$\Sigma(\xi)$	Interpolation function of interface element
σ, $\tilde{\sigma}$	Stress (scalar value), stress in tensor form
σ_1	Longitudinal (normal) stress in chord direction ("ply-direction")
σ_2	Normal stress in transverse direction.
σ_3	Normal stress in the thickness direction or opening stress.
σ_c	Critical stress
Σj	Total number of iterations
σ_r	Radial normal or opening stress
$\sigma_{r\theta}$	Radial shear stress
σ_x, σ_{xy}, σ_{xz}	Normal stress in x-axis, shear stress in y-axis, shear stress in z-axis on yz-plane, respectively
σ_y, σ_{yx}, σ_{yz}	Normal stress in y-axis, shear stress in x-axis, shear stress in z-axis on xz-plane, respectively
σ_z, σ_{zy}, σ_{zx}	Normal stress in z-axis (generally to the page direction), shear stress in y-axis, shear stress in x-axis on xy-plane, respectively
σ_θ	Hoop stress

τ	Pseudo-time
φ, $φ_i$	Xu-Needleman cohesive zone model potential function, potential function in mode-i (i = I,II,III), respectively
χ	Strain energy density
$χ_{KE}$	Kinetic energy density
ψ, Ψ	Airy stress function, phase angle, respectively
ω	Angle between axial load and beam cross-section
Ω	Set of nonlinear equations

ABBREVIATIONS

AC   Acoustic Emission

BL   Bilinear (Cohesive Zone Model)

CFRP   Carbon Fiber Reinforced Plastics

CLPT   Classical Laminated Plate Theory

CNT   Carbon Nano Tubes

CTOD   Crack Tip Opening Displacement

CZM   Cohesive Zone Method/Model

EASA   European Aviation Safety Agency

FAA   Federal Airworthiness Authority

FE   Finite Element

FEA   Finite Element Analysis

ILNS   Interlaminar Normal Stress

ILSS   Interlaminar Shear Stress

PSE   Principle Structural Elements

RD   Rate-dependent (Cohesive Zone Model)

UD   Unidirectional Ply

VCCT   Virtual Crack Closure Technique

XN   Xu-Needleman (Cohesive Zone Model)

CHAPTER 1

INTRODUCTION

In the first part of this chapter, the design and applications of L-shaped composite laminates are demonstrated. Next, mechanical loads on L-shaped structures are defined where the rib structures in aircraft wings are taken as reference. Delamination phenomenon in composite structures is briefly mentioned. The definition of the delamination problem in L-shaped composite laminates is made. In the second part, literature review is presented for the delamination of L-shaped composite laminates and thick-curved laminates. The main contributions are presented for each paper for the sake of drawing the total picture in the L-shaped composite laminates to the best of our knowledge. The studies are chronologically presented.

1.1. L-Shaped Structures in Industry

Box structures or *torque boxes* are designed to carry both rotational and translational loads. They are characteristically composed of orthogonal shells forming a closed section [1]. Shells should be connected to each other for continuous load flow within a closed section. As shown in Figure 1, the orthogonally positioned shells require "L" shaped links which have two arms connected to each of the shells. As a result, the load flow is established between the orthogonal surfaces.
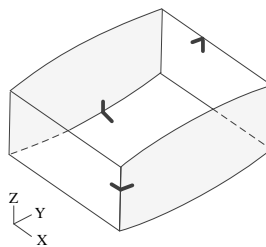
Figure 1 Torque box composed of orthogonal shells connected with L-shaped structures.

In aerospace industry, box structures are encountered in aircraft wings, ailerons, vertical and horizontal tail planes (Figure 2a). A typical assembly of a passenger aircraft wing is shown in Figure 2b. *Skins* are stiffened longitudinally by *spars* and perpendicularly by *ribs*. *Stringers* are generally used to provide out-of-plane stiffness to the skins for enhancing stability of the skins [2]. The wing is indeed a pattern formation of unit torque boxes where a unit torque box is composed of two adjacent ribs, two facing spar sections and two enclosing skins sections. Cross-sections of spars are generally in "C" or "Z" shape as shown in Figure 2c and Figure 2d, respectively. Ribs are similar structures with thinner profile and may involve stringer cutouts (Figure 2e). Spars and ribs are attached to the skins using *fasteners*. Flanges of spars and ribs in the shapes of "C" or "Z" can be decreased to an L-shape as highlighted in Figure 2c-e.

Wind turbine blades are also considered as box structures (Figure 3a). In many cases, spars are laid along the blade span with a rectangular cross-section. Spars work as primary load carrying members in wind turbine blades [3] (Figure 3b). Formations of L-shaped structures can be also seen in the spars of the blades at the corners as shown in Figure 3c.

Several structural configurations of L-shaped parts are illustrated in Figure 4. The L-shaped parts can be a continuation of the remaining structure that is connected to the skin through bolts and nuts (simply by fasteners)(Figure 4a). Or, they can be separate structures fastened to the main body such as illustrated in Figure 4b, so called *L-Bracket*. In highly loaded cases, L-brackets can be mounted to the back of the main structure in a "back-to-back" configuration (Figure 4c).

(a)

Skin

Skin

Ribs

Spar

Spar

Stringers

(b)

Fasteners

Spar

Skin

Rib

Stringer

Cutouts

(c)

(d)

(e)
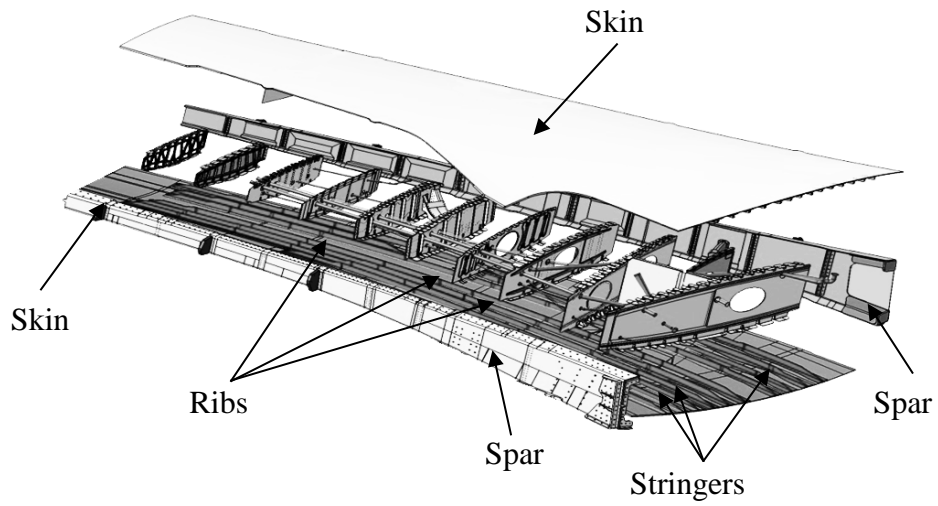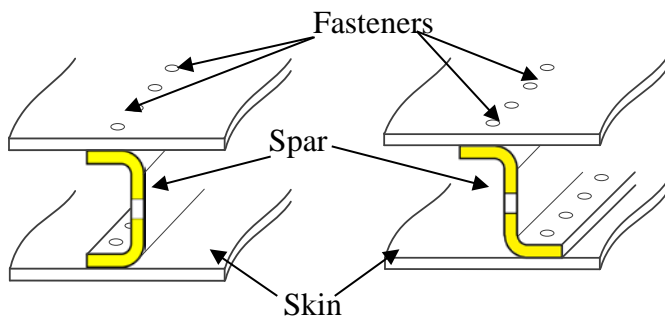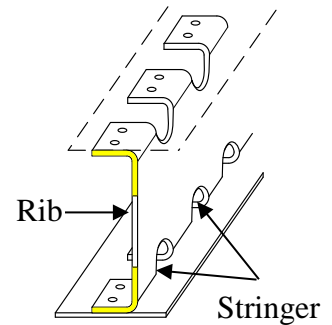
Figure 2 (a) An aircraft with typical box structure locations, (b) wing assembly composed of skins, spars, ribs and stringers where L-shaped formations are highlighted in the assemblies of (c) C-shaped spar, (d) Z-shaped spar and (e) wing rib.

(a)
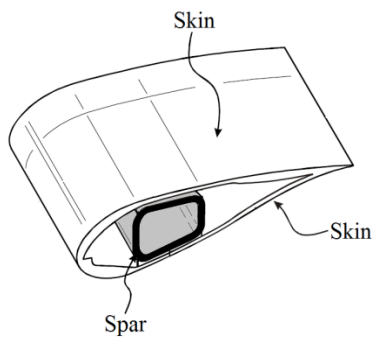
(b)
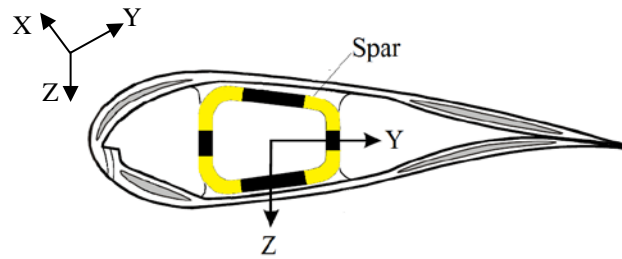
(c)

Figure 3 (a) A wing turbine and its blade, (b) structural details of the blade as a box structure together with (b) spar cross-section where L-shaped flanges are highlighted.
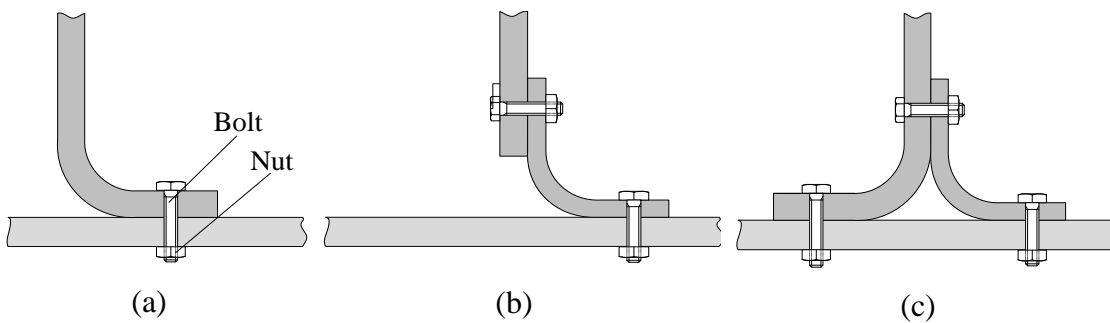
(a)

(b)

(c)

Figure 4 L-shaped parts in the forms of (a) flange of rib/spar, (b) separate part *-L-Bracket-* and (c) "back-to-back" configuration.

1.2. L-Shaped Composite Laminates

Lightweight products are highly preferred in aerospace and wind energy industries. For instance, fuel consumption of an aircraft linearly increases with the weight [4]. A lighter aircraft would either carry more payload or have a longer range with lower carbon emission.

Composite materials have higher *specific strength*, the ratio of the failure stress per unit mass, compared to conventional materials such as Aluminum and Steel [5]. Because of this reason, composite materials are demanded in the market. For example, the new aircraft such as Airbus A350 XWB aircrafts has 53% [6] and Boeing B787 has 50% of composite material in mass, [7]. *Carbon Fiber Reinforced Plastic* (CFRP) material is generally preferred by aerospace industry whereas *Glass Fiber Reinforced Plastic* (GFRP) is typically used in wind blades. Although CFRP is more expensive than GFRP, the CFRP has higher specific strength [5]. In our study, CFRP laminates are concerned.

Aerospace industry has been using composite laminates in planar shapes; such as skins of the wings (Figure 2b). Today, as the composite manufacturing technology advances, composite laminates can be produced in more complex geometries; such as the "L" shape. As a result, metallic L-shaped parts are being replaced by composite counter parts for saving weight.

The manufacturing process of the L-shaped composite laminates is a sensitive process. It is experienced that the manufacturing process directly affects the strength of the L-shaped composite laminates [8]. In industry, several manufacturing trials may be required to reach the desired quality in terms of constant thickness, radius tolerance, surface quality, straightness of the plies, and homogeneity of resin [8,9]. A typical manufacturing assembly of an L-shaped composite laminate for an autoclave curing process is shown in Figure 5. A rigid *Lay-up Tool* works as a smooth surface for supporting the plies at the desired geometry. Noting that, the geometry of the lay-up tool should consider spring back effects after the curing [9]. The material of the lay-up tool can be aluminum, composite, steel or invar according to the thermal effects and cost [9]. A *Release Film* can be located between the laminate and the tool in order to peel off the cured laminate after the process. Laminate plies are laid at desired orientations over the release film. On the top of the laminate plies, *a Bleader*

Ply is laid. The role of the bleader ply is to enhence the vacuuming effect during the curing thanks to its porous surface allowing air flow. By that way, the product has a better surface quality. Next, *Breather* is laid over the bleader ply, which ensures that the vacuum is homogeneously distributed over the laminate during the curing cycle. To the top of them, *Bagging* is covered to insulate the assembly by sealing from the ends. Next, *vacuum lines* are appropriately positioned over the bagged assembly. In some cases, additional tools such as *Caul Plates* can be used in order to control the resin flow and relative motion of the plies during the curing [9]. The curing cycle takes 2 to 4 hours under a pressure of 5 - 7 bars with several temperature steps up to 180°C.
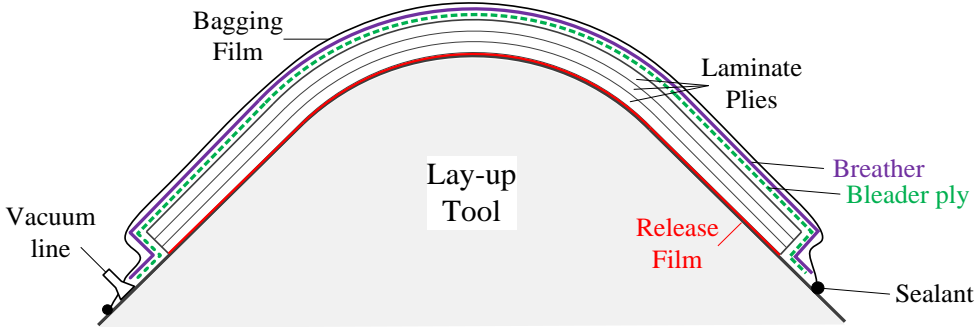
Figure 5 Manufacturing assembly of L-shaped laminate to be cured in an autoclave.

1.2.1. Mechanical Loads on L-Shaped Structures

According to airworthiness certification documents [10], spars and ribs are Principle Structural Elements (*PSE's*) of which failures catastrophically affects the structural integrity of the airplane. Moreover, these parts are highly loaded during the flight. Structural integrity of their L-shaped flanges is therefore critical.
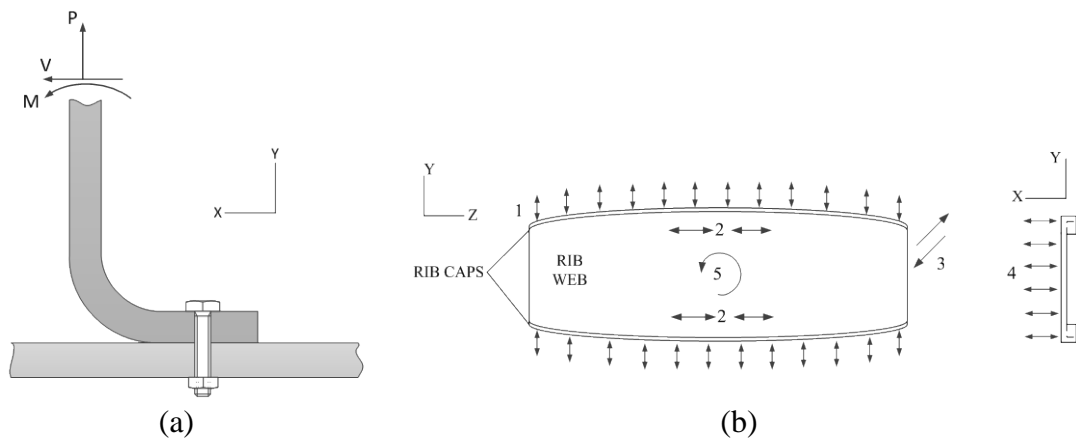
Figure 6 (a) In-plane sectional forces on an L-shaped rib flange and (b) types of loads observed in aircraft wing ribs.

In-plane sectional loads on an L-shaped part are *axial load*, P, *moment*, M and *shear load*, V as shown in Figure 6a. Mechanical loads on the wing ribs can be used to understand physical sources of the sectional loads on the L-shaped rib-flanges. Figure 6b shows the types of loads by numbered from "1" to "5" which are described as follows [2];

Load Type "1": This type of loading is generally induced by aerodynamic and fuel pressure. A compressive load can be induced due to the wing bending, so called "crushing load" or "brazier load". Load Type "1" yields axial force, P, and the moment, M, on the section of the L-shaped rib flanges (Figure 6a).

Load Type "2": It includes compressive and tensile loads in the x-direction (Figure 6b-right). It is created by the Poisson's ratio effect of the skin or related to the end loads of the adjacent spars. The direction of the resulting load is through the page for the L-shaped rib flange given in Figure 6a. Hence, Load Type "2" does not have any influence to the sectional loads in Figure 6a.

Load Type "3": This type of loading is formed by the shear flows in the wing or induced by the large flight control surfaces such as flaps and ailerons. As a result, it yields shear load, V, on the L-shaped rib flanges (Figure 6a).

7

Load Type "4": Fuel pressure and sloshing of the fuel are the main sources of this kind of loads. It causes the axial force, P and the moment, M on the L-shaped parts shown in Figure 6a.

Load Type "5": This is the torque load induced during the flight. As the torque is dominantly reacted by shear forces in yz-plane, it has a negligible impact to the sectional forces shown in Figure 6a.

1.3. The Problem of Delamination in L-Shaped Composite Laminates
1.3.1. Definition of Delamination

In a composite laminate made of unidirectional (UD) or woven fabric plies such as shown in Figure 7a, cracks may exist in three forms; *matrix crack*, *fiber crack* and *delamination* [11]. Matrix crack is the crack passing through the matrix, which is the resin of the material in composite laminates. An example picture of matrix cracks in a laminate made of fabric plies is shown in Figure 7b. The fibers are normal to the page shown by white dots whereas the orthogonal fibers are seen as white lines. The resin material is seen as gray filling the volume between the fiber bundles. Similarly, the cracks at the fibers are the fiber cracks which are indicated in Figure 7b. In general, matrix and fiber cracks are considered as *in-plane cracks* since they stay perpendicular to the lamina plane, xz and yz-planes in Figure 7. Existence of in-plane cracks degrades in-plane strength and stiffness of the laminates [12,13].

Delamination is a longitudinal crack on the ply plane (xy-plane in Figure 7a) that passes through the interfaces between the layers, so called *ply interfaces* or simply *interfaces* (Figure 7a). Figure 7b shows delaminations in a laminate made of fabric layers. It is seen that delaminations follow the ply interfaces along a slightly curved path. Notably, although the microscopic view resembles slight curvature, the macroscopic fractures surface is straight. Delamination in an unidirectional laminate are shown in Figure 7c where the delamination passes through the interface between 0° and 90° plies.

(a)

Fiber cracks

Delamination

Matrix cracks

(b)
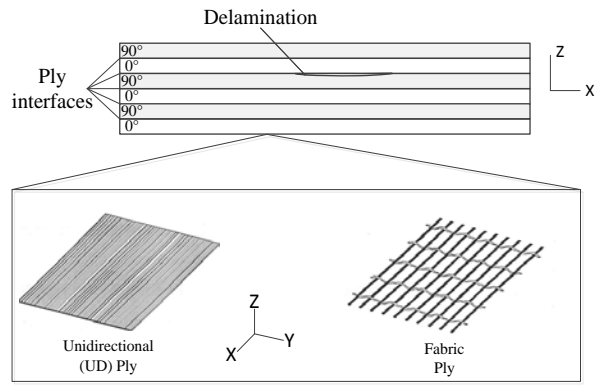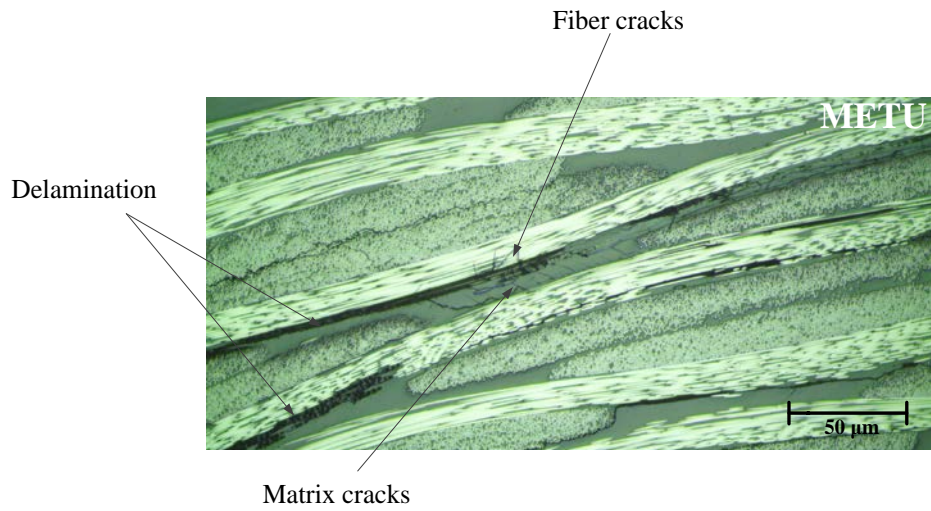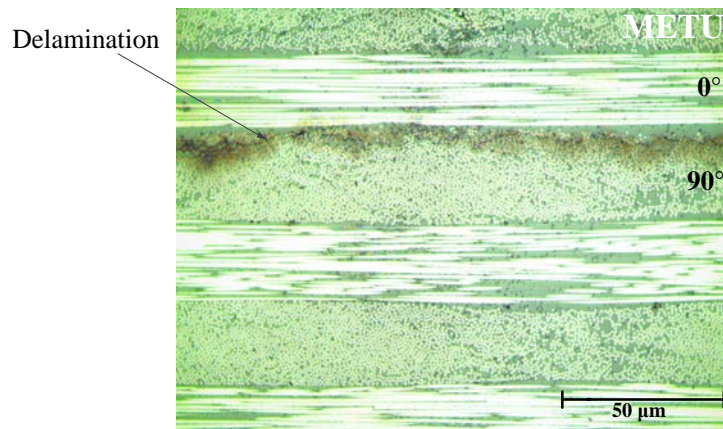
Delamination

(c)

Figure 7 (a) A CFRP laminate made of unidirectional or fabric plies where (b) fiber cracks, matrix cracks and delamination in a fabric laminate and (c) delamination in a laminate made of unidirectional plies are shown. (Courtesy of Department of Aerospace Engineering, METU)

A delaminated laminate loses its flexural stiffness that makes it more sensitive to buckling failure. As seen from Figure 8, the remaining sub-laminates may buckle [12]. Buckling mode of the laminate varies for a single or multiple delaminations. A buckled laminate considerably loses compressive and shear load carrying capacity. In addition to buckling, delamination crack may propagate under cyclic loading [14]. Even for quasi-static loading, the delamination can propagate as in our study. Today, delamination growth is not allowed by the certification authorities (EASA, FAA), no matter it is due to fatigue or static loading [10].
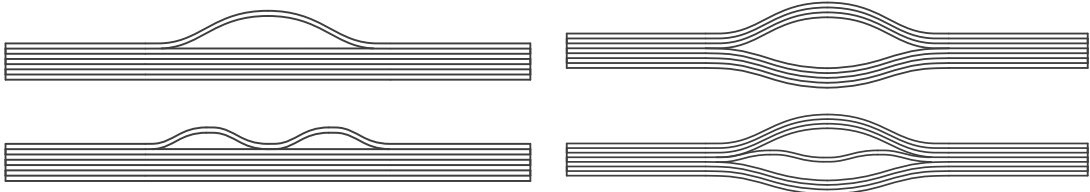
Figure 8 Four typical buckling modes of a laminate with single and multiple delaminations.

1.3.2. Stages of Delamination

There are two stages of delamination failure; *delamination initiation* and *delamination propagation*. Delamination initiation is the stage that the flaw forms on the interface from an intact structure. Generally, initiation stage is studied by using strength of materials approaches based on point-wise stress analysis. On the other hand, the propagation stage is the growth of the initiated or existing crack where the fracture mechanics is considered. It is worthy to note that our method of Cohesive Zone Method is able to handle both the initiation and propagation stages to be discussed in the following sections.

1.3.2.1. Delamination Initiation

Delaminations may initiate during the manufacturing of a laminate. For instance, a forgotten portion of a peel ply or a foreign object that has been left between the plies may lead to delaminations [9]. A wrongly applied drilling process can form delaminations around the exit of the hole [9,15]. Delaminations which are formed

10

during the manufacturing can be captured by the quality control processes such as using non-destructive inspections [9].

In a survey conducted by International Air Transport Association (IATA) in 1991, 40% of composite damages reported by the airliners are because of the impacts during ground handling and the maintenance [11]. For instance, a simple steel hammer used in the maintenance can be mistakenly dropped on the composite laminate, which forms delaminations inside the laminate. As the projectile hit the laminate, the resulting stress waves move through the thickness of the laminate that fractures the lamina interfaces where the stiffness abruptly changes [15]. Actually, the delaminations due to the low-velocity impact are very insidious, and therefore dangerous, since the delamination may not give any indication from the outside [15]. This phenomenon is known as *low-velocity impact* [16,17] which is a dynamic loading condition initiating delamination.

Delaminations can be also spawned from intact composite laminates which do not have any flaws or dynamic impacts. Common sources of delamination in intact laminates are summarized in Figure 9 [15]. It can be inferred that the features shown in the figure are stress concentration regions in conventional aircraft structures. Straight composite laminates may have delaminations at the free edges which are called *free edge effect* [18]. The free edge effect is formed due to unbalance of out-of-plane loads at the ply interfaces near the end of plies as shown in the middle of Figure 9 [15]. Free edges of holes and cut-outs may have delaminations because of the same reason. *Drop-offs,* defined by the ends of the plies which are ending in the mid-regions of the laminate, are also other sources of delamination [19]. In stiffened panels, the stiffener can be delaminated starting from the ends due to the mismatch of the stiffness between the skin and the stiffeners. As seen from Figure 9, the corner of L-shaped composite laminates is sensitive to delamination. Certification Authorities consider the onset of delamination as a failure of the component [10].
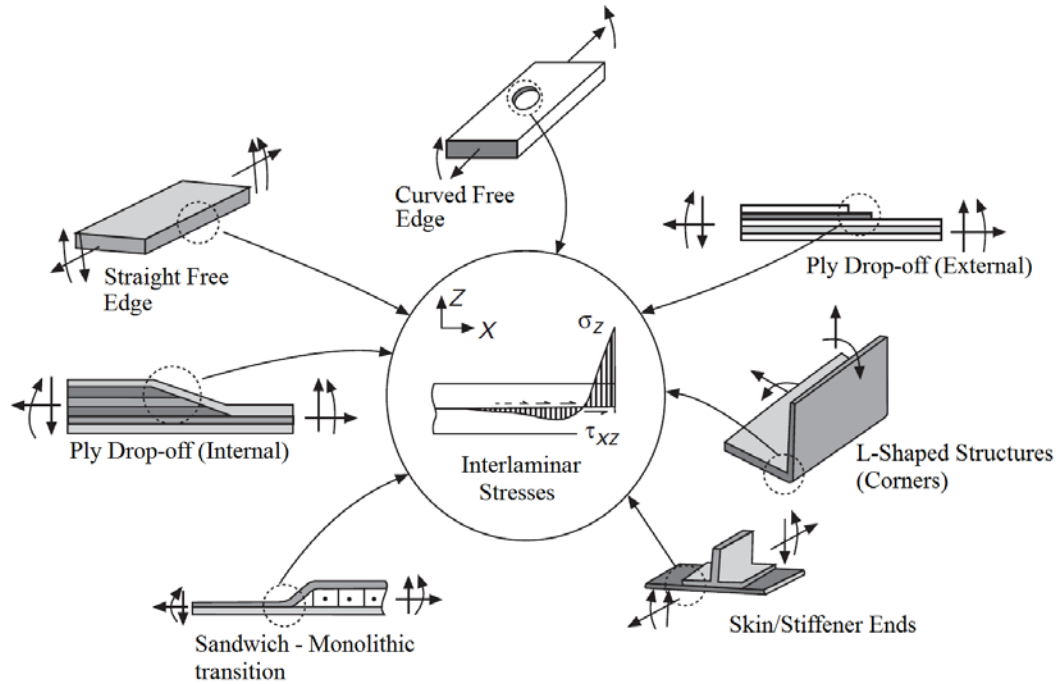
Figure 9 Common sources of delamination in composite structures under specific configurations [15].

The out-of-plane shear and normal stresses on the ply interfaces are called *Interlaminar Shear Stress* (ILSS) and *Interlaminar Normal Stress* (ILNS), respectively. The delamination is initiated as the tractions exceed the ILSS and ILNS strength of the interfaces. There are numerous delamination initiation criteria for multi-axial stress or traction states, such as Chang and Springer [20], Hill [21], Tong-Tsai [22], Norris [22], Tong-Norris [22], Kim and Soni [23], Ye [24], Brewer and Lagace [25] and Puck [26]. These models are mostly quadratic functions forming elliptical surface in terms of applied and critical interlaminar stresses/tractions. The critical tensile and shear interface strengths are called *interlaminar tensile strength* and *interlaminar shear strength*, respectively. In this study, interlaminar (interfacial) tensile and shear strengths are denoted by $T_{o,II}$ and $T_{o,I}$, respectively. The interfacial strengths correspond to *through-the-thickness* or *transverse strengths* of the laminate. Through-the-thickness strengths are experimentally determined, which are determined by the laminate material, stacking and manufacturing processes [27]. Test procedures for the determination of transverse strengths can be found in American Society for Testing and Materials (ASTM). ASTM-D6415 [28] and

12

ASTM-D2344 [29] are used to determine the interlaminar tensile and shear stresses of the laminates.

1.3.2.2.   Delamination Propagation

Residual Strength is the strength of a delaminated part which can still carry load without failure [2]. The propagation of delamination may yield to the ultimate failure of the structure until it exceeds the residual strength. Although delamination propagation is not allowed by the certification authorities, great effort is made to predict the details of delamination propagation in composite materials that would be probably possible in near future.

<div align="center">

(a)   (b)   (c)
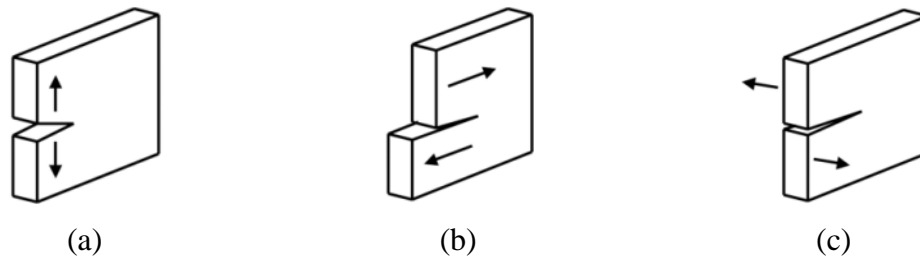
Figure 10 (a) Mode-I, (b) Mode-II and (c) Mode-III fracture modes.

</div>

Energy dissipated to grow a crack by formation of newly created surfaces per length is called *Energy Release Rate,* G [30]. The critical energy release rate required propagating a crack is called *Fracture Toughness*, G_c [31] which is a material/interface property. It can be stated that smaller the fracture toughness, it is easier to propagate the delamination. Energy release rate can be related to *Stress Intensity Factor,* K, which is a stress based approach based on the stress singularity at the crack tip. However, several assumptions in the Stress Intensity Factors, such as the sharp crack assumption, are not applicable to the composite materials. Therefore, energy release rate approach is generally used for delamination analysis in composite materials [31].

In fracture mechanics, the process of crack growth takes place in three modes [31]; Mode-I, Mode-II and Mode-III which are illustrated in Figure 10. The fracture energies and critical stress intensity factors at each mode are independent material

parameters that are respectively denoted by G_{ic} and K_{ic}, i = I, II, III. In Figure 10, it can be inferred that ILNS and ILSS are related to mode-I and mode-II, respectively [31]. They are experimentally acquired for each fiber/resin system, stacking and curing process. Double Cantilever Beam (DCB) (ASTM D5528, [32]) and End-Notched Flexure (ENF) (ASTM WK22949, [33]) tests can be used to determine the mode-I fracture toughness (G_{Ic}) and mode-II fracture toughness (G_{IIc}), respectively. In engineering applications, the delamination generally takes place in mixed-mode condition [34] which is the combined loading of mode-I, mode-II and mode-III. The mixed-mode fracture toughness, G_c, can be experimentally calculated by Mixed-Mode Bending Test (MMB) (ASTM D6671/D6671M, [35]). There are several interaction curves to predict propagation of delaminations in mixed-mode fracture conditions such as Benzeggagh-Kenane (B-K) [36], Reeder [37] and Wu and Reuter [38] criteria. It is noted that propagation criteria are based on fracture mechanics which is different from the delamination initiation criteria based on point-wise stress/traction states. The Problem of Delamination in L-Shaped Composite Laminates

The delamination in L-shaped composite laminates (Figure 11c) is a concrete problem which has been recently raised in aerospace industry. Millions of dollars was paid to repair the L-shaped composite parts since delaminations had been observed at the curved regions of the L-shaped composite laminates in in-service aircraft according to New York Times [39]. More weight is added to the vehicle by repairing the aircraft or by using more layers for strengthening the L-shaped laminates. This results in loss of performance and/or reduction in the range of the aircraft which are not favored by customers. As a result, both the industry and the academy are working on this problem to understand the failure mechanism and take precautions from the design stage.

Manufacturing defects are frequently observed at the curved regions of the L-shaped composite laminates which act as initiation sites for delamination. However, the problem in the L-shaped composite laminates is not because of the manufacturing. There is a much simpler reason specific to the geometry which spawns delamination problem even for the intact laminates which is perfectly produced without any defect. Once a thick beam takes a curved shape, the sectional loads induce radial normal

14

stresses. This fact was analytically shown by Timoshenko and Goodier [40] for isotropic curved beams. For cylindrically anisotropic curved beams, Lekhnitskii [41] proved the formations of opening radial stresses under end forces and moments. In other words, it can be stated that the development of radial normal stress is due to the curved geometry and not related to the type of material or any other reason. Figure 11a provides the positive sign convention for the sectional loads which "opens" the curved region of the L-shaped specimen. The stress state in an infinitesimal element taken from the corner has cylindrical shear ($\sigma_{r\theta}$) – simply the "shear stress" -, hoop (σ_θ) and radial normal stresses (σ_r). The shear and normal radial stresses correspond to ILSS and ILNS on the ply interfaces, respectively. As seen in the opening deformation, a positive value of ILNS means tensile load acting normal to the interface. As a result, positive ILNS promotes mode-I fracture in L-shaped composite laminates [41] (Figure 11b).

Classical Laminated Plates Theory (CLPT) states that the mismatch of the stiffness between the adjacent layers would induce ILSS at the ply interfaces [5]. This means that ILSS develops in any kind of multi-directional laminated composite materials. Therefore, mode-II dominated delamination driven by the ILSS is a well-known phenomenon in the industry. On the other hand, development of positive ILNS is a new issue for the industry as they are used to work with planar laminates (e.g. wing skins), normally do not have positive ILNS due to the straight geometry. However, in L-shaped composite laminates, positive ILNS promotes mode-I together with the mode-II.

The delamination problem because of the development of positive ILNS in L-shaped laminates becomes clearer once the fracture toughness and interlaminar strength of the composite materials are considered. It is known that the mode-I fracture toughness, G_{Ic}, is much smaller than mode-II fracture toughness, G_{IIc}, for conventional composite laminates [27]. For example, the experimental curve of mixed-mode fracture toughness, G_c, as a function of G_{II}/G, where $G = G_I + G_{II}$, is presented in Figure 12 for IM7/8552 laminate [42]. It is seen that involvement of mode-I ($G_{II}/G \approx 0$) reduces the mixed-mode fracture toughness, G_c, simply the toughness of the laminate. From the initiation point of view, the same situation is observed as the normal interfacial strength is weaker than the shear strength in most

of the composites [27]. The weakness at mode-I and interfacial strength in normal direction makes the delamination at the curved region of the L-shaped composite laminates become problematic for the industry (Figure 11c).
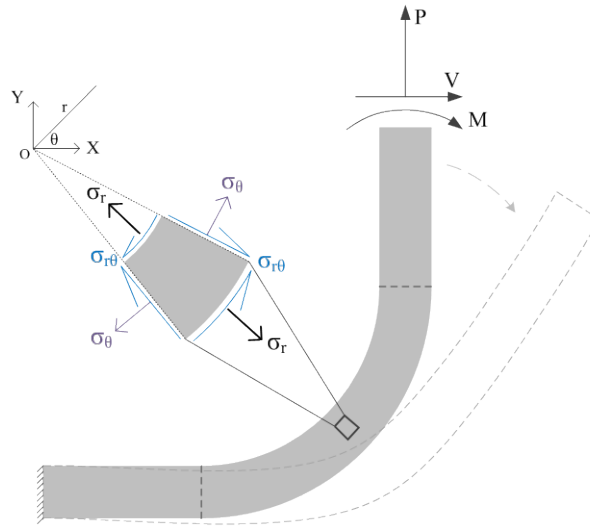
(a)
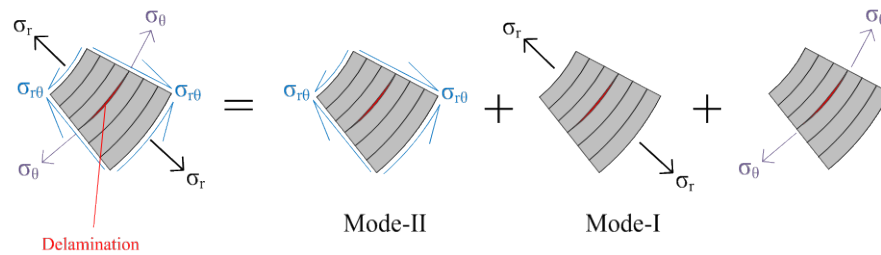
(b)
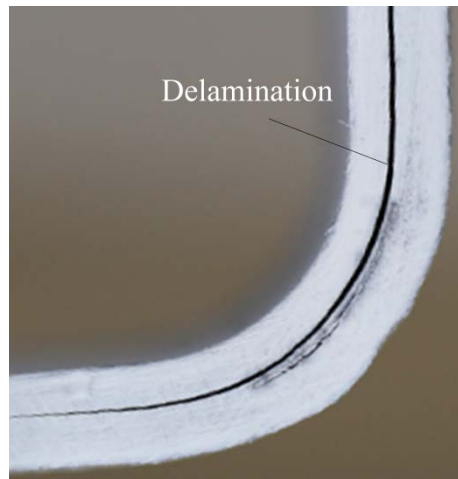
(c)

Figure 11 (a) Stress state of the curved region of an L-shaped composite laminate under positive M, V and P loads, (b) the effects of stress states to the modes of fracture and (c) picture of a delaminated L-shaped composite laminate.

(Courtesy of Department of Aerospace Engineering, METU)

17
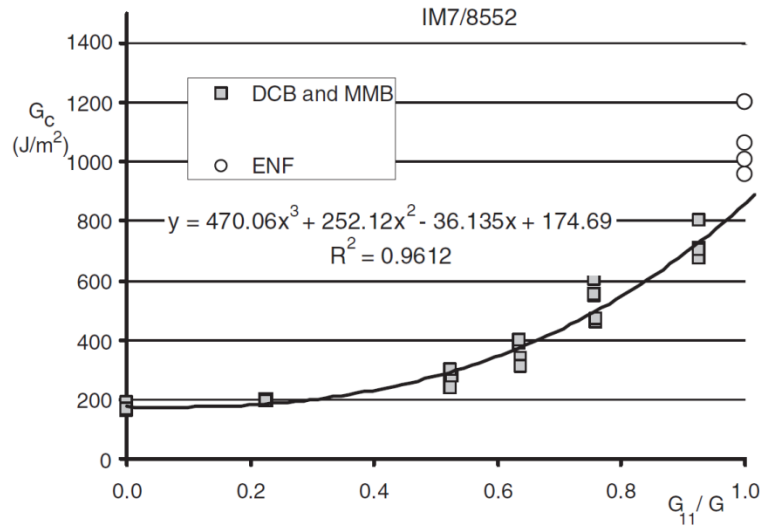
Figure 12 Experimental results of mixed-mode fracture toughness (G_c) as a function of G_{Ic}/G ($G = G_I + G_{II}$) for IM7/8552, [42].

1.4. Studies on Delamination in L-shaped Composite Laminates

In this part, the contributions of the studies about the failure of L-shaped composite laminates are chronologically presented. In some cases, this chapter presents graphs and charts that are worthy to be noted and therefore discussed in detail. This chapter provides the total picture and definitions of some critical information about the subject. It should be noted that some of the studies mention about "curved composite laminates" instead of "L-shaped composite laminates" which are kept as the original in this chapter. Both of the wordings mean the same since the curved region of the L-shaped composite laminates is indeed "curved composite laminate". The nomenclature in this section is kept same with the original studies in order to refer to the corresponding graphs and charts. Hence, the general nomenclature is not applicable to the literature survey presented here.

Until mid-1980's, no studies about the delamination of L-shaped composite laminates has been found in open literature to best of the author's knowledge. In 1986, one of the earliest studies about the failure of L-shaped composite laminates was performed by Chang and Springer [20] in which L-shaped laminates were numerically investigated. The specimen configurations were unidirectional symmetric cross-ply laminates with 0°/90° plies and multidirectional laminates composed of ±30° and ±45° plies. The influences of the layups as well as the

geometrical parameters such as length of the arms (L), inner radius (R_i), total angle of the corner (α) and the thickness (B) were investigated. An in-house finite element code was used. The predictions of the proposed finite element analyses were verified based on hoop stress profile over the thickness for a simply supported composite beam under flexural loading (q) as shown in Figure 13a. The verification was based on comparisons with the results of CLPT and the elasticity solution derived by Pagano [43]. The developed finite element code perfectly agreed with Pagano's elasticity solution whereas CLPT disagreed due to its linear response as shown in Figure 13a. It is seen that the prediction of the CLPT under-predict the stress levels as well as the results are very different compared to the analytical and FEA. In-plane failures were predicted using Tsai-Hill criterion [13]. Furthermore, an elliptical onset of delamination criterion was proposed by Chang and Springer [20].

The effects of the geometrical parameters and stacking sequence were analyzed using the developed finite element code by Chang and Springer [20]. From Figure 13b-d, it can be seen that the strength of the L-shaped laminates is enhanced with increasing the ratio of R_i/B. Addition of 0° plies near the inner and outer radiuses improves the strength of the specimen as shown in Figure 13b. A remarkable observation about the loading direction was reported by Chang and Springer [20]. In all configurations of the parameters, the shear load, F in Figure 13b-c, directed towards the positive x_2-axis fails the specimen in lower loads than the case of shear loading acting towards the opposite direction (Figure 13c). In other words, the load that increases the angle of the corner is more critical than the loads decreasing the angle according to Chang and Springer [20]. As the inner radius increases, this difference is reduced as shown in Figure 13b-d. The strength can be reduced by increasing the length of the arms respect the thickness, L/B, according to Figure 13d. It is due to fact that the moment acting on the corner increases in longer arms. The effect of angle of the corner, α, is not as conclusive as the other parameters from the figures. It was reported that the delamination was found to be the main failure mode. It can be inferred that delamination is the failure mode, without regarding the stacking and the geometrical parameters, as long as the radius is small and the shear loading is in positive direction which "opens" (increases the corner angle) the curved region of the L-shaped laminate.

19
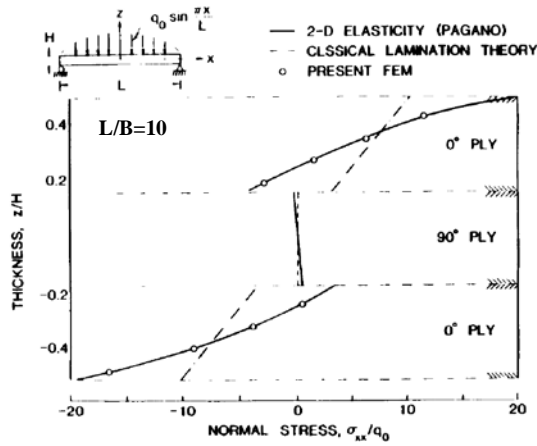
(a)
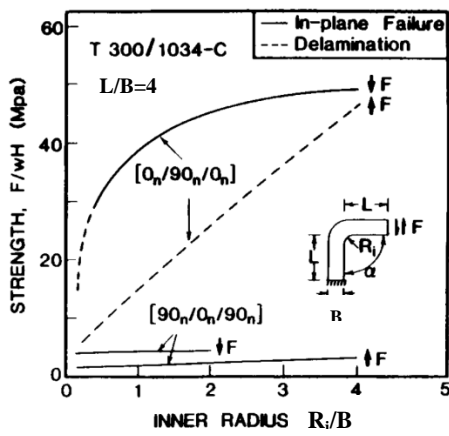
(b)
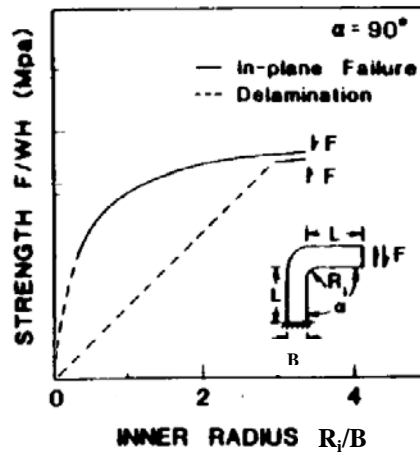
(c)
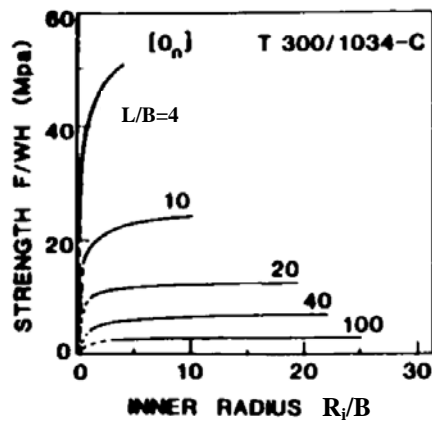
(d)

Figure 13 (a) Hoop stress divided by the maximum distributed load as a function of thickness, (b) normalized strength versus ratio of inner radius to thickness R_i/B plots for (b) effect of stacking, (c) loading direction and (d) the length of arm (L/B) [20].

20

Sun and Kelly [44-46] performed sets of experimental and numerical studies in which the failure of L-shaped composite laminates was investigated in detail. The L-shaped composite laminates were made of CFRP and GFRP plies. The length of the arms and the inner radius were 3. and 0.18 inches, respectively, and the widths of specimens were changed between 1. to 2. inches. Three different layups were studied; "Layup-H": $[90/0_3/90_2/0_3/90]_s$ made of CFRP, "Layup-I": $[90_3/0/90_3/0/90/0]_s$ made of CFRP and "Layup-J": $[90_3/0_3/90_2/0_3/90]_s$ made of GFRP. The experimental setup is shown in Figure 14a where the load is applied by the load cell through a mechanism which creates bending moment and the shear force on the curved region. An optical microscope was located near the corner so as to observe formations of matrix cracks during the experiments. In Layups-H and J, initial failure was caught by the optical microscope as radial matrix cracks at 0° plies near the inner radius. It was reported that the formation of radial matrix cracks did not cause failure of the specimens without any indication in the load-displacement curves. It was reported that the failure always occurred due to delamination revealing an abrupt drop in the load carrying capacity. The load levels of initiation of the radial matrix cracks varied form 60% to 90% of the failure load. It was thought that the delaminations were formed due to the propagation of the initiated radial matrix cracks through the interfaces. In Layup-I, delamination took place at the 0°/90° interface near the inner radius without any formation of matrix cracks. A finite element method with plane strain assumption was used by Sun and Kelly [44] for the numerical analysis. The predictions of the numerical models were verified by elasticity solution proposed by Timoshenko and Goodier [40] for homogeneous isotropic curved beams. For predicting the initiation of matrix cracks, Hill [21] and Tsai-Hill [13] criteria were used. Hill criterion successfully predicted the required load for matrix cracks within an error margin of 5%. On the other hand, Tsai-Hill criterion underestimated the failure load which is not conservative. The elliptical criterion proposed by Chang and Springer [20] was used for the onset of delamination. The numerical results were in good agreement with the experimental results for both the initiation of matrix cracks using Hill criterion and t onset of delamination using Chang and Springer criterion.
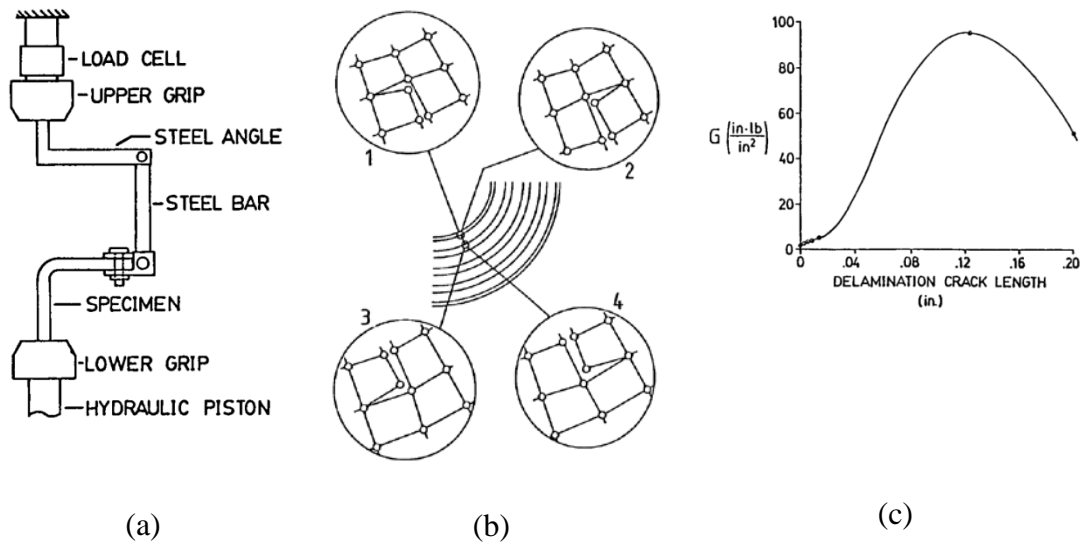
Figure 14 (a) Experimental setup, (b) possible paths of matrix crack branching towards ply interfaces that form delamination and (c) typical energy release rate profile as a function of delamination crack length by Sun and Kelly [44-46]

The delamination failure was rigorously investigated in the second part of the study of Sun and Kelly [46]. Virtual Crack Closure Technique (VCCT) [47] was used. Noting that, no crack propagation was simulated; VCCT was only used for calculating energy release rates at discrete lengths of cracks. Since the delamination was initiated by radial cracks in the experiments presented in their previous study [45], an initial radial matrix crack was modeled by disconnecting the nodes. Four possible branching paths of the radial matrix crack are shown in Figure 14b. For each path, the crack was extended by a small amount and the corresponding energy release rates were calculated using VCCT. The branching path providing the maximum energy release rate was selected and the model was re-meshed, accordingly. The energy release rate curves as a function of delamination length were found for the layups. All the curves resembled similar profile just like the one shown in Figure 14c. The energy release rate increases up to a maximum value after when the curve goes down but never reaches below the initial value. This indicates that the delamination growth is unstable inside the curved region. This conclusion was supported by the experiments in that delaminations were always able to be trapped at the arms. Actually, these are typical observations that were repeatedly reported by

22

the other authors working on L-shaped laminates as going to be mentioned in the following paragraphs.

Sun and Kelly [46] proposed to use adhesive films between the interfaces of 0°/90° plies in order to strengthen the laminate against delamination. The idea was to increase the maximum interlaminar tensile strength and toughness by minimally affecting the stiffness and the weight of the laminate. The experiments showed that the maximum load capacity was increased by at least +55% using adhesive films. Moreover, delamination never started at the interfaces where adhesives were applied. In addition, Sun and Kelly [46] suggested using caul-plates during manufacturing of L-shaped composite laminates.

Kedward et al. [48] proposed a simple strength of materials approach to calculate the maximum stresses in the curved region for engineering design applications. The proposed equations provide the maximum normal radial stress ($\sigma_r^{max}(\theta)$) and the maximum shear stress ($\sigma_{r\theta}^{max}(\theta)$) on the section at any angular location, θ, as shown in Figure 15.
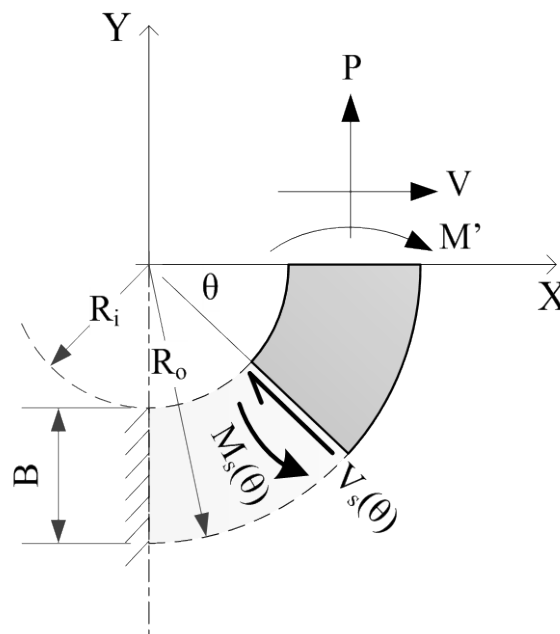
Figure 15 Freebody diagram of the curved region of an L-shaped beam.

The formulations derived by Kedward et al. [48] have been widely used in aerospace industry. The maximum out-of-plane stresses at the corner were given as follows, [48];

$$\sigma_r^{max}(\theta) = \frac{3}{2} \frac{M_s(\theta)}{B\sqrt{R_i R_o}}, \qquad \sigma_{r\theta}^{max}(\theta) = \frac{3}{2} \frac{V_s(\theta)}{B} \qquad (1)$$

where B is the thickness of the beam, R_i is the inner radius, and R_o is the outer radius. $M_s(\theta)$ is the moment force and $V_s(\theta)$ is the shear force acting on the section as a function of θ, which can be found from the freebody diagram given in Figure 15;

$$M_s(\theta) = M - PR_m[1 - \cos(\theta)] + VR_m \sin(\theta)$$

$$V_s(\theta) = -P\sin(\theta) + V\cos(\theta)$$

$$(2)$$

where R_m is the mean of R_i and R_o. Eqns.(1) and (2) were verified by Kedward et al. [48] with the analytical solution and finite element analysis. Interestingly, the strength of materials approach provided satisfactorily good results compared to the analytical solution and finite element analysis.

Kardomateas [49] derived analytical solution for the stress states of cylindrically orthotropic curved beams with linearly varying elastic constants under bending. It was one step ahead of Lekhnitskii's equations [41] since the equations of Kardomateas allowed linear variations of elastic constants through the thickness. This is a better approximation to multidirectional composite laminates. However, the resulting solution was provided in terms of infinite series functions that are hard to be applied. In the next study, Kardomateas [50] presented analytical solution for generally anisotropic curved beams with linearly varying elastic constants under end forces. However, the analytical solution included both complex as well as infinite series functions.

A semicircular composite specimen was proposed by Ko and Jackson [51] for investigating the delamination behavior under mode-I condition. Moreover, a multilayer analytical model based on anisotropic elastic theory of Lekhnitskii [41] was also proposed. The derivation was similar to the one performed by Tolf [52] who conducted the stress analysis of curved composite laminates using continuous and

discrete methods. The equations of Ko and Jackson [51] covered both the moment and the translational loads. The profile and the location of the maximum radial normal stresses were calculated using the proposed equations and the results were compared to the FEA and anisotropic elastic theory of Lekhnitskii. It was seen that the derived formulations demonstrated better results than Lekhnitskii's equations compared to the FEA.

The specimens proposed by Ko and Jackson [51] may induce mode-II delamination at the edges of the loading points. Therefore, Ko and Jackson [53] proposed new types of specimens for the analysis of mode-I delamination in curved composite laminates. Ko and Jackson [53] proposed a horse-shoe shape specimen and an elliptical shape specimen for ensuring mode-I delamination. They also analyzed the delamination of curved sandwich structures. They showed that elliptic specimen was not suitable for the analysis of de-bonding strength in sandwich structures whereas the horse-shoe specimen was suitable for sandwich structures.

Hiel et al. [54] also proposed experimental semicircular and elliptical specimens for determining through-the-thickness strength of laminated composites. It was shown that the elliptical specimens were unusually stronger than the circular ones under static and fatigue loads. On the other hand, circular specimens were more sensitive to flaws that could exist from the manufacturing stage. Surprisingly, the curved composite laminates did not indicate any change of compliance prior to fatigue damage. It was shown that through-the-thickness strength was reduced by increasing the moisture content in the laminate.

O'Brien and Salpekar [55] investigated the effect of specimen volume to through-the-thickness strength (interlaminar shear and interlaminar tensile strengths) of unidirectional CFRP laminates including L-shaped beams. A remarkable observation was made that through-the-thickness strength reduces as the thickness increases. No conclusion could be made about the effect of width due to large scatters in the data. They concluded that flaws of micro voids and resin rich pockets increase with thickness. As a result, thick composites have weaker interlaminar shear and tensile interfacial strengths ($T_{o,I}$ and $T_{o,II}$) due to accumulation of microflaws by increasing the thickness.

One of the pioneering researches was performed by Martin [56] from NASA. According to Martin [56], initiation of delamination is driven by excessive interfacial tensile stresses, compressive matrix crack formation near the inner radius or free edge effect as illustrated in Figure 16a. In the experiments, an L-shaped composite laminate was loaded by shear loading. The specimen was 24-ply unidirectional CFRP laminate with 3mm of thickness. Martin [56] observed that the failure was always due to delamination in the form of single and multiple delaminations (Figure 16c). However, large scatters in the failure load were reported in the experiments. The propagation of delamination was reported as instantaneous and unstable. The delamination had propagated to ends of the arms where they were trapped. Analytical study based on orthotropic elastic solutions by Lekhnitskii [41] and FEA with 2D plane strain assumption using NASTRAN [57] were performed to calculate the stress states along the specimen. Initiation and propagation of delamination were not predicted by Martin [56]. It was noted that the maximum radial normal stress was attained near the middle of the thickness but close to the inner radius. Martin [56] suggested that the thick and thin sub-laminates successively fail after the first delamination forms in the original laminate.

Martin [56] used VCCT method to calculate energy release rate for several lengths of delamination. They noted that mode-I energy release rate reaches the maximum near the middle regions of the curved region after when it starts to decrease closer to the ends of the corner. The mode-II energy release rate became apparent near the ends of curvature where mode-I energy release rate was to diminish. In other words, mode-I dominated delamination propagation occurred inside the corner whereas mode-II became apparent near the ends of curved region.

In 1993, Martin and Jackson [58] studied two stacking configurations in cross-ply CFRP L-shaped laminates under static and fatigue loading. The layups were "Layup-A" of $[0_4/90_3/0_5]_s$ and "Layup-B" of $[0_4/90_3/0/90_2/0_2]_s$. The experiments were conducted on the same setup with the same specimen given in Martin [56]. They reported that all the specimens were failed due to delamination. For Layup-A, tensile matrix cracks were observed at 90° ply batch. However, matrix cracking did not yield to failure of the specimen. Afterwards, subsequent delaminations were seen due to excessing the interlaminar tensile strength at 0° ply batches. For Layup-B, a

straight matrix crack was formed at both of the 90° ply batches due to the in-plane tensile loading. It was concluded that 90° plies tend to create delamination because in-plane tensile cracks propagated to the interface.

In addition to the experimental study, numerical analysis of the problem was also studied by Martin and Jackson [58] on NASTRAN [57] using 2D and 3D elements. It is important to note that the results of 2D models with plane strain assumption were in perfect agreement with the prediction of 3D models. Furthermore, Martin and Jackson [58] revealed the free edge effect by 3D FEA using VCCT method. It was shown that energy release rates were the highest at the free edges. Prediction of failure point using the interfacial strengths obtained from the centerline was in well agreement with the experimental results compared to the predictions based on the free edge effect. In other words, structural analysis based on free edge effect was mentioned as "over-conservative". The maximum radial stress was found using the equations of Lekhnitskii and compared to the experimental data. For the interlaminar shear cracking, Tsai-Hill [13] criterion was used. The transverse static and fatigue tensile strength of the matrix were acquired by 90° flat coupon tests. On the other hand, interlaminar tensile strengths were directly obtained from curved laminates. The fatigue and static strengths of the cross-ply L-shaped laminates were experimentally revealed.

In 1993, equations of motion for thin and moderately thick curved laminated composite beams were derived by Qatu [59]. Rotary inertia as well as shear deformation was included into the equations for moderately thick curved beams. Influences of rotary inertia, inner radius, thickness, material properties and shear deformation on the natural frequencies were also discussed.
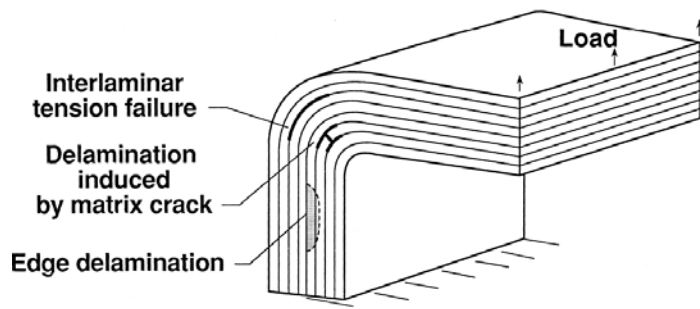
(a)
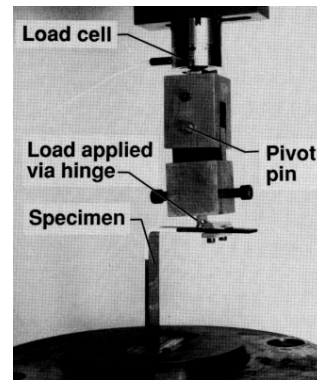
(b)
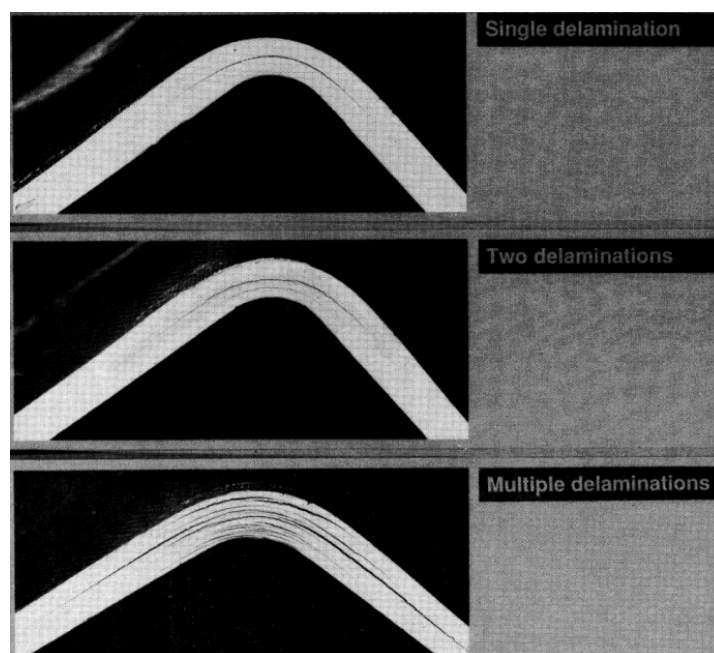
(c)

Figure 16 (a) Summary of failure modes in L-shaped composite laminates, (b) experimental setup and (c) pictures of single, double and multiple delaminations observed in experiment by Martin [56].

Lu et al. [60] formulated the energy release rate of circumferential cracks in cylindrically orthotropic curved beams under bending. The problem was considered as a superposition of an intact curved beam under end moment loading and a cracked curved beam with opening radial tractions acting on the crack interface (Figure 17). As the intact beam has no stress singularity, the stress intensity factor of the original problem is equal to the stress intensity factor of the cracked curved beam with opening radial tractions acting on the crack interfaces.
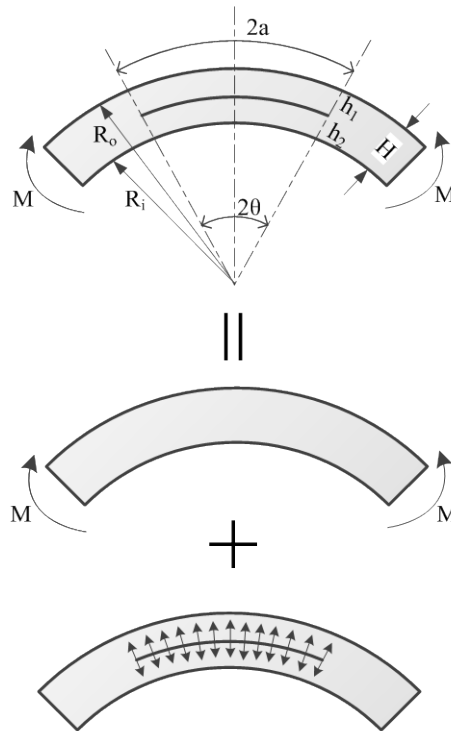
Figure 17 Problem of a cracked curved beam under moment loading and superposition of an intact curved beam under moment and a cracked curved beam with opening radial traction acting on crack interfaces.

For a small crack in the middle of the beam, the crack was considered in pure mode-I condition. By this assumption, energy release rate with small crack assumption, G_I^s (superscript, "*s*" stands for small crack) was derived by Lu et al. [60];

29

$$G_I^s(\theta_c) = \frac{M^2}{B^3 E_1} \pi \lambda^{-3/4} \left(\frac{a}{B}\right) \left(\frac{\sigma_r B^2}{M}\right)^2 \sqrt{\frac{1+\rho'}{2}} \qquad (3)$$

where E_1 is elastic modulus in hoop direction and σ_r is radial stress where the former is a material property and the latter can be calculated analytically [40,41]. The dimensionless numbers are defined as; $\lambda = E_2/E_1$ and $\rho' = (E_1 E_2)^{1/2}/(2G_{12})-(\nu_{12}\nu_{21})^{1/2}$ where E_2 is elastic modulus in radial direction, G_{12} is shear modulus and $\nu_{12}\nu_{21}$ is the multiplication of Poisson's ratios. Normalized energy release rate curves $(G_I^s E_1 B^3/M^2)$ with small crack assumption as a function crack angle, θ_c, for $R_i/R_o = 2/3$ at various $\eta = h_1/h_2$ are shown in Figure 18a. It can be observed that the energy release rate is reduced after a critical value between $\theta_c = 40°$ and $\theta_c = 60°$. This means that the crack growth becomes stable after reaching a critical crack length. Moreover, the energy release rate monotonically increases as the crack approaches to inner curvature.

Lu et al. [60] also studied the energy release rate for "large" cracks in cylindrically orthotropic curved beams. The energy release rate was calculated by J-integral around the crack tips using FEA. For an isotropic material ($\lambda = \rho' = 1$), curves of normalized mixed-mode energy release rate as a function of the crack angle, θ_c, for $R_i/R_o = 2/3$ at various $\eta = h_1/h_2$ are presented in Figure 18b [60]. Same observations for the small crack assumption (Figure 18a) are applicable to Figure 18b for the large cracks. Importantly, it is observed that there is a stable crack length. "Mode-mixity" defined by $\tan^{-1}(K_{II}/K_I)$ versus the crack angle, θ_c, is given in Figure 18c. An important observation can be made from Figure 18c is that mode-II becomes dominant as the crack tip approaches to the ends of the corner ($\theta_c = 90°$). It was concluded that the crack may become purely mode-II at the ends of the corner. The modulus in radial direction, E_2, also affects the energy release rate as seen from Figure 18d. It can be inferred from Figure 18d that orthotropy of the material is an important parameter for the delamination response in L-shaped composite laminates.
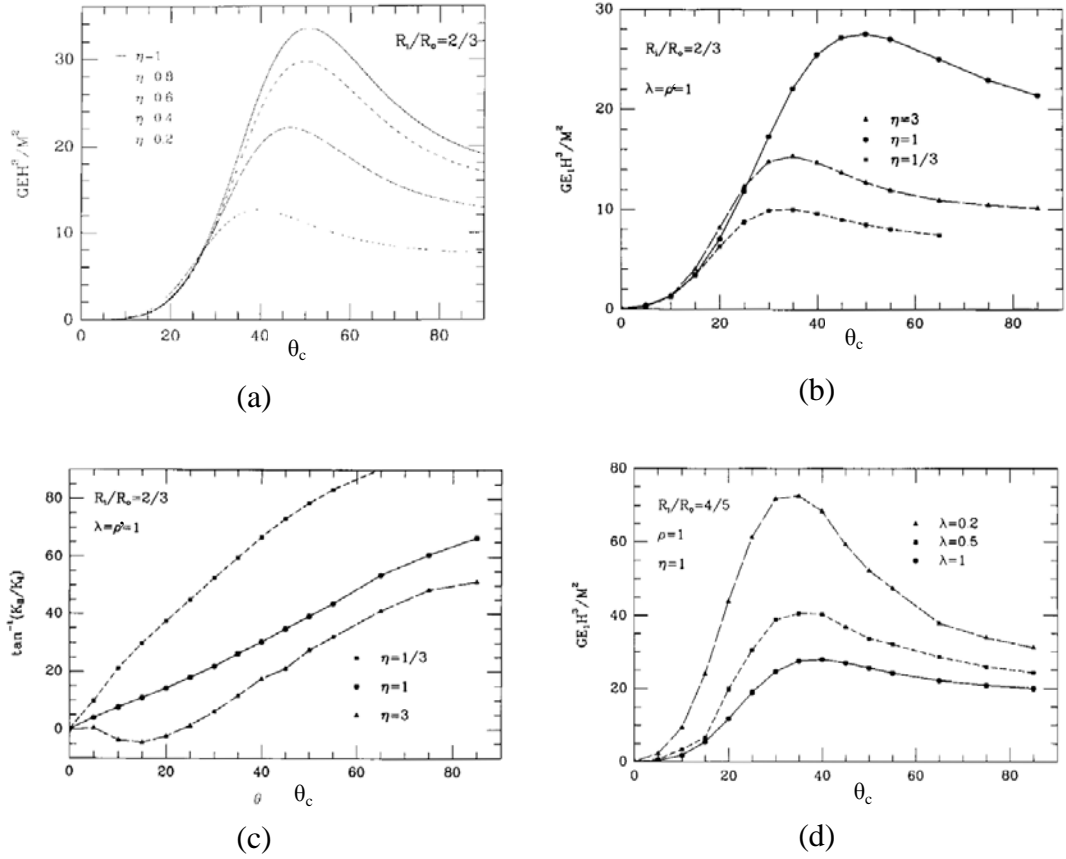
Figure 18 (a) Normalized energy release rate with small crack assumption, (b) normalized mixed-mode energy release rate for large cracks, (c) mode-mixity versus the crack angle, θ_c, for $R_i/R_o = 2/3$ at various $\eta = h_1/h_2$ for isotropic material; i.e. $\lambda = \rho' = 1$ and (d) normalized energy release rate for large cracks versus θ_c for $R_i/R_o = 4/5$ at various λ for $\eta = \rho' = 1$ [60].

In 1994, Shivakumar et al. [62] proposed a test procedure for the determination of interlaminar tension strength of unidirectional L-shaped composite laminates. The specimens were made of 16, 24 and 32 CFRP plies. The proposed test method guaranteed the formation of delamination at mid-layers and center of the curved region. During the experiment, they reported a sound of "pop" at 20% of failure load. They claimed that this was the sound of matrix cracking. The radial locations of the delamination were seen at 45%, 44% and 43% of the thickness for 16, 24 and 32 ply specimens, respectively. The interlaminar tensile stress distribution was calculated using Lekhnitskii's equations and in-house finite element tool with plane strain

31

assumption. The authors also used the strength of materials based approach proposed by Kedward et al. [48] to determine the maximum interlaminar tensile stress in the specimens. Among the three methods, the strength of materials approach of Kedward et al. [48] perfectly predicted the location of the delaminations in 24 and 32 ply laminates. On the other hand, Lekhnitskii's formula provided the best prediction for the 16 ply laminate. Although the difference between the predictions of the three methods was less than 3%, the strength of materials approach proposed by Kedward et al. [48] was favored by Shivakumar et al. [62] due to its simplicity. Shivakumar et al. [62] showed that the interlaminar tension strength of the L-beams decreases as the thickness and the width of the specimen increase. In other words, increasing the specimen volume reduces the interfacial strength of the laminate as shown in Figure 19. This conclusion is a one step further of O'Brien and Salpekar [55] who revealed the same effect on the thickness but not on the width. Actually, this phenomenon is known as *volumetric effect* which is defined by the decrease of the interfacial strengths ($T_{o,I}$ and $T_{o,II}$) by increasing the specimen volume. The reason is to having more microscopic flaws in larger specimens that reduces the interfacial strength of the specimen.
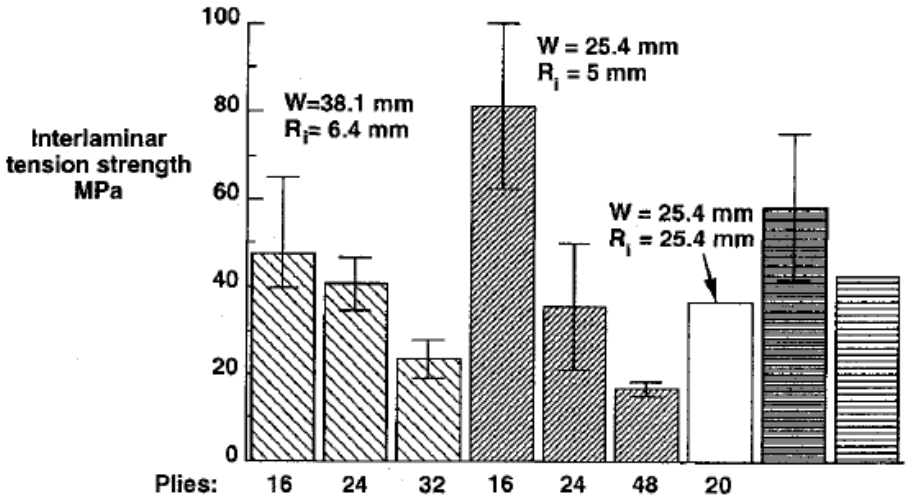
Figure 19 Effect of specimen width, inner radius and thickness to the interlaminar tension strength [62].

Wisnom and Jones [63] studied thick and curved composite laminates with terminating plies at the middle of the specimen under pure bending. The objective was to study two initiation features acting together; interlaminar tensile stresses due to curved geometry and free edge effect due to terminated plies. In the experiments, delamination started at the ends of the terminated plies as expected. Next, the delamination branched into upper and lower interfaces of the terminated plies and propagated along the specimen. Eventually, the terminated plies were separated from the remaining of the laminate. A linear failure criterion was proposed in terms of the interaction of curved geometry and free edge effect. The critical moments for initiating the delamination in an intact curved laminate and a straight cut ply laminate were obtained for using the criterion.

Cui et al. [64] used curved composite beams for determining the interlaminar tensile strength of the composite laminates. The specimen was a semicircular beam with horizontal arms. The beam was loaded by four-point bending which yields pure moment on the middle of the curved region. Cui et al. [64] compared the differences between the predictions of linear and nonlinear FEA. Radial normal stress distributions along the thickness for linear and nonlinear finite element analysis for a curved composite laminate under pure bending are shown in Figure 20. It is seen that linear analysis overshoots the maximum interlaminar stress. It is a crucial observation for aerospace applications where linear static analysis is generally preferred [10]. Hence, the interlaminar tensile strength of the composite laminates can be calculated by nonlinear analysis whereas linear analysis can be used for calculating the actual stress distribution under real loading.
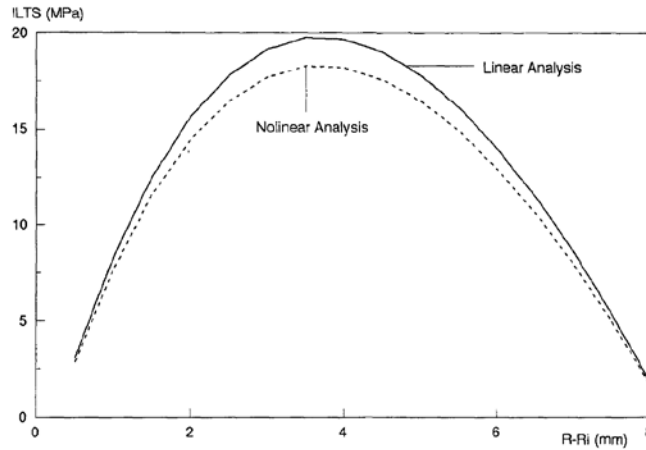
Figure 20 Radial normal stress distributions along the thickness for linear and nonlinear finite element analysis for a curved composite laminate under pure bending calculated by Cui et al. [64].

Cox et al. [65] investigated the influences of through-the-thickness stitching to the delamination in L-shaped composite laminates under pure bending (Figure 21). The objective of stitching was to bridge the crack front. Stitching was aimed to change an unstable delamination growth to a stable bridged delamination growth. A successful stitching was defined as being both stiff and numerous. *Stitching density*, f_c, was defined as the ratio of total cross-section area to the area covered by the stitch fibers. The required stitching density to suppress the unstable delamination propagation was derived based on the study of Lu and Hutchinson [66] where the stitching had been considered as continuous closing tractions on the crack interface. For design purposes, it was mentioned that f_c should be proportional to $(B/R_m)^2$ (Figure 21). Moreover, the suppression was possible after "moderately curved laminates" which was defined as $B/R_m < 0.2$. The stitching was not very effective for thin laminates. For thick parts, the required stitching was lower than the estimated stitching density by the proposed formula since the efficiency of the load transfer between the stitching fibers and the laminate matrix would be better. Stitching density was suggested to be greater than 4% for inhibiting unstable delamination propagation in conventional CFRP laminates with moderate curvatures. The failure mode was expected to be switched to in-plane compression of inner plies as the delamination propagation had been suppressed by stitching.

34
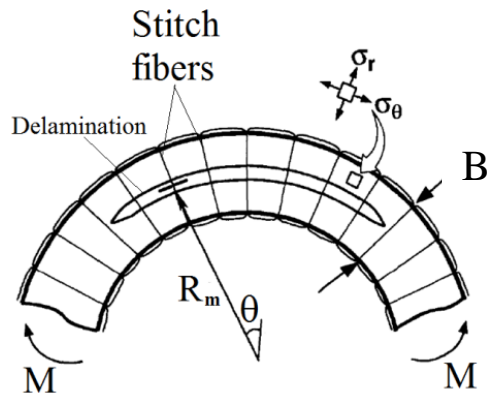
Figure 21 Schematic view of delamination in a stitched curved composite laminate.

In 1997, Fraternali and Bilotti [67] derived a 1D analytical model for L-shaped composite laminates having "bi-modular" plies which is defined by having different compressive and tension modulus. Indeed, conventional CFRP laminates are generally bi-modular. By discretization of the 1D model, finite element model was derived. Each ply was modeled as 1D beam elements and connected by a penalty technique which forces the mating 1D elements in a perfectly bonded condition. The derived finite element model was suggested to be used for analyzing the free edge effect and the influence of bi-modularity of the composite L-shaped laminates.

The free edge effect in curved laminates was investigated by Kaczmarek et al [68], both experimentally and numerically. They noted that classical fracture mechanics is not possible to be applied as there is no asymptotic value of energy release rate in edge delamination. Therefore, although their experimental specimens did not have an initial crack, they postulated an initial crack size which was calculated by the relation between fracture toughness and crack size in the plane strain assumption. On the other hand, the conventional stress analysis method was considered as inconvenient as the free edge delamination has a stress singularity. They proposed an improved fracture-mechanics approach to predict the delamination due to free edge effect. The approach was experimentally validated. The experiment setup was a 4-point bending where a highly curved laminate was used. They noted that the failure of delamination was instantaneously occurred. The method of numerical analysis was VCCT and performed in ABAQUS/Standard using 3D elements [69]. They used Multi-Point-Constraints [69] to model the boundary conditions for a free edge in a

single element. Thermal residual stresses were also included in the model. They concluded that the edge effect was much more severe in curved laminates comparing to the straight laminates where the critical energy release rate was much lower.

The effects of manufacturing process to the thickness variation, fiber volume fraction and eventually the strength of the L-shaped composite laminates were studied by Naji and Hoa [70]. The curing was performed in autoclave at 5.84 bars with two and three temperature stepped cycles. Four specimens, made of 50 layers of CFRP plies, were in different combinations of pressure, number of bleader plies and number of curing steps. First specimen with one layer of bleader ply was cured by 2-step curing cycle while pressurization, so called *debulking,* at each 10 layers had been successively applied. The process of debulking was suggested to remove trapped air from the layers; however, it took additional time. The second specimen with one layer of bleader ply had been exposed to the debulking process at every 5 layers which was introduced to 3-step curing cycle. In the third trial, all the layers had been laid without any debulking process and introduced to 2-step curing with 2 layers of bleader films. The final specimen was made by debulking at every 10 layers of plies by 3-step curing together with two layers of bleader plies. It was seen that the best thickness variation was reached at the third and fifth specimens. Actually, the differences of the thicknesses among the specimens were so small that the effect of curing was not clear. In all the cases, the fiber volume fraction was decreased. A very slight increase of fiber fraction was reached by 3-step curing. No wrinkles or waviness in the plies were observed. The manufacturing process was also numerically simulated. Partial differential equations of heat transfer, resin flow, thermo-kinetic and viscosity were used in two-dimensional finite difference method. The finite difference solution, which is an explicit scheme, was applied to the 2-step and 3-step curing cycles. The thicknesses, the volume fractions and the temperatures of the specimens were well predicted by the numerical analysis. The specimens were tested in axial loading. A remarkable observation was made that the strength of the specimens considerably varied among the manufacturing trials. For instance, the failure load of the third and the fourth specimens had the difference as much as 90%. The number and the locations of the delaminations were also different. This is an important conclusion that the fracture is greatly affected by manufacturing process in the L-shaped composite laminates.

In 2001, Shenoi and Wang [71] derived an analytical solution for laminated curved beams capable of considering stiffness variations in the radial direction. For the derivation, it was assumed that the curved beam was laid on an elastic foundation under moment loading. The reaction of the elastic foundation was taken as the boundary condition using the classical lamination theory. The methodology was applied to monolithic and sandwich laminates so as to investigate the influences of inner radius and layup to the stress distribution. It was shown that the stacking sequence had a considerable effect. For instance, unidirectional laminate showed a rather continuous stress profile whereas a four layer-cross ply laminate revealed a clear piecewise stress profile along the thickness.

Münch and Ousset [72] proposed a numerical method for simulating the propagation of delamination in curved interfaces. Theoretically, it was based on stationary points in total energy of the system that was discretized into mechanical and fracture energies. The discretized model was solved by Newton-Raphson method. The method was shown as a fast method in terms of convergence rate. However, it was noted that it should be coupled with remeshing procedures for the design applications.

Figiel and Kaminski [73] numerically studied delamination propagation driven by thermal fatigue of two layered boron/epoxy-aluminum curved laminates. They predicted the propagation using Paris – Erdogan fatigue model as a function of energy release rate under constant compressive load with cyclic thermal loads. They used commercial FEA package of ANASYS [74] to perform the numerical analysis where contact modeling and Coulomb friction were considered. It was observed that the friction coefficient greatly affected the fatigue life. It showed that increasing the friction coefficient increases the fatigue life. They noted that the contact modeling enabled heat conduction between the boron/epoxy and the aluminum layers. This yielded more realistic simulations in thermal fatigue loading cases. Hence, modeling of contact and friction in the fatigue analysis of curved bi-material laminates were suggested by the authors.

Two years later, Figiel et al. [75] analyzed the effects of elastic constants (i.e. modulus and Poisson ratio) to the delamination propagation for the same specimen under cyclic shear loading. The motivation was based on the uncertainties in the

elastic constants coming from the manufacturing process of boron/epoxy. They used 3D-FEA with a local refinement at the front of a crack at the middle of the specimen. Similar to the previous study [73], Coulomb friction and Paris-Erdogan fatigue model were used. It was seen that the change of moduli was more effective than the change of Poisson ratio. Particularly, increasing the stiffness of the epoxy/boron decreased the fatigue life whereas variations in Poisson ratio negligibly influenced the fatigue life.

In 2005, a remarkable study was conducted by Feih and Shercliff [76] who investigated the failure of L-shaped composite laminates adhesively bonded to composite base and a vertical rib. FEA was carried out using ABAQUS/Standard with UMAT user-subroutine [69], which was used to implement constant damage terms to degrade in-plane and out-of-plane stiffness of the laminate. In-plane damages were calculated using Hashin's criterion for fiber tensile failure, fiber compressive failure, matrix tensile cracking and matrix compressive cracking. The values of anisotropic damage constants, changing from 0.01 to 1.0, were experimentally found. On the other hand, Tong-Norris criterion was used to predict the onset of delamination. The constitutive model of the adhesive layer was based on true stress - true strain data with appropriate plasticity model. 2D plane strain was assumed in the numerical analysis. It was stated that plane strain assumption neglects the free edge effect which was considered as negligible. The plane strain assumption was referred to the study of Wisnom [77] who suggested that plain strain is a good approximation for width to thickness ratios greater than 10. The anticlastic curvatures was related to the magnitude of the term; $v_{12}v_{21}$. It was noted by Feih and Shercliff [76] that the term of $v_{12}v_{21}$ was small for CFRP laminates. For the element formulation, the difference between using quadratic and linear elements was found as 5%. For the sake of performance issues, 4-node linear CPE4 type of elements in ABAQUS/Standard [69] was used. The height of the elements was equal to one ply thickness. The boundary conditions were fine tuned for reaching the same load-displacement curve with the experimental results. The load was applied by displacement input in order to mimic the experimental setup and increase numerical stability. The most realistic loading for L-shaped laminated at the rib flanges are stated as the combined loading of axial and moment. The combined loading was applied by fixing the axial displacement with a prescribed vertical displacement. By

that way, the vertical displacement induced moment loading whereas the fixed axial displacement induced axial load as the arm deforms vertically.
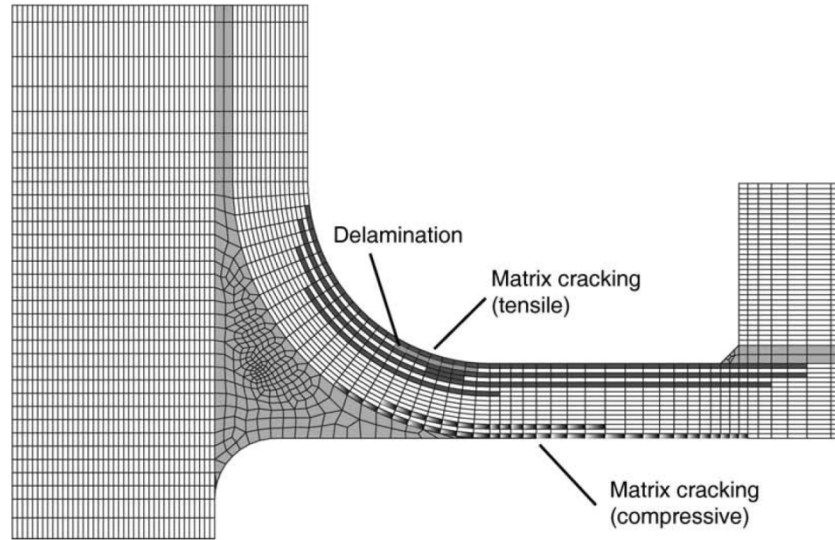
Figure 22 Failure modes observed by Feih and Shercliff [76] in the L-shaped composite laminate.

The experimental specimens used by Feih and Shercliff [76] were cross-ply unidirectional CFRP laminates. The components were exposed to debulging process by vacuuming for 5 min in every four layers in order to get rid of any voids and wrinkles at the corner of the specimens. Thickness deviation in the order of 7-10% was recorded. The effect of spring back was measured as 2° which was considered as negligible. In the numerical analyses, the failure modes are summarized in Figure 22. Delamination was observed between the top and the adjacent plies at the corner. Delamination was the failure mode in the experiments. However, before the formation of delamination, the first failure was obtained at the top 45° ply as tensile matrix cracking about 20% – 28% of the failure load. Afterwards, tensile matrix cracks were observed at the adjacent three 45° plies by then jumping to 0° and 90° plies. The next failure mode was recorded as compression matrix cracking at the bottom 45° plies corresponding to 55% - 84% of the maximum load. Meanwhile, a small portion of 90° plies was failed by tensile matrix cracking at the same load. They noted that none of the matrix cracks are visible from the load-displacement

curves. However, as a rule of thumb, 30% of the failure load was suggested to be considered by the designers as the first failure of the structure for matrix cracking. The delamination strength was overshoot by the numerical model as 17% which was considered as satisfactory by the authors. Actually, over estimation of failure loads were generally the case in the study of Feih and Shercliff [76]. This result was explained by not modeling the residual stresses in the finite element analysis. In order to compensate, three artificial modifications to the maximum loads were proposed. The first proposal was to reduce the fiber strength as -15%. Second was to reduce the through-the-thickness strength by -55%. The final proposal was combined reduction of through-the-thickness strength by -20% and the fiber strength by -10%. The effect of interlaminar shear strength was considered as negligible. Moreover, no fiber breakage was reported in the study. They suggested that the internal radius should be larger than 15 mm and the ratio of internal to external radiuses should be less than 0.75, and preferably less than 0.6, in order to have the strongest L-shaped design. It was shown that L-shaped beams with small radius tend to fail at the inner sides of the corner whereas corners with larger radiuses fail at the outer plies under bending. Keeping the arm lengths as the same, it was shown that increasing the radius enhances the maximum load capacity of the structure. They also analyzed the effect of stacking to the maximum failure load. Putting 90° plies closer to the symmetry line increased the maximum load capacity of the L-shaped laminates. Finally, they proposed an elliptical failure criterion of axial and moment loading can be used for design purposes.

Ecsedi and Dluhi [78] proposed a 1D analytical model for static and dynamic analyses of non-homogeneous curved beams due to radial material and geometric variations. The curved beam was assumed as Rayleigh-Bernoulli-Euler beam which is a modified version of Euler-Bernoulli beam with rotary inertia. The equations of motion for free and forced un-damped vibration were derived. Examples for simply supported and clamped boundary conditions were demonstrated. Natural frequencies and mode shape factors were calculated for various cross-sections.

Numerical analysis of delamination initiation and propagation in L-shaped composite laminates was conducted by Wimmer et al. [79] in 2006. The specimen was a cross-ply CFRP laminate composed of 15 plies with the thickness of 2.25 mm, inner radius

of 2.25 mm and arm length of 6.4 mm. Quasi-static loading of shear displacement was applied to the vertical arm while the bottom of horizontal arm was clamped. The simulations were carried using ABAQUS/Standard with plain strain elements in the size of 1 μm. The numerical simulation was divided into two parts. The first part was the initiation analysis based on Puck criterion [26] which is capable of estimating matrix cracking, fiber cracking and delamination initiation failures as well as the relative risk factors, i.e. *Reserve Factors*, for each failure mode. Map of risk factors for failures and failure modes are shown in Figure 23a and Figure 23b, respectively. The highest risk is seen in delamination failure inside the laminate between 5th and 6th plies which is one ply inside from the middle of the specimen. In the second step of the analysis, VCCT was used in conjunction with ABAQUS/Standard under quasi-static loading. The mesh was updated for various cracks lengths at the critical delamination location determined by the Puck criterion. It should be noted that CZM had been also used by Wimmer et al. [79] for verification of the method. The results of VCCT and CZM were in perfect agreement. The snap-back behavior in the load-displacement curves of the L-shaped composite laminates were revealed as shown in Figure 23c. They concluded that the delamination propagation is unstable in L-shaped composite laminates that can be seen from the snap-back behavior in the load-displacement curve.

Ross et al. [80] developed an analytical model for calculating interlaminar normal stress (ILNS) in curved laminates. Generally, ILNS is calculated by using 3D dimensional elements. Hence, Ross et al. [80] studied shell elements in order to obtain transverse stresses such as ILNS. They formulated the displacement of a curved and thick orthotropic laminate by assuming constant thickness and constant shear angle during the shear deformation. ILSS and ILNS were reformulated by proposing an appropriate displacement field. The results of 3D FEA in ANSYS and their methodology were in well agreement. They had also conducted an experiment of a moderately thick curved unidirectional and cross-ply specimen. In the experiments, they used Acoustic Emission (AC) devices for locating the failures. AC provided noises before the delamination occurs which pointed matrix cracking. More noises were recorded by AC during the abrupt load drop in the load-displacement curve. They observed more scatter in the results of ILTS compared to ILSS.

(a)

(b)

(c)
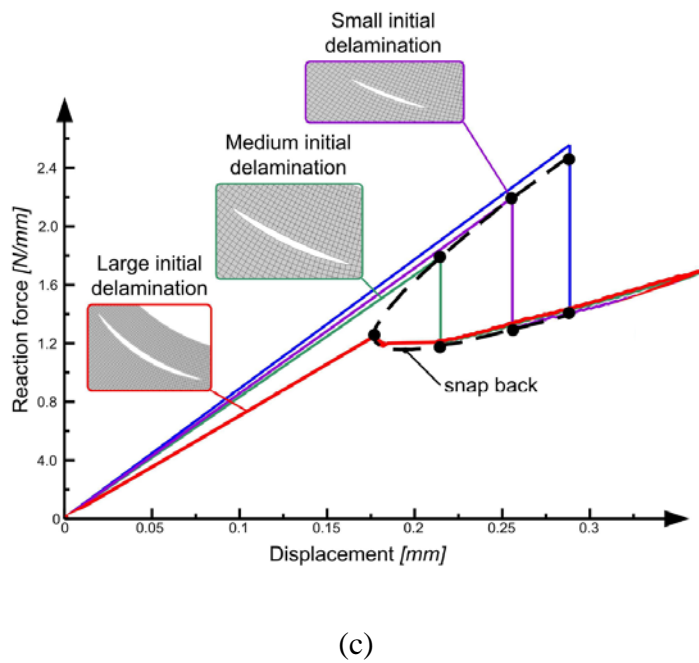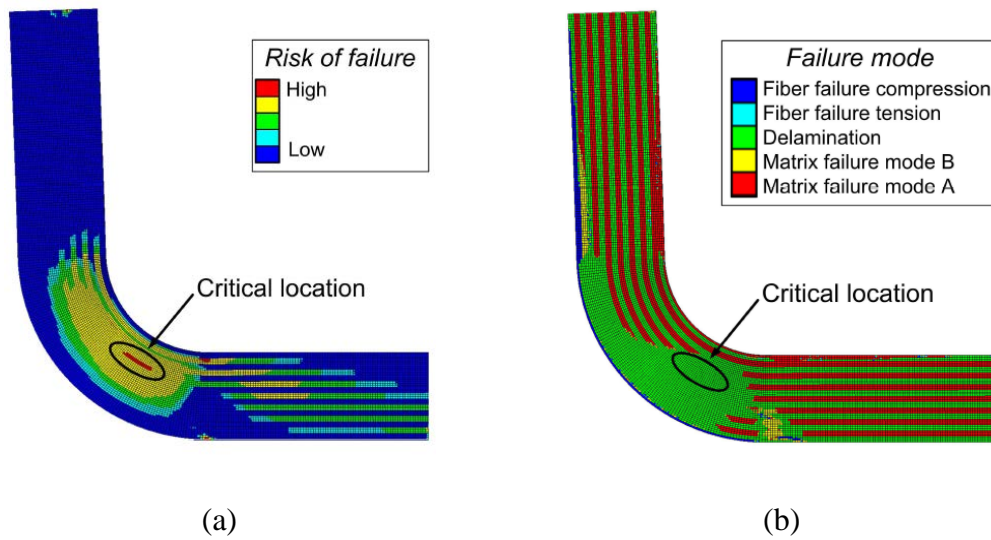
Figure 23 (a) Map of risk factors and (b) failure modes predicted by the Puck criterion and (c) load-displacement curves obtained by Wimmer et al. [79].

Vanttinen [81] studied the delamination initiation in L-shaped composite rib flanges. The main purpose was to find a failure prediction method for the strength of composite rib flanges. The loading case was axial loading and specimens are CFRP laminates made of fabric plies. Several laminate thicknesses, inner radiuses, bolt diameters and the layup configurations have been studied. Laminate thicknesses varied from 5.36 mm to 14.92 mm and inner radiuses changed between 5mm and 10 mm. Fastener diameters of 6.35mm, 9.52 mm and 12.7 mm were also studied. The idea of using different fastener diameters was to investigate the stress concentration effects. The layup of the laminate were symmetric and balanced in various configurations composed of 45°/0° orientations. Vanttinen [81] proposed an experimental setup to determine the interlaminar tensile strength of composite laminates and compared to ASTM D6415 tests. It was observed that ASTM D6415 provided the minimum scatter in data as well as conservative results compared to the proposed experimental setup. No FEA was performed by Vanttinen [81]. Instead, an iterative analytical method was used. Firstly, the moment distribution along the corner was calculated by the equations given in ESDU 84039 [82]. The equations in ESDU consider the contributions of the bolt and nut to the load distribution. Next, Lekhnitskii's equations were used to calculate the stresses at sets of angles using the moment distribution found in the previous step. Afterwards, the failure load for the onset of delamination was calculated using Puck and Tsai-Hill criteria. By using this method, the influences of the mentioned design parameters were found. A useful table, which summarizes of the effects of design features of L-shaped composite flanges, is presented in Table 1. It is seen that the strength of the part increases with larger bolts or higher modulus of the bolt material. It was explained that stiffer bolts induce higher moments acting on the laminate. Similarly, increasing the distance between the bolt and the vertical arm was stated as a reduction factor for the strength. The accuracy of the predictions made by Puck and Tsai-Hill criteria were also revealed by Vanttinen [81]. It was shown that Puck criterion always overshot the delamination failure compared to experimental results. Conversely, Tsai-Hill always provided conservative failure estimations such that failure loads in the experiments were always higher.

A semi-analytical model for the simulation of delamination in laminated composite structures was proposed by Wimmer and Pettermann [83]. The analyzed L-shaped

specimen was a 15 ply CFRP laminate with a thickness of 2.25 mm, inner radius of 2.55 mm and arm length of 6.4 mm. The part was clamped from one of the arms while a horizontal quasi-static displacement was applied to the other arm. The Griffith's crack growth criterion [30] was used to predict the required load for the propagation. The rate of change of compliance with respect to the change of crack length was calculated using ABAQUS/Implicit. An initial delamination was given at the interface which is one ply inside from the mid-layer. Influences of spatial parameters defining the location of the tips of delamination crack were investigated. Griffiths' stability condition based on the minimum potential energy [30] was used to define the stability of the crack propagation for different locations of crack tips. Zones of stable and unstable propagation as a function of the spatial parameters were calculated. It was seen that larger delaminations tended to be more stable in L-shaped composite laminates. In parallel to the Griffiths' theory, the stable cases had no snap-back behavior. On the other hand, snap-back behavior was obtained for the unstable cases.

Table 1 Effects of design parameters to strength of L-shaped laminates [81].

Design Parameter	Change in parameter	Effect on interlaminar shear strength	Effect on interlaminar tension strength
Nut outer diameter	+	0	+ L
Washer outer diameter	+	0	0
Washer thickness	+	0	0
Specimen thickness	+	+ L	+ N
Arm length	+	0	+ N
Distance from bolt to corner	+	0	- N
Elastic modulus of fastener	+	0	+ N
Specimen width	+	+ L	+ L
Corner Radius	+	+	+
"+": Strengthen/increase "-": Weaken/decrease "0": No effect "L": Linear effect "N": Nonlinear effect			

One year later, both initiation and propagation of delamination in L-shaped composite laminates were experimentally and numerically investigated by Wimmer et al. [84]. The L-shaped composite specimen was a cross-ply CFRP laminate of which thickness was 3.75 mm, the length of horizontal arm was 50 mm and the length of vertical arm was 29.5 mm. Two sets of specimens were manufactured; specimens including an initial delamination of 3mm on the interface and intact specimens without delamination. One of the arms was clamped while the other was pulled quasi-statically with displacement control. During the experiment, the corner section of the L-shaped specimen was observed by Digital Image Correlation System (DIC) which is a 3D image correlation photogrammetry ARAMIS system. The system was used for acquisition of the deformation that was used to obtain contours of principle strains during the experiment. ABAQUS/Standard is used for the numerical analysis of delamination. The two step method proposed and used by Wimmer et al. [79]. The total length of the failed elements predicted by the Puck criterion was taken as the initial delamination length as shown in Figure 24a by the solid line. Next, VCCT analysis was performed for various lengths of initial delaminations as shown in Figure 24a by dash line. The intersection of the solid and dash lines was considered as "the critical delamination length" which is assumed as the initial delamination. The initial delamination corresponds to point "1" of the load-displacement curve as shown in Figure 24b. It is seen that the load increases to 800 N in 2.3 mm of displacement when a sudden load drop occurs. After the peak load, the finite element model having the calculated initial delamination of 0.55 mm was run by VCCT method to simulate the propagation. It was stressed that unstable delamination propagation took place between the points "1" and "3" in Figure 24b. On the other hand, stable propagation was reported between the points "3" and "4" in Figure 24b. The load-displacement curves obtained from the experiments are shown in Figure 24c. In some specimens, second load drop can be observed from Figure 24c where a second delamination was initiated and propagated. Hence, no single way of delamination was observed. It is seen that deviations in failure loads of the experimental specimens were too high. Moreover, the predicted curve is quite different than the experimental curves in terms of compliance and failure load. Authors reported some slippage of the specimens from the test apparatus during the loading that might be the reason for the compliance difference. "Kinking", which is

defined as switching of delamination to adjacent interfaces by passing inside the plies (Figure 24d), was also studied by Wimmer et al. [84]. High levels of shear stresses were stated as relevant to the kinking phenomenon in the L-shaped composite laminates. It was stated that if the top of the delamination front has negative shear stresses, delamination kinks with a positive angle towards 90^0 plies. Reversely, the delamination would kink with a negative angle towards 90^0 plies as the crack front is under positive shear.

Wimmer and Pettermann [85] also studied delamination growth under fatigue loading in L-shaped composite laminates. Similar to the previous studies, the load was applied in shear mode to one of the arms whereas the other arm was clamped. The fatigue analysis was performed on ABAQUS/Standard in conjunction with MATLAB for post processing. The amplitude of the cyclic force oscillated between 1N and 8N. A Paris-Erdogan type fatigue law proposed by Dahlen and Springer [14] for composite materials was implemented into the semi-analytical method early proposed by Wimmer and Pettermann [83]. Starting from zero to 6 mm of initial delamination lengths, the required force and displacement for the propagation were found. It was shown that the required force for fatigue growth was reduced for larger initial delamination lengths. S-N curves were experimentally acquired. After 5×10^3 cycles, considerable growth in the crack tip near the clamped arm took place. For the other crack tip close to the loading point, 10^7 cycles were needed to start delamination growth. This means that the delamination tends to grow towards the clamped arm under cyclic loading in L-shaped composite laminates. Moreover, it was shown that the speed of the fatigue growth in the curved region was much faster than the growth in the arms.
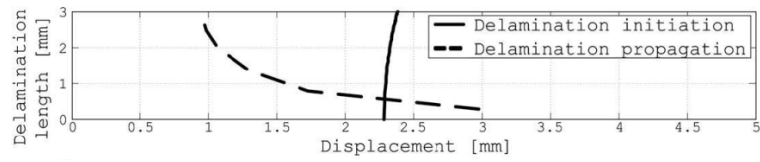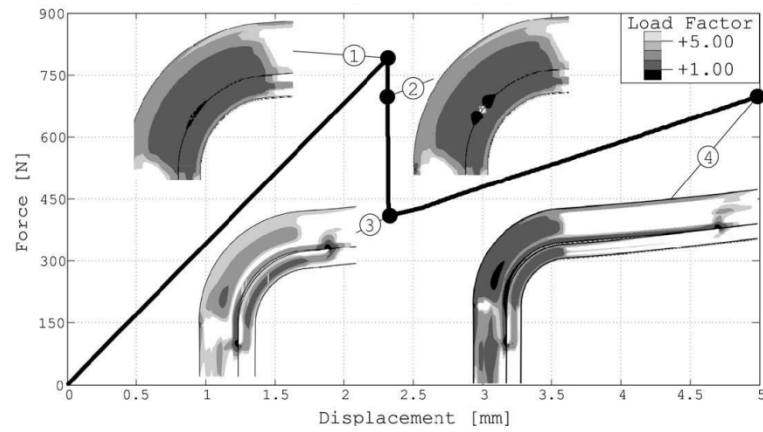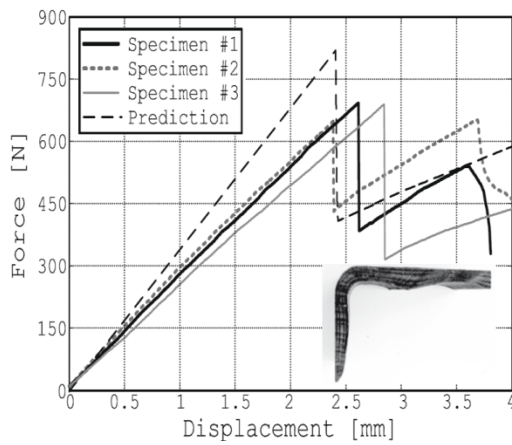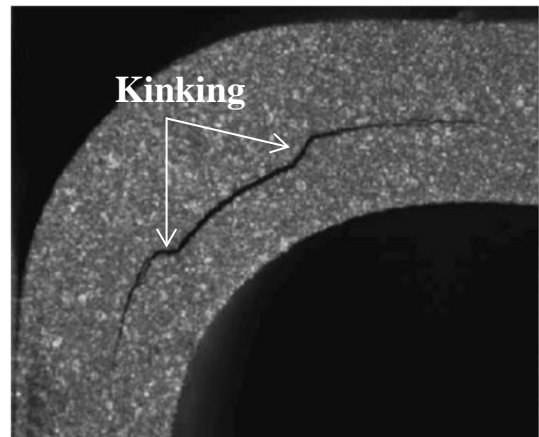
Figure 24 (a) Initial delamination length and propagation curves, (b) load-displacement curves of the numerical simulation, (c) experiments and (d) "Kinking" in L-shaped composite laminates [84].

Avalon and Donaldson [86] investigated the strength of L-shaped composite CFRP laminates by analyzing the effects of inner radius, laminate thickness and introduction of 5% of vapor-grown carbon nano-tubes (CNT's) to the epoxy resin matrix. The numbers of layers of the specimens were 8 and 16 where the inner radiuses were 3.175 mm and 6.35 mm, respectively. They calculated *Curved Beam Strength* (CBS) numerically and experimentally referring to ASTM D6415 [28]. They compared the results of the maximum radial stresses calculated by the analytical formulation given in ASTM D6415 [28]. In the numerical analysis, they also performed 3D-FEA using ABAQUS/Standard to extract the radial stresses. Load-displacement curves were also obtained. It was shown that the results of FEA, experiments and analytical calculations yielded approximately the same results in terms of maximum stress. The maximum radial stress was always between 30 MPa – 32 MPa not regarding the thickness and the radius of the specimen. They noted that CNT's were filtered out by the fabrics during the curing cycle and tended to be moved to the interfaces. Therefore, inclusion of CNT's was expected to increase the interfacial strength since they would act like a through-the-thickness reinforcement on the interface. However, the effect of additional vapor-grown nano-fibers demonstrated nearly no effect on the interfacial strength. An important observation was that the specimens with high thickness to the inner radius ratios and laminates enhanced by carbon-nano-fibers tended to show "slip-stick" failure mechanism resembling a stepped but without abrupt load drop in the load-displacement curves. Although the failure load did not change significantly, the specimens exhibiting slip-stick failures provided higher toughness to the specimen. The second important observation was that the failures showing slip-stick mechanism had always single crack whereas the other specimens showing abrupt failure bearing multiple cracks throughout the laminate.

Hoa et al. [87] experimentally investigated the standard test of ASTM D6415/6415M of a curved unidirectional CFRP laminates using *Digital Speckle Correlation Method* (DSCM). The interlaminar deformation and delamination of the curved laminates at different curvatures and thicknesses were studied. Three different thicknesses with 20, 40 and 60 layers with three different inner radius/thickness ratios (R_i/B) of 0.8, 1.0 and 1.5 were studied. From the experiments, they concluded that the effect of

R_i/B to the laminate compliance was negligible whereas the effect of thickness was dramatic. It was seen that CBS was linearly improved by increasing the thickness. CBS was also increased with higher R/B values but not as effective as the thickness. Oppositely, the maximum radial normal stress was decreased with increasing the thickness. This phenomenon was explained by the volumetric effect in L-shaped composite laminates. Hoa et al. [87] obtained directional strains prior to the failure by DSCM. They recorded that the strain energy was highly dissipated during the fracture process. The authors always observed the first failure at 0°/0° interfaces. They noted that the toughness of the interfaces between 0°/90° and -45°/45° plies were four to two times more than 0°/0°, respectively. The damage zone at the crack was observed in the form of fiber pullout, matrix micro-cracking and fiber-matrix interface failure. The major failure modes were declared as delamination, matrix cracking along the fiber direction and fiber failure.

In 2012, Gozluklu and Coker [88-90] numerically investigated the unstable dynamic delamination propagation in unidirectional L-shaped composite laminates. An initial delamination of 1 mm was located in the middle of the L-shaped laminate with the arm length of 10 mm, inner radius of 5 mm and the thickness of 3 mm. The loading case was the axial loading which is applied quasi-statically. It was shown that the stress distribution under axial loading yielded considerably high mixed-mode profile compared to the shear loading case as shown in Figure 25a where the mode-mixity is defined by absolute value of the ratio of opening radial stress to shear stress. The strong mode-mixity in the axial loading case further motivated the authors for performing dynamic analysis which is known as critical in the mixed-mode condition [91]. For this purpose, interface elements having Bilinear CZM in ABAQUS/Explicit [69] were used to model the dynamic fracture. As the loading was quasi-static, the analyses would take too much time by the explicit solver. Hence, linear-elastic part of the response was solved using implicit analysis (Figure 25b). The remaining part, including the snap-back behavior and the delamination propagation, was solved using the explicit solver (Figure 25b). The solution scheme ameliorated the convergence issue due to the snap-back behavior during the load drop as well as the dynamics of the propagation stage was revealed by the explicit solver.
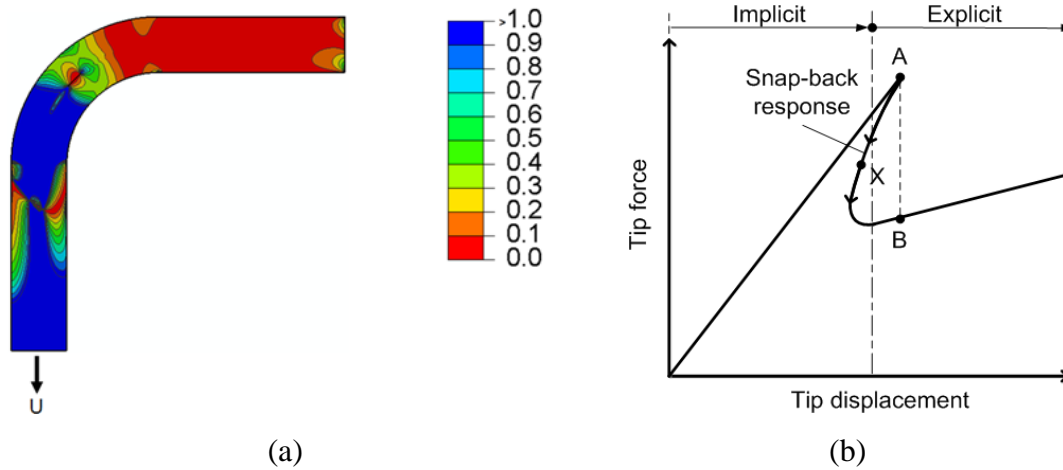
Figure 25 (a) Contours of mode-mixity defined by absolute value of the ratio opening radial stress to the shear stress and (b) two-step numerical scheme composed of an implicit analysis followed by an explicit solution [88-90].

Gozluklu and Coker [88-90] presented crucial information about the dynamics of delamination during the load drop. The energy balance was acquired as given in Figure 26a where kinetic energy, strain energy, damage dissipation and external work are shown. At the tip displacement of U = 0.625 mm, delamination started to propagate while kinetic energy developed to 0.20 J where it oscillates around 0.12 J. It was an important conclusion that the kinetic energy reached considerable levels only triggered by the delamination propagation although the loading was quasi-static. Moreover, elasto-dynamic radial stress concentration fields were observed in motion as shown in Figure 26b. Such fields were not observed in static analysis by using implicit solver which is given in Figure 26c. It was shown that the stress fields in front of the delamination were disturbed by these stress concentration fields once they reached to the crack tip. It was noted that it is interesting to observe compressive stresses along the traction-free interface since no contact was modeled. A remarkable observation was made on the crack tip speeds of the delamination in L-shaped composite laminates. The mode-mixity reached by axial loading created shear loading on the right crack tip where mode-II was dominated during the propagation towards the clamped end. Oppositely, mode-I dominated crack propagation took place on the left crack tip. As a result, the crack tip speeds at the right crack tip reached to Rayleigh wave speed of the material whereas the left crack tip moved

50

rather slowly. This result complies with the previous observations in the dynamic fracture in the straight plates [91]. Finally, a secondary crack formation near the clamped straight arm was reported in thick specimens with small initial delaminations. It was shown that the secondary crack was formed and coalesced with the initial crack during the fracture.
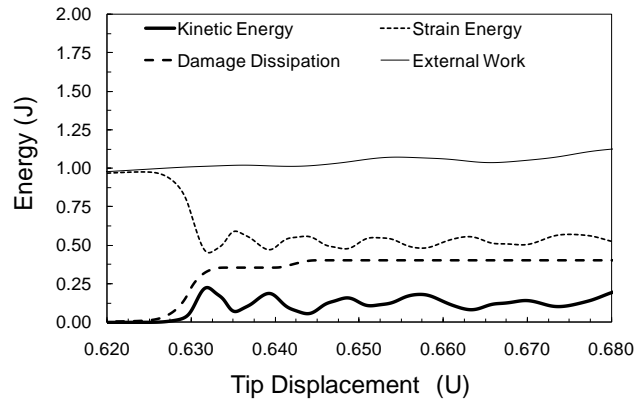
(a)

Figure 26 (a) Energy balance and contours of radial normal stress during delamination propagation obtained by FEA using (b) explicit and (c) implicit methods [88].

Formation of a secondary crack near the straight arm was further studied by Gozluklu et al. [92] and MSc thesis of Yavas [94]. Successive numerical analyses by varying the thickness and the length of the initial delamination were performed. Yet, the thickness was changed between 3.0 mm to 6.0 mm whereas the length of delamination size varies between zero to 8 mm. It was shown that there were three types of fracture process in L-shaped unidirectional composite laminates. A summary

51

map of the fracture process is illustrated in Figure 27. The first of the modes is the growth of the initial delamination. The second type is the initiation and propagation of a secondary crack initiated near the loaded arm while the initial delamination does not grow albeit both cracks eventually coalescence. The third is a combination of the first two as the initial crack and the secondary crack simultaneously grow and finally coalescence. The formation of the secondary crack also influenced the strength of the L-shaped laminates. Curves of failure loads as a function of various initial crack lengths are shown in Figure 28a. It can be seen that the L-shaped composite laminate tends to form a secondary crack at large thicknesses with smaller cracks. This was noted as an important observation for design purposes. It seems the initial delamination inside the corner might be irrelevant to the fracture and the strength of the structure. Hence, Gozluklu et al. [92] and Yavas et al. [93] started a discussion about a possible damage tolerance property of the L-shaped composite laminates. The strength of the laminate was further normalized by the cross-section area that provided the "maximum applied stress" while the effects of thickness (B) and length of delamination (a) were combined as a/B. The maximum applied stress versus a/B is shown in Figure 28b. Surprisingly, the curves collapse on a single linear band after a/B ≈ 0.4. Prior to that point, the strength does not increase just like the "expected line" as shown in the figure when the specimen fails because of the secondary crack formation.
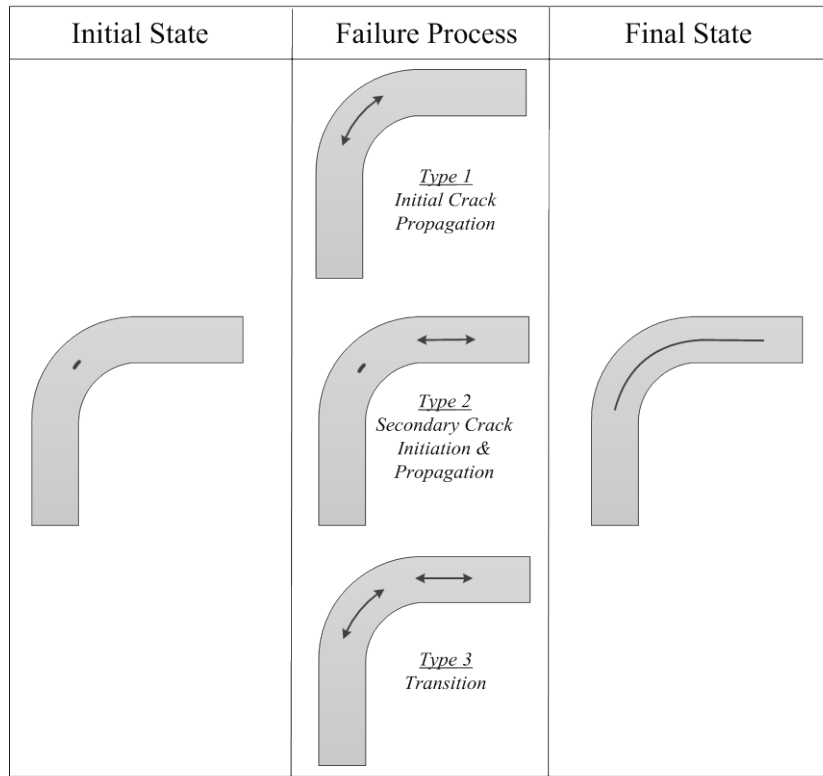
Figure 27 Map of failure for delamination of L-shaped unidirectional composite laminates proposed by Gozluklu et al. [92] and Yavas [94].

(a)

(b)
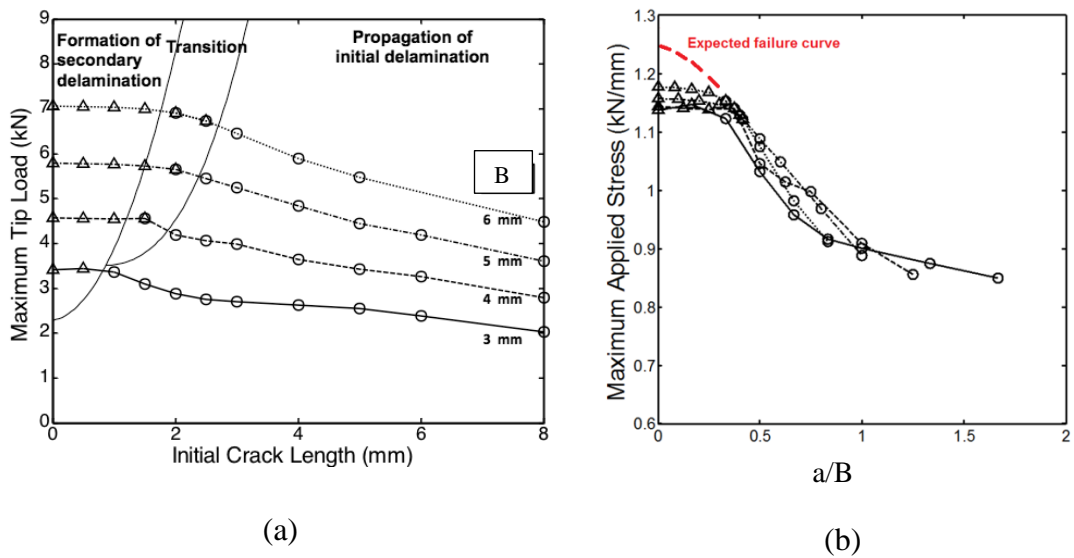
Figure 28 (a) Maximum tip load vs. initial crack size and (b) maximum applied stress vs. normalized initial crack length (a/B) for different specimen thicknesses from 3-mm to 6-mm [92,94].

Yavas et al. [93] and Yavas [94] further focused on experimental and numerical analyses of adhesively bonded L-shaped Polycarbonate beams. The idea behind using Polycarbonate laminates was to simplify the problem into a homogenous material with a weak interface. Two L-shaped Polycarbonate beams were bonded by leaving a pre-crack at the middle of the corner where the bonded interface was considered as the weak interface. Bilinear CZM was used in two-dimensional finite element analyses performed by ABAQUS/Implicit and ABAQUS/Explicit. One of the remarkable contributions was to find a reliable experimental fixture for accurately applying the shear load to the L-shaped beams since numerous problems had been reported in literature about loading of L-shaped composite laminates. The boundary condition was theoretically simulated by clamping at one end whereas the other end was being pulled for opening the corner of the L-shaped beam. As mentioned earlier, the difference between the stiffness in experiments and finite element models did not totally agree at shear loading case. Yavas [94] studied on three types of experiment fixtures. In Type-1 (Figure 29a), the displacement controlled machine head pulls the arm through a cylindrical device which is in contact with the lower end of the horizontal arm while the vertical arm is clamped. The second fixture type, Type-2, has a roller bearing that allows the rotation by the machine head while both arms are clamped (Figure 29b). At the last fixture of Type-3, the pivot point is located near the machine head while the whole specimen is able to move through slide rail in the x-direction as shown in Figure 29c. The load-displacement curves obtained using the three fixture types and the finite element model were found for Polycarbonate material as shown in Figure 29d. It can be observed that Type-1 and Type-2 fixtures provide softer response compared to the numerical model. On the other hand, Type-3 fixture perfectly agrees with the results of the FEA. Hence, the experimental results referred in our study were found by Type-3 fixture.
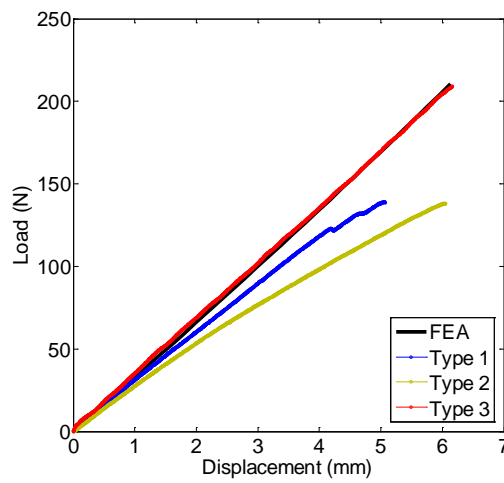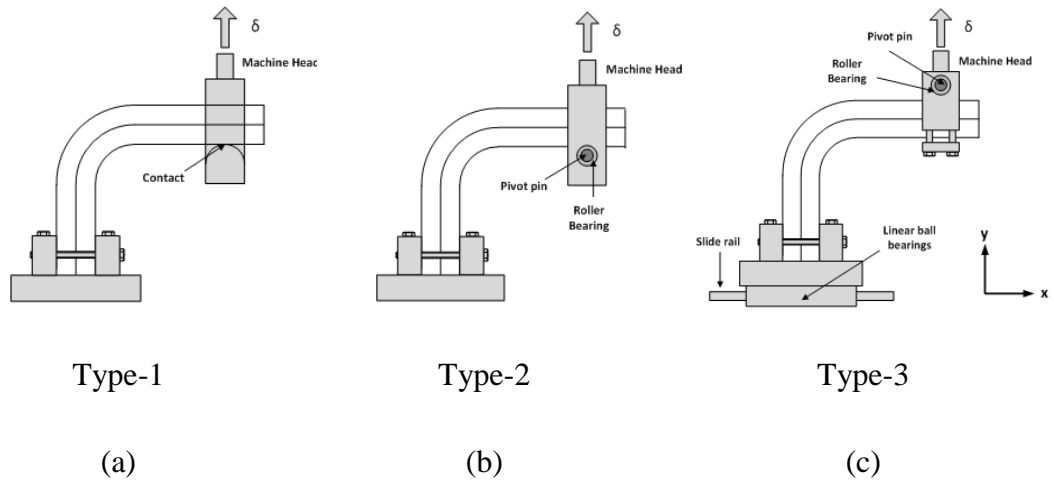
Figure 29 Experiment fixtures of (a) Type-I, (b) Type-II, (c) Type-III and (d) load-displacement curves including finite element analysis [94].

Load-displacement curves of Polycarbonate and L-shaped CFRP laminates with different initial crack lengths were experimentally studied by Yavas [94]. Importantly, the load-displacement curves exhibited the same behavior no matter it was a Polycarbonate or CFRP. An example is shown in Figure 30a where stable and unstable curves obtained for various initial crack lengths in CFRP specimens are given. Abrupt load drops are explicitly seen for the unstable cases whereas stable propagations show further load capacities after the propagation. The curves for Polycarbonate are very similar to the results of CFRP. It can be inferred that the stability of the L-shaped composite laminates with respect to initial crack size

55

exhibits the same behavior in terms of load-displacement curves. Crack tip speeds were calculated by locating the crack tips using ultra-high speed camera capable of 1 M frm/s. The crack tip speed data for CFRP specimens is shown in Figure 30b. It is seen the crack tip speed exceeds shear wave speed of the material revealing intersonic crack propagation. For the Polycarbonate specimens, the delamination process was observed using Photoelasticity method provided contours of maximum shear strain using ultra-high speed camera. A shear Mach wave on the interface was observed during the delamination propagation which is shown in Figure 30c. This supports the fact that the crack tip speed is also intersonic for Polycarbonate L-shaped specimens.

Finally, a geometrically nonlinear finite element scheme was studied by Fraternali et al. [95] for buckling and post-buckling analyses of composite curved beams. Both in-plane and lateral buckling modes of the delaminated composite curved beams were investigated. The finite element scheme covered the bi-modularity in the composite materials. It was shown that the ratio of tension to compression modulus considerably affected the buckling response of curved composite laminates such that higher tension modulus provided more stability against buckling.
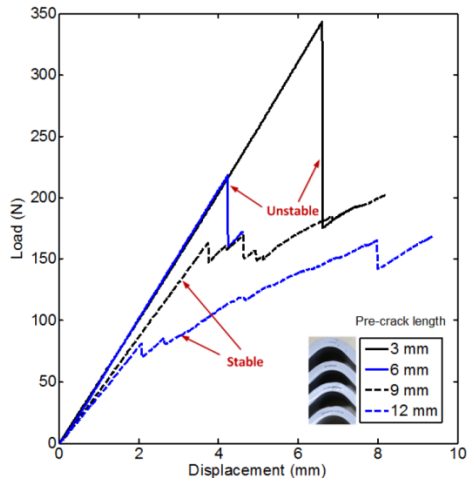
(a)
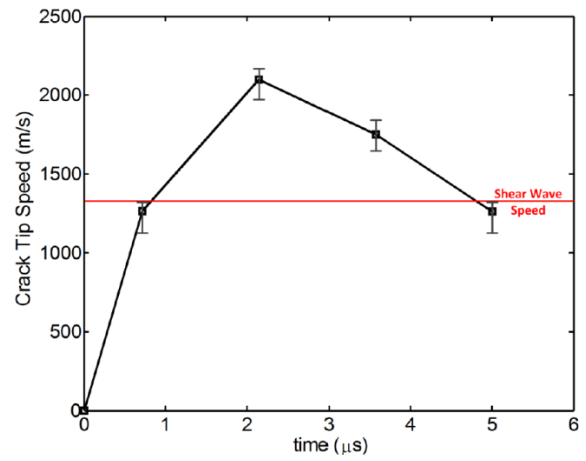
(b)
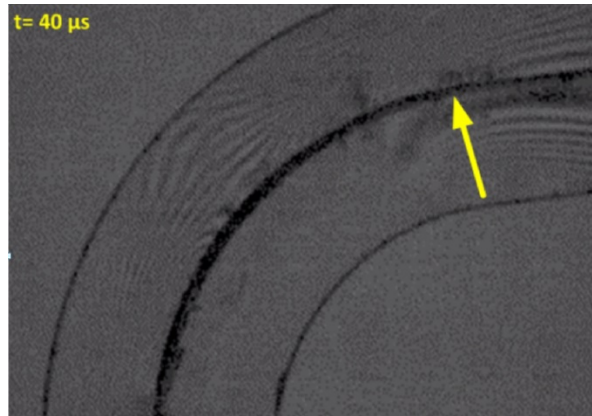
(c)

Figure 30 (a) Experimental load-displacement curves for CFRP L-shaped laminates with various initial crack lengths, (b) crack tip speed calculated using ultra-high speed camera for CFRP L-shaped laminates and (c) observation of shear mach wave by Photoelasticity in Polycarbonate laminate [94].

CHAPTER 2

THEORETICAL BACKGROUND

2.1. Analytical Solution of Stresses in L-shaped Orthotropic Plates

There are numerous studies in literature for obtaining an analytical solution of stress states in thick-curved composite laminates [41,48-53,59,67,71,78]. The analytical approaches either assume that the structure is an orthotropic plate or using CLPT for directly having a laminated composite material. In this chapter, the study of Lekhnitskii [41] is taken as the basis. Lekhnitskii only provided the solution for orthotropic plate assumption for plane stress case. In this study, the solutions for plane strain cases are also provided referring to Appendix A.

2.1.1. Pure Bending

The equations of equilibrium is satisfied by Airy stress function, $\psi(r,\theta)$, such that;

$$\sigma_r = \frac{1}{r}\frac{\partial \psi}{\partial r} + \frac{1}{r^2}\frac{\partial^2 \psi}{\partial \theta^2}$$

$$\sigma_\theta = \frac{\partial^2 \psi}{\partial r^2} \tag{4}$$

$$\tau_{r\theta} = -\frac{\partial}{\partial r}\left(\frac{1}{r}\frac{\partial \psi}{\partial \theta}\right)$$

An orthotropic curved beam under pure bending is shown in Figure 31. The orthotropy pole is the origin and the polar axis lies along the symmetry axis of the beam. The inner and outer diameters are denoted as R_i and R_o, respectively. The moment, M, acts on the beam ends is determined by the angular location, θ; i.e. $\theta <$ 2π. The width (through the page dimension) and the thickness of the beam are donated by "w" and "B", respectively, where $B = R_o - R_i$.
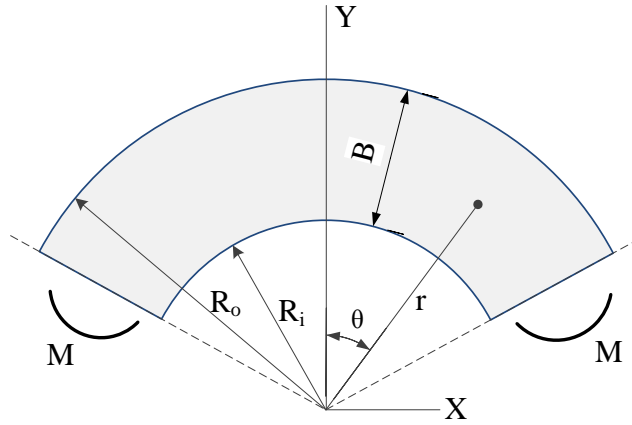
Figure 31 Pure bending of an orthotropic curved beam

No shear stress exists for a pure bending of orthotropic curved beams. Hence, generalized 2D Hooke's law for orthotropic materials can be written as below;

$$\varepsilon_r = a_{11}\sigma_r + a_{12}\sigma_\theta + a_{13}\sigma_z$$

$$\varepsilon_\theta = a_{12}\sigma_r + a_{22}\sigma_\theta + a_{23}\sigma_z \qquad (5)$$

$$\gamma_{r\theta} = a_{66}\tau_{r\theta}$$

The stress does not depend on the angular location, θ, due to the orthotropy. As σ_z is very small compared to σ_r and σ_θ, terms of σ_z are neglected in eqn (5). The compatibility equation can be written as follows;

$$\frac{d^4\psi}{dr^4} + \frac{2}{r}\frac{d^3\psi}{dr^3} + k_L^2 \frac{1}{r^2}\left(\frac{1}{r}\frac{d\psi}{dr} - \frac{d^2\psi}{dr^2}\right) = 0 \qquad (6)$$

where the dimensionless factor of "k_L" is given by Lekhnitskii;

$$k_L = \sqrt{a_{11}/a_{22}} \quad \text{(generalized case)}$$

By using the plane stress constants [5], "k_L" takes the below form for the plane stress;

$$k_L = \sqrt{E_\theta/E_r} \quad \text{(plane stress)}$$

In Appendix A, the elastic constants of orthotropic materials for plane strain case are derived as follows;

$$k_L = \sqrt{((1-\nu_{rz}\nu_{zr})E_\theta)/((1-\nu_{\theta z}\nu_{z\theta})E_r)} \qquad \text{(plane strain)}$$

For the solution of the ordinary differential equation in eqn.(6), Lekhnitskii [41] provided the Airy stress function for the pure bending, $\psi_M(r)$;

$$\psi_M(r) = A + Br^2 + Cr^{1+k_L} + Dr^{1-k_L} \tag{7}$$

where A, B, C, and D are constants and subscript "M" denotes for pure bending of a curved beam (Figure 31). From eqn.(4), radial stress, $\sigma_{r,M}$, and hoop stress, $\sigma_{\theta,M}$, can be found as follows ($\tau_{\theta,M} = 0$)

$$\sigma_{r,M} = 2B + (1+k_L)Cr^{k_L-1} + (1-k_L)Dr^{-k_L-1}$$

$$\sigma_{\theta,M} = 2B + (1+k_L)Cr^{k_L-1} - (1-k_L)Dr^{-k_L-1} \tag{8}$$

The constants of A, B, C, and D can be found by the boundary conditions which are;

$$\sigma_{r,M} = 0 \quad \text{if} \quad r = R_i \quad \text{and} \quad r = R_o \tag{9}$$

$$\int_{R_i}^{R_o} \sigma_{\theta,M} dr = 0 \quad , \quad \int_{R_i}^{R_o} \sigma_{\theta,M} r dr = -M$$

By using eqn.(8), the stress functions in the orthotropic curved beam under pure bending are found;

$$\sigma_{r,M} = -\frac{M}{R_o^2 w g_M}\left[1 - \frac{1-c^{k_L+1}}{1-c^{2k_L}}\left(\frac{r}{R_o}\right)^{k_L-1} - \frac{1-c^{k_L-1}}{1-c^{2k_L}}c^{k_L+1}\left(\frac{R_o}{r}\right)^{k_L+1}\right]$$

$$\sigma_{\theta,M} = -\frac{M}{R_o^2 w g_M}\left[1 - \frac{1-c^{k_L+1}}{1-c^{2k_L}}k_L\left(\frac{r}{R_o}\right)^{k_L-1} + \frac{1-c^{k_L-1}}{1-c^{2k_L}}k_L c^{k_L-1}\left(\frac{R_o}{r}\right)^{k_L+1}\right] \tag{10}$$

$$\tau_{r\theta,M} = 0$$

where

$$c = \frac{R_i}{R_o}$$

$$g_M = \frac{1-c^2}{2} - \frac{k_L}{k_L+1}\frac{(1-c^{k_L+1})^2}{1-c^{2k_L}} + \frac{k_L c^2}{k_L-1}\frac{(1-c^{k_L-1})^2}{1-c^{2k_L}}$$

It can be seen that the stresses are independent of angular location, θ. The dimensionless factor, k_L, is the only material property affecting the stress states in the beam. Noting that, the eqn.(10) is still applicable to cylindrically anisotropic beams. Eqn.(10) is singular for isotropic materials with $k_L = 1$. The limit of the eqn.(10) for $k_L \to 1$ is provided by Lekhnitskii [41] as follows;

$$\sigma_{r,M} = -\frac{M}{R_o^2 w g_M}\left\{c^2\ln(c)\left[1-\left(\frac{R_o}{r}\right)^2\right]-(1-c^2)\ln\left(\frac{R_o}{r}\right)\right\}$$

(11)

$$\sigma_{\theta,M} = -\frac{M}{R_o^2 w g_M}\left\{1-c^2+c^2\ln(c)\left[1+\left(\frac{R_o}{r}\right)^2\right]-(1-c^2)\ln\left(\frac{R_o}{r}\right)\right\}$$

$$\tau_{r\theta,M} = 0$$

where

$$g_M = \left(\frac{1-c^2}{2}\right)^2 - c^2[\ln(c)]^2$$

The stresses across the thickness can be calculated by using eqn.(10) for the L-shaped laminate studied by Gozluklu and Coker [88] where $E_r = 8.5$ GPa, $E_\theta = 56.7$ GPa, $R_i = 10.0$ mm and $R_o = 13.42$ mm. The normalized tangential and radial stress profiles across the normalized thickness direction are shown in Figure 32a where the normalization is performed with respect to their corresponding maximums. The radial stress reaches the maximum at ~43% of the thickness; i.e. $r \approx 11.47$ mm. An interesting figure is given in Figure 32b which shows the normalized radial stress profiles along the normalized thickness for $r/R_i \to 0$, $r/R_i = 1.0$ and $r/R_i \to \infty$ with $R_i = 5.0$ mm. As the thickness or the inner curvature of the specimen increases, the location of the maximum radial stress moves from 0.5B to inner curvature line. This can be an important observation for designers that the laminate becomes sensitive

against delamination near the inner radius once the thickness and/or the inner radius is increased. Figure 32c shows maximum radial and tangential stress plots as a function of B/R_i where the stresses exponentially decay as the thickness increases.

(a)

(b)

(c)
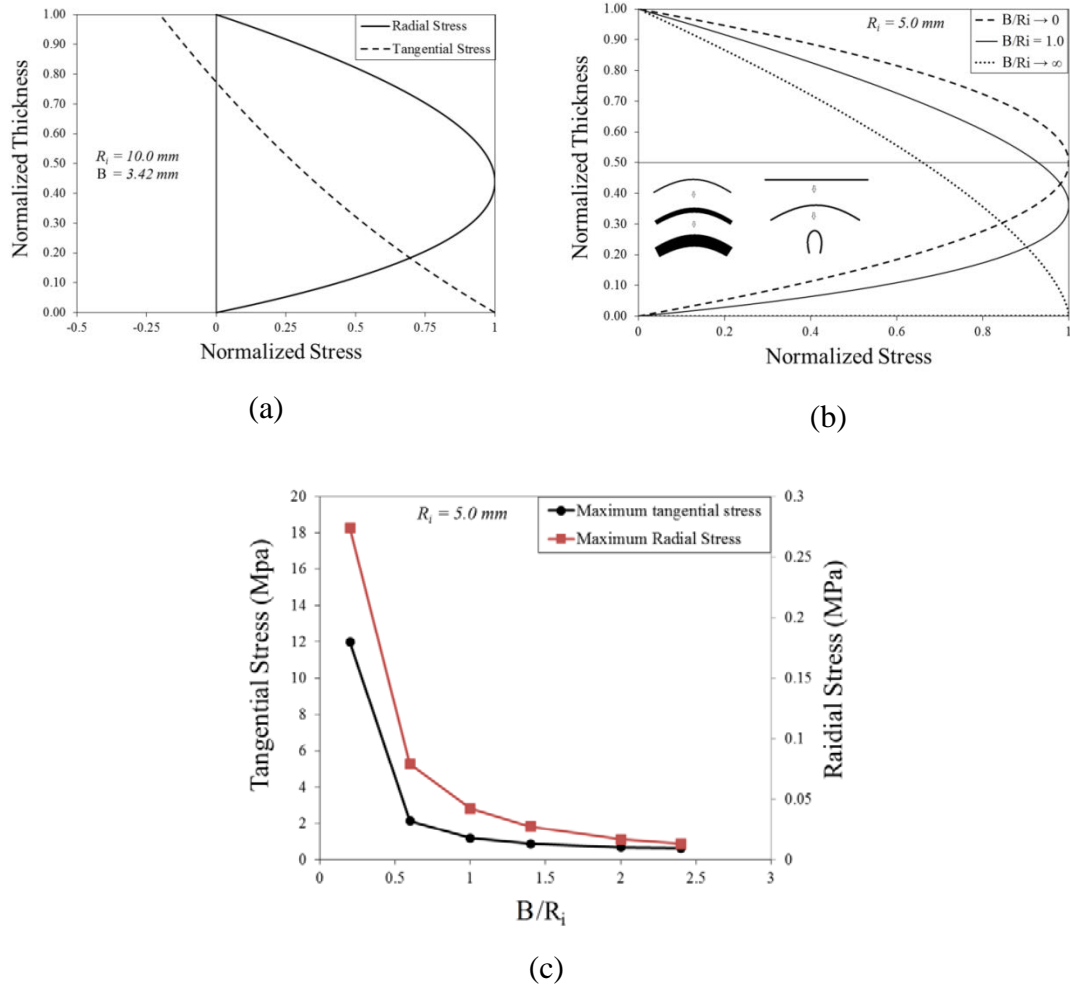
Figure 32 Normalized stresses as a function of thickness for (a) radial and tangential stress for R_i = 5.0 mm and R_o = 8.42 mm, (b) normalized radial stress profile across the thickness in various B/R_i and (c) maximum radial and tangential stress plots as a function of B/R_i.

Positive moment deforms the curved beam in a way that the beam "opens" as it becomes straighter (Figure 33a). This is the positive sign convention of the moment loading since radial normal stresses are tensile ($\sigma_r > 0$) under opening moment

63

loading ($M > 0$). On the other hand, if the moment acting on the beam is the one shown in Figure 33b, the beam is being "closed". The inner radius of an opened beam is greater than the inner radius of a closed beam; i.e. $R'_{i,+} > R_i > R'_{i,-}$. Cracks are not active under radial compressive stresses ($\sigma_r < 0$) in case of a closed beam if there is no shear stress. It means that closing radial normal stresses ($\sigma_r < 0$) are irrelevant to the delamination problem in the L-shaped composite laminates under pure moment loading. In both cases, compressive longitudinal stresses ($\sigma_\theta < 0$) would be critical for the buckling of the delaminated plies.
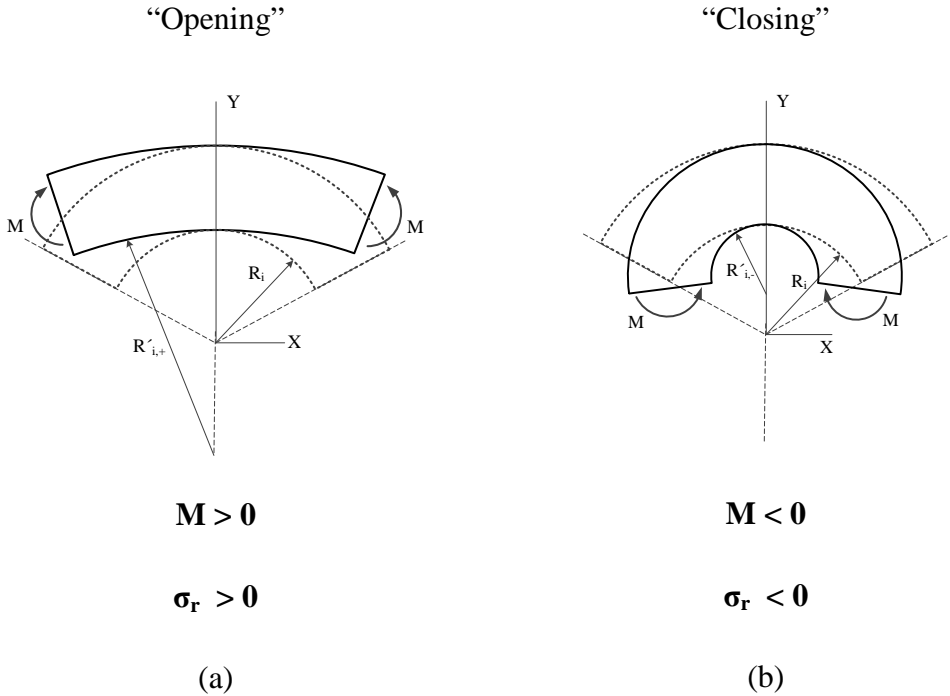
Figure 33 Representative deformations for (a) "opening" and (b) "closing" of curved beams.

2.1.2. Translational End Force

The loads on L-shaped composite laminates can be also translational forces. An orthotropic curved beam under translational end force, P, with an oblique angle of ω, is shown in Figure 34.
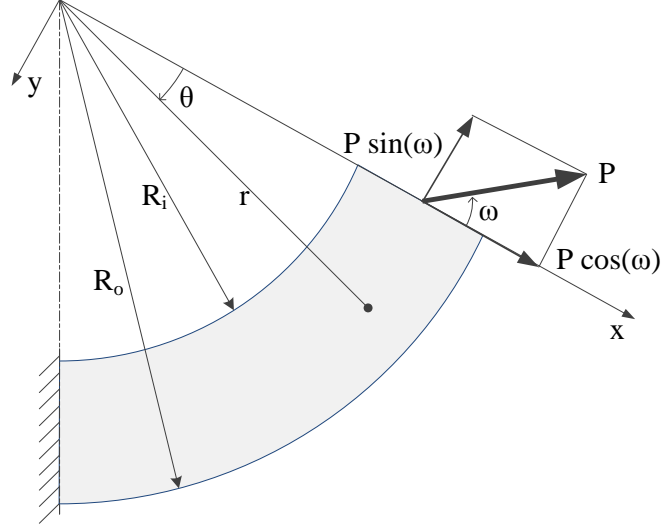
Figure 34 Orthotropic curved beam under translational end force, P.

The form of the solution of eqn.(6), $\psi_P(r,\theta)$, is given by Lekhnitskii [41] as follows;

$$\psi_P(r,\theta) = \left(Ar^{1+\zeta} + Br^{1-\zeta} + Cr + Dr\ln(r)\right)\cos\theta + \left(A'r^{1+\zeta} + B'r^{1-\zeta} + C'r + D'r\ln(r)\right)\sin\theta \quad (12)$$

where A, B,…D are constants, the subscript "P" denotes for pure translational tip loading of a clamped curved beam (Figure 34) and the dimensionless parameter "ζ" is defined as;

$$\zeta = \sqrt{1 + \frac{a_{11} + 2a_{12} + a_{66}}{a_{22}}} \quad (13)$$

For plane stress;

$$\zeta = \sqrt{1 + \frac{E_\theta}{E_r}(1 - 2\nu_{r\theta}) + \frac{E_\theta}{G_{r\theta}}} \quad (14)$$

Using the elastic constants derived in Appendix-A, "ζ" for the plane strain case is given below;

$$\zeta = \sqrt{\frac{2E_x G_{xy}(1 - 2\nu_{yx} - 2\nu_{zx}\nu_{yz} - \nu_{yz}\nu_{zy}) + E_y(E_x + 2G_{xy}(1 - \nu_{xz}\nu_{zx}))}{2E_x G_{xy}(1 - \nu_{yz}\nu_{zy})}} \quad (15)$$

65

The constants of A, B,…D are found by applying the boundary conditions of $\sigma_r = 0$ and $\tau_{r\theta} = 0$ and assessing the stresses at the free end reducing to, P;

$$\sigma_{r,P} = \frac{P}{wg_P r}\left[\left(\frac{r}{R_o}\right)^{\zeta} + c^{\zeta}\left(\frac{R_o}{r}\right)^{\zeta} - 1 - c^{\zeta}\right]\sin(\theta + \omega)$$

$$\sigma_{\theta,P} = \frac{P}{wg_P r}\left[(1+\zeta)\left(\frac{r}{R_o}\right)^{\zeta} + (1-\zeta)c^{\zeta}\left(\frac{R_o}{r}\right)^{\zeta} - 1 - c^{\zeta}\right]\sin(\theta + \omega) \tag{16}$$

$$\tau_{r\theta,P} = -\frac{P}{wg_P r}\left[\left(\frac{r}{R_o}\right)^{\zeta} + c^{\zeta}\left(\frac{R_o}{r}\right)^{\zeta} - 1 - c^{\zeta}\right]\cos(\theta + \omega)$$

where

$$g_P = \frac{2}{\zeta}(1 - c^{\zeta}) + (1 + c^{\zeta})\ln(c)$$

2.2. Fracture Mechanics

In this chapter, main physical and mathematical definitions of Fracture Mechanics are presented. Related studies from literature are referred chronologically, especially in the *dynamic fracture mechanics* section, so as to establish a basis for our methods and evaluation of our results.

The chapter starts with Linear Elastic Fracture Mechanics (LEFM). Specific subjects for delamination (cracks) in laminated composites are further presented in LEFM section. Next, Elastic-Plastic Fracture Mechanics (EPFM) is briefly presented as EPFM is generally applied for our case. Following the discussions about EPFM, Dynamic Fracture Mechanics section is presented. Elastic stress waves, dynamics of sub-Rayleigh and intersonic crack propagations are briefly explained.

In the last chapter, Cohesive Zone Method (CZM) is presented. The theory of CZM, types of CZMs, and their applications are briefly mentioned. Xu-Needleman (XN) and bilinear (BL) CZMs are derived. Next, effect of rate-dependency is discussed where a rate-dependent (RD) CZM is also proposed. Finally, the friction phenomenon is briefly presented.

It should be noted that the influence of mode-III to the delamination is still polemical in literature [96]. In our study, in-plane sectional loads are acting on balanced and symmetric layups. As a result, there is no discussion about mode-III loading in our study.

2.2.1. Linear Elastic Fracture Mechanics (LEFM)

Brittle materials exhibit low fracture toughness and characterized by linear relationship between Fracture Toughness and failure stress as shown in Figure 35. Such problems are generally analyzed by Linear Elastic Fracture Mechanics (LEFM). Moderate-to-high toughness materials exhibit nonlinear behavior and they are treated by nonlinear fracture mechanics which will be discussed in the following chapters. For high toughness materials, simple limit load analysis is adequate.
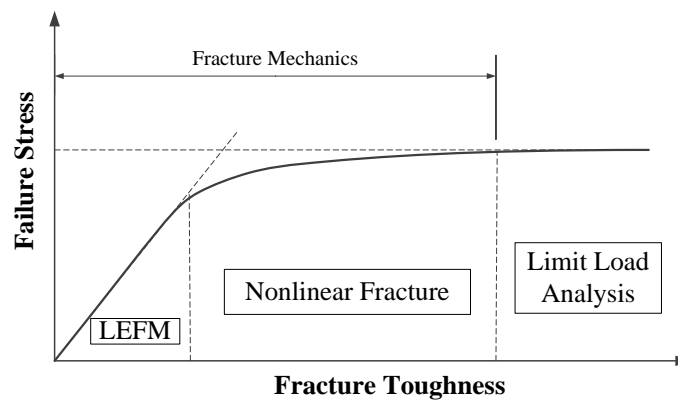
Figure 35 Influence of fracture toughness to structural analysis method

In 1920's, Griffith [30] studied brittle fracture observed in glass. In the experiments, uniform tensile stress of 100 MPa yielded failure, whereas, theoretically, tensile stress of 10,000MPa was expected to break the glass. It was concluded that the weakness was due to flaws inside the material, such as *cracks* (Figure 36a). Once a crack is analyzed like an elliptical hole with a diminishing radius of curvature, as shown in Figure 36a by dash line, local stress in front of the crack tip goes to infinity using equations of elasticity [97]. Hence, the theory of elasticity does not work in the

cracked bodies. This fact points to Fracture Mechanics as a new tool in solid mechanics.

(a)   (b)
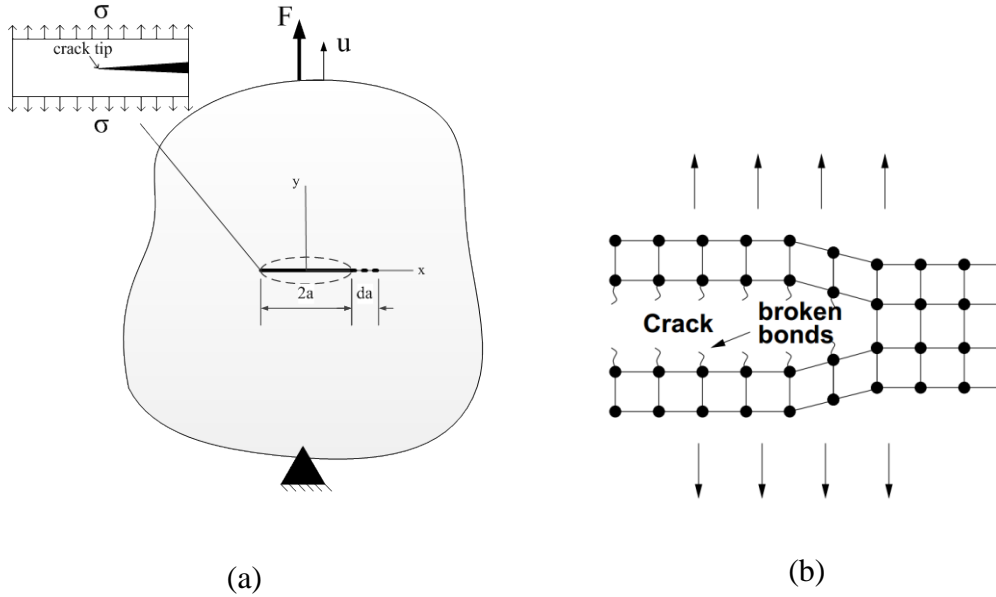
Figure 36 (a) A cracked plate under force, F or displacement, u, and (b) broken atomic bonds during crack formation yielding two new crack surfaces.

Griffith proposed required supply energy for propagating a crack by expanding its surfaces which is characterized by *surface energy density*, γ_s [30]. Creation of new surfaces was analogized to breaking the atomic bonds as illustrated in Figure 36b. Griffith determined stress distribution in a cracked body using potential energy change before and after the crack formation using Inglis's equations [97]. The multiplication of failure stress, σ_c, and square root of half the crack length, a, was observed to be a constant for the brittle fracture of linear elastic glass cracked plates [30];

$$\sigma_c \sqrt{a} = \sqrt{\frac{2E\gamma_s}{\pi}} = const. \tag{17}$$

where E is the elastic modulus of the glass. During 1940's, it was seen that peak stresses in front of a crack tip in ductile materials, such as metals, cause plastic

deformation. During loading and unloading of a cracked body, crack tip dissipates energy as the form of heat due to plastic deformation. Orawan [98] proposed additional phenomenological surface energy density, γ_p, for eqn.(17) considering the plastic energy dissipation [98];

$$\sigma_c \sqrt{a} = \sqrt{\frac{2E(\gamma_s + \gamma_p)}{\pi}} = \text{const.} \qquad (18)$$

In 1956, Irwin [99] recognized that the corresponding plastic zone in front of a crack tip is small compared to the crack and specimen size. Released fracture energy during the propagation of a crack is deduced from total potential energy available for supplying the crack propagation. This available energy is defined as the difference between external work, Π_e, and internal energy, Π. Rate of change of the available fracture energy with respect to crack extension is called *(Strain) Energy Release Rate*, G which is postulated by Irwin[30] as;

$$G = -\frac{1}{B}\left(\frac{d\Pi_e}{da} - \frac{d\Pi}{da}\right) \qquad (19)$$

where B is the thickness. Crack growth takes place when the energy release rate exceeds a critical value called *Fracture Toughness,* G_c which is a material property.
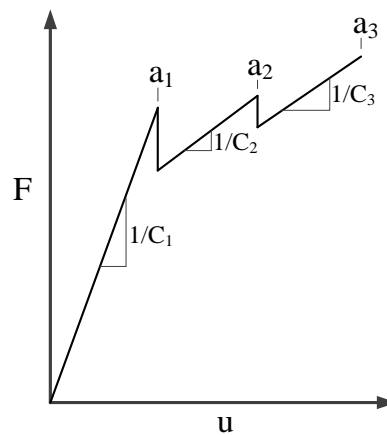
Figure 37 Definition of compliance, C, in a load-displacement curve at various crack lengths, a's.

The external energy, Π_e, can be foumd for a prescribed force, F, or a prescribed displacement, u (Figure 36a). In general, load-displacement curves refer to "external" loads and "external" displacements acting on a point. The external work done can be written as $\Pi_e = F \cdot u$ for one of a prescribed input. The internal energy can be $\Pi = 1/2 \cdot F \cdot u = 1/2 \cdot F^2 \cdot C$ where, C is *compliance* of a linear elastic cracked body which is a function of crack length, material property and geometry. As a result, eqn. (19) is expanded for a fixed displacement case as follows;

$$G = [G]_u = -\frac{1}{B}\left[u\frac{\partial F}{\partial a} - FC\frac{\partial F}{\partial a} - \frac{1}{2}F^2\frac{\partial C}{\partial a} \right]_u = \frac{1}{2B}F^2\frac{\partial C}{\partial a} \qquad (20)$$

Noting that eqn.(20) comes out to be the same for a prescribed force.
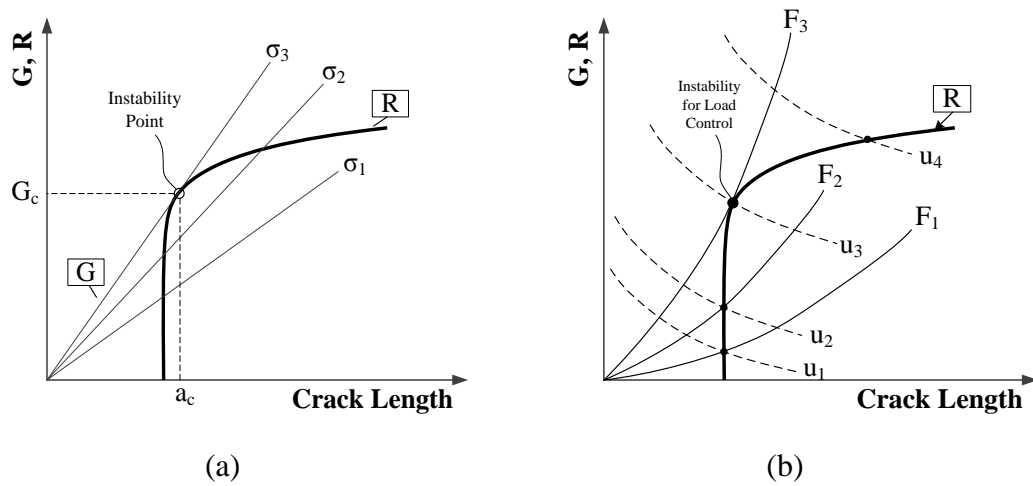
Figure 38 Example of R-curves for (a) various uniform stresses and (b) typical load and displacement control.

Uncontrolled crack propagation due to an infinitesimal quasi-static increase of load/displacement is called *unstable crack propagation*. The stability of a crack is assessed by *Resistance Curves* or *R-curves*. R-curves represent the resistance of a cracked body against crack propagation under uniform applied load that can be either force or displacement. A crack is stable as long as its energy release rate curve is able to intersect with the R-curve of the material. An example is shown in Figure 38a where the thin lines represent energy release rate curves for applied stresses ($\sigma_1 < \sigma_2 <$

σ_3) and the thick line is the resistance curve. The energy release rate curves for the applied stresses of σ_1 and σ_2 yield stable crack propagation due to possible intersection points. On the other hand, energy release rate curve for σ_3 does just intersect with the R-curve. Namely, any stress level above σ_3 triggers unstable crack propagation. Hence, the maximum attained intersection point corresponds to instability point where the fracture toughness, G_c, is reached. Another example is given in Figure 38b where energy release rate curves for displacement or force loads are shown. Although the values of the energy release rates are the same for displacement and force controlled loading, their behaviors are different. It is seen that the energy release rate curves for force controlled loading has an instability point which can be actually a stable point for displacement control load. It is known that displacement control yields more stable crack growth; therefore, displacement control loading is generally preferred in experimental fracture mechanics. For the same reason, displacement loading is used in this study. In the light of these graphical depictions in the figures, the crack growth is stated to be stable under below circumstances [31];

$$G = R \qquad \text{and} \qquad \frac{dG}{da} \leq \frac{dR}{da} \tag{21}$$

In parallel to the energy approach, solution for spatial stress distribution in front of a sharp crack tip was established by Westergaard [99] and Williams [101]. The main assumption is having a sharp crack tip which is characterized by diminishing radius of curvature at the crack tips. This geometrical feature yields stresses theoretically in infinite magnitudes at the crack tips. An illustration of the singular stress profile is shown in Figure 39a where the stresses goes to infinity by the singularity of $1/\sqrt{r}$. Remarkably, all cracked linear elastic bodies have the same stress singularity of $1/\sqrt{r}$. The difference comes out to be "how severe" the singularity which is depicted a constant, so called *Stress Intensity Factor (S.I.F.)*, K_n, which is defined for mode-I, mode-II and mode-III (n = I, II, III). The equations of stress distribution in terms of S.I.F. are given for as follows [31];

$$\sigma_{ij}^{(n)} = \frac{K_n}{\sqrt{2\pi r}} f_{ij}^{(n)}(\theta) + \sum_{m=0}^{\infty} D_m r^{m/2} g_{ij}^{(n)}(\theta) \tag{22}$$

71

where $f_{ij}^{(n)}$ and $g_{ij}^{(n)}$ are trigonometric functions in terms of angular location, θ, and D_m are constants. In eqn.(22), the last term on the right-hand-side does not have any singularity. It can be shown that the last term on the right hand side term is overwhelmed by the singularity of the first term. The zone where the singularity dominates the stress distribution is called *singularity zone* or *K-dominated zone* (Figure 39a). The last term on the right-hand-side of eqn.(22) is actually neglected in the LEFM. Inside the singularity zone, the influences of bulk material and geometry are negligible. The critical value of S.I.F. is called *Critical S.I.F.* which is a material property like the fracture toughness. S.I.F. as a function of the specimen thickness, B, is shown in Figure 39b. It is seen that the critical S.I.F. decreases at higher thicknesses. The minimum value is reached at the plane strain condition which is denoted as K_{Ic}. Consequently, plane strain fracture toughness is frequently used for design purposes.

(a)   (b)
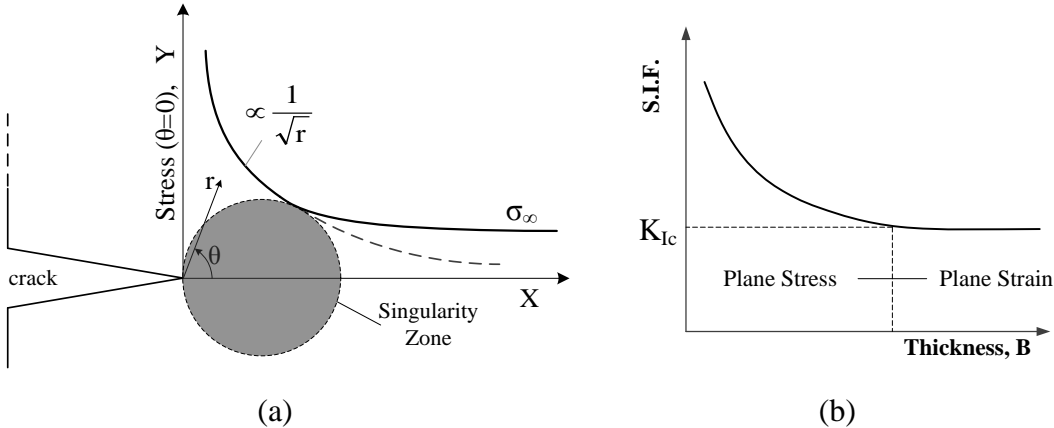
Figure 39 (a) Stress distribution in front of a crack tip at $\theta = 0$ with $1/\sqrt{r}$ singularity zone and (b) thickness effect to critical stress intensity factor, K_{Ic}, within plane stress and plane strain.

Energy release rate and stress intensity factors can be related for a self-similar crack growth where the shape and the plane of the crack do not change [31];

$$G = \frac{K_I^2}{E'} + \frac{K_{II}^2}{E'} + \frac{K_{III}^2}{2\mu} \qquad (23)$$

where $E' = E$ for plane stress, $E' = E / (1 - v^2)$ for plane strain, μ is shear modulus and v is Poisson's ratio. The energy release rate, G, in eqn.(23) is the total energy release rate; i.e. $G = G_I + G_{II} + G_{III}$. The energy release rates for pure modes can be extracted from the eqn.(23) as; $G_I = K_I^2 / E'$, $G_{II} = K_{II}^2 / E'$, $G_{III} = K_{III}^2 / 2\mu$.
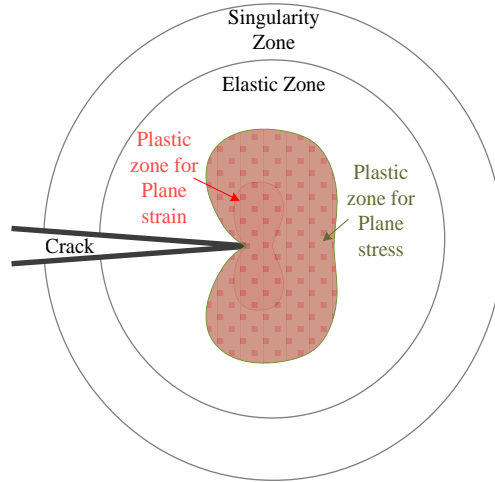
Figure 40 Shape of plastic zones for plane strain and plane stress cases in front of a crack, elastic zone and singularity zone for small-scale-yielding.

Although both of the energy release rates (G) and stress intensity factors (K) are used in LEFM, differences should be contrasted. The former treats the energy dissipated per crack growth that is indeed a more global parameter considering the whole cracked body. On the other hand, stress intensity factor locally defines the stress distribution in the vicinity of the crack. Moreover, stress intensity factor defines more delicate data about the stress field. For our study, S.I.F. is not used since it requires sharp crack tip assumption that is not a case for delamination cracks [15].

In reality, magnitudes of stresses near the crack tip do not develop to infinity. The radius of curvature at the tips is actually finite due to inelastic phenomena; such as

plasticity in metals, crazing in polymers or fiber bridging in composite materials. Similar to the region of singularity, there is a zone of plasticity in front of a crack tip as shown in Figure 40. The size of the plastic zone in plane strain is smaller than plane stress. Figure 40 also representatively shows the order of relative sizes for singularity zone, elastic zone and plastic zone in order to apply LEFM. It means that the plastic zone should be considerably smaller than the singularity zone that is to be dominated by an elastic region. Having a small region of plastic zone is called *small-scale yielding* in Fracture Mechanics. This is a concrete requirement for LEFM analysis. Otherwise, Elastic-Plastic Fracture Mechanics is used such as in our case of delamination observed in L-shaped composite laminates.

2.2.1.1. LEFM for bi-material interface cracks

Delamination is a crack located at the interfaces of composite laminates, which are between the plies. Due to layup, adjacent plies may have different stiffness such as in the case of a cross-ply laminate. The cracks located between two dissimilar materials, as shown in Figure 41, are called *bi-material interface cracks*.
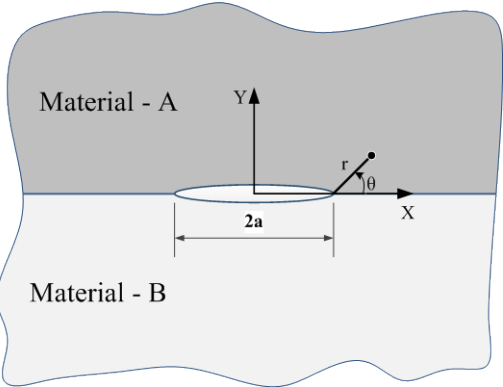
Figure 41 Bi-material interface crack

In bi-material interfacial cracks, surface tractions, T, are considered instead of stresses since an interface is a surface. The tractions on the interface are derived by Erdogan [102] in the complex form as follows;

$$T = \left(\sigma_y + i\tau_{xy}\right)_{\theta=0} = \frac{Kr^{i\gamma}}{\sqrt{2\pi r}} \tag{24}$$

where

$$\gamma = \frac{1}{2\pi} \ln\left(\frac{\mu_A + \kappa_A \mu_B}{\mu_B + \kappa_B \mu_A}\right) \tag{25}$$

and $\kappa = 3 - 4\nu_j$ (j = A,B). The S.I.F. in eqn.(24) is a complex S.I.F. defined as follows [102];

$$K = \left(K_1 + iK_2\right)\sqrt{\pi}\cosh(\pi\gamma) \tag{26}$$

where different nomenclature is used for the dependent terms of K_1 and K_2, respectively used for S.I.F.'s for mode-I and mode-II so as to be differentiate them from K_I and K_{II} which are independent terms for conventional cracks as defined in the previous paragraphs. A crucial observation in eqns.(24) and (26) is that the crack propagation in bi-material interfaces never occurs in pure mode since both K_I and K_{II} are induced. Strain energy release for an interface crack between two isotropic layers is derived by Raju et al. [103] as follows;

$$G_I = \lim_{\Delta a \to 0} \mathrm{Re}\left(D_1 + D_2(\Delta a)^{i\gamma}\right) \tag{27}$$

$$G_{II} = \lim_{\Delta a \to 0} \mathrm{Re}\left(D_1 - D_2(\Delta a)^{i\gamma}\right) \tag{28}$$

$$G = G_I + G_{II} = \lim_{\Delta a \to 0} \mathrm{Re}\left(2D_1\right) \tag{29}$$

where Re(.) is the real part of the complex function inside the brackets, D_1 and D_2 are constants. From eqns.(27), (28) and (29), it can be inferred that G_I and G_{II} have no well-defined limits yet dependent on Δa whereas the total energy release rate has a well-defined limit but independent of Δa.

Phase angle, Ψ, is generally used to assess the "mode-mixity" of the crack propagation defined as follows [31];

$$\Psi = \tan^{-1}\left(\frac{K_2}{K_1}\right) \tag{30}$$

It can be seen that the phase angle, Ψ, converges to 0° and 90° for a pure mode-I and mode-II, respectively. In our simulations, energy release rate in mode-I and mode-II are used instead of stress intensity factors in eqn.(30).
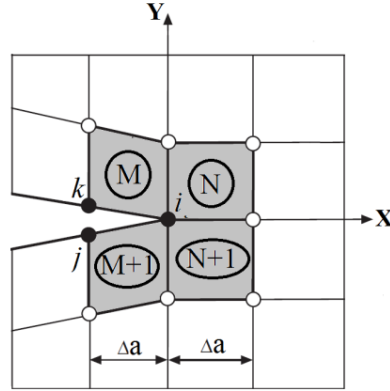
Figure 42 FEA scheme of VCCT for a 2D mesh composed of 4-noded quadrilateral elements.

In FEA of delamination in composite laminates, the most frequently used method is the Virtual Crack Closure Technique (VCCT) [47]. This technique is based on *crack closure integral* proposed by Irwin [104] which assumes that the fracture energy released in crack propagation is equal to the work required to close the crack to its original length by a small amount. In 1977, Rybicki and Kanninen [104] proposed using crack closure technique in the FEA as VCCT. Figure 42 presents an example for FEA scheme of VCCT for 4-noded quadrilateral elements in a 2D case. Nodal force vector, $\hat{F}$, at the tip of the crack, node-*i*, and the relative displacement vector, $\hat{u}$, between the nodes *k* and *j*, are extracted using FEA. Hence, the energy release rate for Δa can be found [104];

$$\hat{G} = \frac{1}{2\Delta a} \hat{F} \cdot \hat{u} \qquad (31)$$

where $\hat{G}$ is a vector of which components correspond to G_I and G_{II}.

VCCT can be used for calculating energy release rates for individual pure modes as well as the total energy release rate. However, an easier method can be used for only

calculating the total energy release rate, G, based on the global energy history of the component [15];

$$G = -\frac{\Delta\Pi + \Delta\Pi_{KE}}{\Delta a}$$

(32)

where $\Delta\Pi$ and $\Delta\Pi_{KE}$ are, respectively, the change of strain energy and kinetic energy per crack growth, Δa. Alternatively, eqn.(20) can be used in conjunction with load-displacement curves as illustrated in Figure 37.

Several examples of energy release rates as a function of delamination lengths in laminates composite structures were provided by Martin and Jackson [58] as shown in Figure 43. In an edge delamination, energy release rate abruptly converges to fracture toughness (G_c) as shown in Figure 43a. For the case of a drop-off, energy release rate reduces after reaching fracture toughness as illustrated in Figure 43b. Two behaviors of energy release rate versus delamination length were mentioned by Martin and Jackson [58] as shown in Figure 43c and Figure 43d. It is seen that the energy release rate continuously increases for the curved laminated composites.

The fracture toughness varies with the interface located for each pair of plies with different orientations. This makes the problem not limited to the material also dependent to the layup of the laminate. For instance, Allix et al. [106] concluded that the interfaces between 0°/0° plies had the minimum fracture toughness. An example of the fracture toughness of M18/M55J material for specific experiments at different orientation pairs are given in Figure 44. It is seen that the minimum toughness was always reached for the interface between 0°/0° plies.
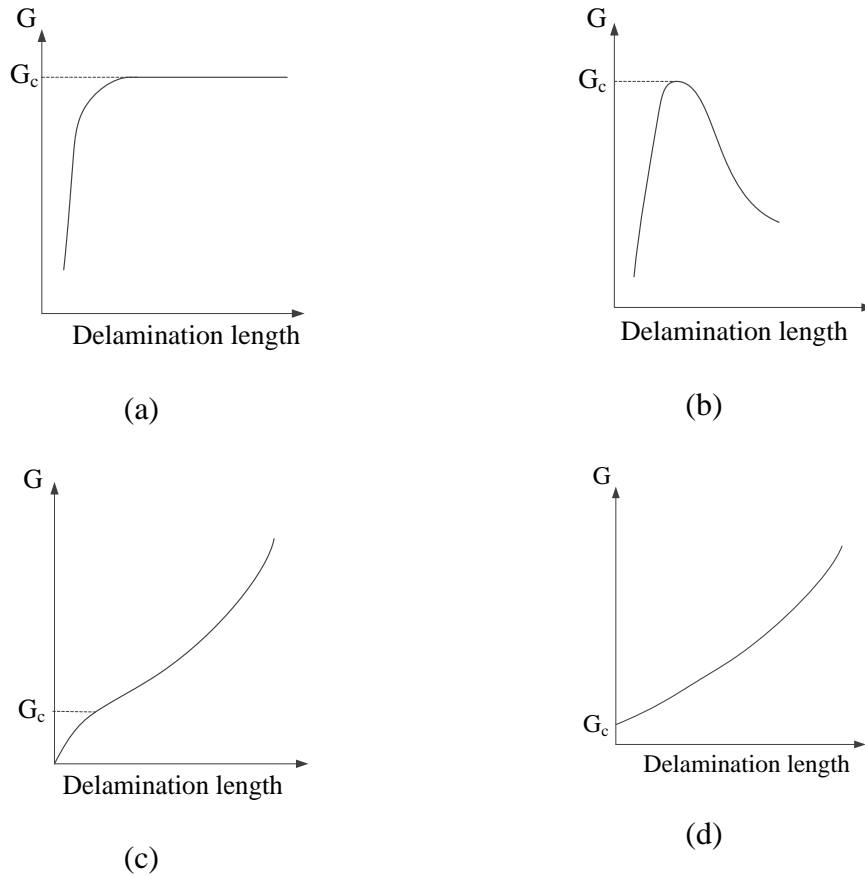
Figure 43 Energy release rate as a function of delamination length for (a) edge delamination, (b) drop-off, (c) first example and (d) second examples of curved laminates.
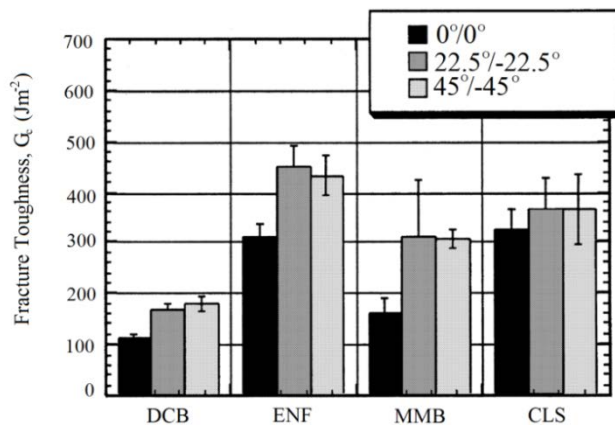
Figure 44 Fracture toughness for interface experiments for M18/M55J – (CLS: Cracked Lap-Shear test) [107]

2.2.2. Elastic-Plastic Fracture Mechanics

In 1961, Wells [108] observed that sharp crack tip becomes blunt prior to propagation through the plastic zone in ductile materials (Figure 45). The relative distance between the blunted crack surfaces is called *Crack Tip Opening Displacement* (CTOD). Wells [108] proposed CTOD as a measure of fracture toughness in ductile materials. CTOD can be related to energy release rate (G) as follows [31];

$$\text{CTOD} = \frac{4}{\pi} \frac{G^2}{\sigma_y} \tag{33}$$

where σ_y is the yield strength. The major advantage of CTOD is that the crack tip plasticity is incorporated. This makes CTOD a unique candidate for problems with significant crack tip plasticity.
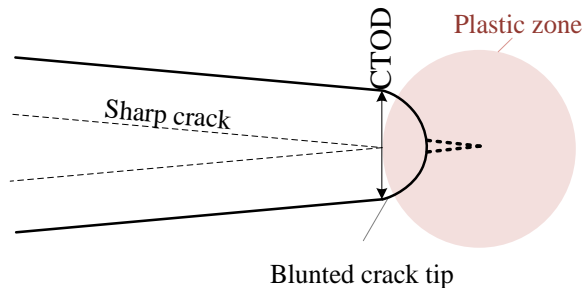
Figure 45 Blunted crack during crack propagation in a ductile material and definition of CTOD.

In 1968, Rice [61] proposed a path independent contour integral around a crack tip. It was shown that the value of the path-independent contour integral, so called *J-integral*, is equal to the energy release rate for a linear elastic cracked body; i.e. J = G. As soon as there is no unloading or a crack propagation that has no plastic wake left behind, in other words, if a material is linear elastic and monotonically loaded, the equality of J = G works.
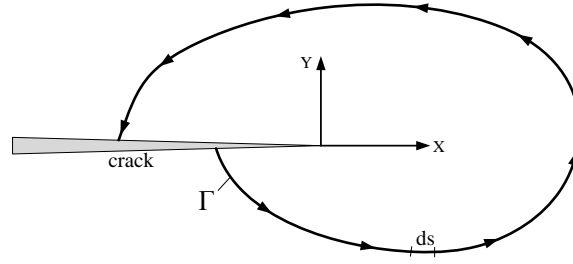
Figure 46 Path-independent J-integral with a counterclockwise path around a crack tip.

The J-integral with a counterclockwise path around a crack tip is illustrated in Figure 46. The J-integral is defined as below [61];

$$J = \int_{\Gamma} \left(\chi dy - T_i \frac{\partial u_i}{\partial x} ds \right) \tag{34}$$

where χ is the strain energy density, T_i are components of the traction vector normal to the contour of Γ ,u_i are the displacement vector components, and ds is an increment of the contour of Γ (Figure 46). Strain energy density, χ, is defined as;

$$\chi = \int_0^{\varepsilon_{ij}} \sigma_{ij} d\varepsilon_{ij} \tag{35}$$

J-integral is a versatile method which is also used in Cohesive Zone Method (CZM).

2.2.3. Dynamic Fracture Mechanics

Dynamic Fracture Mechanics is relatively a new field in Fracture Mechanics which deals with dynamic crack propagation under the influences of inertia, stress waves and kinetic energy. In literature, dynamic crack propagation is triggered by impact loading, explosive loading or loading at high-displacement rates [31,91,109,110]. Dynamic crack propagation under quasi-static loading is observed in earthquakes [111] and it is generally studied by geophysics.

2.2.3.1. Wave Propagation in Elastic Solids

Before the discussion of dynamic fracture mechanics, propagation of stress waves in an elastic body is presented. There are three types of stress waves in elastic medium; dilatational wave (C_d in Figure 54a), shear wave (C_s in Figure 54b), and Rayleigh wave (C_R in Figure 54c). Dilatational wave is transfer of pressure waves due to normal stresses whereas shear wave is made of shear stress pulses. Dilatational wave and shear wave travel through the bulk. On the other hand, Rayleigh wave moves on surfaces by means of rotational movement of particles as show in Figure 54c. If an impact takes place at a surface as shown in Figure 54d, the impact emanates dilatational waves and shear waves propagating through the bulk whereas Rayleigh wave moves over the surface in all directions. For a crack like surface in a medium under instantaneous normal stress loading, dilatational and shear waves travel in the formations of pulses as circular and straight lines (Figure 54e). Figure 54f illustrates a similar case but for an instantaneous shear stress loading where similar behavior can be observed. One of the observations from Figure 54d-f is that the dilatational waves propagate as horizontal and vertical straight and circular lines whereas shear waves show further formations of oblique waves.
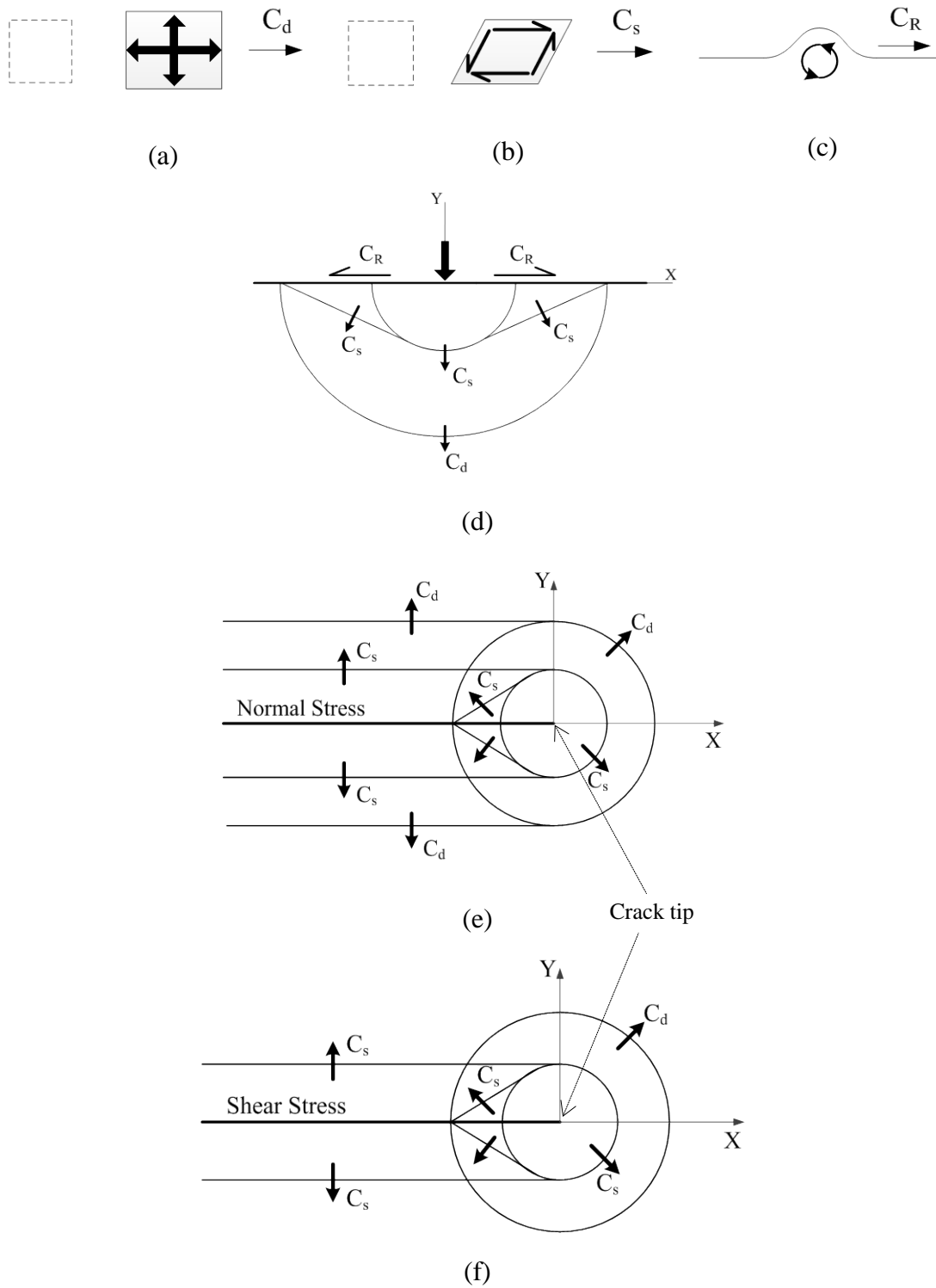
Figure 47 (a) Dilatational wave, (b) shear wave, (c) Rayleigh wave propagation in elastic medium, and (d) Rayleigh, dilatational, shear wave propagation due to surface impact, (e) shear and dilatational wave due to instantaneous loading of normal stress and (f) shear and dilatational wave due to instantaneous loading of shear stress.

The speeds of the stress waves are material properties and their magtidues are $C_d >$ $C_s > C_R$. Crack tips travel below the Rayleigh wave speed is called *sub-Rayleigh crack growth*, moving above shear wave speed but below the dilatational speed is called *intersonic crack growth*. There is no definition of the crack tip speeds between shear and Rayleigh wave speeds since theoretically it is not possible to propagate between those speed limits [109]. Actually, this unattainable interval of speed zone is generally called *forbidden zone*.

ZX-Plane
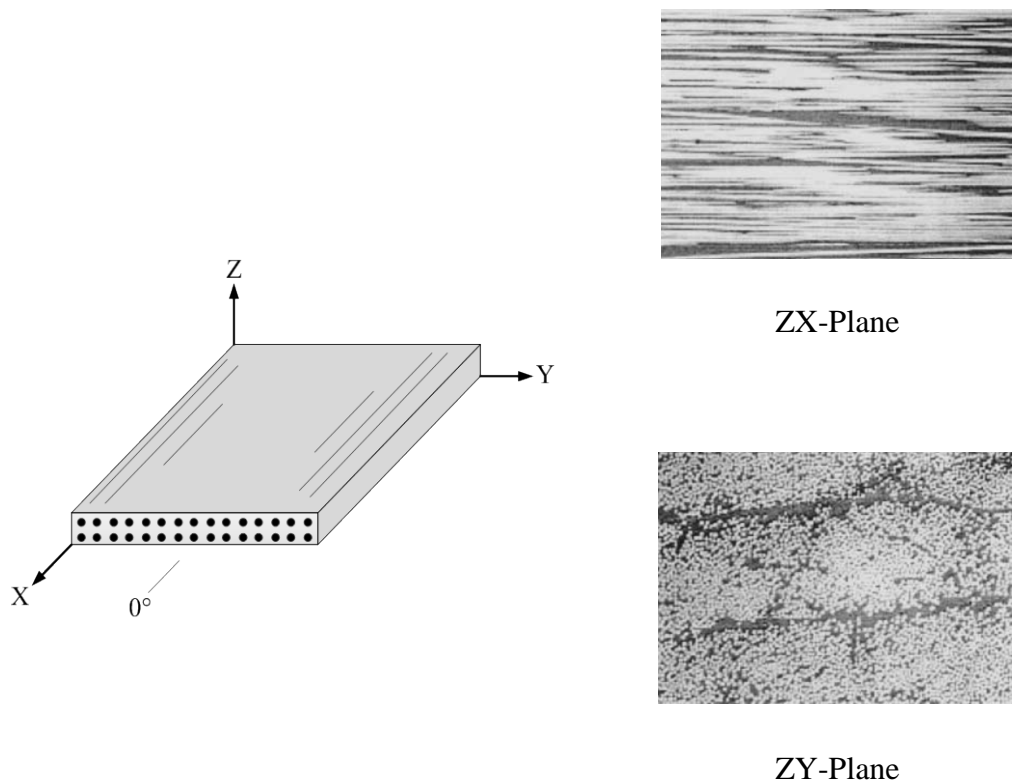
ZY-Plane

Figure 48 Coordinate system of a unidirectional 0° composite ply with cross-section cuts on ZX and ZY-planes.

A unidirectional fiber reinforced composite ply is shown in Figure 48 with the cut views showing the ply directions on ZX and ZY planes. Single ply is transversely isotropic of which elastic constitutive relation is characterized by five independent moduli written as follows [5];

$$
\begin{bmatrix} \sigma_{11} \\ \sigma_{22} \\ \sigma_{33} \\ \sigma_{23} \\ \sigma_{13} \\ \sigma_{12} \end{bmatrix} = \begin{bmatrix} S_{11} & S_{12} & S_{12} & 0 & 0 & 0 \\ S_{12} & S_{22} & S_{23} & 0 & 0 & 0 \\ S_{12} & S_{23} & S_{22} & 0 & 0 & 0 \\ 0 & 0 & 0 & S_{44} & 0 & 0 \\ 0 & 0 & 0 & 0 & S_{66} & 0 \\ 0 & 0 & 0 & 0 & 0 & S_{66} \end{bmatrix} \begin{bmatrix} \varepsilon_{11} \\ \varepsilon_{22} \\ \varepsilon_{33} \\ \varepsilon_{23} \\ \varepsilon_{13} \\ \varepsilon_{12} \end{bmatrix}. \tag{36}
$$

The engineering moduli, E_{11}, E_{22}, μ_{23}, μ_{12} and ν_{12} are related as follows;

$$
E_{11} = S_{11} - \frac{2S_{12}^2}{S_{22} + S_{23}}, \qquad E_{22} = \frac{(S_{22} - S_{23})(S_{11}S_{22} + S_{23}S_{11} - 2S_{12}^2)}{S_{11}S_{22} - S_{12}^2} \tag{37}
$$

,

$$
\mu_{12} = S_{66}, \qquad \mu_{23} = S_{44} = \frac{S_{22} - S_{23}}{2}, \tag{38}
$$

$$
\nu_{12} = \frac{S_{12}}{S_{22} + S_{23}}, \qquad \nu_{21} = \frac{S_{12}(S_{22} - S_{23})}{S_{11}S_{22} - S_{12}^2}, \qquad \nu_{23} = \frac{S_{23}S_{11} - S_{12}^2}{S_{11}S_{22} - S_{12}^2}. \tag{39}
$$

Following the engineering moduli, dilatational wave speed in the fiber direction, $C_d^{\parallel}$, dilatational wave speed normal to the fiber direction, $C_d^{\perp}$, and the shear wave speeds in 12/13-planes C_s follows the below relations;

$$
C_d^{\parallel} = \sqrt{\frac{S_{11}}{\rho}} \quad , \qquad C_d^{\perp} = \sqrt{\frac{S_{22}}{\rho}}, \qquad C_s = \sqrt{\frac{S_{66}}{\rho}} \tag{40}
$$

where ρ is the density. For an isotropic material, eqn.(40) can be written in terms of Lame's constants, λ and μ;

$$
C_d = \sqrt{\frac{\lambda + 2\mu}{\rho}} \quad , \qquad C_s = \sqrt{\frac{\mu}{\rho}} \tag{41}
$$

The Rayleigh wave speed is the smallest root of the below equation [110];

$$
\left(2 - \frac{C_R^2}{C_s^2}\right)^2 - 4\left(1 - \frac{C_R^2}{C_d^2}\right)^{1/2}\left(1 - \frac{C_R^2}{C_s^2}\right)^{1/2} = 0 \tag{42}
$$

For an isotropic material, eqn.(42) converges to the below form;

$$C_R \cong C_s \frac{0.862 + 1.14\nu}{1 + \nu} \qquad (43)$$

Dilatational, shear and Rayleigh wave speeds of various materials are summarized in Table 2. It is seen that the highest wave speeds belong to composite materials.

Table 2 Dilatational, shear and Rayleigh wave speeds calculated for various materials

	AISI 4340 Steel	Al 6061	PMMA	CFRP*
C_d (m/s)	5980	6610	2700	7380
C_s (m/s)	3195	3330	1300	1560
C_R (m/s)	2960	3105	1210	1548

* In the longitudinal direction for Graphite/Epoxy material taken from Coker et al. [112]

A shear Mach wave can be emanated from the crack tip as soons as the crack tip exceeds the shear wave speed of the material (Figure 49). Assume that, the crack tip moves from point-A to point-B in duration of time, Δt, at an intersonic speed, V. The distance between the two points is equal to $V \cdot \Delta t$. As the information of shear stress does not catch up the crack tip, a stress front of Shear Mach wave is emanated in the angle of θ_s. Geometrically, it can be written as $\sin(\theta_s) = C_s \cdot \Delta t / V \cdot \Delta t$. Noting that, another Mach wave is emanated if the crack tip exceeds the dilatational wave speed.
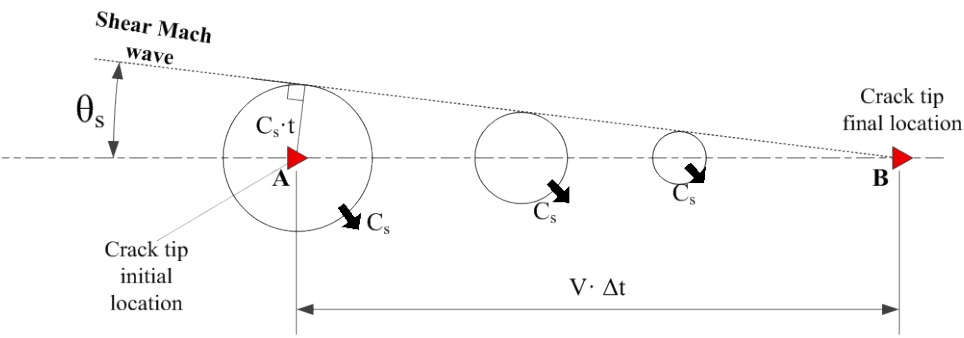
Figure 49 A shear Mach wave and the angle of wave front for an intersonic crack propagation.

2.2.3.2. Dynamic Crack Propagation

In theory, the crack tip under mode-I loading must move below sub-Rayleigh speeds; i.e. $V \leq C_R$ [113]. According to Yoffe [114], crack growth tends to occur in the direction of maximum asymptotic hoop stress. This results in *crack branching* (Figure 50a) after an impact loading to a homogeneous isotropic cracked body. Experimental evidences show that the limiting crack tip speed in homogeneous isotropic elastic materials in mode-I fracture moves between 30% - 60% of Rayleigh wave speed without branching [115]. Afterwards, crack starts to branch around 70% of Rayleigh wave speed no matter how much energy is used in the impact. In 1994, Washabaugh and Knauss [116] has conducted mode-I impact experiments in PMMA plates with a weak plane as shown in Figure 50b. The idea is to suppress crack branching by forcing the crack to travel along the weak interface. Washabaugh and

Knauss [116] showed that the crack tip speed reaches to Rayleigh wave speed for the mode-I loading shown in Figure 50b. Hence, the theoretical value can be attained once the crack branching is suppressed by putting a weak plane.

<center>(a)   (b)</center>
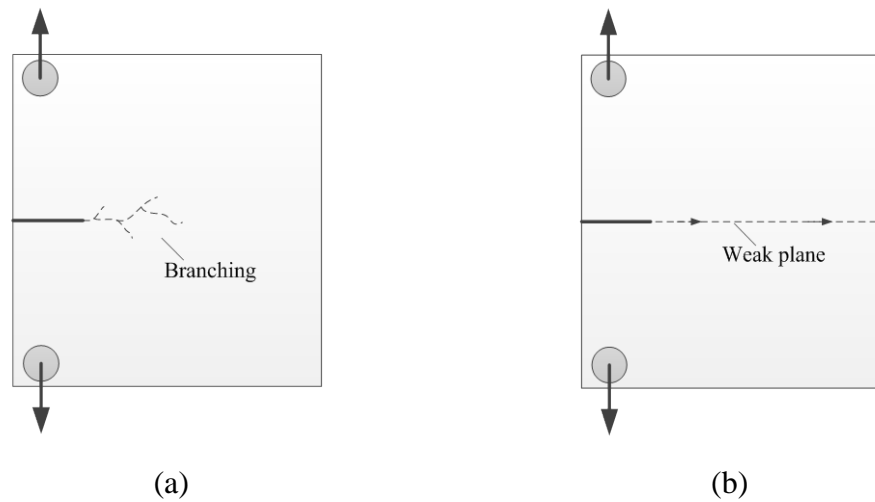
Figure 50 Directions of crack propagation for (a) crack branching in homogeneous isotropic elastic materials and (b) along a weak interface.

In mode-II fracture, cracks move in sub-Rayleigh regime and above C_s at intersonic speeds if adequate fracture energy is sustained. In 1987, Kalthoff and Winkler [119] showed that the angle of branching approaches to zero by increasing the loading rates in homogeneous isotropic materials. In 1999, Rosakis et al. [111] conducted mode-II dynamic fracture experiments on polymers with a weak interface under asymmetric impact loading (Figure 51 - left). High speed camera was used to record shear stress contours with photo-elasticity method. It was shown that the intersonic crack growth occurs and shear Mach waves are captured as shown in Figure 51. Later, Hao et al. [120] successfully simulated the same experiment using Cohesive Zone Method.
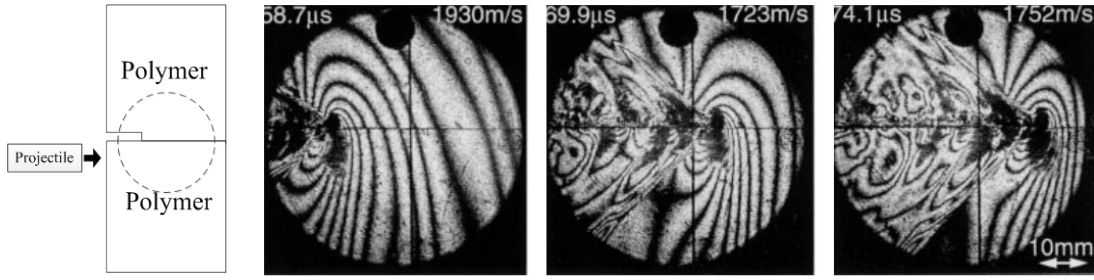
Figure 51 Intersonic mode-II crack growth in polymers captured by Rosakis et al.
[111]

In 2001, Coker and Rosakis [118] conducted experiments of symmetrical and asymmetric impact loading at unidirectional composite plates with a weak interface by adhesively bonding the plates. In the experiments, the impact loading was applied near the interface from the crack-free side. Symmetric loading yielded mode-I fracture whereas asymmetric loading caused mode-II fracture. Hence, both mode-I and mode-II dominated fracture were studied in the same setup. Figure 52a presents the crack tip speeds as a function of crack extension for mode-I and mode-II calculated by Coker and Rosakis [118]. It is seen that crack tip speeds in mode-I condition can never exceed the limit of Rayleigh wave speed no matter how much energy is applied. On the other hand, crack tip speeds in mode-II condition accelerate from shear wave speed up to a maximum level of *critical speed*, V_c, below the dilatational wave speed [118]. They noted that the crack propagates sustainably at the critical speed, V_c, in such a way that the crack tip speed tends to travel at discrete speeds bands [118]. Huang et al. [121] analytically derived the critical speed of V_c for plane stress as follows;

$$V_c = \left(\frac{S_{11}S_{22} - S_{12}^2}{S_{66}(S_{12} + S_{22})} \right)^{1/2} C_s \tag{44}$$

where S_{ij} are the stiffness of the orthotropic plate given by eqn.(37), eqn.(38) and eqn.(39). Eqn.(44) is reduced to $V_c = \sqrt{2}C_s$ for isotropic materials. Dwivedi and Espinosa [122] successfully modeled the experiment by Coker and Rosakis [118] using CZM in conjunction with FEA.

88
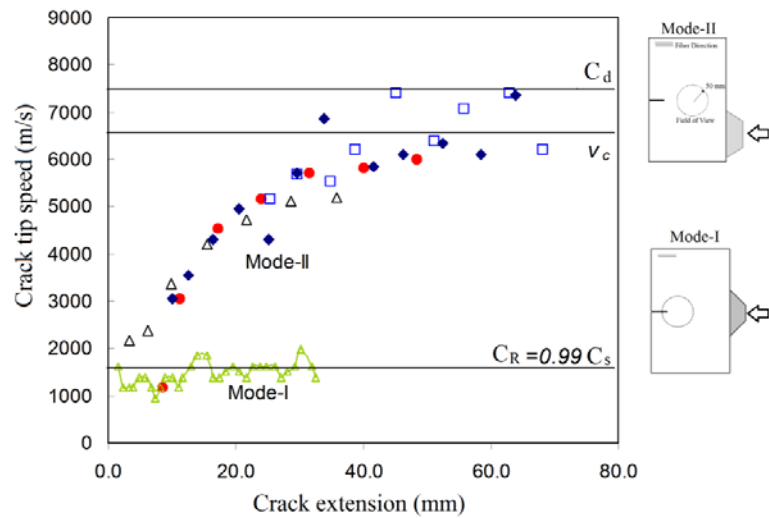
(a)
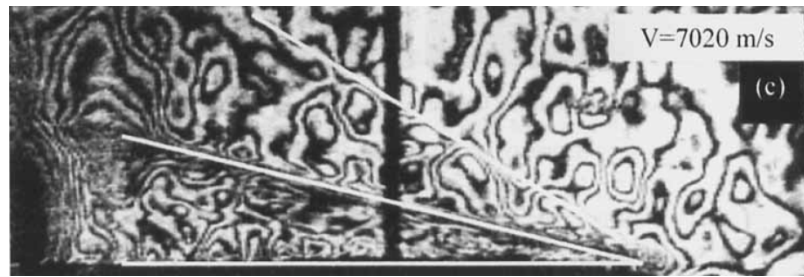
(b)

Figure 52 (a) Crack tip speed as a function of crack extension for mode-I and mode-II fracture and (b) two shear Mach waves observed during intersonic fracture of unidirectional composite laminates by Coker and Rosakis [118].

In 2003, Coker et al. [112] studied dynamic fracture at a weak interface between polymer-composite plates under asymmetrical impact loading. In this pair, the Rayleigh wave speed of the composite is greater than the shear wave speed of the polymer. It was firstly shown that the crack can propagate at such high speeds that the crack tip may even exceed the dilatational wave speed of the polymer. Hence, the speed of the crack propagation was not limited by the more compliant material. In addition to that, *mother-daughter crack mechanism* [123], in which a small "daughter" crack is followed by a larger "mother" crack, was observed in the experiments. Initially, single crack starts to propagate as shown in Figure 53a. As the

crack tip speed approaches to Rayleigh wave speed of the composite, a smaller "daughter" crack emerges in front of the "mother" crack as shown in Figure 53b. At this point, the crack tip speed approaches to the forbidden zone ($C_R < V < C_s$). Next, the "mother" and "daughter" cracks instantly coalesce, as shown in Figure 53c. As a result, the crack "jumps over" the forbidden zone due to the action of coalescence. Afterwards, the resulting crack propagates at intersonic speeds. During the coalescence, shear Mach waves are formed due to excessing the shear wave speed of the polymer (Figure 53c-e).

(a)

(b)
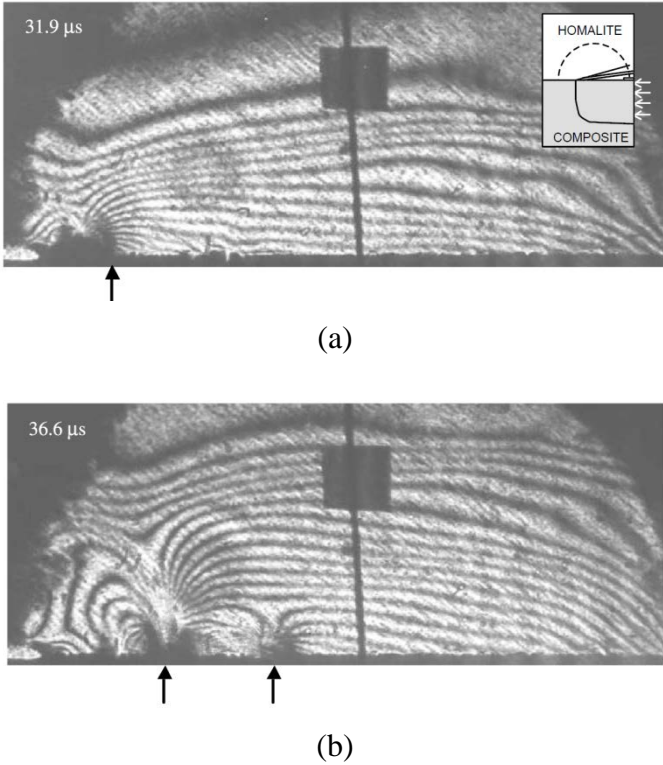
Figure 53 Stress fringes in Homalite where (a) main ("Mother") crack at t = 31.9 µs, (b) "Mother" and "daughter" crack at t = 36.6 µs, (c) coalescence that creates shear Mach wave at t = 50.5 µs taken from Coker et al. [112], (d) illustration of "mother" - "daughter" cracks, (e) coalescence and formation of shear Mach wave.

(c)

(d)

(e)
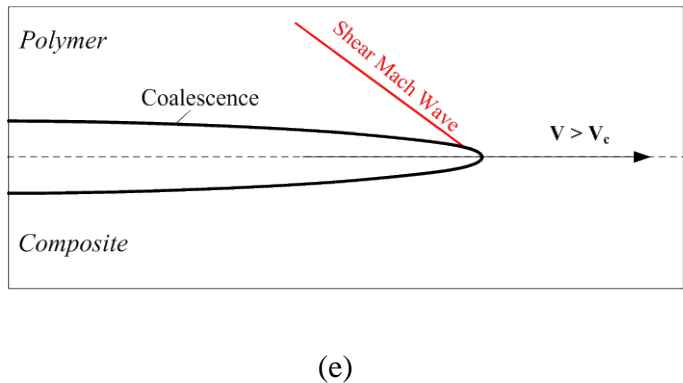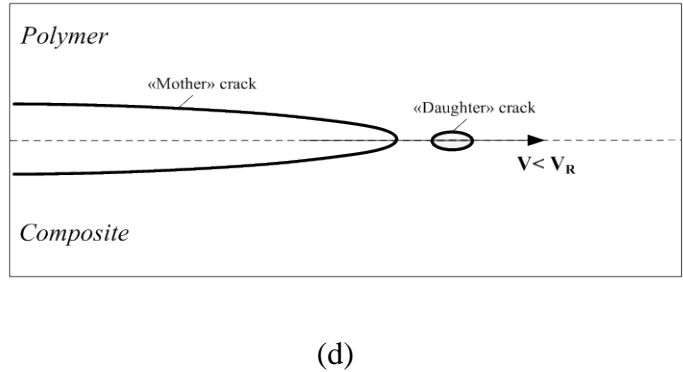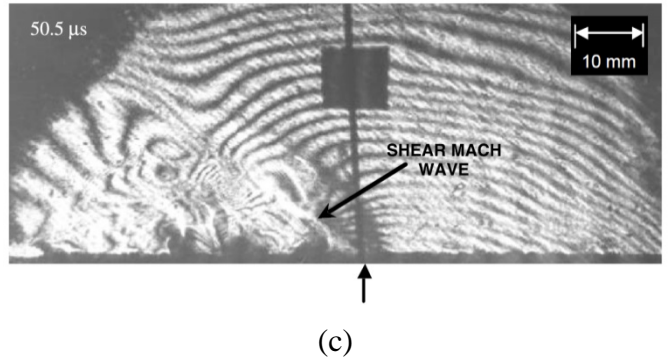
Figure 53 (Continued)

2.2.3.3. Dynamic Stress Intensity Factor and Energy Release Rate

Closed-form solutions of dynamic stress intensity factor, $K_i(t)$ i=I,II are available in literature. The dynamic stress intensity factors for a semi-infinite crack can be written as; $K_I(t) \propto \sigma_0\sqrt{tC_d}$ and $K_{II}(t) \propto \tau_0\sqrt{tC_s}$, respectively [109,110]. It is seen that the dynamic S.I.F. of a semi- infinite crack continuously increases in the form of

$\sqrt{t}$. However, this is not a general case. Dynamic S.I.F. for a crack at the center of an infinite plate was numerically calculated by Sih et al. [124] in which the dynamic S.I.F. had a maximum value after when it started to decrease. In all cases, dynamic S.I.F. is time dependent and related to material wave speeds.

The definition of dynamic energy release rate includes the terms of kinetic energy, Π_{KE}, as follows [15];

$$G(t) = -\frac{1}{B}\left(\frac{d\Pi_e}{da} - \frac{d\Pi}{da} - \frac{d\Pi_{KE}}{da}\right) \tag{45}$$

Similar to the definition of dynamic energy release rate, J-integral also includes kinetic energy density, χ_{KE}, as firstly proposed by Atkinson and Eshelby [125];

$$J = \lim_{\Gamma \to 0} \int_{\Gamma}\left[(\chi + \chi_{KE})dy - T_i\frac{\partial u_i}{\partial x}ds\right] \tag{46}$$

where χ_{KE} is given;

$$\chi_{KE} = \frac{1}{2}\rho\frac{\partial u_i}{\partial t}\frac{\partial u_i}{\partial t} \tag{47}$$

Moreover, the strain energy density, χ, can be represented in the below formation for a visco-elastic material in which rate-dependency is important [31];

$$\chi = \int_{t_0}^{t}\sigma_{ij}\dot{\varepsilon}_{ij}dt \tag{48}$$

An important observation in eqn.(46) is the contour Γ which is localized around the crack tip. Atkinson and Eshelby [125] showed that the integral is path-independent as long as the integral starts from the lower surface and ends at the upper surface of the crack for dynamic crack propagation.

A different version of dynamic J-integral is proposed by Nakamura et al. [126] in which energy flux entering into the contour are considered and earlier elasto-dynamic effects are covered as below [126];

$$J = \lim_{\Gamma \to 0} \left\{ \int_{\Gamma} \left[(\chi + \chi_{KE}) dy - T_i \frac{\partial u_i}{\partial x} ds \right] + \int_{A} \left[\rho \frac{\partial V_i}{\partial t} \frac{\partial u_i}{\partial x} - \rho V_i \frac{\partial V_i}{\partial x} \right] dA \right\} \qquad (49)$$

where $V_i = \partial u_i / \partial t$.

R-curves provide further information about the dynamics of crack propagation. It is important to notice that excessive energy release rate is converted to kinetic energy [126] (Figure 54). Hence, an unstable crack growth with large available fracture energy, kinetic energy will be considerably large. High values of kinetic energy cause high crack tip speeds, fostering the dynamic phenomenon occurred during the process [126].
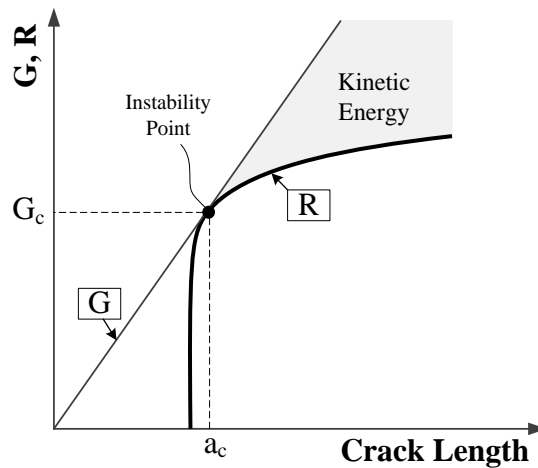
Figure 54 Kinetic energy zone due to excessive energy release rate in an unstable crack growth.

Stress waves may emerge due to the loading itself. Hence, output of a J-integral during the early stages of loading may be misleading [109]. Nakamura et al. [128] investigated the inertial effects due to the loading waves in a three-point-bending impact test that is dedicated for pure mode-I dynamic fracture. Nakamura et al. [128] showed that kinetic energy (Π_{KE}) might be much greater than the strain energy (Π) at early stages of impact as shown in Figure 55. In time, the kinetic energy initiated by the loading is being damped. Consequently, they proposed a time interval required be

elapsed (t_{elp}) until at least having an equality between the strain energy and the kinetic energy, i.e.; $\Pi_{KE}(t_{elp}) = \Pi(t_{elp})$ in order to apply J-integral. An example is given in Figure 55 for the three-point-impact test. Initially, kinetic energy jumps due to the impact. Later on, kinetic energy is damped and the ratio of Π_{KE}/Π converges to lower values below the unity. In our study, the loading is quasi-static that implies no kinetic energy can be imposed by the loading.
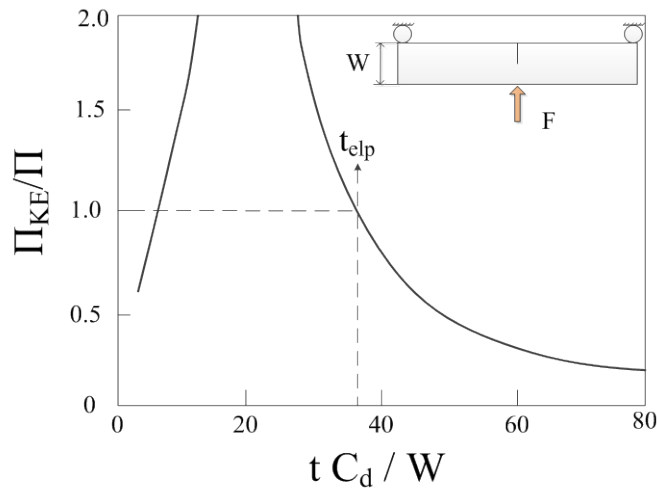
Figure 55 Ratio of kinetic energy (Π_{KE}) to strain energy (Π) as a function of normalized time in a three-point-bending impact test and time interval suggested by Nakamura et al. [128].

2.2.4. Definition of Cohesive Zone (CZ)

In the vicinity of crack tip, Dugdale [128] and Barrenblatt [130] proposed a small transition zone, so called *Cohesive Zone* (CZ), between traction free crack surfaces and elastic body. In 1960, Dugdale [128] proposed a yield strip model at the crack tip in that the plasticity limits the stress singularity at the yield stress. Dugdale [128] also derived mathematical relations between CTOD and the finite stresses at the CZ. In 1962, Barrenblatt [130] described the CZ in a more general aspect by relating cohesive tractions (T) (Figure 56) and relative displacement (δ), so called *traction-separation law* concept in the cohesive zone. Moreover, Barrenblatt [130] stated that the length of CZ, l_{CZ}, the shape of distribution and the magnitude of the cohesive

94

tractions prior to the crack growth are independent of the specimen geometry and the applied load. These properties make CZ as a material dependent phenomenon instead of a problem specific issue.
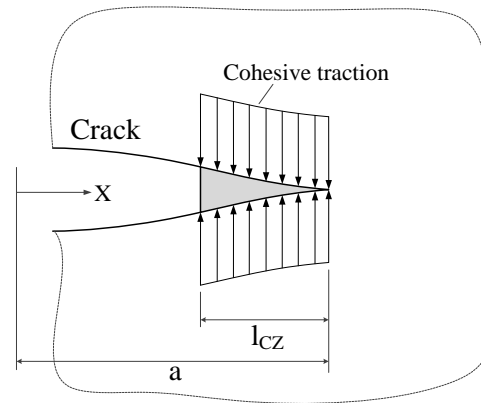
Figure 56 Cohesive Zone (CZ) in front of a crack tip with cohesive tractions proposed by Dugdale [128] and Barrenblatt [130].

Dugdale [128] and Barrenblatt [130] remarkably asserted the existence of CZ in a phenomenological way. Today, CZs are observed by optical techniques. For instance, in our case of delamination in CFRP laminates, the polymeric matrix dominates the physical appearance of the CZ. One of the physical phenomena in polymeric matrix is the *crazing* [131] (Figure 57). Long molecular chains in polymers, so called *fibrils*, tend to elongate through the crack tip in bundles as shown in Figure 57a. *Micro-voids* and *micro-cracks* are formed due to the bundling of fibrils, which segregate in front of the crack tip resembling crazes in a larger view. Microscopic photographs during the development of micro-cracks under ILSS are shown in Figure 57b for a brittle resin material. The characteristic view of shear micro-cracks is a canted crack with the angle of 45° from the main crack.

Delamination may breach to the adjacent fiber regions during propagation in composite laminates. In these cases, crazing is not adequate to explain the physical phenomenon in the cohesive zone. Fibers or beam-like ligaments may bridge the crack tip [132] as shown in Figure 58. This phenomenon is called *Fiber Bridging* that is a common feature creating cohesive tractions in front of the crack tip.

95

(a)

5 µm
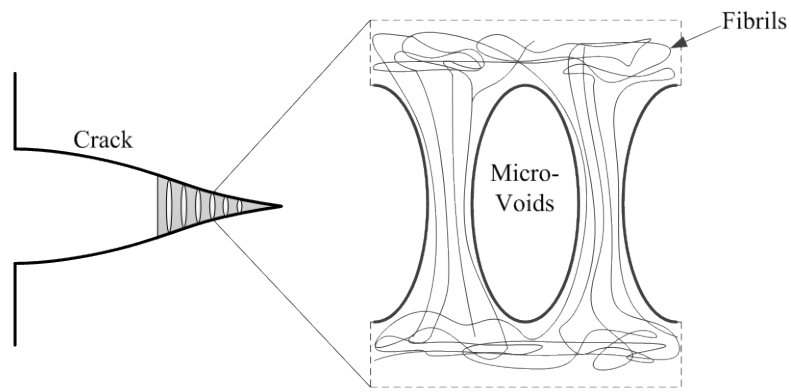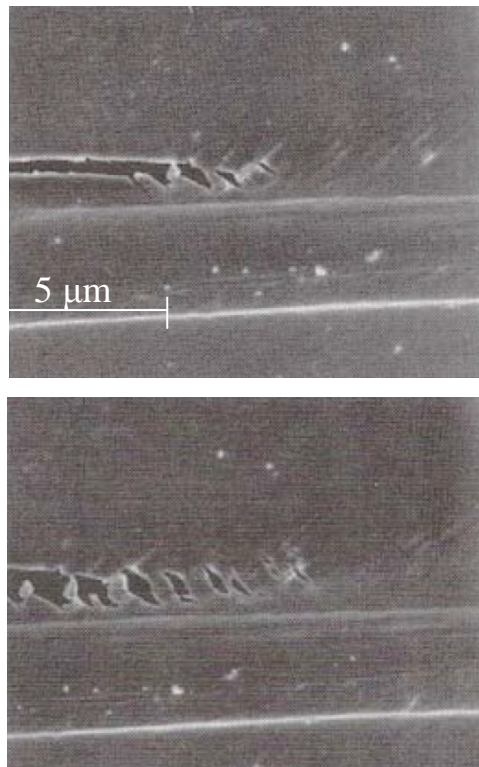
(b)

Figure 57 (a) Representative illustration of microvoids in a cohesive zone and (b) microscopic view of microcracks formed out of shear loading in a resin material (Photos are taken from Anderson [31]).
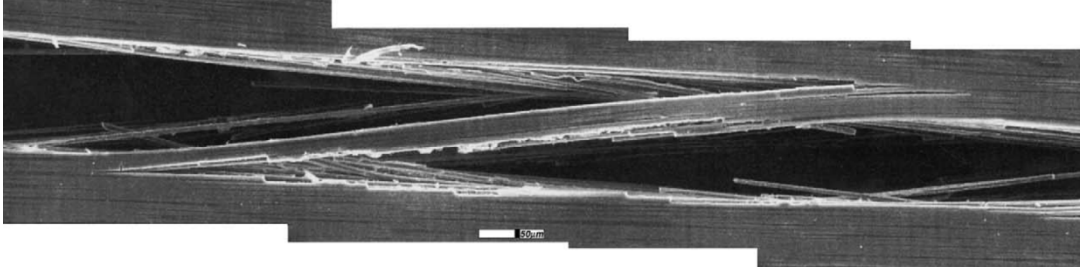
Figure 58 Fiber bridging made of fibers or beam-like ligaments made of fibers and portion of matrix material (Photo is taken form Sørensen and Jacobsen [132]).

2.2.5. Cohesive Zone Method (CZM)

Numerical analysis of crack propagation by modeling the constitutive law of CZ is called *Cohesive Zone Method* or *Cohesive Zone Modeling* (CZM). CZMs are generally functions of traction (T) and relative displacement of the crack surfaces, so called *separations* (δ). A constitutive law of a CZM is illustrated by springs in Figure 59 that is shown along a cohesive region with crazing in front of a delamination. CZ starts after a *traction free zone* at δ_c; i.e. $T(\delta_c) = 0$ and ends by reaching the maximum traction at δ_o; i.e. $T(\delta_o) = T_o = \max$. The corresponding separations for the maximum traction may be zero or so small that it is always smaller than δ_c; i.e. $\delta_c > \delta_o$. In references, δ_c and δ_o are called as *critical* and *onset separation*, respectively. Noting that, the subscripts of "c" and "o" respectively refer to critical and onset separations throughout this study. Referring to the CTOD, critical and onset separations are indeed material or interface properties. In between these two extremities, traction distribution resembles the characteristic softening behavior. One of the first FEA applications was performed by Hillerborg et al. [133] in 1976 to the best of author's knowledge.

For a contour of Γ surrounding the upper and lower surfaces of a cohesive zone, J-integral can be calculated with the assumption of $\delta_c \ll l_{CZ} \ll a$;

$$J = \int_{\Gamma}\left(\psi dy - T_i \frac{\partial u_i}{\partial x} ds\right) = \int_{\Gamma}\left(-T_i(X)\left(\frac{d\delta_i}{dX}\right)dX\right) = -\int_{\Gamma}\frac{d}{dX}\left(\int_0^{\delta'} T_i(X)d\delta_i\right)dX = \int_0^{\delta'} T_i(X)d\delta_i \quad (50)$$

where $X = x - l_{CZ}$ and $dy = 0$ along the selected contour.

97
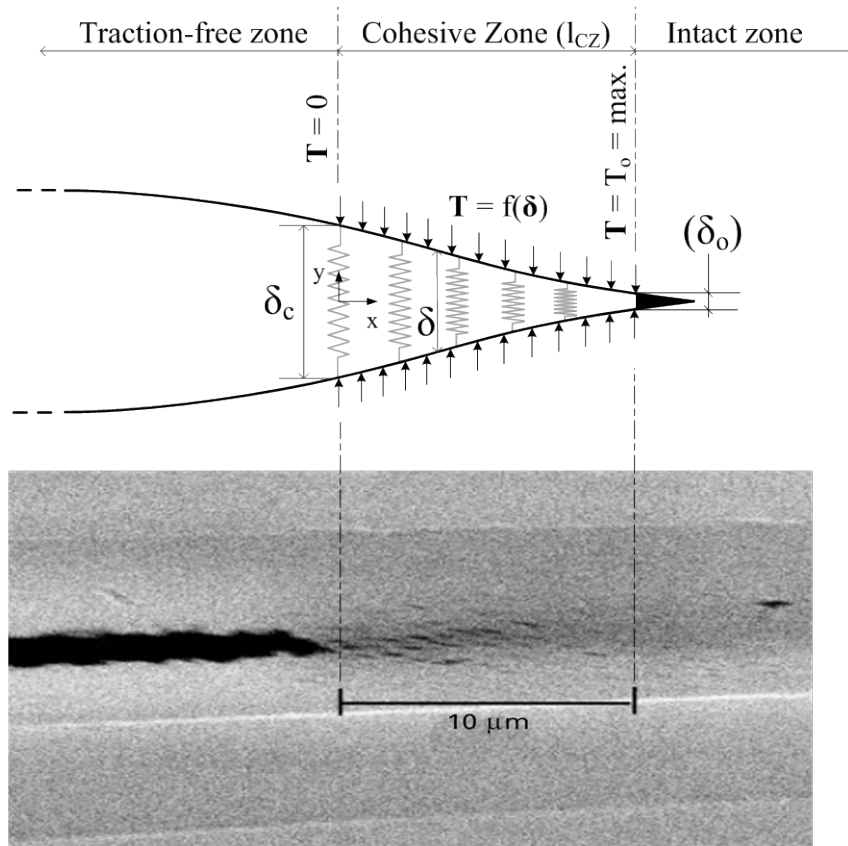
Figure 59 Cohesive zone method illustration show on an example of a physical cohesive zone in a delamination crack (The photo at the bottom is taken from Sridharan [15]).

For a self-similar crack growth and the assumption of small cohesive zone, the below equation can be written;

$$J = \int_{0}^{\delta'} T_i(X) d\delta_i = G \tag{51}$$

Eqn.(51) states that the area covered by the CZM traction-separation law is equal to the energy release rate, G (Figure 60a). If the vector components, *i*, in eqn.(51) is kept at one direction, eqn.(51) will give energy release rate in mode-*i*; i.e.: $J_{(i)} = G_i$. Similarly, the total area covered by the T-δ constitutive law is equal to the fracture toughness, G_c, such that;

$$J = \int_{0}^{\delta_c} T_i(X)d\delta_i = G_c \tag{52}$$
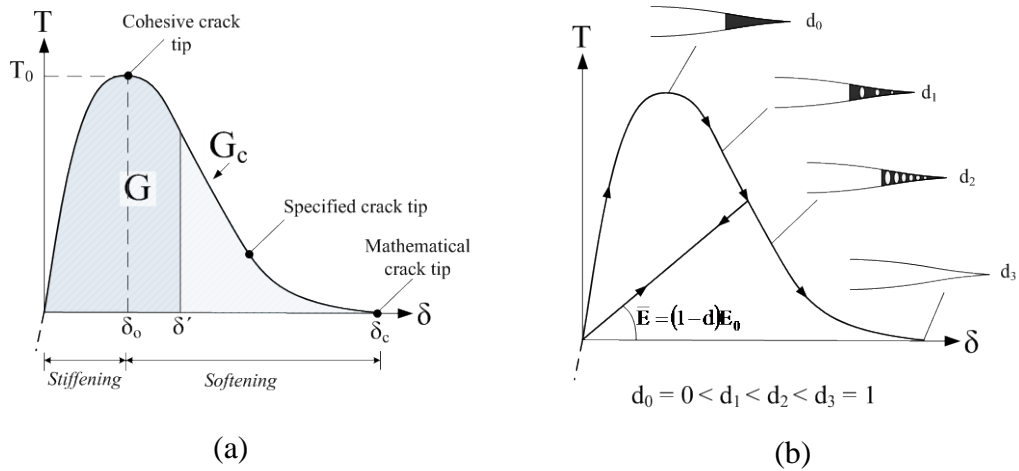
Figure 60 (a) A traction, T, and relative displacement, δ, CZM profile together with energy release rate, G, fracture toughness, G_c, and the possible crack tip definitions, (b) loading and unloading with development of damage, d.

In general, CZMs have *stiffening* reaching a maximum traction which is followed by a decrease in the stiffness, so called *softening* (Figure 60a). This behavior can be analogized to atomic potential [134] that relies on the assumption made by Barrenblatt [130] and generally which is continued by other authors to be mentioned in the following paragraphs.

Up to now, no distinction has been made between mode-I and mode-II. In our study, the subscripts of "I" and "II" are used for relating separations and tractions to mode-I and mode-II, respectively, whereas the mixed-mode separations and tractions do not have subscripts of "I" and "II". In general, a constitutive law in mode-I considers fracture energy in an opening relative displacement for mode-I (δ_I); i.e. $\delta_I > 0$ as shown in Figure 61a. The area covered in mode-I would be G_{Ic} in $\delta_c \leq \delta_I \leq 0$. Highly stiff response is exerted by the model for negative mode-I relative displacement; $\delta_I < 0$, in order to avoid interpenetration of the mating crack surfaces. On the other hand, an anti-symmetric CZM traction-separation law is mostly observed in mode-II case

99

as shown in Figure 61b. Similarly, the area covered by each region in the figure is equal to G_{IIc}.
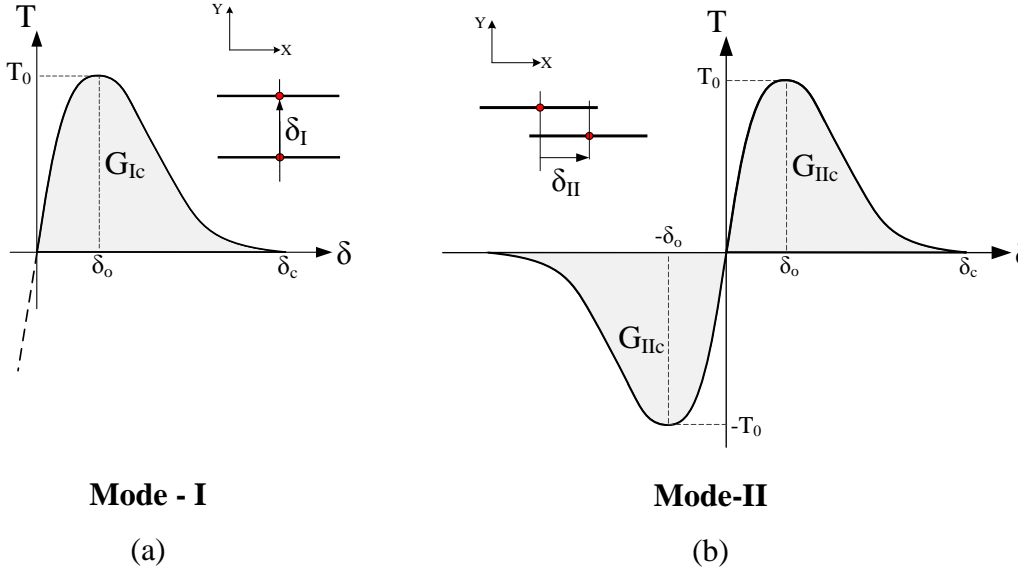
Figure 61 CZM constitutive laws for (a) mode-I and (b) mode-II

An issue of compatibility is come across in the mixed-mode scenario. In theory, a cohesive interface would fail if the total released fracture energy is equal to the toughness. In numerical analysis, however, the load may vary. As a result, the energy release rate might be continuously changing through the numerical solution in terms of mode-I and mode-II dominancy for a mixed-mode case. For example, a CZM traction separation law may reach the critical displacement of δ_c where G_{Ic} was already covered as shown in Figure 61a. In that case, the interface is assumed to be "failed" by mode-I although G_{IIc} would not be dissipated. Hence, the interface is still capable of reacting mode-II loads from modeling point of view. In theory, if an interface is failed, no matter it is due to mode-I or mode-II loading, there should be no response from the CZ. Therefore, compatibility should be sustained in CZM constitutive law through the solution scheme. A detailed discussion was made by Gozluklu [135] about incompatible and compatible CZMs in the literature and their influences into the numerical solution schemes.

One may realize that no initial crack is required to use CZM although, theoretically, CZ exists in front of a crack tip. This makes CZM a great tool regarding the conventional fracture methods such as VCCT. In 2000, Mohammed and Liechti [136] studied crack initiation at a sharp bi-material edge between aluminum and epoxy as shown in Figure 62. Mohammed and Liechti [136] reached excellent agreement with the experimental results for the initiation analysis.
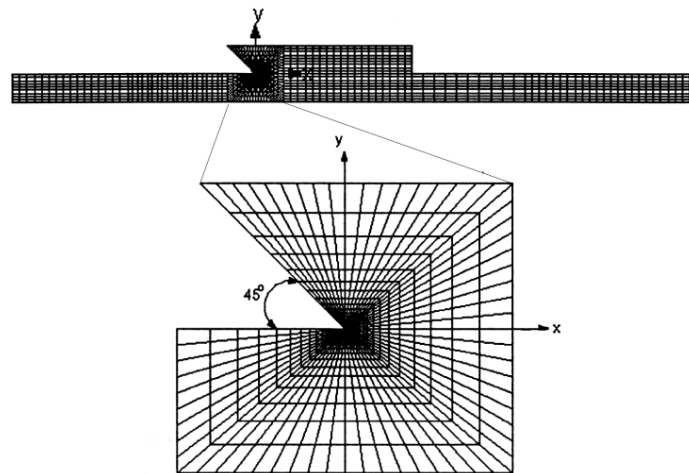
Figure 62 Application of CZM by Mohammed and Liechti [136] for initiation of a crack in bi-material sharp interfaces.

2.2.5.1. Definition of the crack tip in CZ

The definition of crack tip in CZ is not definite since it is a transition region. According to Shet and Chandra [137], there are three possible definitions. The first is the *mathematical crack tip* which is defined by the critical separation of δ_c (Figure 60a). Mathematical crack tip is the nearest point to the traction-free surfaces and generally represents the observable crack tip in the experiments. Geubelle and Baylor [175] used mathematical crack tip by seeking $d = 1$ in their BL CZM. The next possible definition is the cohesive crack tip as shown in Figure 60a. Cohesive crack tip corresponds to the maximum traction at $\delta = \delta_o$. According to Shet and Chandra [137] and Yang and Cox [11], physical appearance of cohesive phenomenon gets into shape in the softening region which starts after $\delta > \delta_o$. In other words, cohesive

crack tip can be associated with the start of softening phenomena such as formation of crazes and/or fiber bridging etc. The first two of the definitions can be attributed to physical appearance of the CZM. On the other hand, *specified crack tip* can be used at any location between these two definitions as shown in Figure 60a. Such an approach was used by Xu and Needleman [138] in which the displacements of $2\delta_o$ – $6\delta_o$ are specified as a crack tip. They reported no considerable difference between using $2\delta_o$ and $6\delta_o$ in the results [138]. For mode-II dominated fracture, locating the mathematical might be unsuccessful from the stress plots due to large shear stress concentration regions and deformation of mode-II fracture which may physically hide the crack tip. Coker and Rosakis [112] considered a specified definition of crack tip based on the separation value of $\delta = 5\delta_0$. Unlike the conclusion of Xu and Needleman [138], Coker and Rosakis [112] reported different crack tip speeds for different definitions of the crack tips.

2.2.5.2. Irreversibility and Damage Mechanics

Formation of new surfaces during crack propagation is an irreversible unless there is crack healing [139]. Namely, CZM represents an irreversible process. Figure 60b shows a CZM constitutive law in which loading and unloading are shown by rightward and leftward arrows, respectively. It can be seen that unloading takes place through a linear path connected to the origin as firstly proposed by Allix and Ladeveze [140], Corigliano and Allix [107] and Camacho and Ortiz [141]. Next, the loading goes over the same path towards the right due to the irreversibility. This is a typical behavior of CZM during loading/unloading after a finite value of fracture energy is released.

The irreversibility is taken into account by *Continuum Damage Mechanics* which is originally proposed by Kachanov [142] for metal creep in 1958. Although the original work of Kachanov did not refer to micromechanics or CZM, continuum damage mechanics works well from micromechanics points of view and CZM [143].
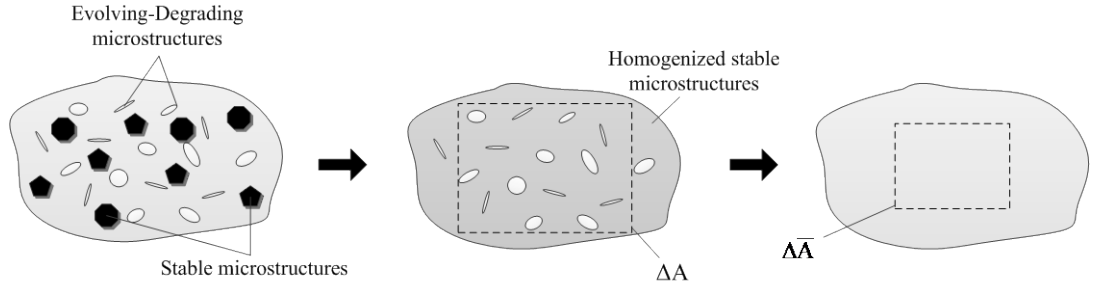
Figure 63 Original microstructure made of evolving-degrading constituents (left) that is homogenized for stable microstructures (middle) where an area, ΔA, is shown that is homogenized with a reduced damaged area, $\Delta\overline{A}$ (right).

The damages, such as voids and cracks, degrade the stiffness of the body as they develop in time. Besides, there are stable microstructures as illustrated in Figure 63 – left. In continuum damage mechanics, stable constituents are homogenized so as to isolate the degrading microstructures (Figure 63-middle). An enclosed area of ΔA is shown in Figure 63-middle where the total area formed by voids and cracks are denoted as ΔA_{deg}. Voids and cracks can be removed from the enclosed area, ΔA, to obtain the effective area, $\Delta\overline{A}$; i.e. $\Delta\overline{A} = \Delta A - \Delta A_{deg}$ (Figure 63-right). For each plane having a normal vector of **n**, the ratio of ΔA_{deg} to ΔA is equal to *damage*, $d_{(n)}$, as follows [143];

$$d_{(n)} = \frac{\Delta A_{deg}}{\Delta A} \tag{53}$$

Damage becomes free from planes such that $d_{(n)} \approx d$ for an isotropic damage as in our case of delamination. As a result, damage is scalar parameter in $d \in [0,1]$. Following this definition, the effective area can be defined as;

$$\Delta\overline{A} = (1-d)\Delta A \tag{54}$$

An example is given for a delamination at an interface of which CZM is provided in Figure 60b. The development of CZM due to loading is illustrated by formations of crazes at the crack tip and the corresponding damage values are given in the figure. The damage starts with $d_0 = 0$, implying "zero damage"- no degradation in the CZ.

As the loading develops, damage gradually increases as $d_1 < d_2 < 1$. Finally, the damage grows up to unity, $d_3 = 1$, meaning that the interface is totally failed. Hence, the stiffness of damaged interface, $\overline{E}$, can be written in the below form for a linear damage in the form of eqn.(54) [144];

$$\overline{E} = (1 - d)E_0 \tag{55}$$

where E_0 is the stiffness of the cohesive zone when $d = 0$. E_0 is generally called as *penalty stiffness* or *the initial slope* of the CZM. The irreversibility of the damage can be given as;

$$d(\tau) = \max_{0 \le \tau' \le \tau}\left[d(\tau')\right] \tag{56}$$

where τ is the current pseudo time and τ' is the pseudo time. The stiffness of a damaged interface in the light of irreversible damage becomes the slope of the unloading curve (Figure 60b). However, damage mechanics is not always used for the irreversibility in the cohesive literature. For instance, Allix and Corigliano [145] pioneered using the maximum attained separation whereas Camacho and Ortiz [141] proposed a force term in the form of eqn.(56) to consider irreversibility. Qiu et al. [146] used a non-dimensional history term determined by an elliptical equation based on the separations at normal and shear directions. Another approach was used by Borg et al. [139] in which total fracture energy released until that stage of loading was continuously removed from the toughness.

2.2.5.3. Constitutive laws for CZM

There are extensive number of studies about CZM in civil, mechanical and aerospace engineering literature. In this chapter, widely used CZM constitutive laws and their breakthrough applications are briefly presented. A summary of CZM constitute profiles at normalized axes are shown in Figure 64.

One of the widely used CZMs is the Exponential CZM, as shown in Figure 64a. Exponential CZMs are characterized by continuous exponential functions in which the full separation is reached asymptotically by $\delta/\delta_c \to 0$. One of the earliest exponential CZMs was proposed by Rose et al. [147, 149] based on universal metallic binding potential for mode-I fracture. Next, Xu and Needleman [138,147]

proposed their so called *Xu-Needleman (XN) CZM* for both mode-I and mode-II. These models have been derived from potential energy functions that were somehow based on atomic potentials as also studied by Needleman [150] and Rice and Wang [151]. Besides, Shahwan and Waas [152] proposed an exponential function to have a decaying constitutive behavior specific to the delamination propagation. The magnitude of the maximum traction is generally phenomenological; e.g. it was taken as 1/100 of the elastic modulus by Xu and Needleman [138]. However, Coker et al. [112] used experimentally determined failure stress of the interface. A modified version of XN CZM was proposed by van den Bosch et al. [153] for mixed-mode failure case. A similar exponential law was proposed by Rice and Wang [151] who studied interfacial embrittlement by solute segregation such as carbon, phosphorus and sulfur in iron. Another model with monotonically increasing exponential function without having a finite softening region was proposed by Davies et al. [154]. In that model, delamination analysis of composite laminates was studied. Moreover, Corigliano et al. [155,156] modified the XN model in order to include rate-dependency for dynamic delamination.

XN CZM has been successfully applied to dynamic fracture simulations. Needleman and Rosakis [157] modeled steel-PMMA bi-material dynamic crack propagation. Coker et al. [112] simulated dynamic crack propagation of polymer-composite under asymmetrical impact load using XN CZM. Their FE model predicted the same shock waves observed in the experiments (Figure 65a) as well as the crack tip speed as a function of time was also in agreement with the experimental results. Remarkably, mother-daughter crack mechanism was first simulated using XN CZM (Figure 65a).

Figure 64b shows the second type of CZM that was proposed by Dugdale [128] for elastic-plastic metals. This model exhibits a constant stress, the yield stress, along the CZ. This model is one of the earliest CZMs. A similar model was applied by Wisnom and Chang [158] for the delamination problem in notched composite laminates under interlaminar shear loading. Wisnom and Chang [158] implemented a sharp stiffening region starting from the origin. This was required for their numerical simulations in order to have a finite tangent stiffness matrix at the beginning of the implicit numerical scheme.
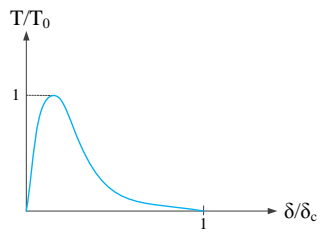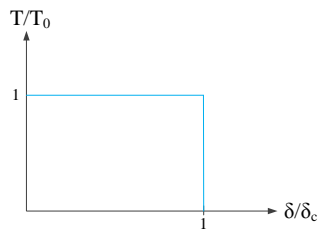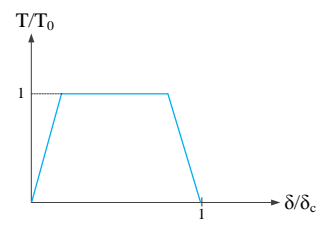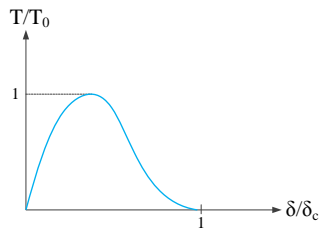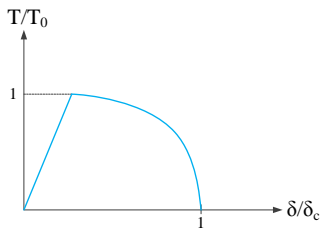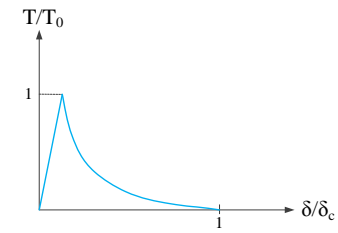
Figure 64 (a) Exponential, (b) Dugdale, (c) Piecewise Linear, (d) Polynomial, (e) Linear-Polynomial, (f) Linear-Decaying, (g) Rigid-Decaying (h) Rigid- Linear and (i) Bilinear (BL) CZMs.

The third type is the Piecewise Linear CZM initially proposed by Tvergaard and Hutchinson [159] (Figure 64c). In this model, the maximum traction is reached by typical stiffening from the origin. Afterwards, the traction stays at the maximum level which is followed by a softening region. This CZM was used for modeling the crack propagation in elastic-plastic materials by Tvergaard and Hutchinson [159]. A similar model was proposed by Yang and Thouless [160] for peeling of adhesively bonded T-shaped and L-shaped legs under mixed-mode conditions. Gustafson and Waas [161] used Piecewise Linear CZM for investigating the influences of the cohesive parameters to the results of DCB, ENF and MMB tests. Scheider [162] modified the model of Tvergaard and Hutchinson [159] in the way of smoothing the slope of the stiffening and softening regions in order to analyze the ductile fracture causing a cup-cone shape at the fracture surfaces.

Another shape is the Polynomial CZM as drawn in Figure 64d. Polynomial CZMs are similar to exponential CZMs except that the formulation is a polynomial function. Polynomial CZMs are generally referred to Tvergaard [164] who studied the fiber debonding (Figure 66) from a metal matrix fiber reinforced composite structure. Tvergaard [164] proposed a quadratic polynomial function. Espinosa et al. [165] successfully applied Tvergaard's polynomial CZM to dynamic fragmentation analysis of ceramic materials under impact loading. Pinho et al. [166] has used second and third order polynomial CZMs in explicit FEA. At the load-displacement curves of DCB and ENF test simulations, Pinho et al. [166] reported less oscillatory behavior in the polynomial CZMs compared to linear CZMs. Barrenblatt [130] proposed a CZM in a polynomial form. Also, Needleman [150] started with polynomial models for the mode-I fracture before the XN CZM.
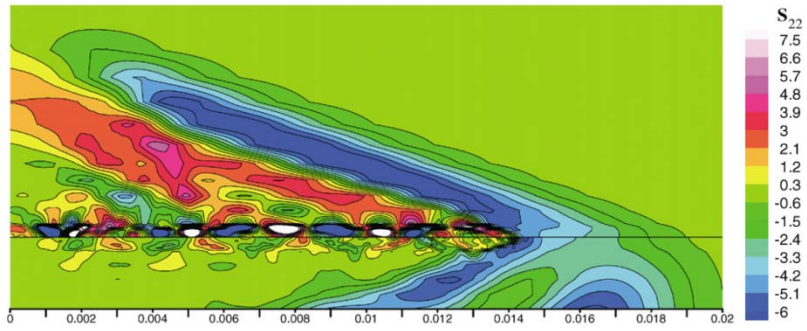
(a)
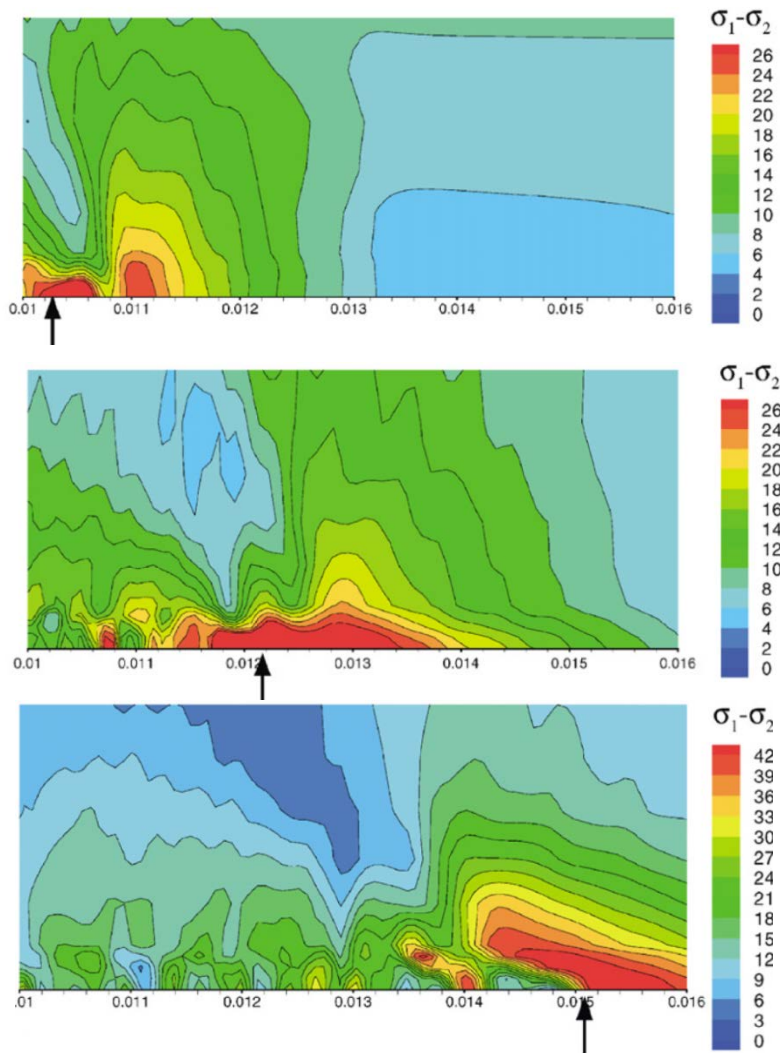
(b)

Figure 65 (a) Observations of intersonic crack proapagtion yielding a shear Mach
wave and (b) development of "mother-daughter" crack mechanism [112].
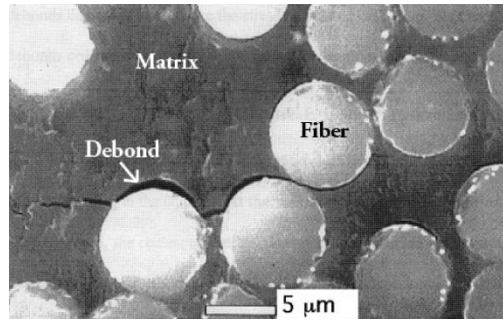
Figure 66 Debonding of fibers from the matrix

(from the lecture notes of Talreja [163])

A Linear-Polynomial type of CZM, as shown in Figure 64e, was proposed by Allix and Ladeveze [140]. The CZM has a linear part in the stiffening region after whereas a polynomial function is active at the softening region. It is one of the earliest CZMs that has been applied to delamination problem in laminated composites by Allix and Ladeveze [140]. Moreover, Allix and Corigliano [145] simulated the mixed-mode delamination in laminated composite laminates using linear-polynomial type of CZM. Corigliano and Allix [107] further extended the Linear-Polynomial CZM by including rate-dependency and analyzed delamination using the rate-dependent CZM. For in-plane fracture of composites, Li et al. [167] proposed a linear-polynomial type of CZM with two peaks in which the first one was for the matrix cracking while the second was used for the fiber cracking.

The sixth one is the Linear-Decaying CZM that is shown in Figure 64f. It is characterized by linear stiffening and exponential softening. Linear-Decaying CZM was firstly proposed by Reinhardt and Cornelissen [168] for fatigue analysis of concretes under cyclic loading. A similar model without having a stiffening region, a *rigid* type, is shown in Figure 64g. Rigid type of model is specifically called Rigid-Decaying CZM which was originally proposed by Planas and Elices [169]. This model has been rarely used.

In 1996, Camacho and Ortiz [141] proposed a Rigid-Linear type of cohesive model as shown in Figure 64h for the analysis of dynamic fracture in brittle solids under impact loading. The constitutive model starts directly from the maximum traction point which is followed by a linear softening region. The constitutive equations of

the CZM proposed by Camacho and Ortiz [141] have been expanded to 3D analysis by Ortiz and Pandolfi [170]. Later on, these models have been accurately used in the simulations of dynamic fracture where fragmentation of glasses was further achieved by Repetto et al. [171]. Also, Han et al. [172] successfully used the model of Ortiz and Pandolfi [170] for the delamination of composite sandwich panels. Yu et al. [173] used the CZM of Ortiz and Pandolfi [170] for simulating the dynamic crack propagation of asymmetrical dynamic loading of composite plates of Coker and Rosakis [116]. Their models correctly predicted the intersonic crack propagation as well as having a good agreement with the original numerical study performed by Coker et al. [112] using XN CZM.

(a)   (b)
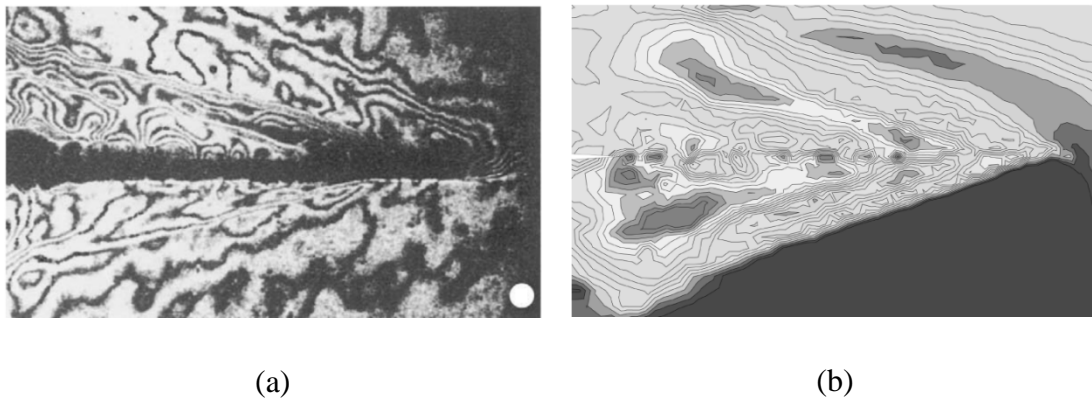
Figure 67 Double shear Mach waves (a) captured in the experiments of Coker and Rosakis [118] and (b) numerical simulation of Yu et al. [173] using Rigid-Linear type of CZM proposed by Ortiz and Pandolfi [170].

Bilinear (BL) CZM is one of the most popular CZMs in the composite literature for simulating the delamination. The characteristic of BL CZM is having linear stiffening and softening regions that result in a triangular shape as shown in Figure 64i. The pioneers of this type of CZM are Reedy et al. [174], Geubelle and Baylor [175] and Mi et al. [176] in which all of them studied the delamination in composite laminates. Specifically, Geubelle and Baylor [175] used BL CZM for the modeling of delamination due to low velocity impact in explicit FEA. On the other hand, Reedy et al. [174] used linear coupling of energy release rates in pure modes whereas

Mi et al. [176] used quadratic coupling of energy release rates in implicit FEA. Later on, Alfano and Crisfield [144] further extended the BL CZM with a more robust formulation by deriving the tangent stiffness matrix to be used with Arc-Length Methods [177] for the implicit solvers. The BL CZM of Alfano and Crisfield [144] separately manipulates the damage terms for each pure mode that yields the incompatibility between mode-I and mode-II at mixed-mode conditions. In order to compensate the incompatibility, Camanho et al. [178] proposed using single damage term instead of separate terms. Later on, Camanho and Davila [179] used a mixed-mode fracture criterion in order to make the BL CZMs compatible for both modes. On the other hand, Qiu et al. [146] used a non-dimensional term for sustaining the compatibility.

There are many applications of BL CZM in composite literature. Davila et al. [180] proposed a shell element, using BL CZM, so as to work as an interface element between 3D elements. Chen [181] analyzed delamination of repaired stiffened composite panels using BL CZM. Chen et al. [182] simulated the debonding and delamination of T-shaped composite part using the BL CZM. De Moura et al. [183] and Aoki et al. [184] simulated the low-velocity impact driven delamination in composite laminates. Robinson et al. [185] implemented a Paris-Erdogan type fatigue law into the BL CZM proposed by Mi et al. [176] so as to simulate fatigue driven delamination in composite materials.

Generally, BL CZM has been used in implicit analysis. For explicit FEA, Warrior et al. [186] applied the BL CZM in the simulation of DCB test. They reported oscillations in the load-displacement curves even from the beginning of the simulation which were considered as numerical artifacts (Figure 68a). Actually, oscillatory load-displacement curves are very common in the applications of explicit FEA. Similar observations of oscillatory responses were also reported by Pinho et al. [166] for the BL CZM. Similarly, Borg et al. [139] also applied BL CZM into explicit FE solvers in order to analyze stable mixed-mode delamination under quasi-static loading in which large solution durations were reported. Later on, Gozluklu and Coker [88] solved this issue by using smooth step loading profile of which initial slope was gradually increasing from a zero slope (Figure 68b). However, Gozluklu and Coker [88] reported strong oscillations after the start of dynamic delamination in

the L-shaped composite laminates. In addition to the oscillatory response, long solution durations for quasi-static loading using explicit solvers were reported by Borg et al. [139]. A numerical scheme based on a combination of implicit and explicit solutions was used by Gozluklu and Coker [88] which had considerably reduced the solution durations of quasi-static loading in explicit solvers.

(a)

(b)
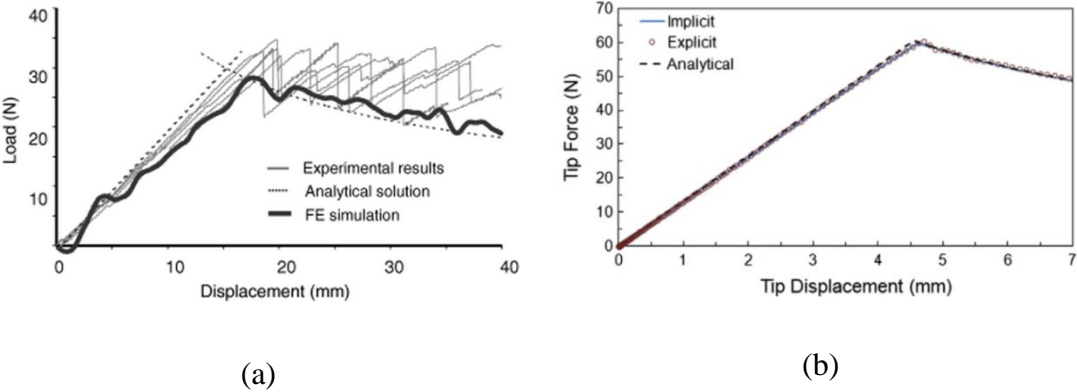
Figure 68 (a) Oscillatory load-displacement curves of DCB simulation using Explicit FE solver found by Warrior et al. [186] and (b) stable response obtained by Gozluklu and Coker [88].

There are BL CZMs which are variable in shape during the simulations. One of them was proposed by Hu et al. [187] where the maximum traction was increased by keeping the fracture toughness as the same (Figure 69a). The idea was to artificially increase the cohesive length to reduce the number of elements required in a cohesive zone for an accurate simulation and having easier convergence for implicit solvers. Another variable profile was proposed by Corigliano and Ricci [188] in which rate-dependency was included into the constitutive law. In that case, the maximum traction as well as the toughness is variable as shown in Figure 69b.

| (a) | (b) |
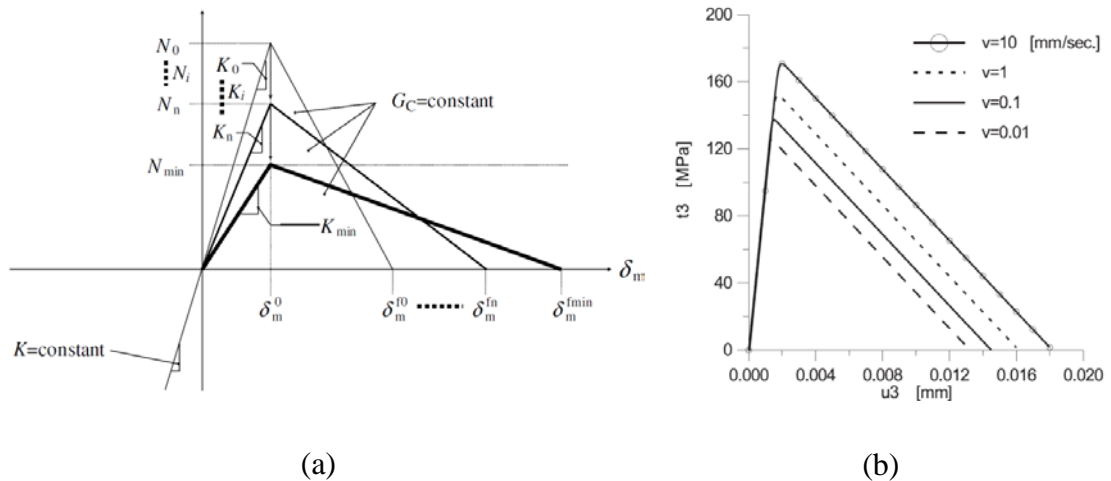
Figure 69 (a) Modification of the maximum traction (N) value of the BL CZM for reduction of mesh size proposed by Hu et al. [187] and (b) change of BL CZM due to rate dependency proposed by Corigliano and Ricci [188].

BL CZMs has been successfully applied for the analysis of dynamic crack propagation. Dwivedi and Espinosa [122] successfully applied the BL CZM of Espinosa et al. [189] to the numerical simulation of the asymmetric impact loading of composite plates of Coker and Rosakis [118]. Dwivedi and Espinosa [122] successfully captured the shear Mach waves in the simulations where they further included frictional effects into their numerical analysis. Recently, Gozluklu and Coker [88-90,92] applied BL CZM for revealing the dynamic crack propagation under quasi-static loading in delamination of L-shaped composite laminates. The modeling approach of Gozluklu and Coker [88-90,92] was also applied to the dynamic delamination of bonded L-shaped polymer beams [93,94].

In this chapter, several cohesive profiles have been discussed. Yet, the influences of cohesive profiles to the predictions were reported to be negligible by Williams and Hadavinia [190] and Tvergaard and Hutchinson [159] for stable crack propagation. For unstable dynamic fracture, Falk et al. [191] studied the effect of initially rigid and linear CZM to the branching of cracks under impact loading for isotropic homogeneous material. It was reported that the branching is hard to achieve for initially rigid CZMs. Other than that point, no considerable difference was reported

for the dynamic fracture in the references. In this study, BL CZM, XN CZM and a rate-dependent (RD) CZM will be used to further investigate the influences.

2.2.5.4.   Application and Issues in FEA of CZM

The simplicity of the constitutive laws makes the CZM a great tool for finite element applications. The traction-separation law of a CZM is implemented into *interface elements*, which are located between the mating surfaces; in our case, it is the interfaces between the plies. The interfaces, which include the cohesive interface elements, are called *cohesive interfaces* and the elements exhibiting CZM constitutive law are called *cohesive interface elements* (or simply *the interface elements*). For instance, the interface between the upper and lower laminates in a DCB test would be the cohesive interface (Figure 70a). The stress/traction distribution in front of a crack tip, length of the cohesive zone, l_{CZ}, and the corresponding load-displacement curves are illustrated in Figure 70b. In that figure, behaviors of five cohesive elements are given under monotonic loading. In the early stages of loading, the first element near the crack tip softens which degrades the stress/traction distribution near the crack tip. Noting that, the length of the degraded region represents the cohesive zone. There is no effect of the degredation in the first cohesive element to the load-displacement curve. As the loading continues, the first element in front of the crack tip reaches to the critical separation that results in total failure of the interface element. At that moment, the length of the cohesive zone is totally developed and the crack starts to propagate. In parallel, the maximum load is achieved. Afterwards, the load will drop, gradually. This is a typical development of the stress field and the interface element for CZM applications. Same behavior is applicable to the delamination of L-shaped composite laminates only with the difference of the length of the cohesive zone which changes according to fracture mode.

There should be adequate number of interface elements located in CZ in order to correctly model the cohesive behavior. The adequate number of interface elements also helps the convergence of FEA for implicit solvers. Turon et al. [192] suggested that the minimum number of cohesive elements should be 3 in a CZ for implicit solvers. Therefore, the resulting cohesive element length, w_e, can be defined as;

$$w_e \leq \frac{l_{CZ}}{3} \tag{57}$$

There are several proposals of formulations for calculation of the length of cohesive zone, l_{CZ}. The length of the cohesive zone has the below form for plane stress;

$$l_{CZ} = \kappa \left(E_{33} \frac{G_c}{T_o{}^2} \right) \tag{58}$$

where E_{33} is the modulus in the normal to the CZ direction, G_c is the fracture toughness, T_o is the maximum interfacial traction, and κ is the constant which has been differently used by authors as given in Table 3. Notably, Harper and Hallet [193] noticed that the cohesive zone length obtained by eqn.(58) is not the same with the one calculated using FEA.

The required length of the cohesive elements generally determines the mesh density of the finite element model since it would be the smallest dimension in the mesh. As seen from eqn.(58), the length of the cohesive zone is proportional to the inverse of $T_o{}^2$. It implies that the length of the CZ will be increased in the order of two as the maximum traction is reduced. For a longer CZ, the required length of the cohesive element will be larger; therefore, it would reduce the mesh density. Consequently, the duration of the numerical solution is reduced. The effects of the artificial increase of cohesive length by reducing the interfacial strength have been widely studied by Turon et al. [192], Harper and Hallet [193], and Hu et al. [187]. They successfully reduced the required mesh density and reached nearly the same results compared to the results obtained using original strengths. However, excessive reduction of the maximum traction can result in an artificial increase of the compliance of the model as reported by Harper and Hallet [193]. Moreover, Turon et al. [192] noted that the stress distribution at the CZ would be inaccurate. Gustafson and Waas [161] studied the influences of the cohesive parameters of fracture toughness and interfacial strengths to the predictions of the CZM. They showed that the fracture toughness greatly affects the results whereas the interfacial strength indicated negligibly small effect. Borg et al. [139] also pointed that the influence of varying the interfacial strength of the interfaces to the prediction of DCB, ENF and MMB simulations was

115

negligible. "Fine tuning" of the interfacial strength is a common application in references. However, it should be applied with caution.
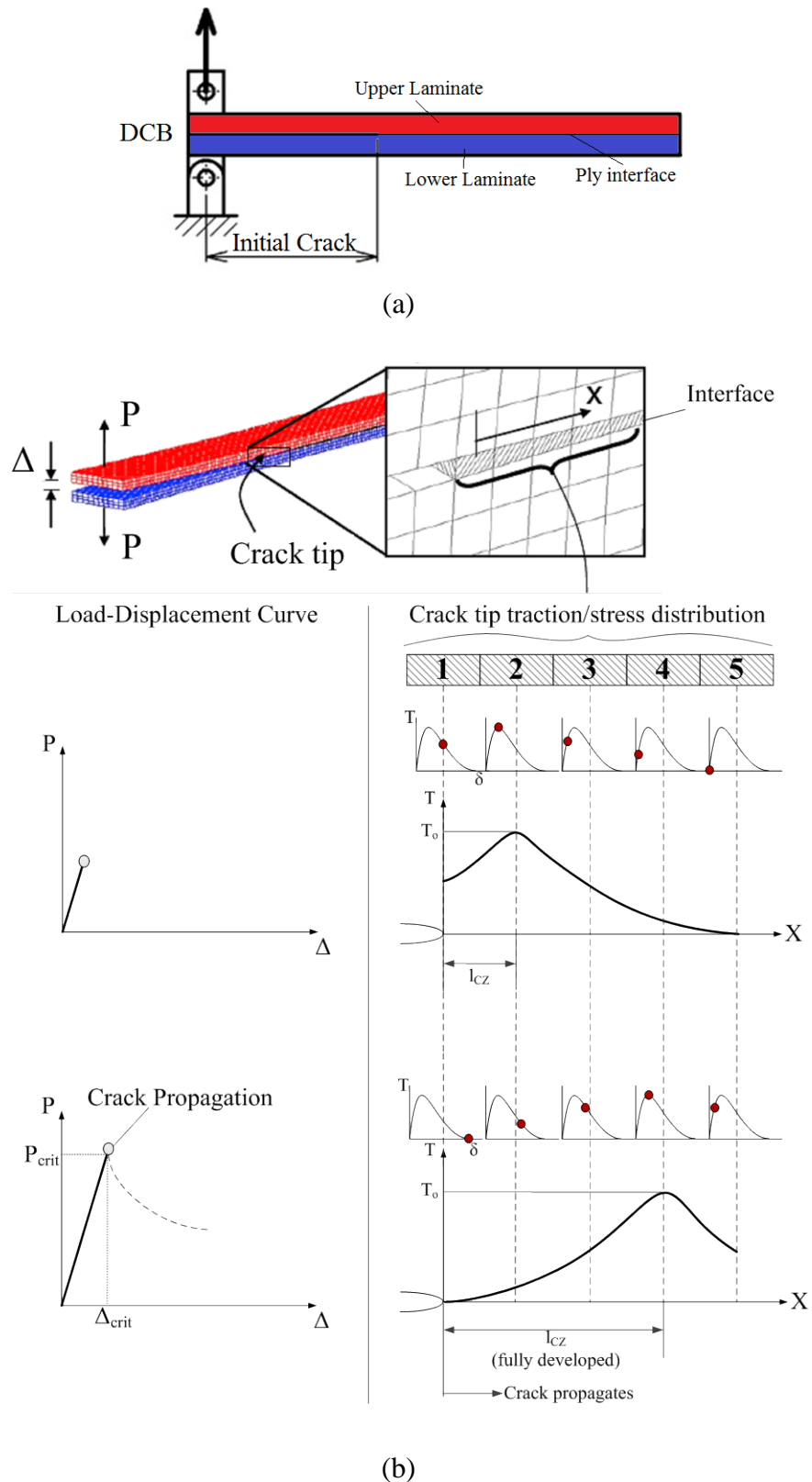
Figure 70 (a) DCB test and (b) development of CZM constitutive law, stress/traction distribution in front of a crack tip, length of cohesive zone and the corresponding load-displacement curve of DCB test model.

Table 3: κ values for the calculation of cohesive zone length, l_{CZ}, in eqn.(58)

	κ (in eqn.(58))
Hui et al. [194]	$2/3\pi$
Irwin [195]	$1/\pi$
Dugdale [128] and Barenblatt [130]	$\pi/8$
Falk et al. [191]	$9\pi/32$
Hillerborg et al. [133]	1.0

Using larger cohesive elements may cause osscilations at the load-displacement curves due to the harmonic vibrations and/or wrong estimation of the failure load. Figure 71a shows load-displacement curves of various element sizes for DCB test using implicit FEA [196]. The stiffness of the component and the failure load are artificially increased by decreasing the mesh density. Moreover, load-displacement curves reveal more osscilations with larger cohesive elements. Figure 71a shows typical response of delaminating specimen using larger cohesive elements.

(a)   (b)
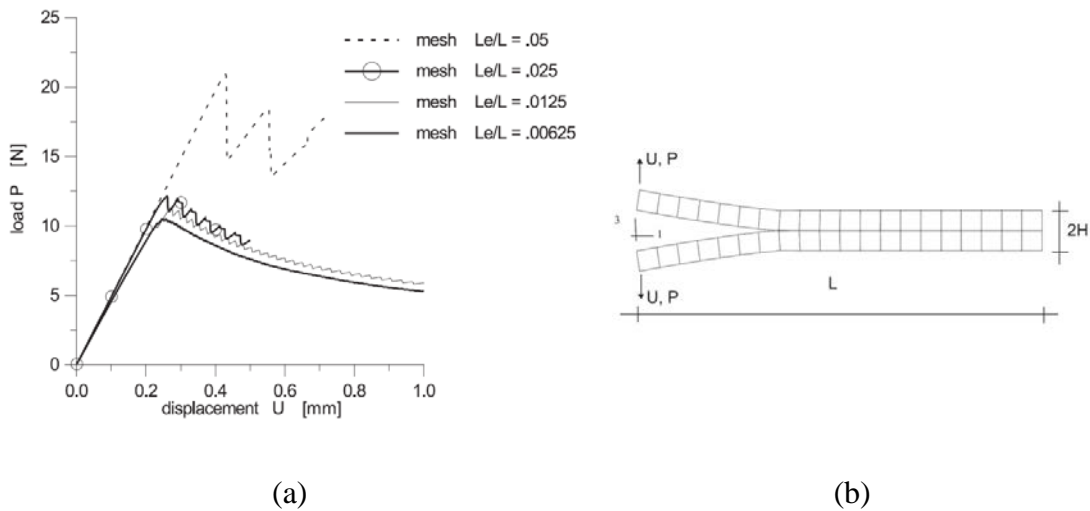
Figure 71 (a) Load-displacement curves of (b) DCB test with various element sizes [196] ($L_e = w_e$).

Cohesive elements are generally located between the body elements to form a weak plane. Cohesive element can be *discrete spring* (Figure 72a) or *continuum line* (Figure 72b) interface element for 2D-FEA. In most of the previous studies, cohesive elements were line interface elements. Xie and Waas [197] specifically named the method using discrete spring cohesive elements as "Discrete Cohesive Zone Method". For the 3D models, the continuum line elements become surfaces as shown in Figure 72c which was proposed by Sprenger et al. [197] and Davila et al. [180].

From the Figure 72, it can be observed that the interface elements do not have any thickness in the y-direction. Otherwise, they allocate a finite space that may result in an artificial increase of the thickness of the body. As CZM deals with traction-separation laws, instead of stress-stain relations, strains are not calculated. This enables using zero-thickness interface elements based on relative displacements of the nodes instead of strains. Besides, there are several studies which proposes using finite thickness in the interface elements such as Sprenger et al. [198], El-Sayed and Sridharan [199,200] where the CZM was based on stress-strain relations. In ABAQUS [69], there is continuum line cohesive element called *COH2D4,* that uses traction-separation laws such as BL and Linear-Decaying CZMs. Surprisingly, ABAQUS [69] requires finite thickness as an input even though it uses traction-separation laws. The reason of this requirement and the effect of the thickness are not well understood. Hence, BL CZM is re-implemented in the ABAQUS [69] via user-subroutines although BL CZM has been already available. Noting that, ABAQUS [69] has a feature of *cohesive surface* which can also define BL CZM relation between the element faces without defining an interface element. This type of modeling is similar to contact modeling, which is not common in literature to the best of author's knowledge.
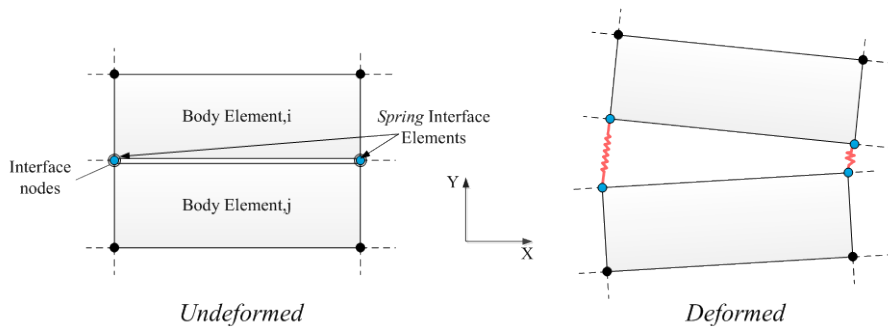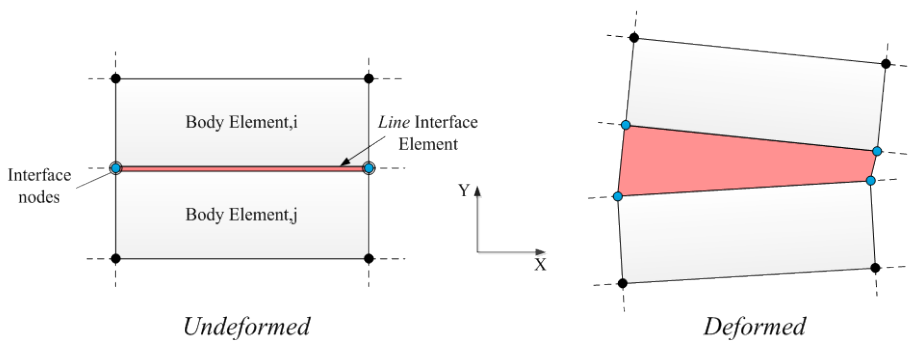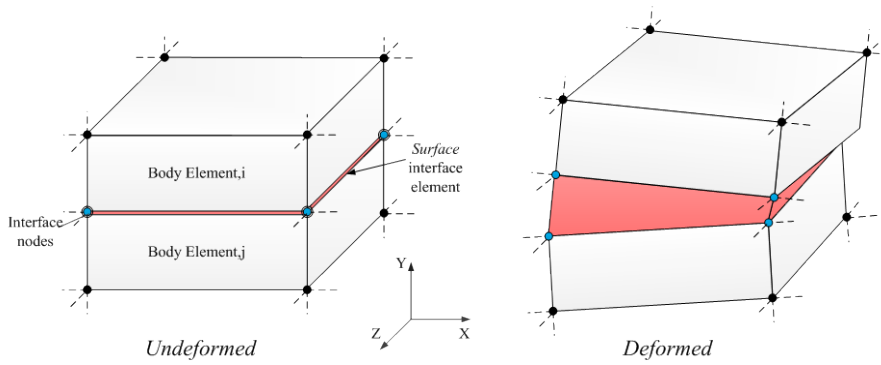
Figure 72 Undeformed and deformed (a) spring (discrete), (b) line, and (c) surface continuum interface elements.

One of the disadvantages of using cohesive elements is fixing the possibilities of crack propagation paths by the mesh. In order to increase the possibilities, one can put cohesive elements between all of the body elements. For instance, a mesh composed of triangular elements connected by line cohesive elements are given in Figure 73a. In this case, the crack is able to propagate through the cohesive elements such as indicated by arrows in the figure. Figure 73b shows the fragmentation of a glass specimen which was obtained by failure of cohesive elements under impact loading. Even though the interface elements are located between the triangular elements, the morphology of the mesh still restricts the movement of the crack. Moreover, working with large number of cohesive elements artificially increases the compliance of the finite element model because cohesive interface elements further introduce compliance at the connecting nodes (Figure 72). The order of the influence is directly dependent to the stiffness of the stiffening region of the used CZM which is studied in section 5.3.2.3.2. Hence, a CZM is supposed to have a relatively stiff initial value for avoiding artificial increase of compliance. Noting that, controlling the initial stiffness may not be possible for some CZMs, especially the ones derived from a potential function such as XN CZM.

In addition to using large number of cohesive elements, complex remeshing techniques might be required for enabling totally free crack path [141]. According to de Borst [202], remeshing techniques do not totally free the crack path. Moreover, the numerical solution becomes more cumbersome. A recent method enables the propagation passing through the elements because of a smeared representation of CZM in terms of shape functions. By that way, the crack propagation becomes mesh independent. This method is called *Extended Finite Element Method*, so called "XFEM" in literature [203], which is out of scope of this study.

121
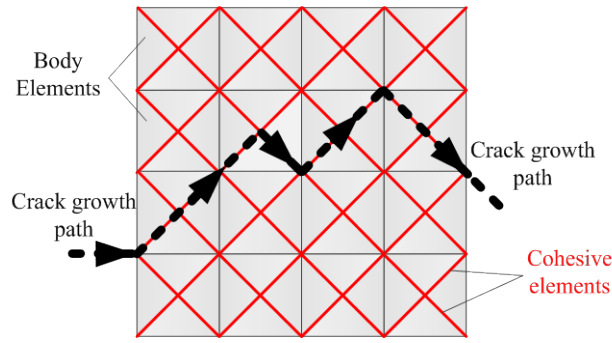
(a)
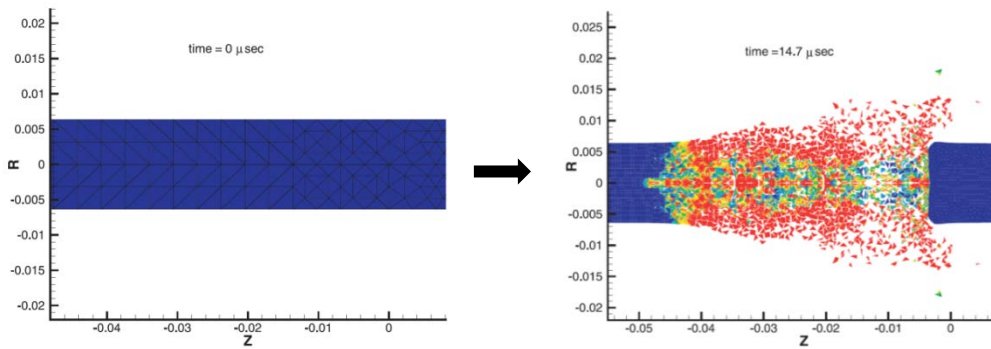
(b)

Figure 73 (a) A possible crack path in a mesh composed of triangular elements bonded by cohesive interface elements and (b) an example of fragmentation modeled by cohesive elements performed by Repetto et al. [171].

Extensive discussion about the numerical integration schemes of cohesive interface element can be found in the references [144,146,176,178,179,182,192,193,197,204]. It has been reported that inappropriate numerical integration schemes create similar effect of using inadequate mesh density such as spurious oscillations in the load-displacement curves. Schellekens and de Borst [204] investigated this issue in detail. Schellekens and de Borst [204] proposed using lumped integration schemes; such as Newton-Cotes instead of conventional Gauss method. It can be realized that the continuum cohesive elements become spring elements included into Discrete Cohesive Zone Modeling by Xie and Waas [197] once the Newton-Cotes scheme is selected.
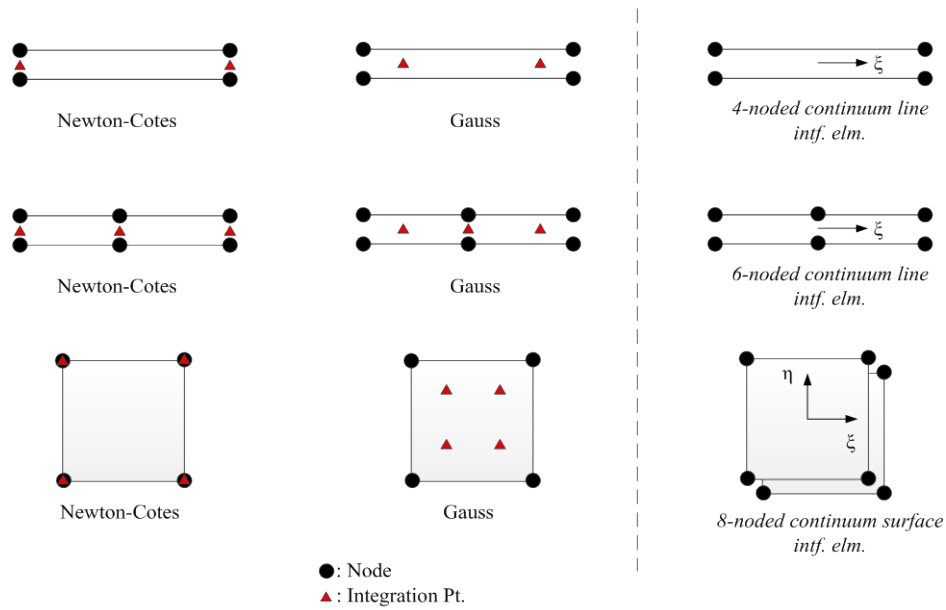
Figure 74 Integration points for Newton-Cotes and Gauss schemes for 4-noded line, 6-noded line and 8-noded surface continuum interface elements.

2.2.5.5. Derivation of Bilinear (BL), Xu-Needleman (XN) and Rate-Dependent (RD) Cohesive Zone Models (CZMs)

In our study, BL, XN and RD CZMs are used. The reason for using BL CZM is due to successful applications of the model to the composite delamination analyses. On the other hand, XN CZM has been successfully applied to high speed dynamic crack propagation analyses. Moreover, XN CZM provides a smooth profile compared to BL and RD CZMs. Besides, the rate-dependency in the interfacial properties of fracture toughness and interfacial strength foster for using RD CZM.

2.2.5.5.1. Bilinear Cohesive Zone Model (BL CZM)

BL CZM, the one proposed by Mi et al. [176], is used in our study. BL CZM is selected because it has been successfully used in the simulation of composite delamination by both explicit and implicit solvers   [146,166,177-182,200,192,193]. The derivation made by Camanho and Davila [179] is taken as the reference study.
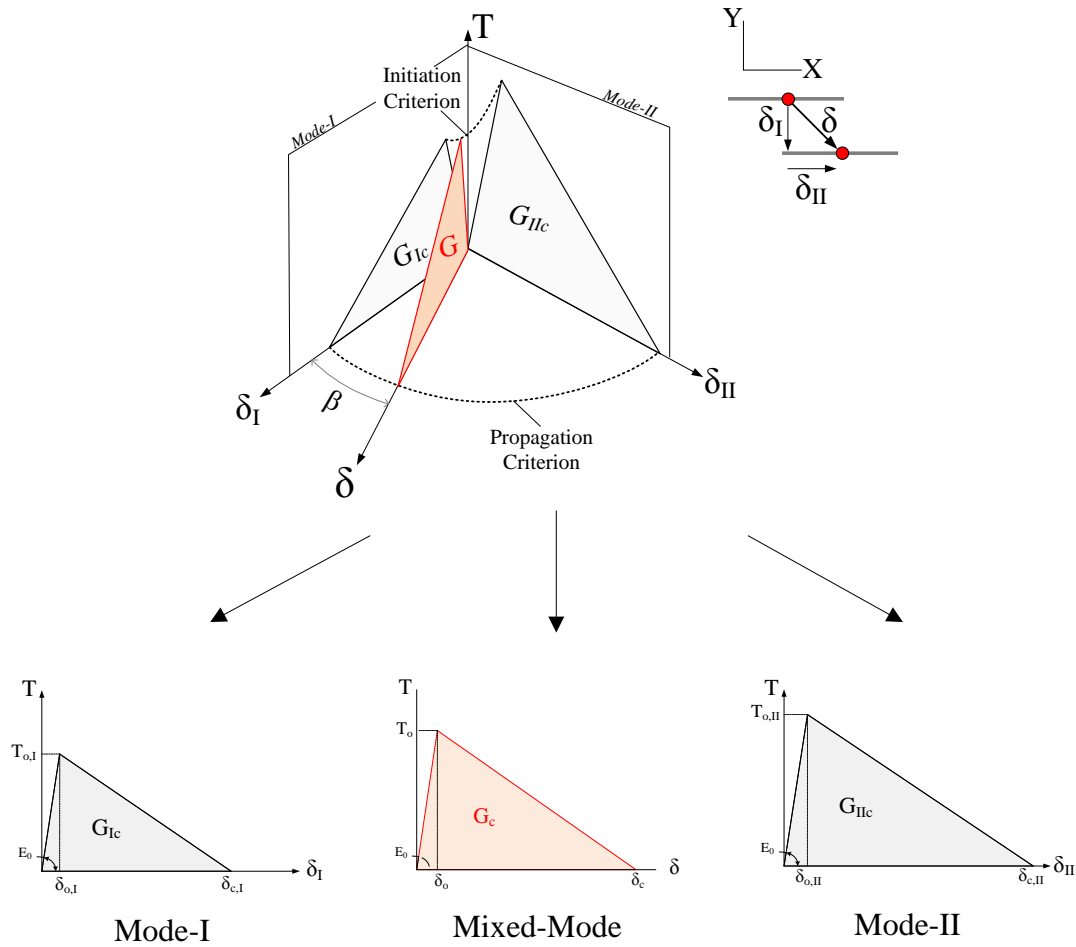
Figure 75 Constitutive law of BL CZM in mixed-mode, mode-I and mode-II.

One of the reasons behind the success of the BL CZM in the composite applications is linked to its constitutive law which is established by independent delamination initiation and propagation criteria. Figure 75 shows the mixed-mode BL CZM on mode-I and mode-II planes in which the maximum traction in mixed-mode condition (T_o) are related through the delamination initiation criterion [20-26]. The critical separation in mixed-mode condition (δ_c) are associated with the propagation criterion [36-38]. In those criteria, it is assumed that the pure mode parameters of the interface; $T_{o,I}$, $T_{o,II}$, G_{Ic}, and G_{IIc} are found by experiments mentioned in section 1.3.2.

The initial slope of the BL CZM (E_0) is called *penalty stiffness*. The penalty stiffness is generally taken as large as possible in order to minimize the elastic energy stored

in the cohesive element. Because all the energy dissipated by the CZM should be dedicated to the softening region that should be solely the fracture energy. Moreover, the implicit solvers require the tangent stiffness at the first iteration where penalty stiffness is used. However, excessively large penalty stiffness may result in numerical problems during the matrix operations in FEA scheme. Generally, trial-and-error method is used to determine the value of penalty stiffness.

The onset separation in pure modes ($\delta_{o,I}$ and $\delta_{o,II}$) can be found using the slope of the CZMs in pure modes as follows;

$$\delta_{o,I} = \frac{T_{o,I}}{E_0}, \qquad \delta_{o,II} = \frac{T_{o,II}}{E_0} \qquad (59)$$

where the maximum traction values of $T_{o,I}$ and $T_{o,II}$ can be obtained by the experiments such as ASTM D6415/D6415M [28] and ASTM D2344 [29], respectively.

Similarly, the critical separations in pure modes ($\delta_{o,I}$ and $\delta_{o,II}$) can be found by relating the area of the traction-separation law to the fracture toughness, G_{Ic} and G_{IIc};

$$\delta_{c,I} = 2\frac{G_{Ic}}{T_{o,I}}, \qquad \delta_{c,II} = 2\frac{G_{IIc}}{T_{o,II}} \qquad (60)$$

From Figure 75, the mixed-mode separation, δ, can be written as follows;

$$\delta = \sqrt{\langle \delta_I \rangle^2 + \delta_{II}^2} \qquad (61)$$

where δ_I is inside the Mc-Cauley brackets, $<x>$, that is $(x + |x|)/2$. With this method, negative separation in mode-I condition can be removed as CTOD < 0.

The angle between the mixed-mode and the mode-I separations is defined as, β, from Figure 75;

$$\tan(\beta) = \frac{\delta_{II}}{\delta_I} \qquad (62)$$

Up to now, the pure mode separations are derived from basic geometry and experimental values where the compatibility is established. Firstly, the maximum tractions are related to *onset of delamination* [146,166,177-182, 192, 193, 200]. This

is based on the theory that the energy release rate develops in the softening region of the CZM, in that a "crack" would be already initiated as the maximum traction was reached. In the light of this statement, the maximum mixed-mode traction can be related through the point-wise initiation criterion using the pure mode strengths. In our study, *elliptical* or *quadratic initiation criterion* [20-24] is used to derive the pure mode tractions, T_I and T_{II}, as below;

$$\left(\frac{T_I}{T_{o,I}}\right)^2 + \left(\frac{T_{II}}{T_{o,II}}\right)^2 = 1 \tag{63}$$

Substitution of the eqn.(59) and eqn.(62) into the eqn.(63) gives the mixed-mode onset of separation, δ_0, as below;

$$\delta_o = \begin{cases} \delta_{o,I}\delta_{o,II}\sqrt{\dfrac{1+[\tan(\beta)]^2}{\delta_{o,II}^2 + (\tan(\beta)\delta_{o,I})^2}} & if \quad \delta_I > 0 \\[4ex] \delta_{o,II} & if \quad \delta_I \leq 0 \end{cases} \tag{64}$$

where the interpenetration scenario is suited by $\delta_I < 0$.

For the propagation of delamination, the criterion proposed by Benzeggagh and Kenane [36] (B-K criterion) is applied. B-K criterion is a curve fitting equation with a curve fit constant of "η" based on experiments of DCB, ENF and MMB (Figure 76). B-K criterion is given as below;

$$G_c = G_{Ic} + (G_{IIc} - G_{Ic})\left(\frac{G_{II}}{G_I + G_{II}}\right)^\eta \tag{65}$$
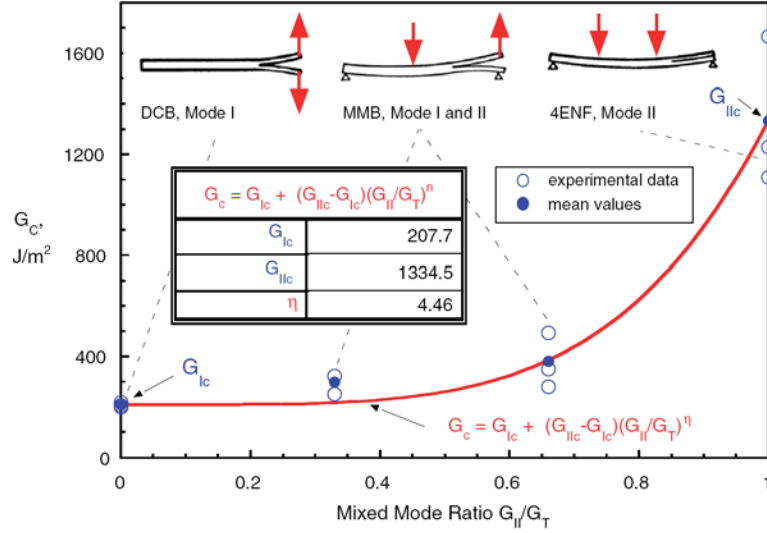
Figure 76: Application of B-K criterion using DCB, MMB and 4ENF tests for CFRP laminate by Turon et al. [200].

The pure mode onset and critical separations found in eqn.(59) and eqn.(60) are not applicable to the mixed-mode condition. The compatibility during the development of the separations under mixed-mode condition gives;

$$\delta_{o,I}^{M} = \delta_0 \cos(\beta), \qquad \delta_{o,II}^{M} = \delta_0 \sin(\beta), \tag{66}$$

$$\delta_{c,I}^{M} = \delta_c \cos(\beta), \qquad \delta_{c,II}^{M} = \delta_c \sin(\beta) \tag{67}$$

where superscript "M" refers to pure mode parameters under the mixed-mode condition (Figure 75). Assuming the same penalty stiffness at pure modes, the pure mode energy release rate under mixed-mode conditions, G_i^M (i = I, II), can be found as follows;

$$G_I = \frac{\delta_c \delta_o \cos^2(\beta) E_0}{2}, \qquad G_{II} = \frac{\delta_c \delta_o \sin^2(\beta) E_0}{2} \tag{68}$$

By substituting the eqn.(68) into the B-K criterion, the critical mixed-mode separation, δ_c, is obtained as below;

$$\delta_c = \begin{cases} \dfrac{2}{\delta_o E_0} \left[G_{Ic} + (G_{IIc} - G_{Ic}) \left(\dfrac{\tan(\beta)^2}{1 + \tan(\beta)^2} \right)^{\eta} \right] & if \quad \delta_I > 0 \\[4mm] \delta_{c,II} & if \quad \delta_I \leq 0 \end{cases} \tag{69}$$

In the above equation, the critical separation represents the failure of the interface. The critical separation becomes the mode-II critical separation in case of closing mode-I separations.

The unloading behavior of BL CZM is treated by the continuum damage mechanics. Isotropic damage, d, can be defined using the linear interpolation between the separations at zero damage d = 0 and fully damage d = 1;

$$d = \begin{cases} 0 & if \quad \delta \leq \delta_o \\[3mm] \dfrac{\delta_c (\delta - \delta_o)}{\delta (\delta_c - \delta_o)} & if \quad \delta_o < \delta < \delta_c \\[3mm] 1 & if \quad \delta \geq \delta_c \end{cases} \tag{70}$$

In addition to the above equations, eqn.(55) and eqn.(56) are used in the BL CZM. Afterwards, the mixed-mode tractions can be found as $T = \overline{E}\delta$.

2.2.5.5.2. Xu-Needleman Cohesive Zone Model (XN CZM)

Xu and Needleman [147] proposed a potential function of $\varphi(\boldsymbol{\delta})$. Total works of the separations in mode-I (δ_I) and mode-II (δ_{II}), are denoted as φ_I and φ_{II}, respectively. The works of separations are equal to G_{Ic} and G_{IIc}, respectively. Following those definitions, the potential function was provided by Xu and Needleman [147] as;

$$\varphi(\boldsymbol{\delta}) = \varphi_I + \varphi_I \exp\left(-\frac{\delta_I}{\delta_{o,I}} \right) \left\{ \left[1 - r + \frac{\delta_I}{\delta_{o,I}} \right] \frac{1-q}{r-1} - \left[q + \left(\frac{r-q}{r-1} \right) \frac{\delta_I}{\delta_{o,I}} \right] \exp\left(-\frac{\delta_{II}^2}{\delta_{o,II}^2} \right) \right\} \tag{71}$$

where $q = \varphi_{II}/\varphi_I$, $r = \delta_I^* / \delta_{o,I}$ with δ_I^* is the separation in normal direction for a total failure of the interface due to mode-II without normal traction. The potential function of inverse power can be referred to Lennard-Jones potential energy function [134].

The onset of separations of $\delta_{o,I}$ and $\delta_{o,II}$ can be found using the below relations [138];

$$\delta_{o,I} = \frac{\varphi_I}{T_{o,I}\exp(1)}, \qquad \delta_{o,II} = \frac{\varphi_{II}}{T_{o,II}\sqrt{\exp(1)/2}} \qquad (72)$$

where $T_{o,I}$ and $T_{o,II}$ refer to the maximum tractions in mode-I and mode-II conditions. The tractions in mode-I and mode-II are defined as; $T_I = \partial\varphi_I/\partial\delta_I$ and $T_{II} = \partial\varphi_{II}/\partial\delta_{II}$, respectively, which gives;

$$T_I = -\frac{\varphi_I}{\delta_{o,I}}\exp\left(-\frac{\delta_I}{\delta_{o,I}}\right)\left\{\frac{\delta_I}{\delta_{o,I}}\exp\left(-\frac{\delta_{II}^2}{\delta_{o,II}^2}\right) + \frac{1-q}{r-1}\left[1-\exp\left(-\frac{\delta_{II}^2}{\delta_{o,II}^2}\right)\right]\left[r-\frac{\delta_I}{\delta_{o,I}}\right]\right\} \qquad (73)$$

$$T_{II} = -\frac{\varphi_I}{\delta_{o,I}}\left(2\frac{\delta_{o,I}}{\delta_{o,II}}\right)\frac{\delta_{II}}{\delta_{o,II}}\left\{q+\left(\frac{r-q}{r-1}\right)\frac{\delta_I}{\delta_{o,I}}\right\}\exp\left(-\frac{\delta_I}{\delta_{o,I}}\right)\exp\left(-\frac{\delta_{II}^2}{\delta_{o,II}^2}\right) \qquad (74)$$

The figures of the constitutive law of XN CZM for mode-I and mode-II are shown in Figure 77a and Figure 77b, respectively, where $q = r = 1$. In mode-I case, negative normal separations is exposed to exponentially increasing stiffness acting as a resistance to interpenetration. The maximum normal traction, $T_{o,I}$, is attained at $\delta_I = \delta_{o,I}$. Beside, an anti-symmetric exponential function is observed in mode-II condition where the maximum tangential traction, $T_{o,II}$, is attained at;

$$\delta_{II}^{T-max} = \frac{\sqrt{2}}{2}\delta_{o,II} \qquad (75)$$
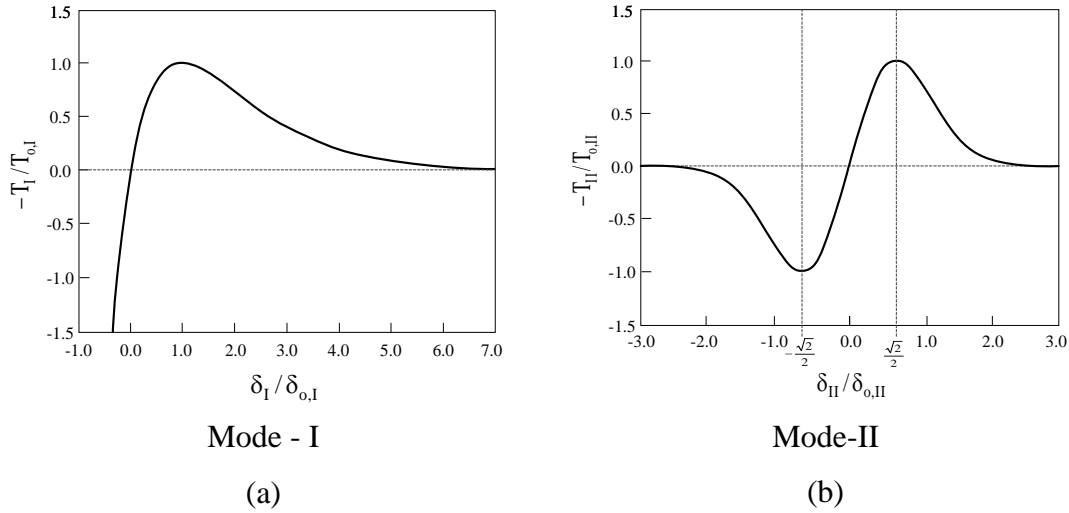
Figure 77 Constitutive law of XN CZM for (a) mode-I and (b) mode-II.

The maximum tangential traction normalized by the maximum normal traction at $\delta_I = 0$ as a function of normalized normal separation for $q = 0.5$ with $r = 0.2, 0.5$, and 0.8 are given in Figure 78a. The maximum normalized tangential traction is increased by increasing the negative normalized mode-I separation at $q = r$. Actually, this acts like a friction when $q = r$ and under compressive normal traction. On the other hand, the direction of the traction unrealistically changes with positive mode-I separation for $r > q$. Similarly, the friction lowers by increasing the negative normalized mode-I separation for $r < q$, which is not realistic either. Hence, the constitutive law in mode-II condition does not behave unless $r = q$.

The equality of $r = q$ can be taken as a rule and the same investigation can be done for the mode-I case. The maximum mode-I traction normalized by the maximum mode-II traction without any tangential separation as a function of normalized mode-II separation for $q = r = 0.2, 0.5, 0.8$, and 1.0 is shown in Figure 78b. It can be seen that the normal traction never goes to zero which is not realistic as the critical shear separation has been reached, except for $q = 1.0$. Hence, the constitutive law in mode-I does not behave realistically other than the case of $q = 1.0$. In mixed-mode conditions, XN CZM is applicable for $q = r = 1$, which implies that $\varphi_I = \varphi_{II}$ that is $G_{Ic} = G_{IIc}$. This equality is not very realistic in composite materials [18]. This means that

130

the original XN CZM proposed by Xu and Needleman [147] does not behave realistically in mixed-mode conditions with $G_{Ic} \neq G_{IIc}$.

Van den Bosh et al. [153] proposed to substitute q = 1 into eqn.(71). Next, the derivative of eqn.(71) with respect to the tangential separation gives the mode-II traction equation. Afterwards, they replaced φ_I by φ_{II} in the mode-II traction equation. As a result, the traction equations in the modified XN CZM become;

$$T_I = \frac{\varphi_I}{\delta_{o,I}} \left(\frac{\delta_I}{\delta_{o,I}} \right) \exp\left(-\frac{\delta_I}{\delta_{o,I}} \right) \exp\left(-\frac{\delta_{II}^2}{\delta_{o,II}^2} \right), \tag{76}$$

$$T_{II} = 2\frac{\varphi_{II}}{\delta_{o,II}} \left(\frac{\delta_{II}}{\delta_{o,II}} \right) \left(1 + \frac{\delta_I}{\delta_{o,I}} \right) \exp\left(-\frac{\delta_I}{\delta_{o,I}} \right) \exp\left(-\frac{\delta_{II}^2}{\delta_{o,II}^2} \right) \tag{77}$$

After the modification of van den Bosh et al. [153], two consequences come out. The first is that the phenomenological friction is lost. Secondly, the modified CZM does not have a potential function due to the artificial modification to the mode-II traction. However, the modified XN CZM works efficiently under mixed-mode fracture conditions with sustained compatibility between mode-I and mode-II cases.

Van den Bosch et al. [153] argued that the CZMs do not need to have a potential function since CZMs are supposed to be path-dependent. They envisaged two different separation paths of "rough surfaces" as illustrated in Figure 79. It can be seen that the resulting friction will not be the same for path-1 and path-2. Hence, the modified model of van den Bosch et al. [153] complies with the path-dependency.
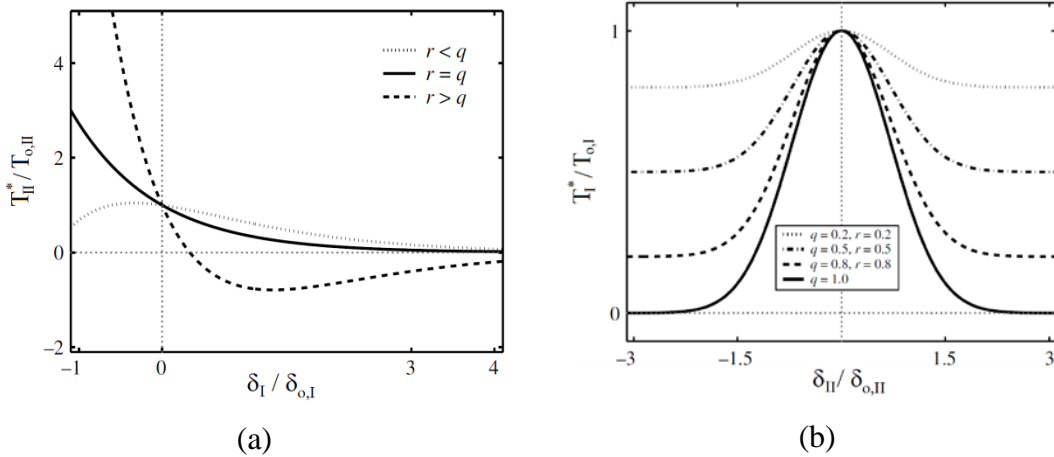
Figure 78 (a) Maximum mode-II traction normalized by the maximum mode-II traction without any normal separation, i.e. $\delta_I = 0$, as a function of normalized mode-I separation for $q = 0.5$ with $r = 0.2$, 0.5, and 0.8 and (b) maximum mode-I traction normalized by the maximum mode-II- traction without any tangential separation, i.e. $\delta_{II} = 0$, as a function of normalized mode-II separation for $q = r = 0.2$, 0.5, 0.8, and 1.0.
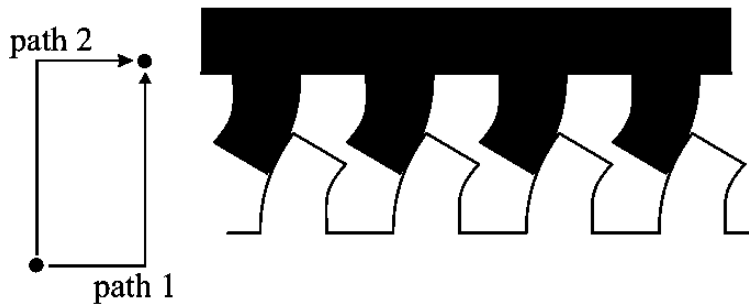
Figure 79 Two different separation paths for mating rough surfaces.

In XN CZM, there is neither damage nor a maximum value of the separation. There is no damage definition in the XN CZM. It means that XN CZM is a reversible model. On the other hand, the interface is assumed to be failed as it reaches to a predefined value of separation which is called critical separation and denoted by $\delta_{c,i}$ ($i = I,II$). In our studies, this value is taken as 20 times the onset values; i.e. $\delta_{c,i} = 20\delta_{o,i}$ ($i = I,II$). After that point, the element is removed from the model.

132
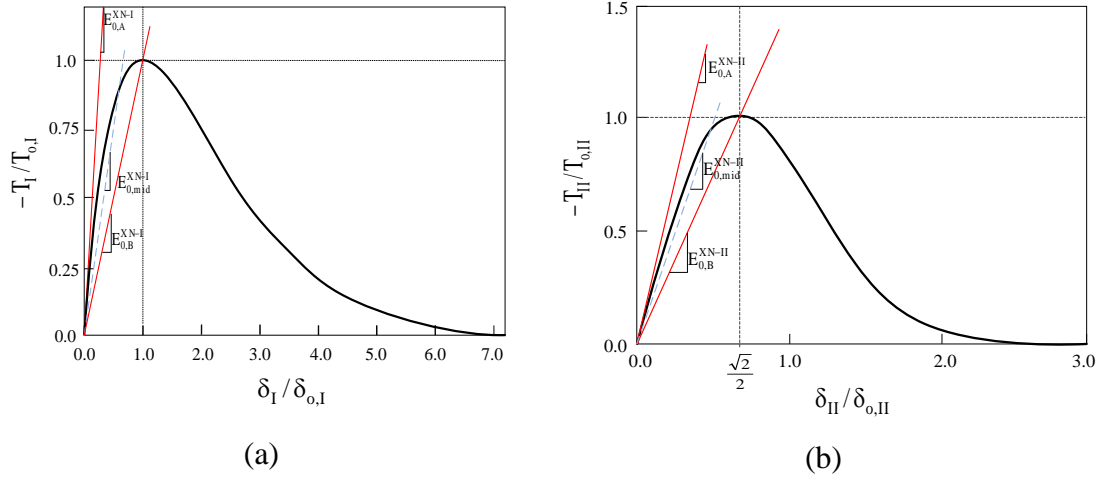
Figure 80 Definitions of possible penalty stiffness values in XN CZM for (a) mode-I
and (b) mode-II.

There is no specific definition of "penalty stiffness" for XN CZM just like seen in
BL CZM. Instead, several definitions of initial slopes of XN CZM can be attributed.
For example, the initial slope at $\delta_I = 0$, denoted by $E_{0,A}^{XN-I}$ in Figure 80a, can be
considered for mode-I. The initial slope, $E_{0,A}^{XN-I}$, can be calculated by taking the
derivative of eqn.(76) with respect to δ_I at $\delta_I = 0$ and $\delta_{II}=0$ (pure mode-I), and by
using the eqn.(72) as follows;

$$E_{0,A}^{XN-I} \cong \frac{\partial T_I}{\partial \delta_I}\Big|_{\delta_I=0} = \frac{G_{Ic}}{\delta_{o,I}^2} = \frac{T_{o,I}^2}{G_{Ic}}\exp(2) \tag{78}$$

Another definition of the penalty stiffness, $E_{0,B}^{XN-I}$, can be $T_{o,I}/\delta_{o,I}$ from Figure 80a. The
new candidate penalty stiffness, $E_{0,B}^{XN-I}$, can be calculated using eqn.(72) as follows;

$$E_{0,B}^{XN-I} = \frac{T_{o,I}}{\delta_{o,I}} = \frac{T_{o,I}^2}{G_{Ic}}\exp(1) \tag{79}$$

The mean of the above initial slopes can be also used as penalty stiffness in XN
CZM. The mean of the slopes, denoted by $E_{0,mid}^{XN-I}$ and shown as blue line in Figure 80a,
can be found as follows;

$$E_{0,mid}^{XN-I} = \frac{E_{0,A}^{XN-I} + E_{0,B}^{XN-I}}{2} = \frac{T_{o,I}^2}{G_{Ic}} \left(\frac{\exp(1) + \exp(2)}{2} \right) \tag{80}$$

Following the same procedure in mode-I, the initial slope for mode-II at $\delta_{II} = 0$ ($\delta_I = 0$), $E_{0,A}^{XN\text{-}II}$, can be calculated using eqn.(77) and eqn.(72) (Figure 80b);

$$E_{0,A}^{XN-II} \cong \frac{\partial T_{II}}{\partial \delta_{II}} \bigg|_{\delta_{II}=0} = 2\frac{G_{IIc}}{\delta_{o,II}^2} = \frac{T_{o,II}^2}{G_{IIc}} \exp(1), \tag{81}$$

Using the eqn.(72) and eqn.(75), the penalty stiffness of $E_{0,B}^{XN\text{-}II}$, is calculated (Figure 80b);

$$E_{0,B}^{XN-II} = \frac{T_{o,II}}{\delta_{o,II}^{T\_max}} = \frac{T_{o,II}^2}{G_{IIc}} \exp(1/2) \tag{82}$$

The mid-value of the slopes for mode-II, $E_{0,mid}^{XN\text{-}II}$, can be found as follows (Figure 80b);

$$E_{0,mid}^{XN-II} = \frac{E_{0,A}^{XN-II} + E_{0,B}^{XN-II}}{2} = \frac{T_{o,II}^2}{G_{IIc}} \left(\frac{\exp(1) + \exp(1/2)}{2} \right) \tag{83}$$

An important observation is that the initial slope of XN CZM is strongly dependent on the interfacial strength in the power of two.

2.2.5.5.3. Rate-Dependent Cohesive Zone Models (RD CZMs)

Two of the cohesive parameters; fracture toughness, G_c, and interfacial strength, T_0, are known to be rate-dependent (RD) material properties [205,206]. For example, fracture toughness as a function of crack tip speed and the interfacial strength versus *separation velocity*, $\dot{\delta}$, are shown in Figure 81a and Figure 81b, respectively for CFRP laminates. From the figures, it can be concluded that the fracture toughness and the interfacial strength exponentially increases with the crack tip speed and the separation velocity.
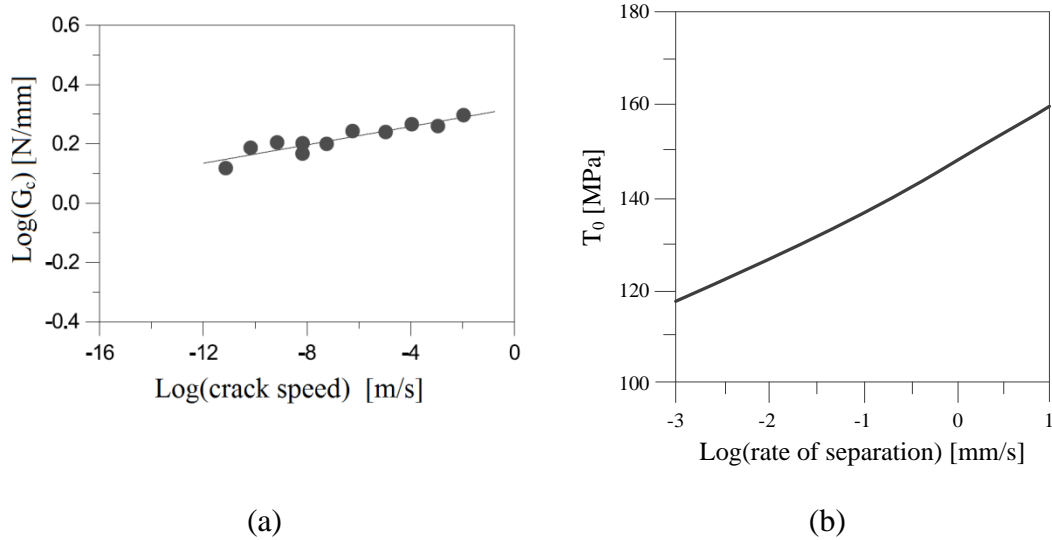
Figure 81 (a) Fracture toughness, G_c, as a function of crack tip speed [205] and (b) maximum traction, T_o, versus separation velocity ($\dot{\delta}$) [206] in CFRP laminates.

There are numerous studies about RD CZMs in literature. Rahul-Kumar et al. [207] proposed a RD CZM which is based on inverse power of the separation velocity. Rahul-Kumar et al. [207] analyzed T-peel test, compressive shear strength and delamination of composite laminates under contact experiments using their RD CZM. Landis et al. [208] derived a rate-dependent formulation for the piece-wise linear Tvergaard and Hutchinson [159] type of CZM. They analyzed the effects of rate-dependency for the fracture of epoxy material. They reported enhancement of fracture toughness and maximum stress at higher loading rates. An opposite behavior was observed for extremely high stresses such as greater than three times of the yield stress. Later, Corigliano and Ricci [196] proposed a rate-dependent BL CZM for implicit solvers and simulated DCB and ENF experiments at various loading rates. Corigliano and Mariani [209, 210] applied RD CZMs to the delamination analysis using implicit FEA. Similarly, Corigliano and Allix [107] proposed a RD Linear-Polynomial type of CZM for implicit FE solvers. Samudrala et al. [211] used a RD CZM, specifically having a linear dependency at the mode-II separation velocity, for the simulation of subsonic and intersonic crack propagation in PMMA plates with a weak plane [212]. It was shown that the fracture energy was considerably rate-sensitive. The fracture energy was enhanced by increasing the loading rate and

135

increasing the crack tip speeds close to the dilatational wave speed. Kubair et al. [213] developed a RD polynomial type of CZM. The polynomial RD CZM was used in conjunction with *spectral method* [213]. Anvari et al. [214] also proposed a rate-dependency in a model composed of polynomial and piecewise linear CZMs for ductile fracture of aluminum. They stated that that the crack tip speed still increases at higher loading rates, although the fracture toughness is enhanced by the strain rate. The reason for the increase was explained by decrease of the plastic zone in front of the crack.

The influence of rate-dependency to the delamination process is polemical. For example, Corigliano and Ricci [196] numerically simulated a DCB test using RD CZMs and compared to the experimental results (Figure 82). It can be seen that the failure load is increased from 73N to 75N even though the loading rate is multiplied by 10. Corigliano and Ricci [196] claimed that numerical analysis of delamination should involve rate-dependent models. However, accurate application of RD CZMs to the delamination problems was mentioned as a challenging process since RD CZMs involve additional material properties that are hard to be obtained. Moreover, RD material properties are too sensitive for the experimental setup [196]. On the other hand, there are studies which successfully simulated intersonic crack tip speeds without using RD CZMs [112,138,165,173]. According to Corigliano et al. [155], the effect of rate-dependency in high speed crack propagation should be debated, especially for the cases with high inertial forces. Despite the discussions about the RD, a rate-dependent BL CZM is proposed based on the approach of Corigliano et al. [155,156]. The RD CZM is used for understanding the influences of the rate-dependency on the dynamic delamination of L-shaped composite laminates.
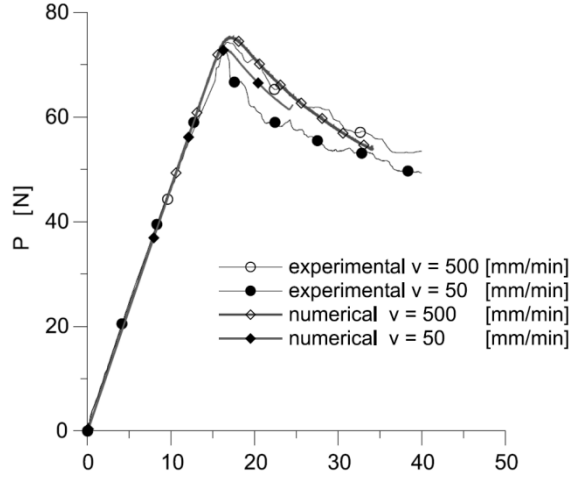
Figure 82 Load-displacement curves obtained using RD CZM and experimental data points for DCB test of a CFRP laminate [196].

2.2.5.5.3.1. A simple rate-dependent model of Corigliano et al. [155]

According to Corigliano et al. [155], the reference studies only work at quasi-static regime. Hence, they derived a simple rate-dependency behavior that had been implemented into CZMs proposed by Rose et al. [147,149], Camacho and Ortiz[141] and Xu-Needleman [147]. Corigliano et al. [156] successfully applied the rate-dependent CZM to the delamination of composite materials for mode-I case. Due to its simplicity, the rate-dependency proposed by Corigliano et al. [156] is used in this study. The rate-dependent onset separation, δ_o, is defined as below;

$$\frac{1}{\delta_o} = \frac{1}{\delta_{o,\infty}} + \left(\frac{1}{\delta_{o,0}} - \frac{1}{\delta_{o,\infty}} \right) \exp\left(-\frac{|\dot{\delta}|}{\dot{\delta}_o} \right) \tag{84}$$

where the separation velocity, $\dot{\delta}$, is defined as $\dot{\delta} = \partial\delta/\partial t$. $\delta_{o,0}$ and $\delta_{o,\infty}$ are the onset separations at *static* and *limit* conditions, respectively. $\dot{\delta}_o$ is the *reference onset separation velocity*, which is related to speed of fracture energy released during a dynamic event. The eqn.(84) can be written for mode-I and mode-II [156].

The rate-dependent onset separation normalized by static onset separation, $\delta_{o,0}$, as a function of the speed of separation, $\dot{\delta}$, normalized by the maximum speed at various reference onset separation velocity, $\dot{\delta}_o$ is provided in Figure 83. It can be seen that the reference onset separation velocity is related to the "damping" of the onset

137

separation, δ_o. Hence, a higher value of the reference onset separation velocity reduces the effect of rate-dependency.
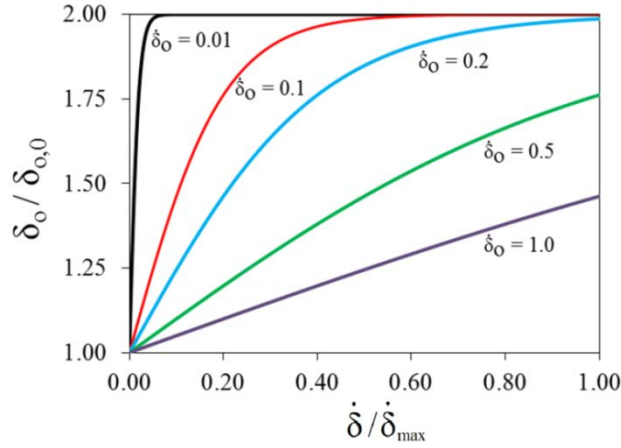
Figure 83 Onset separation, δ_o, normalized by static onset separation, $\delta_{o,0}$, as a function of speed of separation, $\dot{\delta}$, normalized by the maximum value at various reference onset separation velocity, $\dot{\delta}_o$.

In this method, the onset separations at static and limit conditions, $\delta_{o,0}$ and $\delta_{o,\infty}$, are assumed to be material properties. These values are the lower and upper bounds of the onset separations. Similarly, the fracture toughness at static and limit cases, $G_{c,0}$ and $G_{c,\infty}$, are the boundaries of the material fracture toughness. However, none of the boundaries involves time dependency. The reference separation velocity, $\dot{\delta}_o$, determines the time dependency, which is assumed to be known. The RD energy release rate as a function of normalized separation speed at various reference separation velocities are very similar to the Figure 83 between $G_{c,0}$ and $G_{c,\infty}$. The static interfacial strength, denoted as $T_{o,0}$, is also a material property that is determined by the experiments mentioned in section 1.3.2. Using the eqn.(72), the limit traction, $T_{o,\infty}$, in XN CZMs is related to the limit onset separation, $\delta_{o,\infty}$, and the limit fracture toughness, $G_{c,\infty}$, as follows [155,156];

$$T_{o,\infty} = \frac{G_{c,\infty}}{\exp(1)\delta_{o,\infty}} \tag{85}$$

The same rate-dependency equation given in eqn.(84) can be used for the tractions;

$$\frac{1}{T_o} = \frac{1}{T_{o,\infty}} + \left(\frac{1}{T_{o,0}} - \frac{1}{T_{o,\infty}} \right) \exp\left(-\frac{|\dot{\delta}|}{\dot{\delta}_o} \right) \tag{86}$$

Noting that, the curves of traction as a function of normalized speed of separation at various reference separation velocities exhibit the same behavior as shown in Figure 83 between $T_{o,0}$ and $T_{o,\infty}$. Figure 84 presents the constitutive law of the exponential rate-dependent CZM used by Corigliano et al. [155,156] at various separation velocities, $\dot{\delta}$. The figure is drawn using the specified parameters of $\dot{\delta}_o = 70$ m/s, $G_{c,\infty}/G_{c,0} = 5$, $\delta_{o,0}/\delta_{o,\infty} = 1.5$ and $T_{o,0}/T_{o,\infty} = 2.45$ which are taken from [156]. The rate-dependency appears as the increase of the energy release rate as well as the maximum traction at high velocity rates.
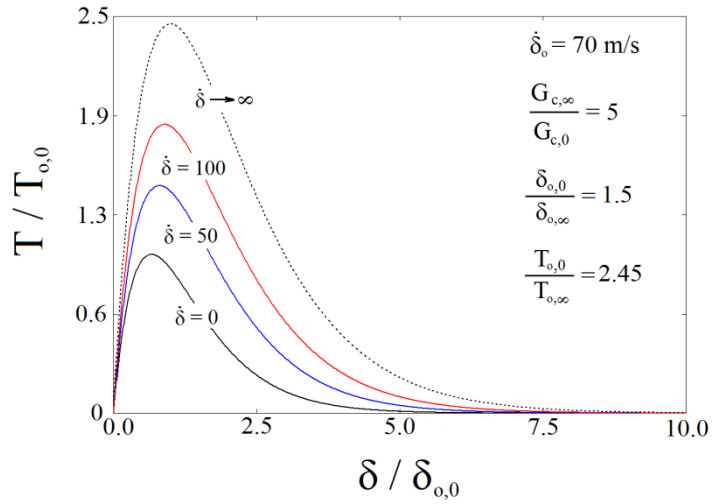
Figure 84 Normalized traction - separation law of the exponential rate-dependent CZM with the parameters of $\dot{\delta}_o = 70$ m/s, $G_{c,\infty}/G_{c,0} = 5$, $\delta_{o,0}/\delta_{o,\infty} = 1.5$ and $T_{o,0}/T_{o,\infty} = 2.45$ for $\dot{\delta} = 0$ m/s, 50 m/s, 100 m/s and ∞.

2.2.5.5.3.2. Derivation of Rate-Dependent Bilinear CZM (RD CZM)

In this section, the conventional BL CZM is converted into a RD CZM based on the rate-dependency proposed by Corigliano et al. [155,156]. The penalty stiffness, E_0, is assumed to be constant because the penalty stiffness is such a large number that the relative effect of rate-dependency can be negligibly small.

The static and limit values of fracture toughness are material properties which are respectively denoted by $G_{ic,0}$ and $G_{ic,\infty}$ where i = I, II. In this derivation, it is assumed that the static and limit maximum tractions are known. In the original study of Corigliano et al. [155,156], the static and limit onset separations were known. The maximum tractions are denoted by $T_{io,0}$ and $T_{io,\infty}$, respectively, where i = I,II for the pure modes. All the onset and critical separations for each mode can be written for the static and the limit definitions of the separations as follows;

$$\delta_{Io,0} = \frac{T_{Io,0}}{E_0}, \qquad \delta_{IIo,0} = \frac{T_{IIo,0}}{E_0}, \tag{87}$$

$$\delta_{Io,\infty} = \frac{T_{Io,\infty}}{E_0}, \qquad \delta_{IIo,\infty} = \frac{T_{IIo,\infty}}{E_0}, \tag{88}$$

$$\delta_{Ic,0} = 2\frac{G_{Ic,0}}{T_{Io,0}}, \qquad \delta_{IIc,0} = 2\frac{G_{IIc,0}}{T_{IIo,0}}, \tag{89}$$

$$\delta_{Ic,\infty} = 2\frac{G_{Ic,\infty}}{T_{Io,\infty}}, \qquad \delta_{IIc,\infty} = 2\frac{G_{IIc,\infty}}{T_{IIo,\infty}} \tag{90}$$

The same procedure presented in the rate-independent BL CZM is followed. Next, the eqn.(64) can be separately written for the static and infinite mixed-mode separations, $\delta_{o,0}$ and $\delta_{o,\infty}$, respectively, as follows;

$$\delta_{o,0} = \begin{cases} \delta_{Io,0}\delta_{IIo,0}\sqrt{\dfrac{1+[\tan(\beta)]^2}{\delta_{IIo,0}^2 + (\tan(\beta)\delta_{Io,0})^2}} & if \quad \delta_I > 0 \\ \\ \delta_{IIo,0} & if \quad \delta_I \leq 0 \end{cases} \tag{91}$$

140

$$
\delta_{o,\infty} = \begin{cases} \delta_{Io,\infty}\delta_{IIo,\infty}\sqrt{\dfrac{1+[\tan(\beta)]^2}{\delta_{IIo,\infty}^2 + (\tan(\beta)\delta_{Io,\infty})^2}} & if \quad \delta_I > 0 \\[20pt] \delta_{IIo,\infty} & if \quad \delta_I \le 0 \end{cases}
\tag{92}
$$

Similarly, critical mixed-mode separation for $\delta_{c,0}$, and $\delta_{c,\infty}$ can be found for the B-K criterion assuming that the factor of "η" is kept constant;

$$
\delta_{c,0} = \begin{cases} \dfrac{2}{\delta_{o,0}E_0}\left[G_{Ic,0} + (G_{IIc,0} - G_{Ic,0})\left(\dfrac{\tan(\beta)^2}{1+\tan(\beta)^2}\right)^{\eta} \right] & if \quad \delta_I > 0 \\[20pt] \delta_{IIc,0} & if \quad \delta_I \le 0 \end{cases}
\tag{93}
$$

$$
\delta_{c,\infty} = \begin{cases} \dfrac{2}{\delta_{o,\infty}E_0}\left[G_{Ic,\infty} + (G_{IIc,\infty} - G_{Ic,\infty})\left(\dfrac{\tan(\beta)^2}{1+\tan(\beta)^2}\right)^{\eta} \right] & if \quad \delta_I > 0 \\[20pt] \delta_{IIc,\infty} & if \quad \delta_I \le 0 \end{cases}
\tag{94}
$$

The rate-dependent mixed-mode onset separation, δ_o, is calculated by eqn.(95). In addition to reference onset of separation, *reference critical separation velocity*, $\dot{\delta}_c$ is proposed which is attributed to the RD fracture toughness as follows;

$$
\frac{1}{\delta_c} = \frac{1}{\delta_{c,\infty}} + \left(\frac{1}{\delta_{c,0}} - \frac{1}{\delta_{c,\infty}}\right)\exp\left(-\frac{|\dot{\delta}|}{\dot{\delta}_c}\right)
\tag{95}
$$

Finally, the damage defined by the eqn.(70) can be used with eqn. (84) and eqn.(95).

The RD CZM is shown in Figure 85a for $G_{c,\infty}/G_{c,0} = 5$, $T_{o,0}/T_{o,\infty} = 2.45$ and $\dot{\delta}_o = \dot{\delta}_c = 70$ m/s. It can be seen that the maximum traction and the fracture toughness increase with increasing the separation speed. On the other hand, the penalty stiffness does not change. The softening region grows parallel with increasing the separation velocity which is due to the equality of $\dot{\delta}_o = \dot{\delta}_c$. Actually, independent controlling the

$\dot{\delta}_o$ and $\dot{\delta}_c$ create more versatility at the rate-dependencies of maximum traction and the fracture toughness comparing to the work of Corigliano et al. [156]. In our model, the material properties are based on static and infinite maximum tractions and fracture toughness instead of the separation values as in Corigliano et al. [156].
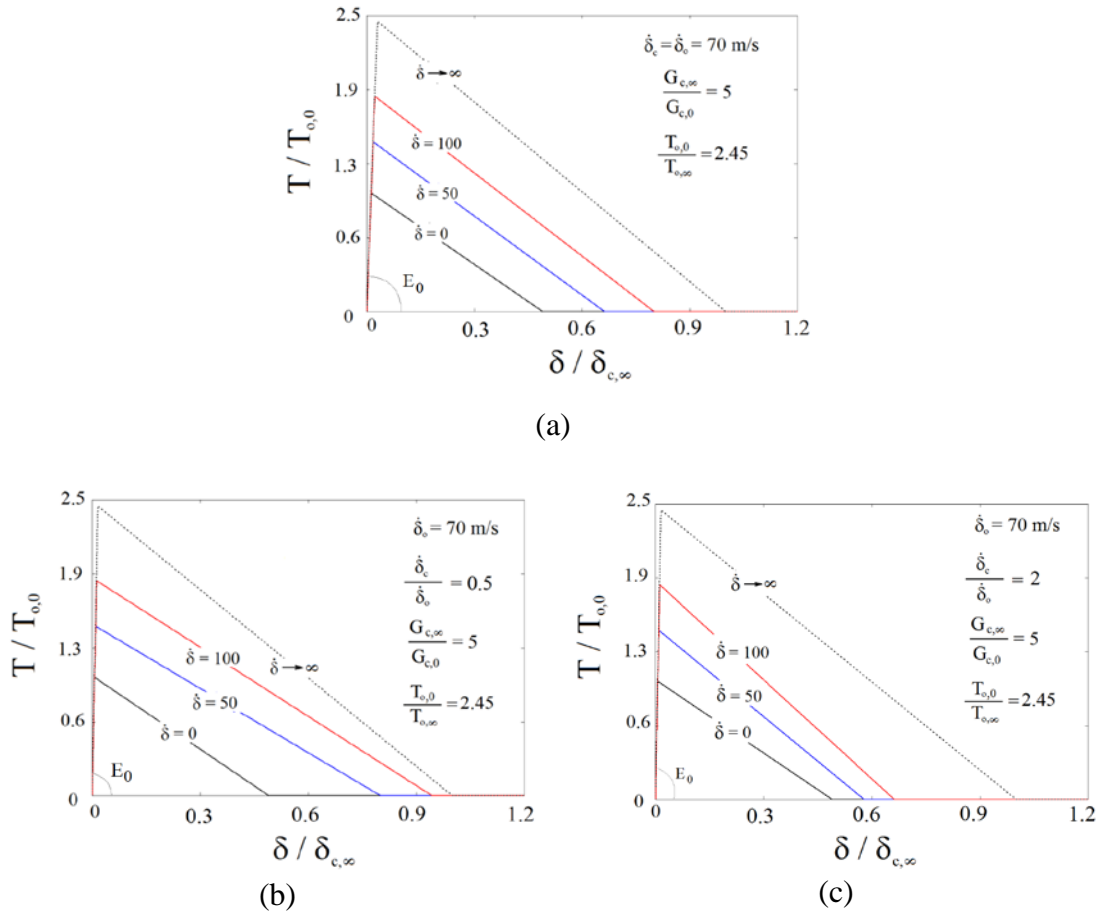
Figure 85 RD CZM for $\dot{\delta} = 0$ m/s, 50 m/s, 100 m/s and infinite velocities with the parameters of $G_{c,\infty} / G_{c,0} = 5$, and $T_{o,0} / T_{o,\infty} = 2.4$ (a) $\dot{\delta}_o = \dot{\delta}_c = 70$ m/s, (b) $\dot{\delta}_c / \dot{\delta}_o = 0.5$ and (c) $\dot{\delta}_c / \dot{\delta}_o = 2.0$.

The effect of the reference onset, $\dot{\delta}_o$, and critical separation velocities, $\dot{\delta}_c$, are revealed in Figure 85b-c. For $\dot{\delta}_c / \dot{\delta}_o = 0.5$, the critical separation develops quickly to the limit value compared to the onset separation as the slope of the softening part is

142

smaller (Figure 85b). The opposite case is shown in Figure 85c where the traction is more rate-sensitive compared to the fracture toughness for $\dot{\delta}_c / \dot{\delta}_o = 2.0$.

2.2.5.5.4. Friction Modeling

The main course of attempts to understand the effect of friction in dynamic fracture is encountered at geophysics, which investigates the earthquakes along fault lines. Generally, the studies about friction in geophysics feed the friction phenomenon in composite laminates [215].

Under compressive stresses and horizontal perturbation, such as shown in Figure 86a, the tangential relative displacement creates *slippage* between two elastic bodies in contact. Slippage occurs in two modes; "crack-like" and "pulse-like" [216]. The former is characterized by the propagation of the slippage along the whole interface like a crack growth (Figure 86b). On the other hand, the latter moves via a small pulse of slippage that travels along the interface (Figure 86c). In some cases, a third mode of sliding occurs as "train of pulses" that exhibits quasi-periodic slip-stick regions as shown in Figure 86d [217]. The conditions for formation of the above modes are based on friction coefficient, slippage speed, compressive load and temperature [216]. The detailed mechanisms and the influence of the friction coefficients are not still well-understood [215].

One of the widely used friction models is the Coulomb friction; $\sigma_{12} = \mu_{ss}\sigma_{22}$, where σ_{12} is the shear stress due to friction, σ_{22} is the compressive normal stress and μ_{ss} is the friction coefficient which is a constant. However, Coulomb friction model is insufficient to explain the complex phenomena occurring in slippage. The deficiency starts with using a constant friction coefficient. Zheng and Rice [218] showed that the friction coefficient exhibits decaying behavior by increasing the slippage speed. Moreover, Coulomb friction has been shown as ill-posed as shown by Adams [219]. For instance, the Coulomb friction force does not converge by increasing the mesh density. Rate and history dependent friction models, such as proposed by Prakash and Clifton [220], provide more accurate results in terms of predicting the sliding modes. Rate and history dependent models are even considered as ad-hoc solutions since no agreed friction model has been proposed in the literature, yet.

Even though the Coulomb friction exposes the mentioned problems, it has been applied to dynamic fracture of composite materials. For example, Dwivedi and Espinosa [122] successfully simulated the experiment conducted by Coker and Rosakis [118] using CZM and Coulomb friction, together. They reported that the effect of friction coefficient to the crack tip speeds was not explicitly evident unless very high values of friction coefficients were used. The angle of the shear Mach waves were slightly increased by using high values of friction coefficient [122].
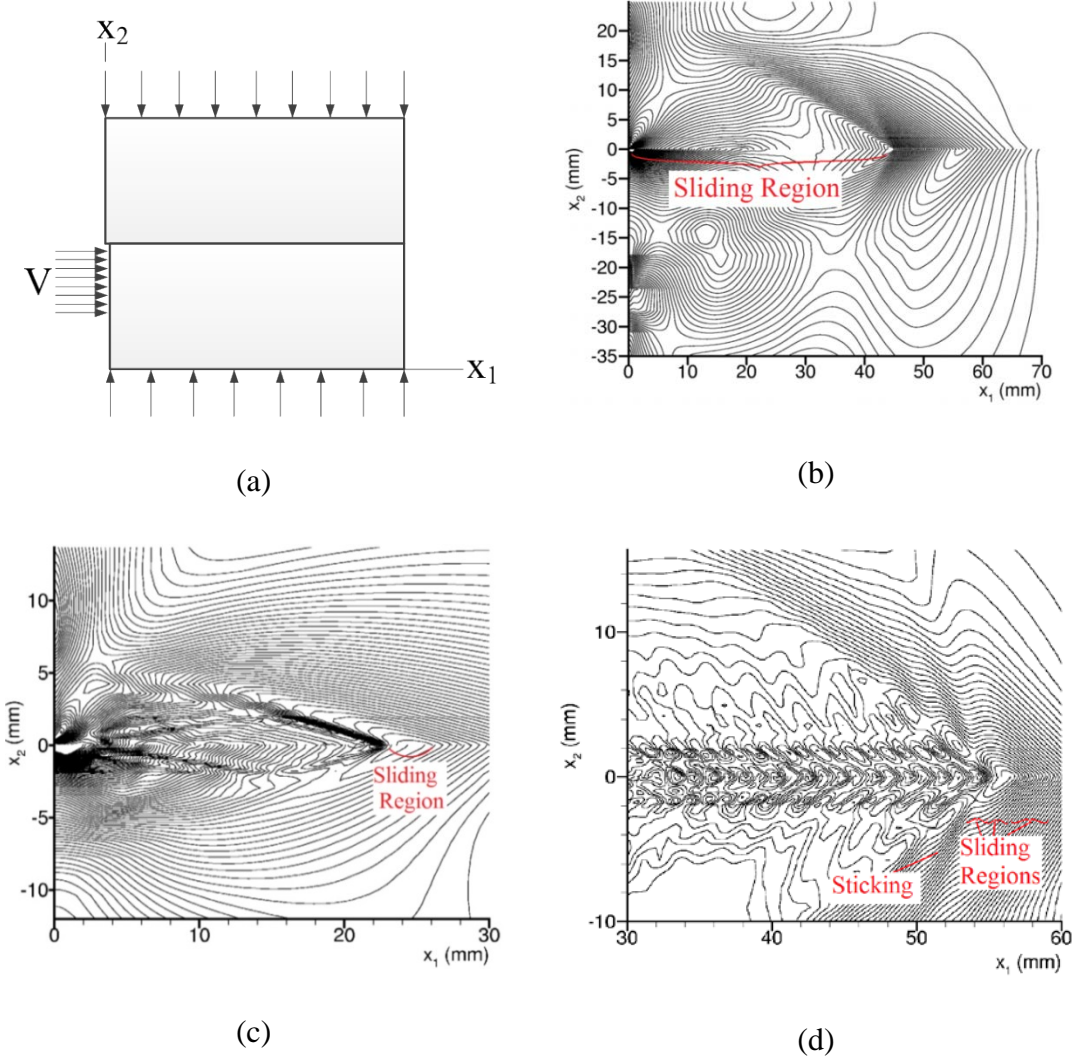
Figure 86 (a) Friction FE model under impact load, contours of maximum shear stress for (a) crack-like, (b) pulse-like and (c) train of pulses due to friction.

In our study, friction is not implemented into the cohesive elements as the effect of the friction was mentioned to be negligible and to simplify the modeling approach in our study. The implementation of Coulamb friction can be easily performed for $\delta_I <$ 0 using $\mu_{ss}E_0\delta_I$ to calculate the tangential traction opposing the mode-II separation motion.

CHAPTER 3

FINITE ELEMENT METHOD

Finite element method is the numerical solution of differential equations that are performed by explicit and implicit methods, so called *implicit* and *explicit FEA*, respectively. In the implicit FEA, the physical state at $t + \Delta t$ is calculated using the states at $t + \Delta t$ [221]. On the other hand, explicit FEA is based on the conditions at current state of "t" to calculate the state at $t + \Delta t$. In this section, implicit, explicit FEA methods and their applications with CZM are provided. Afterwards, derivation of kinematic equations for a 4-noded continuum line interface element is presented.

3.1. Implicit Finite Element Analysis with CZM

The principle of virtual work can be written for a continuum with cohesive interface as follows;

$$\int_V (\tilde{\sigma} : \delta \tilde{\varepsilon}) dV - \int_{S_{ext}} (\hat{T}_{ext} \cdot \delta \hat{u}) dS - \int_{S_{int}} (\hat{T} \cdot \delta \hat{\delta}) dS + \int_V \left(\rho \frac{\partial^2 \hat{u}}{\partial t^2} \cdot \delta \hat{u} \right) dV = 0 \tag{96}$$

where ρ is the density, $\tilde{\sigma}$ is the stress tensor, $\delta \tilde{\varepsilon}$ is the virtual strain tensor, $\hat{T}$ is the cohesive traction vector, $\hat{T}_{ext}$ is the external traction vector and $\delta \hat{u}$ is the virtual displacement vector, S_{ext} is the external area, S_{int} is the cohesive area and V is the volume. It can be seen that the cohesive term acting on the S_{int} is introduced to eqn. (96) comparing to the conventional definitions of FEA without cohesive modeling. After the discretization, the virtual energy becomes;

$$\Omega(\hat{u}) = \int_V (\hat{B}^T \cdot \tilde{\sigma}(\hat{u})) dV - \int_{S_{ext}} (\hat{N}^T \cdot \hat{T}_{ext}) dS - \int_{S_{int}} (\hat{Q}^T \cdot \hat{T}) dS + \int_{S_{ext}} (\hat{N}^T \cdot \rho \frac{\partial^2 \hat{u}}{\partial t^2}) dS = 0 \tag{97}$$

where $\hat{B}^T$ is the transpose of $\hat{B}$ matrix relating the strain tensor to the displacement vector, $\hat{N}^T$ is the transpose of the shape function matrix, $\hat{N}$, $\hat{Q}^T$ is the transpose of the $\hat{Q}$ matrix relating the separation vector to the displacement vector and Ω is the set of

equations. The implicit method iteratively solves the eqn. (97)at t + Δt condition using the numerical schemes such as Newton-Raphson method [221] as follows;

$$\Delta \hat{u}^{(j+1)} = \hat{u}^{(j+1)} - \hat{u}^{(j)} = \left[\frac{\partial \Omega(\hat{u}^{(j)})}{\partial(\hat{u})} \right]^{-1} \widetilde{K}(\hat{u}^{(j)}) \tag{98}$$

$$\widetilde{K}(\hat{u}^{(j)})\Delta \hat{u}^{(j+1)} = -\Omega(\hat{u}^{(j)}) \tag{99}$$

where $\widetilde{K}(\hat{u})$ is the tangent stiffness matrix, $\Delta \hat{u}$ is the displacement increment, and "j" is the iteration number. Equilibrium between the external loads, $\hat{P}$, and the internal loads, $\hat{P}_r$, are iteratively reached at each increment;

$$\hat{P} - \hat{P}_r^{(j)}(\hat{u}^{(j)}) \approx 0 \tag{100}$$

CZM has been dominantly used with implicit FEA. However, softening behavior of the CZM promotes snap-back behavior as shown in Figure 87. In snap-back behavior, convergence becomes a problematic issue especially for conventional methods such as Newton-Raphson. One of the reasons is divergence to infinity as the tangent stiffness matrix diminishes at the peak loads (Figure 87a). Secondly, Newton-Raphson uses constant loads in the iterations, which cannot reverse the iteration towards the internal points as illustrated in Figure 87a. For the solution of snap-back behavior, an arc equation can be augmented in order to reach the internal points as proposed by Crisfield [177], Riks [223], Wempner [224] and Ramm [225]. This method is called *arc-length method*, which has been successfully applied to the implicit FEA with CZM [135,144,146,178,180,182]. However, the arc-length method cannot thoroughly ameliorate the convergence problem.
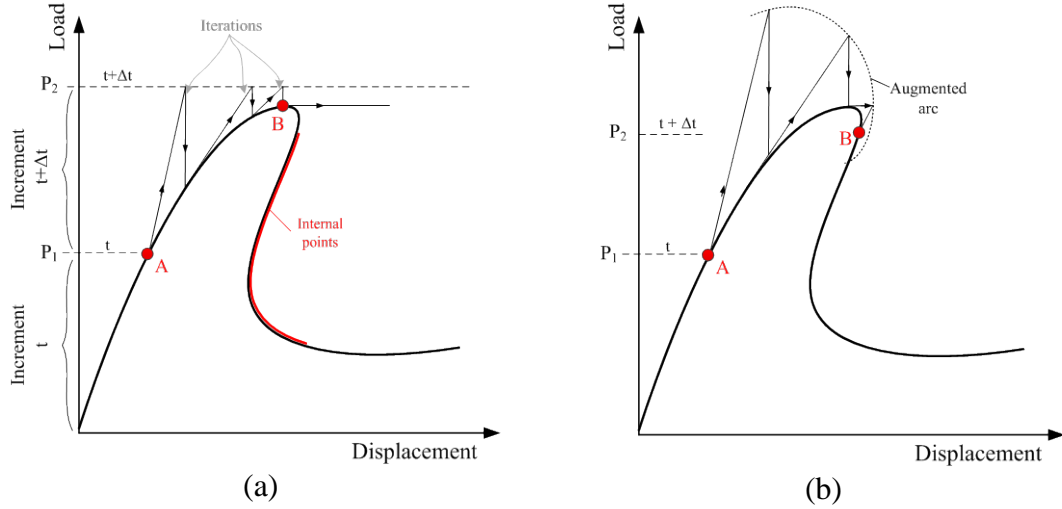
Figure 87 Load-displacement curve of a system with snap-back behavior being iteratively solved by (a) Newton-Raphson and (b) arc-length methods.

Another method for increasing the convergence performance is to artificially include viscosity to the CZM formulation such as proposed by Gao and Bower [226]. This method is known as *viscous regularization* in the CZM literature. However, excessive application of viscous regularization may result in over-estimation of the failure load.

Implicit FEA is very effective for systems exhibiting a relatively linear response. Gozluklu and Coker [88,89,90] used the implicit FEA at the linear part of the L-shaped composite laminate analysis where the snap-back part is continued by the explicit FEA. This sequential approach cannot be used in this study since VUEL subroutines do not enable.

3.2. Explicit Finite Element Analysis with CZM

In explicit FEA, there is no iterative method such as Newton-Raphson and therefore no tangent stiffness matrix. In explicit FEA, the acceleration vector, $\hat{\ddot{u}}$, is directly calculated by Newton's 2nd law;

$$\hat{\ddot{u}}^{(j)} = \hat{M}^{-1} \cdot \left(\hat{P}^{(j)} - \hat{P}_r^{(j)} \right) \tag{101}$$

where $\hat{M}$ is the lumped mass matrix. The displacement field can be calculated by the central difference method (in compliant with ABAQUS [69]);

149

$$\hat{u}^{(j+1/2)} = \hat{u}^{(j-1/2)} + \frac{\Delta t^{(j+1)} + \Delta t^{(j)}}{2} \hat{\ddot{u}}^{(j)} \qquad (102)$$

$$u^{(j+1)} = \hat{u}^{(j)} + \Delta t^{(j+1)} \hat{\dot{u}}^{(j)} \qquad (103)$$

In the explicit procedure, the time increment complies with Courant–Friedrichs–Lewy condition [69] which dictates that adequately small time is required for the delivery of information between two nodes through the smallest distance. This limiting value of the time increment is called *stable time increment*. The stable time increment is calculated by L_e/C_d where L_e is the length of the smallest element in the mesh and C_d is the dilatational wave speed of the material, which is the fastest information speed in the continuum.

Explicit FEA does not have a convergence problem which is a concrete advantage compared to the implicit FEA. Gozluklu and Coker[88] used explicit scheme in the snap-back behavior due to delamination where the convergence is problematic. However, stable time increment is generally so small that the required CPU time for the solution of a quasi-static problem is unattainably inflated. Therefore, explicit FEA is generally preferred for high speed physical phenomena such as impact loading, crash simulations, explosions simulations etc. For quasi-static cases, Borg et al. [139] reported high durations of simulation for the explicit FEA in conjunction with CZM. This can be reduced using "mass scaling" method [69]. However, inappropriate application of mass scaling might yield artificial inertial effects.

(a)   (b)
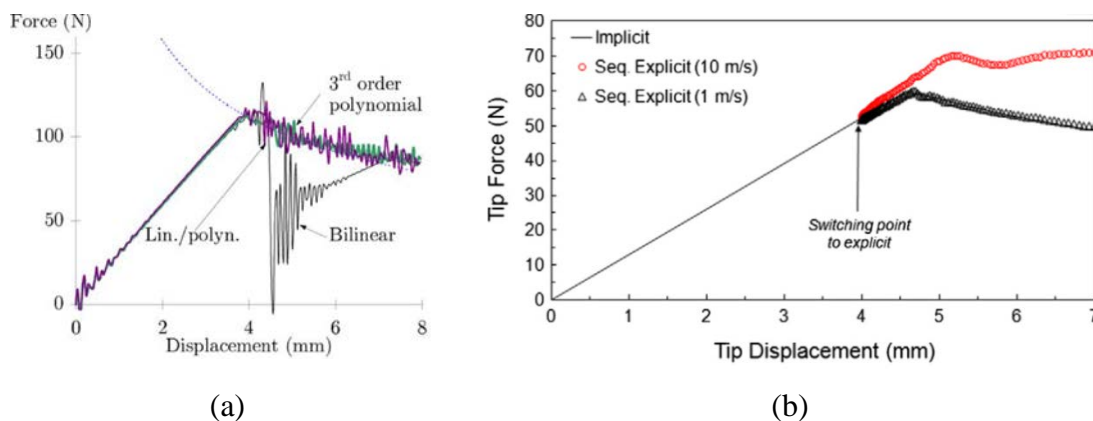
Figure 88 Load-displacement curves for (a) delamination simulation using 3rd order polynomial and BL CZMs [166] and (b) DCB test at various loading rates [88].

Other issues may arise during the application of CZM to quasi-static fracture simulations using explicit FEA. As mentioned by Borg et al. [139] and Pinho et al. [166], start of crack propagation may trigger harmonic vibrations that cause oscillatory reaction forces in the load-displacement curves as shown in Figure 88a. These oscillations are attributed to successive failure of the cohesive elements of which failure create a small disturbance in the specimen eventually leading to specimen wide vibrations. At the early stages of loading, there are small oscillations as seen in Figure 88a. In this case, the profile of the loading was a ramp. This problem can be solved using a smooth step profile which sustains a gradual evolution of the load.

Beside the early stages of loading, the failure load and the compliance may be artificially increased at higher loading rates as shown in Figure 88b. The reason is that the inertial effects may become considerably high. Hence, the loading rates are obtained by trial and error analyses to have both an economic and inertia-free ("pure") load-displacement curves in this study. In case of viscosity, high loading rates may yield considerable viscous response of the system.

The essential concern of using CZMs with the explicit FEA is having harmonic vibrations triggered the start of crack propagation [88, 139,166]. The main reason of the oscillations is the successive failure of cohesive elements one-by-one. Each failure yields a small disturbance in the elastic body. Eventually, the vibrations become a specimen wide phenomenon. Pinho et al. [166] showed that increasing the magnitude of interfacial strength fosters oscillatory response. Coversely, higher order CZMs reduced the oscillations, especially for the mode-I fracture [166]. Pinho et al. [166] showed that using 3rd order polynomial CZM significantly reduced the oscillations in mode-I fracture as shown in Figure 88a compared to the BL CZM which is a first order CZM. In addition to the order of the CZM, using more elements in a cohesive zone reduced the oscillations. Moreover, conventional techniques such as using higher structural damping and/or loading at slower rates also helped to reduce the harmonic vibrations. The conclusions of Pinho et al. [166] will contribute to the discussions of our results.

3.3. Interface Element Formulation

In this chapter, shape functions and kinematic equations for a *4-noded continuum line cohesive interface element* are derived (Figure 89). The kinematic equations together with the constitutive equations, given in the previous chapter, are required to implement the interface element into ABAQUS via VUEL user subroutine [69]. The user subroutine used in the study is provided in Appendix B.
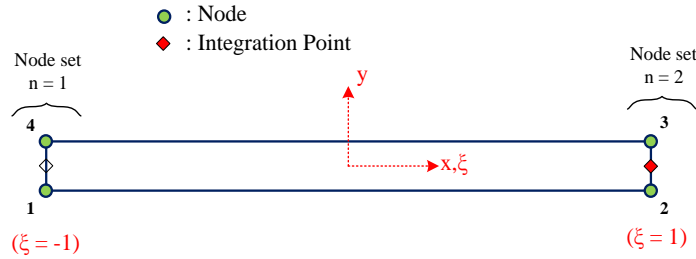
Figure 89 Local coordinate system, node numbering and location of integration points of the 4-Noded continuum line interface element implemented in ABAQUS.

3.3.1. Derivation of Shape Functions

The continuum line interface element has linear interpolation function, $\Sigma(\xi)$, in order to be compatible with the conventional quadrilateral bulk elements;

$$\Sigma(\xi) = A_0 + A_1\xi \tag{104}$$

where A_0, A_1 are constants and ξ is non-dimensional coordinate of x-direction. In order to zero the shape function at nodes 2 and 3, "node set 2" $n = 2$ in Figure 89, possible form of shape function at nodes 1 and 4 ($n = 1$) can be given as follows;

$$N_1(\xi) = C_0(\xi - 1) \tag{105}$$

where $N_1(\xi)$ is the shape function at $n = 1$, and C_0 is a constant. In order to have unity at $n = 1$, the constant, C_0, is found;

$$N_1(-1) = C_0(-1 - 1) = 1 \quad \Rightarrow \quad C_0 = -\frac{1}{2} \tag{106}$$

Similarly, the second shape function at n = 2 can be obtained following the same procedure. The shape functions for n = 1, $N_1(\xi)$, and n = 2, $N_2(\xi)$, are summarized below;

$$N_1(\xi) = \frac{1}{2}(\xi - 1) \qquad , \qquad N_2(\xi) = \frac{1}{2}(\xi + 1) \tag{107}$$

3.3.2. Kinematic Equations

The continuum line interface element should be compatible with *element orientation angle* of θ_e (Figure 90a). Transformation from global to local coordinates is required for calculating the displacement and internal force vectors.
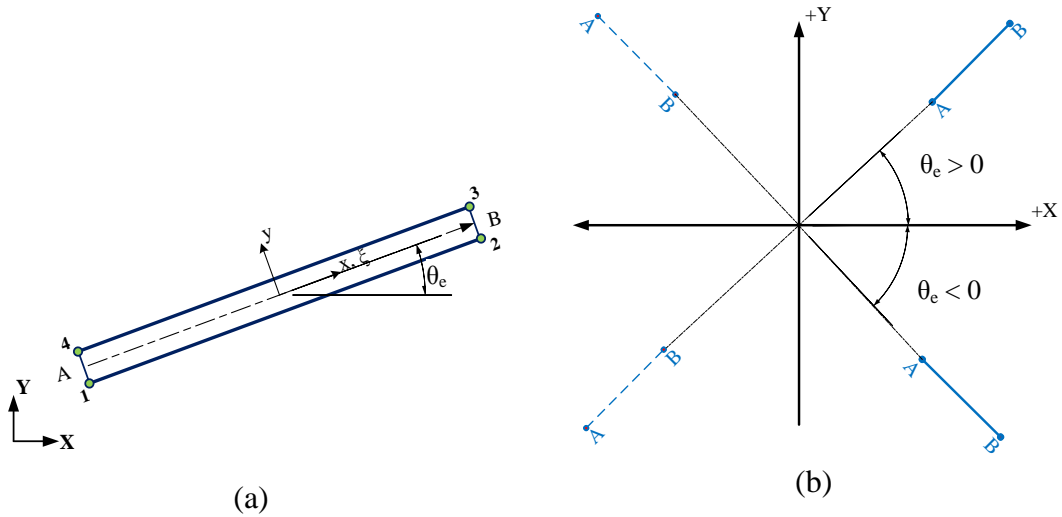
Figure 90 (a) Rotated continuum line interface element and (b) sign conventions of element orientation angle.

Assume that the interface element is rotated through the displacements of nodes, i, (X_i, Y_i) in global coordinate system. The orientation of the element can be calculated based on a vector of $\overrightarrow{AB}$ passing through the points of A and B located at the middle of the node sets 1 and 2, respectively;

$$A(X, Y) = \left(\frac{X_1 + X_4}{2}, \frac{Y_1 + Y_4}{2} \right) \qquad , \qquad B(X, Y) = \left(\frac{X_2 + X_3}{2}, \frac{Y_2 + Y_3}{2} \right) \tag{108}$$

The vector of $\overrightarrow{AB}$ is calculated to find the element orientation angle considering the sign convention for $0° \le \theta_e \le 90°$ as illustrated in Figure 90b;

$$\theta_e = \tan^{-1}\left(\frac{Y_2 + Y_3 - Y_1 - Y_4}{X_2 + X_3 - X_1 - X_4}\right) \tag{109}$$

Figure 90b also shows an interface element located in the negative global X-direction with the element orientation angle of θ_e. It can be seen that the definition of element orientation angle in +X-direction compensates all geometrical configurations.

The transformation matrix, $\widetilde{R}$, is defined in terms of element orientation angle, θ_e, as below;

$$\widetilde{R} = \begin{bmatrix} \cos\theta_e & \sin\theta_e \\ -\sin\theta_e & \cos\theta_e \end{bmatrix} \tag{110}$$

Using the data of the previous increment, eqn. (101) to eqn. (103) are solved by ABAQUS [69] that provides *nodal displacement vector with respect to global coordinate system for the interface element*, $\hat{u}_e$ at the current increment. In the matrix form, the displacement vector in global coordinates is given;

$$\hat{u}_e = \begin{bmatrix} u_{X,1} & u_{Y,1} & u_{X,2} & u_{Y,2} & u_{X,3} & u_{Y,3} & u_{X,4} & u_{Y,4} \end{bmatrix}^T \tag{111}$$

where the subscripts indicate the directions and the node numbers.
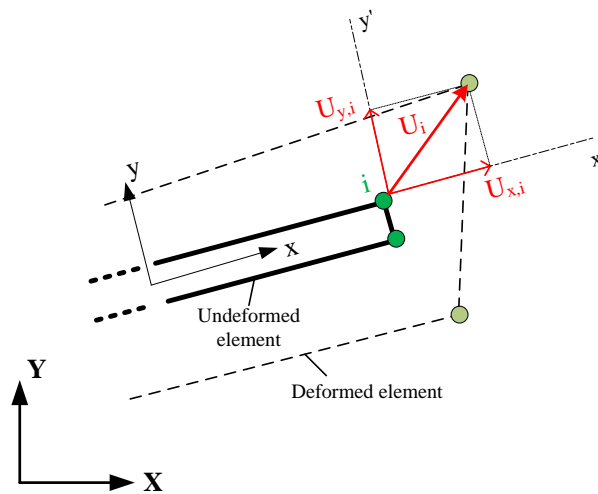
Figure 91 Displacement vector for node-i

In the next step, relative displacement vectors (separation vector) in global coordinates, $\hat{\Delta}^n$, are found for the node sets of $n = 1$ and $n = 2$ using the corresponding shape functions as follows;

$$\hat{\Delta}^n = \tilde{N}^n(\hat{u}_{e,top}^n - \hat{u}_{e,bottom}^n)$$

(112)

where subscripts "top" and "bottom" refer to the nodes 3-4 and nodes 1-2, respectively. Actually, the displacement vectors in eqn.(112) are partitions of $\hat{u}_e$, and $\hat{\Delta}^n$ with $n = 1,2$ are partitions of $\hat{\Delta}$. The matrix form of shape functions at node sets, n, is defined as below;

$$\tilde{N}^{n=1} = \begin{bmatrix} N_1 & 0 \\ 0 & N_1 \end{bmatrix} \quad , \quad \tilde{N}^{n=2} = \begin{bmatrix} N_2 & 0 \\ 0 & N_2 \end{bmatrix}$$

(113)

The *global nodal displacements to separation matrix*, $\tilde{Q}'$, can be written as follows;

$$\tilde{Q}' = \begin{bmatrix} -N_1 & 0 & -N_2 & 0 & N_2 & 0 & N_1 & 0 \\ 0 & -N_1 & 0 & -N_2 & 0 & N_2 & 0 & N_1 \end{bmatrix}$$

(114)

where $\tilde{Q}'$ relates the parameters of $\hat{\Delta}$ and $\hat{u}_e$ by the following relation;

$$\hat{\Delta} = \tilde{Q}'\hat{u}_e$$

(115)

Using the transformation matrix, $\tilde{R}$, separations in local coordinate system (xy-system in Figure 91), $\hat{\delta}$, can be calculated;

$$\hat{\delta} = \tilde{R}\hat{\Delta}$$

(116)

$$\hat{\delta} = (\tilde{R}\tilde{Q}')\hat{u}_e = \tilde{Q}\hat{u}_e = \begin{bmatrix} \delta_{II} & \delta_I \end{bmatrix}^T$$

(117)

where $\tilde{Q}$ is the *global displacement to local separation matrix* that is used to calculate the internal loads, $\hat{P}_r$.

3.3.3. Numerical Integration

The internal force vector due to the cohesive tractions in the element, $\hat{P}_{r,ch}$, can be found using the following integration;

$$\hat{P}_{r,ch} = \int_{S_{int}} (\tilde{Q}^T \cdot \hat{T})dS = w\int_{-1}^{1} \tilde{Q}^T \cdot \hat{T} \det(J)d\xi \tag{118}$$

where w is the width of the specimen and *det(J)* is the determinant of *Jacobian matrix* [221], which can be generalized for a 1D-line element as the *half-length of the element* as follows;

$$\det(J) = \frac{\sqrt{(X_2 + X_3 - X_1 - X_4)^2 + (Y_2 + Y_3 - Y_1 - Y_4)^2}}{4} \tag{119}$$

The integral in eqn. (118) can be calculated numerically by the below equation [221];

$$\int_{-1}^{1} g(\xi) \approx \sum_{j=1}^{3} H_j g(\xi_j) \tag{120}$$

Newton-Cotes integration scheme is used due to the reasons mentioned in section 2.2.5.4. The constants of the integration are $H_1 = H_2 = 1/2$ and $\xi_1 = -1$, $\xi_2 = 1$.

3.3.3.1. Numerical Calculation of Energy Release Rate

The energy release rates (G_I and G_{II}) are calculated using the definition of CZM as provided in eqn. (51). ABAQUS [69] provides the change of displacement that can be used to calculate the change of separations $\Delta\delta^{(j)} = \delta^{(j)} - \delta^{(j-1)}$ at the *j*-th increment. Concerning the FE models in our study, the stable time increments, Δt, are so small that a simple rectangular integration scheme is adequate as illustrated in Figure 92. In that case, the tractions are calculated at the current increment. The below relation is used for the calculation of G_i for i = I, II;

$$G_i = \sum_{j} \Delta\delta_i^{(j)} T_i^{(j)} \tag{121}$$
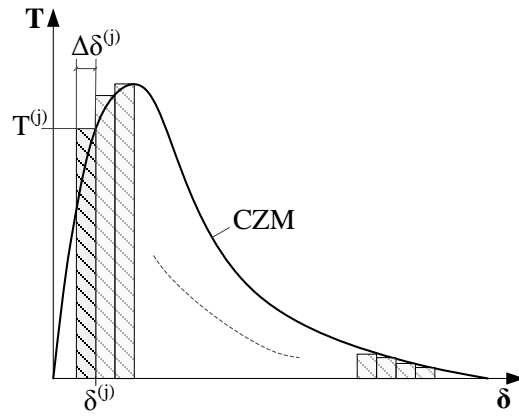
Figure 92 Rectangular integration scheme at the current increment, j.

CHAPTER 4

BENCHMARK TESTS FOR VERIFICATION OF COHESIVE INTERFACE ELEMENT

In this chapter, the implemented cohesive interface elements using BL, XN, and RD CZMs are verified through the benchmark tests taken from the literature. First of the benchmark tests is the Double Cantileve Beam (DCB) tests which represents the quasi-static mode-I delamination. The second one is the End-Load Slip (ELS) test dedicated for the quasi-static mode-II delamination. The next test to be used for the verification is the Three-Point Bending Impact test which represents dynamic mode-I fracture. Finally, experiment of asymmetric dynamic loading of polymer-composite plates is used for modeling a mode-II dominated intersonic delamination problem to verify the implementation. In each tests, numerical issues or modeling parameters are discussed. For the modeling of quasi-static fracture, the loading rate is kept as fast as possible in order to reduce the solution duration. Similarly, the mesh sizes are used referring to the reference study or based on a mesh sensitivity studies.

4.1. Double Cantilever Beam (DCB) Test

Double Cantilever Beam (DCB) Test is used to determine mode-I the fracture toughness (G_{Ic}) of the interfaces. The crack propagation is stable and the loading is quasi-static. The geometry of the DCB specimen is rectangle with an initial crack of a = 50 mm (Figure 94). The length of the specimen is 150 mm and the thickness is 3.96 mm made of Carbon/Epoxy woven fabric plies. The specimen is pulled from the tips of the arms by displacement loading, U(t), of which definition is a "smooth step" formulated as below [69];

$$U(t) = U_L \left[10 \left(\frac{t}{t_L} \right)^3 - 15 \left(\frac{t}{t_L} \right)^4 + 6 \left(\frac{t}{t_L} \right)^5 \right] \tag{122}$$

where U_L is the total loading displacement, t_L is the loading duration, and t is the time. In the simulations of RD and XN CZMs, the loading duration and total loading

displacement are taken as $t_L = 0.0175$ s and $U_L = 3.5$ mm, respectively, which gives a loading profile shown in Figure 93.
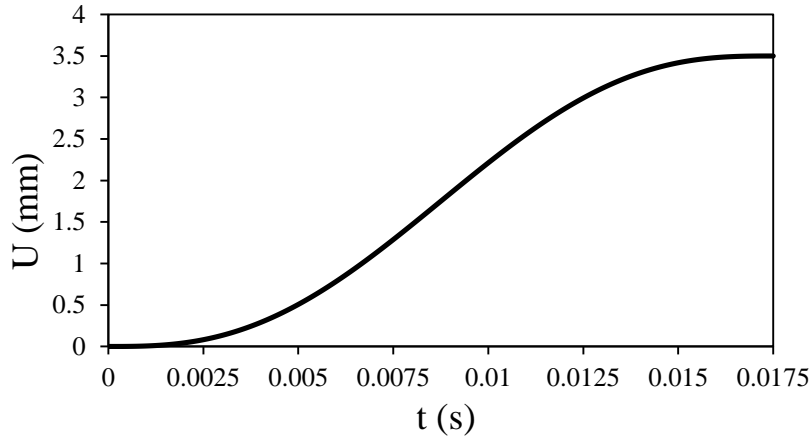
Figure 93 Loading profiles of smooth step with $U_L = 3.5$ mm & $t_L = 0.035$ s and $U_L = 10.$ mm & $t_L = 0.1$ s.

Quadrilateral plane strain elements with single integration point at the centroid, so called "CPE4R" in ABAQUS [69], are uniformly used in the mesh of the specimen bulk. The implemented cohesive interface elements are located along the crack path starting from the crack tip (Figure 94). The width of the elements (dimension in X-direction) is denoted by "w_e" whereas the height of the elements (dimension in Y-direction), h_e, is determined by the number of rows of elements, N_e, in the model (Figure 94). In the simulations, the mesh parameters are taken as; $w_e = 100$ μm and $N_e = 6$ ($h_e = 330$) μm, otherwise stated. The stable time incrementation, Δt, is calculated as 1.268×10^{-8} s by ABAQUS.

The material properties of the specimen is taken from the study of Gozluklu and Coker [88] in which isotropic properties of Graphite/Epoxy woven fabric with modulus was 60 GPa, Poisson's ratio was 0.30 and density was 1600 kg/m^3. The cohesive and interface properties are provided in Table 4 taken from [88]. Noting that the mode-II properties are assumed to be equal to the mode-I properties; i.e. $G_{IIc} = G_{Ic}$ and $T_{o,II} = T_{o,I}$ based on the study of Gustafson and Waas [161] who showed that the influence of mode-II properties is negligibly small in the simulations of DCB

160

test. For the RD CZM, the dynamic interface properties are taken as $G_{Ic,\infty} = 5G_{Ic}$, $T_{Io,\infty} = 2.5T_{o,I}$, $\dot{\delta}_c = \dot{\delta}_c = 70$ m/s, based on the proportions between rate-dependent and independent interface properties presented by Corigliano et al. [156].
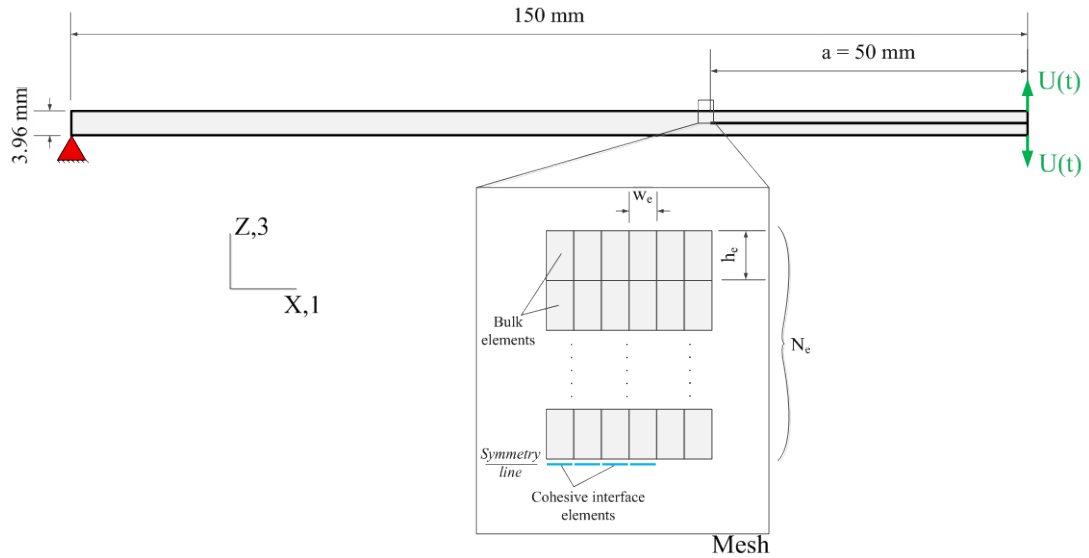
Figure 94 DCB specimen dimensions, boundary conditions and morphology of the mesh.

Table 4 Interface and cohesive properties for DCB.

G_{Ic} (N/m)	$T_{o,I}$ (MPa)	B-K criterion constant, η	Penalty Stiffness, E_0 (N/m^3)
352.3	60	2.25	10^{14}

Fringes of opening stresses (σ_{33}) at various stages of crack propagation are shown in Figure 95. The location of the crack tip can be followed through the stress concentration point which resembles a "butterfly" shape as expected for the plane strain condition.
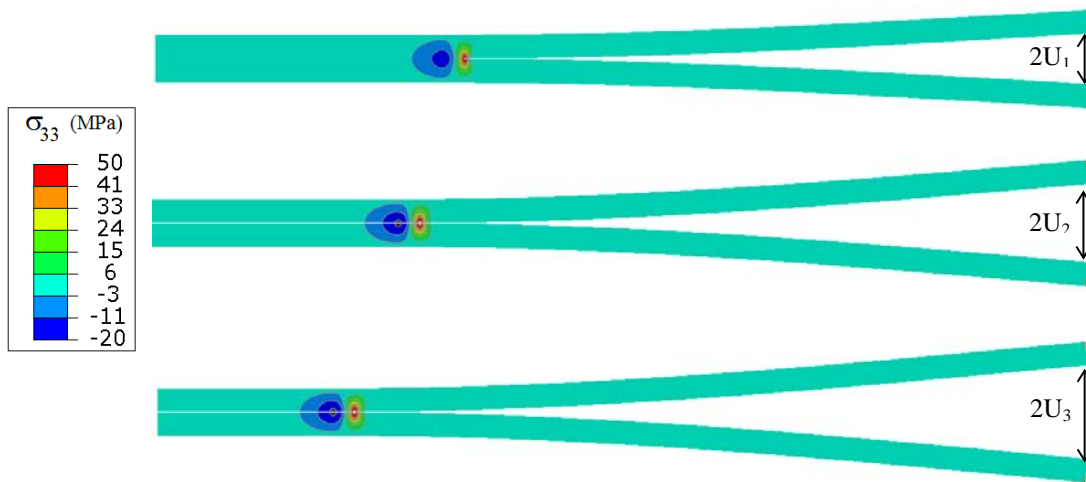
Figure 95 Evolution of crack propagation in DCB (partially shown) specimen and the contours of normal stresses (σ_{33}) from top to bottom ($t_3 > t_2 > t_1$).

The load-displacement curves of DCB test can be analytically derived using the beam theory and the definition of fracture toughness [135]. The analytical solution predicts the failure load at 45.9 N with a displacement of U = 2.61 mm (2U = 5.22 mm). The load-displacement curves of BL and XN CZMs are shown in Figure 96a together with the analytical solution. All curves agree very well with each other. However, spurious oscillations are observed for the BL CZM at the load-displacement curves after the failure load - the start of crack propagation. On the other hand, XN CZM exhibits smoother behavior after the start of crack propagation. Indeed, using higher order CZMs in the DCB simulations is known to reduce the oscillatory response of the load-displacement curves as suggested by Pinho et al. [166] (Figure 88a).
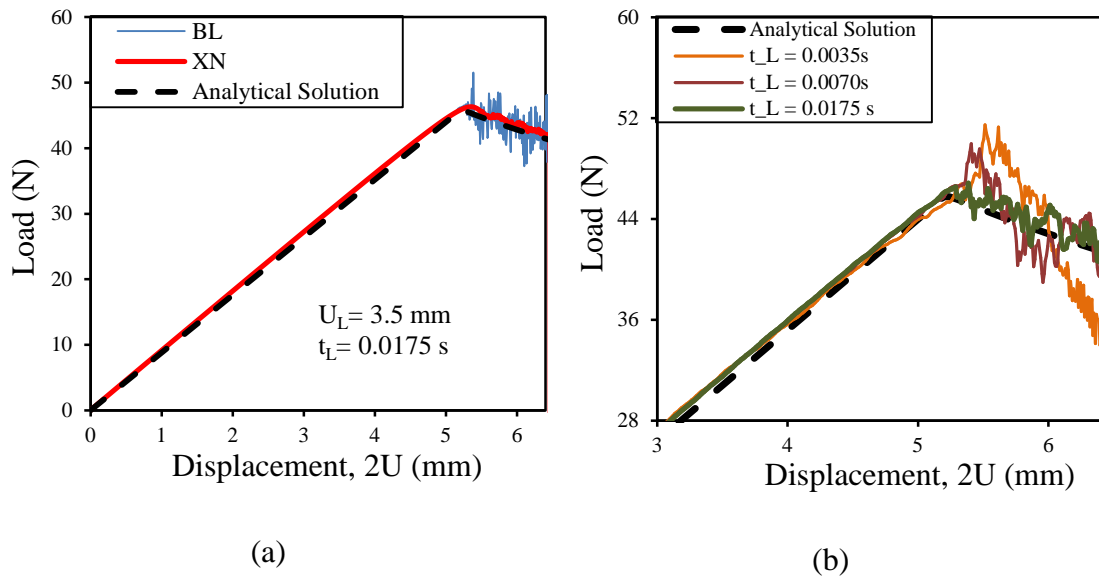
Figure 96 Load-displacement curves for (a) BL, XN and (b) RD CZMs at various loading durations compared to the analytical solution.

The implemented cohesive interface element with RD CZM is used for various loading durations; i.e. $t_L = 0.0175s$, $t_L = 0.0070s$, and $t_L = 0.0035s$. The resulting load-displacement curves are shown in Figure 96b. The curves are drawn by taking an average of four data points in order to reduce the scatter. For the original time of $t_L = 0.0175s$, there is no difference between the predictions of RD and BL CZMs This means that rate-dependent phenomenon is negligible at the original rate of loading. However, the critical load increases upto 50N by increasing the loading rate as shown in Figure 96b. This supports the increase of fracture toughness and the maximum interfacial strengths at higher loading rates (Figure 81). The results are in good agreement with the results of Corigliano and Ricci [196] who reported a same level of increase in the failure load of DCB test (Figure 82). The compliance of the specimen is increased by the inertial effects as the slope of the linear part is increased for the loading durations smaller than $t_L = 0.0035s$. Hence, excessively faster loading rates hide the influence of rate dependency in the interface. Actually, it can be suggested that studing the rate-dependency using DCB test simulations in conjunction with explicit FEA may not be very effective.

The influence of mesh size, w_e, is investigated by the DCB simulations based on the suggestion of Pinho et al. [166] who mentioned that using smaller cohesive elements

decrease the oscillatory response. Load-displacement curves obtained using various element sizes of w_e = 50 µm, 200 µm, and 400 µm are shown in Figure 97. It can be seen that the spurious oscillations in the load-displacement curves are reduced by using smaller cohesive elements. Hence, our results support the suggestion of using smaller elements for reducing the oscillations in the DCB simulations in conjunction with CZM.
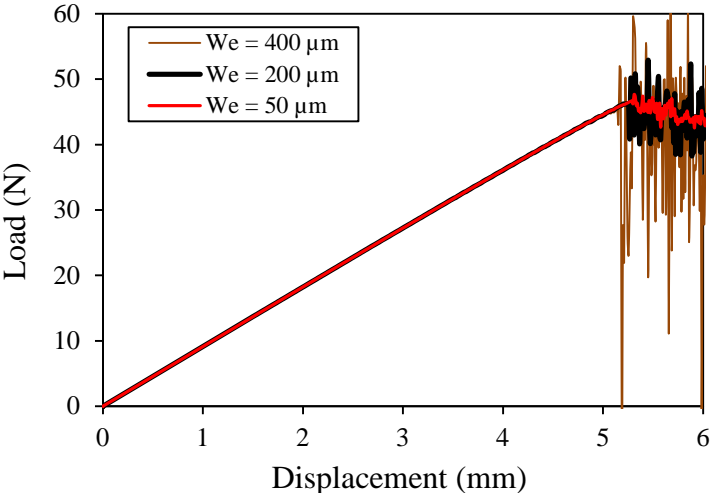
Figure 97 Load-displacement curves using interface element sizes of w_e = 50 µm, 200 µm, and 400 µm for the DCB test.

4.2. End-Load Split (ELS) Test

End-Load Split (ELS) test is used for determining mode-II fracture toughness (G_{IIc}) of composite laminates [227]. In CZM literature, numerical simulation of ELS test was also used for the verification of implemented cohesive interface elements for mode-II fracture such as performed by Chen et al. [228].
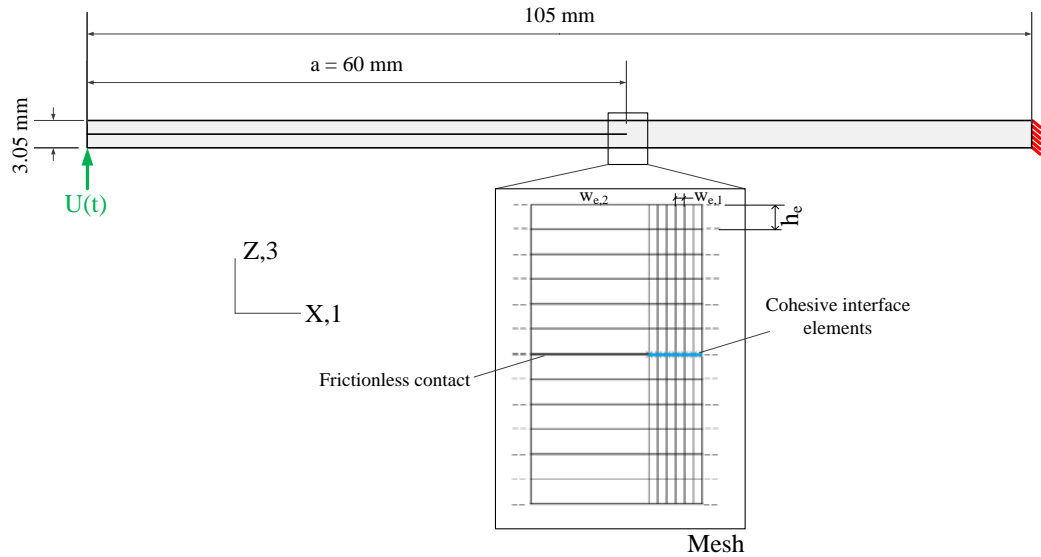
Figure 98 ELS specimen dimensions, boundary conditions and morphology of the mesh.

The specimen dimensions, boundary conditions and morphology of the mesh are shown in Figure 98. The length of the specimen is 105mm, the thickness is 3.05 mm and the length of the initial crack is 60 mm. The part is clamped from the right end whereas the load is applied upwards by a displacement loading from the lower-left corner. The profile of the loading is a smooth step defined by the eqn. (122) with U_L = 25 mm and t_L = 0.10 s. Hence, single loading rate of U_L = 25 mm and t_L = 0.10 s are used in the simulations.

The height of the elements, h_e, is taken as 254 µm for the entire model. The model has a fine mesh zone near the cohesive elements through the crack propagation path where the width of the elements, $w_{e,1}$, becomes 90 µm. The width of the elements in the coarse mesh region, $w_{e,2}$, increases to 1200 µm. A basic definition of frictionless contact, so called "hard contact" in ABAQUS [69], is modeled over the faces of the arms as illustrated in Figure 98. The stable incrementation, Δt, is calculated as 1.104×10^{-8} s by ABAQUS.

The laminate is made of Graphite/Epoxy plies which have the following material properties; E_{11} = 130 GPa, E_{22} = 8 GPa, υ = 0.27, and G_{12} = 6 GPa [227]. However, Chen et al. [228] artificially reduced the original longitudinal modulus, E_{11}, to 100

GPa in order to reach similar results of the experiments conducted by Blackman et al. [227]. They attributed the artificial reduction in the stiffness to the complexity of the boundary conditions in the original study. Hence, the reduced longitudinal stiffness of E_{11} = 100 GPa is also used in our simulations. The interface properties are taken from the study of Chen et al. [228] that are provided in Table 5.

Table 5 Interface and cohesive properties for ELS [228].

G_{IIc} (N/m)	$T_{o,II}$ (MPa)	B-K criterion constant, η	Penalty Stiffness, E_0 (N/m^3)
856	48	2.25	5×10^{15}

Figure 99 shows the development of crack propagation on the partially shown specimen together with the contours of shear stresses. The location of the crack tip can be followed through the stress concentration region. The crack propagates towards the right as the displacement increases.
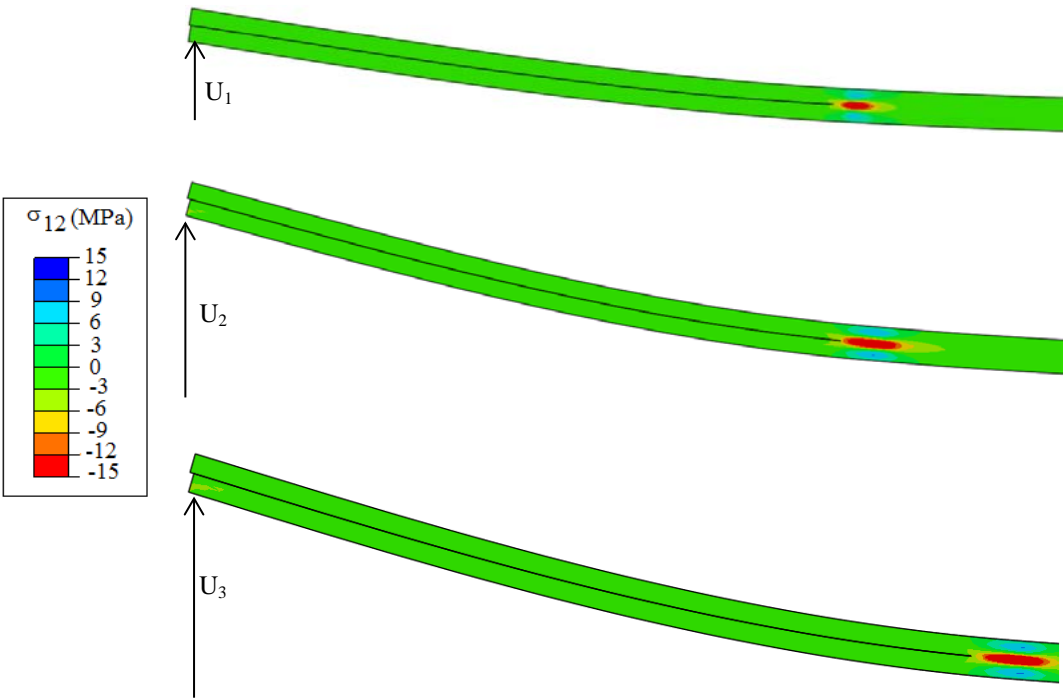
Figure 99 Development of crack propagation in ELS (partially shown) specimen and the contours of shear stresses from top to bottom ($t_3 > t_2 > t_1$).

166

Load-displacement curves of the simulations of ELS test using RD, BL and XN CZMs together with the experiments and the numerical results of Chen et al. [228] are shown in Figure 100. It is observed that the curves obtained by BL and XN CZMs are perfectly in agreement with each other and in a good agreement with the curve obtained by Chen et al. [228].
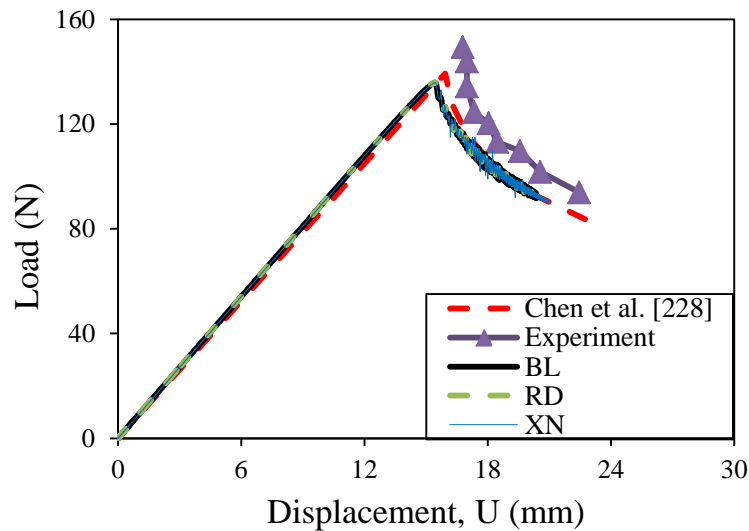
Figure 100 Load-displacement curves for the simulation of ELS test using BL, RD and XN CZM, experimental data and the curves obtained by Chen et al. [228].

In the DCB simulation (section 4.1), locating the crack tip was an easy process as the mathematical crack tip, d = 1 (Figure 60a) is very close to the point of maximum normal stress which can be easily located from the stress concentration region. Moreover, the deformation of mode-I "opens" the arms of the crack as a result the crack tip becomes physically more visible (Figure 10a). On the contrary, locating the crack tip in the ELS simulation is harder. Firstly, the length of the shear concentration region is so large that locating the point of maximum shear stress would be useless and not precious. Moreover, deformation of mode-II fracture physically hides the location of the crack tip as the arms are sliding over each other (Figure 10b). As a result, exact location of the crack tip under mode-II fracture is not agreed in references (section 2.2.5.1). Figure 101 shows contours of shear stresses and the damage distribution during the crack propagation of ELS simulation. The

length of the cohesive zone is found to be around l_{CZ} = 5 mm and the distance between the mathematical crack tip (d = 1) and the center of the stress concentration region is ~3.7 mm. The length of the cohesive zone can be calculated using eqn. (58) and Table 3. The approximated cohesive length can be found around 3 mm which is smaller than the cohesive length found by FEA (l_{CZ} = 5 mm). This result supports the statement of Harper and Hallet [193] about the mismatch between the lengths of cohesive zone calculated by analytical and FEA (section 2.2.5). It can be seen that the distribution of damage is dominated by the damaged zone very close to d → 1.0 but not equal to unity. In short, specified or cohesive crack tip definitions are effective for locating the stress concentration region in mode-II.
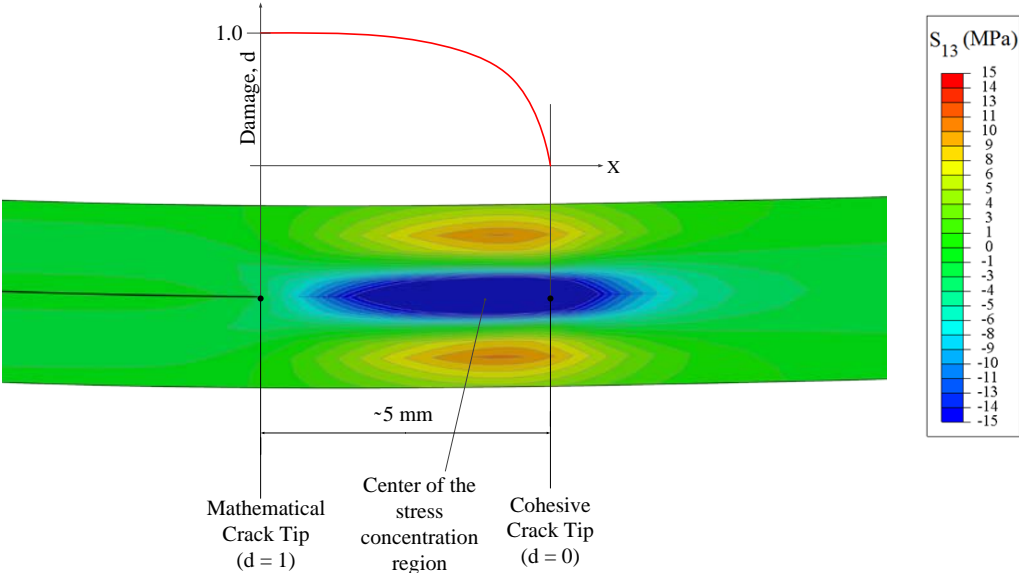
Figure 101 Damage distribution in front of crack tip and positions of mathematical and cohesive crack tips together with shear stress contours in mode-II condition.

4.3. Three-Point Bending Impact Test

Three-Point Bending Impact test is dedicated for investigation of the dynamic failure in mode-I condition. The specimen geometry and the boundary conditions are shown in Figure 102 where the length and height of the specimen are 152mm and 37 mm, respectively. An initial crack with the length of 7.4 mm is located at the lower side (Figure 102). The numerical simulation is based on the study of Zhang and Paulino

[229] who numerically used this experiment for the verification of their cohesive interface elements under dynamic mode-I condition. The case of Glass/Epoxy plate with 40% fiber volume fraction studied by Zhang and Paulino [229] is considered. The size of the cohesive elements is 97 which is the same mesh size in the reference study [229]. Triangular plain strain body elements, so called "CPE3" in ABAQUS [69], are used for the specimen bulk. The material properties of Glass/Epoxy specimen are given in Table 6 [229]. The impact is applied to the middle point of the top side in a triangular velocity profile increasing linearly to 5 m/s in 0.2 ms and linearly decreasing back to zero in 0.2 ms [229]. The stable time incrementation, Δt, is calculated by ABAQUS [69] as 1.32×10^{-8} s.
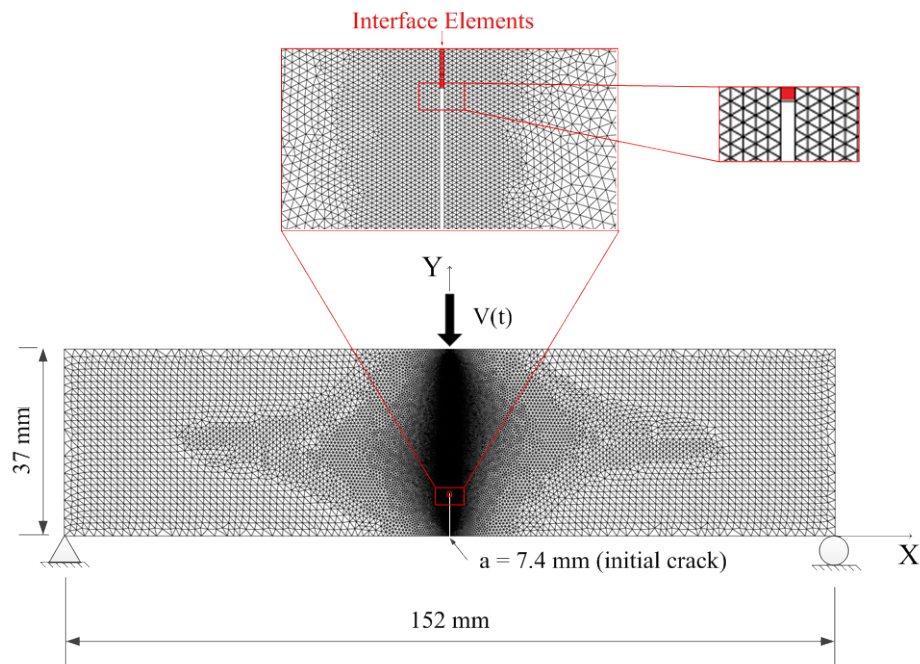
Figure 102 Three Point Bending Impact test specimen geometry, boundary conditions, loading and the mesh of the finite element model.

Table 6: Material and interface properties of Glass/Epoxy composite used in Three-Point Bending Impact test [229]

E (Gpa)	υ	Density (kg/m3)	C_d -dilitational wave speed (m/s)	G_{Ic} (N/m)	$T_{o,I}$ (MPa)	Penalty Stiffness (N/m^3)	B-K Factor
9.010	0.31	1678	2476	1101.8	180.2	10^{14}	2.25

Figure 103 shows the contours of normal stresses in the X-direction at equal time intervals of 40µs starting from t = 420µs. The location of the crack tip can be followed through the stress concentration region. The crack propagates under mode-I conditions taking 140 µs to pass through the entire chord of the specimen. The fringes are in good agreement with eachother and with the results of Zhang and Paulino [229].
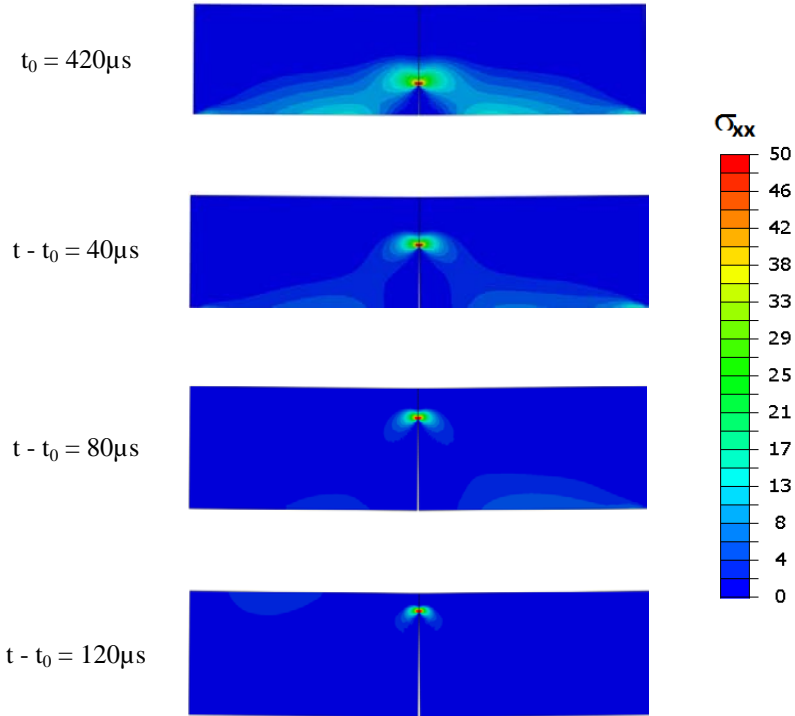
Figure 103 Contours of constant longitudinal stress (σ_{xx} - Figure 102) at equal time intervals of 40 µs starting from t = 420 µs. (t_0 = 0 defines the beginning of impact).

Figure 104a presents the crack tip speed - time graphs obtained using BL and XN CZMs after the start of crack propagation together with the results of Zhang and Paulino [229]. In Figure 104a, the crack starts to grow from 100 m/s reaching a maximum speed of 270 m/s in all cases. After attaining the maximum crack tip speed, there is a second peak at t ≈ 8 μs and a third one at t ≈ 15 μs. The crack tip speed curves of both CZMs and the one obtained by Zhang and Paulino [229] are in good agreement with each other. Noting that, the crack tip speeds were not calculated by $\Delta a/\Delta t$. Instead, 5-point stencil method was used [230]. The 5-pt stencil method reduces the scatter of the speed data as shown in Figure 104b. 5-pt Stencil method was used in reference studies for the calculating the speed of intersonic crack propagations [118].

The effect of the rate-dependent interface parameters to the crack tip speed can be analyzed by Three-Point Bending Impact test by varying the ratio of the infinite to the static toughness, which is denoted by "k"; i.e. $G_{Ic} = G_{Ic,0} = G_{Ic,\infty} / k$. For the interfacial strength, the ratio of "k" is related in the order of two; i.e. $T_{Ic} = T_{Ic,0} = 2T_{Ic,\infty} / k$. The reason is that the ratio of the infinite to the static interfacial strengths are nearly half of the ratio of the fracture toughness based on the composite material properties provided by Corigliano et al. [156]. Figure 105 provides the crack tip speed curves as a function of time for k = 1.0, 1.25, 2.5, 5.0 and 10.0 where k = 1 points to no rate-dependency ("no RD" in Figure 105). The onset and critical separation velocities are equal to 70 m/s ($\dot{\delta}_o = \dot{\delta}_c = 70$ m/s) which is provided by Corigliano et al. [156]. It can be noticed that the maximum crack tip speeds are reduced by increasing the factor "k". On the other hand, the secondary peaks become blunter as the factor "k" increases. In other words, it can be stated that the crack becomes more "viscous" with higher values of "k". An important observation from Figure 105 is that the difference between the curves using k = 5 and k = 10 is smaller than the difference between the curves of k = 1.25 and k = 2.5. The difference is coming from the rate-dependency behavior proposed by Corigliano et al. [156] (Figure 83).
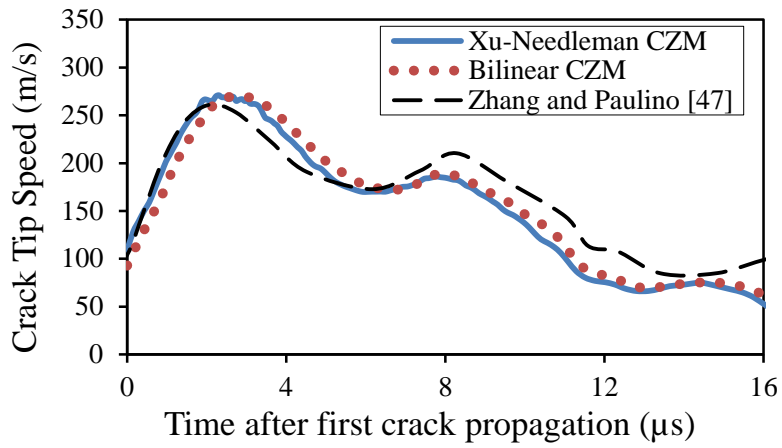
(a)
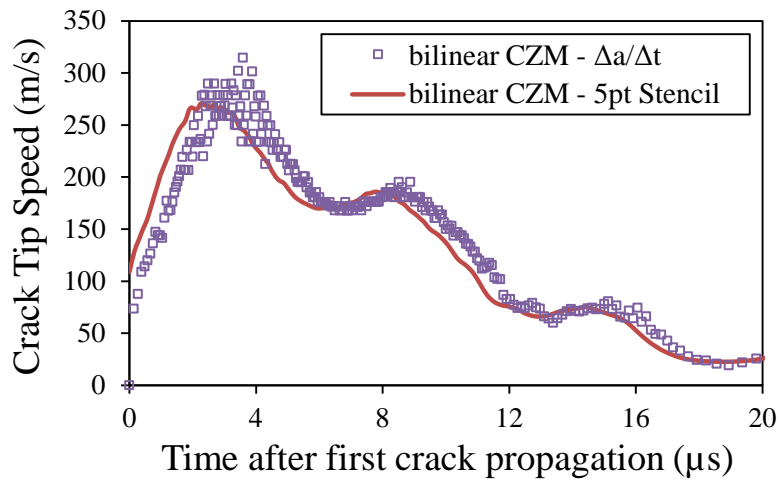
(b)

Figure 104 (a) Crack tip speed vs time graphs for the three point bending impact test using BL and XN CZMs and (b) speed raw data calculated using Δa/Δt and the resulting curve with 5-pt stencil method for BL CZM.
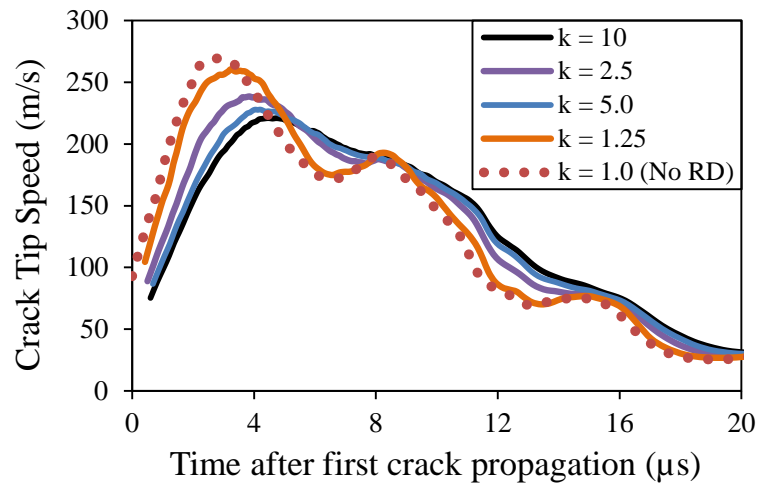
Figure 105 Crack tip speed-time graphs for the three point bending impact test using RD CZM with various k of 1.0, 1.25, 2.5, 5.0 and 10.0 factors, which is defined by $G_{Ic} = G_{Ic,\infty} / k$, and $T_{Ic} = 2T_{Ic,\infty} / k$.

4.4. Asymmetric Dynamic Loading of Polymer-Composite Plate

Dynamic crack propagation under asymmetric impact loading of adhesively bonded polymer-composite plates was studied by Coker et al. [112] in which intersonic crack propagation was investigated (Figure 106). In the bi-material interface, the crack propagation is under mode-II dominated condition albeit it is somehow a mixed-mode condition dictated by the eqn. (26). This experiment is especially used as a verification simulation for the implemented cohesive interface elements in an intersonic crack propagation case.
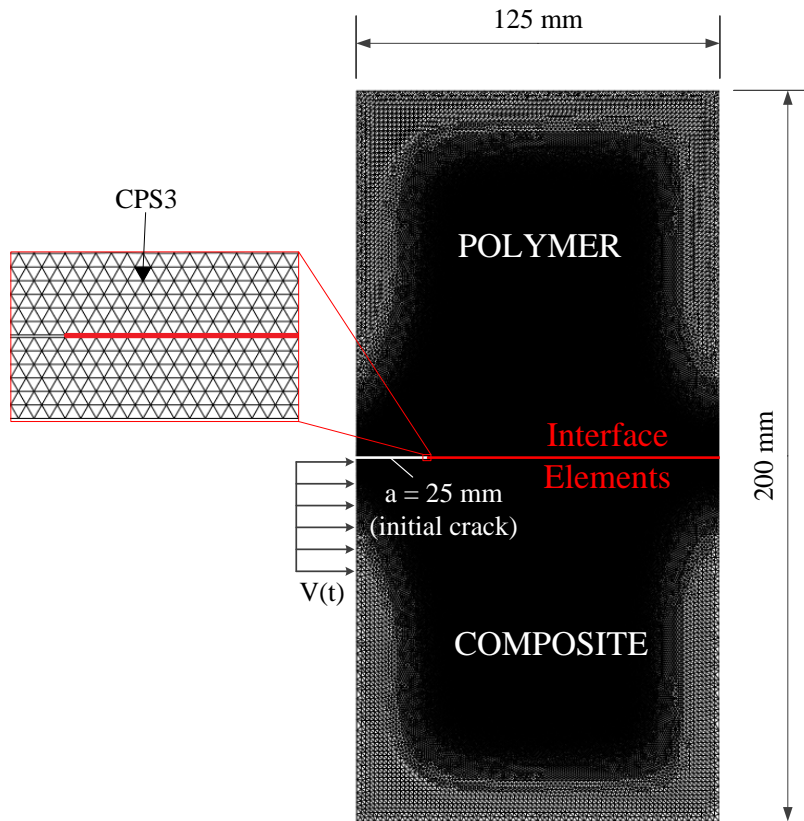
Figure 106 Geometry, boundary conditions, loading and mesh of the finite element model for asymmetric dynamic loading of an adhesively bonded polymer-composite plate [112].

A unidirectional CFRP composite laminate is adhesively bonded to a polymer plate by leaving an initial crack length of 25 mm from the left side as shown in Figure 106. The dimensions of the plates are 125 mm x 100 mm. The impact loading in the x-direction is applied from the left side of the composite plate as illustrated in Figure 106. A stepped-triangular velocity profile with the maximum speed of 40 m/s at t = 25 µs is used so as to model the scenario of "Case-I" in [112]. The same mesh properties of [112] are adopted; triangular plane stress elements, CPS3 of ABAQUS [69], and the element size of 75 µm near the interface are used. The bulk material properties of the CFRP composite and polymer materials are given in Table 7 and Table 8, respectively. The interface properties are provided in Table 9, which are all taken from the study of Coker et al. [112]. The stable time incrementation, Δt, is calculated by ABAQUS [69] as 2.046×10^{-9} s.

Table 7. Material properties of CFRP composite [112].

E_{11} (Gpa)	E_{22} (Gpa)	G_{12} (Gpa)	ν_{12}	ρ (kg/m^3)	C_d (plane stress) - dilatational wave speed (m/s)	C_s (plane stress) - shear wave speed (m/s)	C_R (plane stress) - Rayleigh wave speed (m/s)
80.0	8.9	3.6	0.25	1478	7380	1560	1548

Table 8. Material properties of Polymer (Homalite$^©$) [112].

E (Gpa)	ν	ρ (kg/m^3)	C_d (plane stress) - dilatation wave speed (m/s)	C_s (plane stress) - shear wave speed (m/s)	C_s (plane stress) - Rayleigh wave speed (m/s)
5.2	0.34	1230	2187	1255	1155

Table 9. Interface properties [112].

$G_{Ic} = G_{IIc}$ (N/m)	$T_{o,I} = T_{o,II}$ (MPa)
26.1	28.0

Crack tip speeds as a function of time are plotted in Figure 107a for RD, BL and XN CZMs together with the experimental and the numerical results obtained by Coker et al. [112]. The experimentally determined crack tip speed is provided around 7500 m/s whereas the numerical results shows the crack tip speeds around 7200 – 7300 m/s by Coker et al. [112]. The dilatational wave speed (C_d) is given as 7450 m/s in [112]. In our results, the 5-pt stencil method has been used for the calculation of the speeds aimilar to [112]. All of the three CZMs predict the same crack propagation speeds around the dilatational wave speed that is in good agreement with the results of Coker et al. [112]. Interestingly, the effect of the rate-dependency seems negligible.
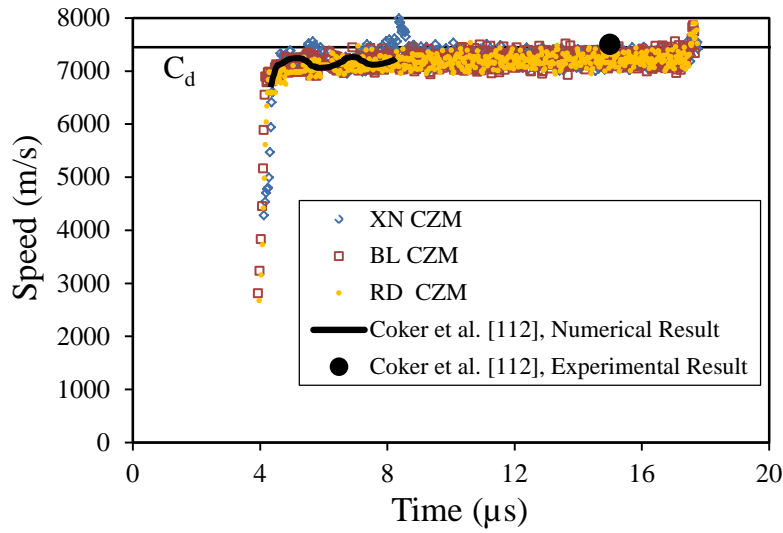
(a)
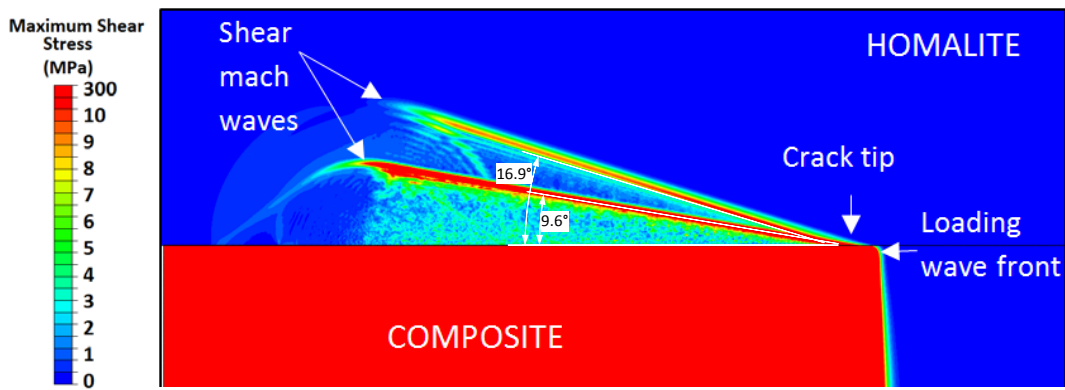
(b)

Figure 107 (a) Crack tip speed-time graph for asymmetric dynamic loading case of an adhesively connected Homalite-Composite plates using BL and XN CZMs compared to the results of Coker et al.[112] and (b) contours of constant maximum shear stresses at t = 12.2 µs after the impact showing two shear Mach waves emanating from the crack tip.

Contours of the maximum shear stress fields are shown in Figure 107b at t = 12.2 µs. As the crack tip speed exceeds both the longitudinal and shear wave speeds of polymer plate, two Mach waves are emanated from the crack tip. The angle of the shear Mach waves are calculated as 9.6° and 16.9°. Using the relation of $\sin(\theta) = C_s/V$, the dilatational wave and the shear wave speeds given in Table 8 can be reached.The study of asymmetric dynamic loading of polymer-composite plate is repeated using CPE4R [69] elements. Exactly the same patterns seen in Figure 107b are observed.

CHAPTER 5

MODELING OF DYNAMIC DELAMINATION IN L-SHAPED COMPOSITE LAMINATES

In this chapter, sectional loads on L-shaped composite laminates are shortly discussed. A recent experimental study that is used as the reference to the simulations is brefly presented. Next, the modeling of L-shaped composite laminate under axial loading is studied using BL CZM. Following, parametric studies for several numerical parameters are conducted by using BL CZM. After the discussion on BL CZM, the analysis is repeated using XN and RD CZMs. Finally, an overall discussion is presented in this chapter.

5.1. Shear versus Axial loading of L-shaped Parts

Three sectional forces; V, P and M are applied to the L-shaped composite laminates as shown in Figure 6a. The first of sectional loads is the "shear loading" denoted by "V" in Figure 108a. The second type of the sectional forces is the axial loading as illustrated in Figure 108b. The deformation shown in Figure 108b is a result of displacement input of U_y.

(a)   (b)
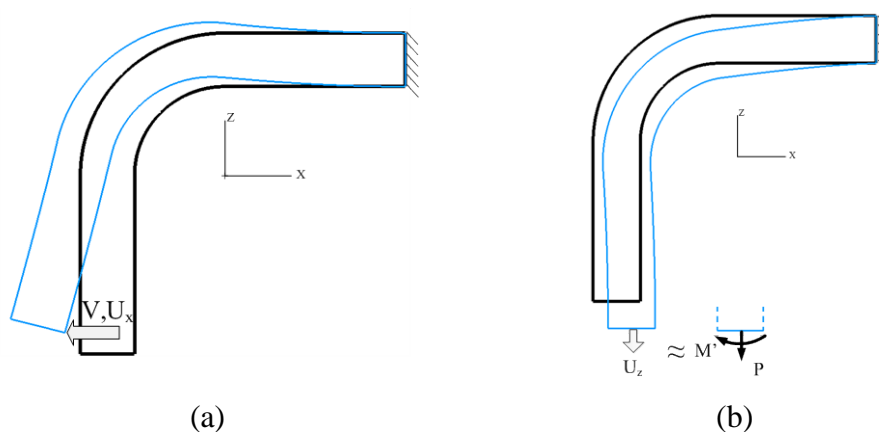
Figure 108 Original shape (black lines) and deformed shape (blue lines) of L-shaped composite laminates under (a) axial and (b) shear loading by displacement and force inputs.

179

Both the shear loading and the displacement controlled axial loading induce moment on the curved region as shown in Figure 109a. In the shear loading, the moment is can be calculated as VxL where "L" is the length of the moment arm. For the displacement controlled axial loading, the moment, M', is induced due to the clamping boundary condition at the arm.

(a)   (b)
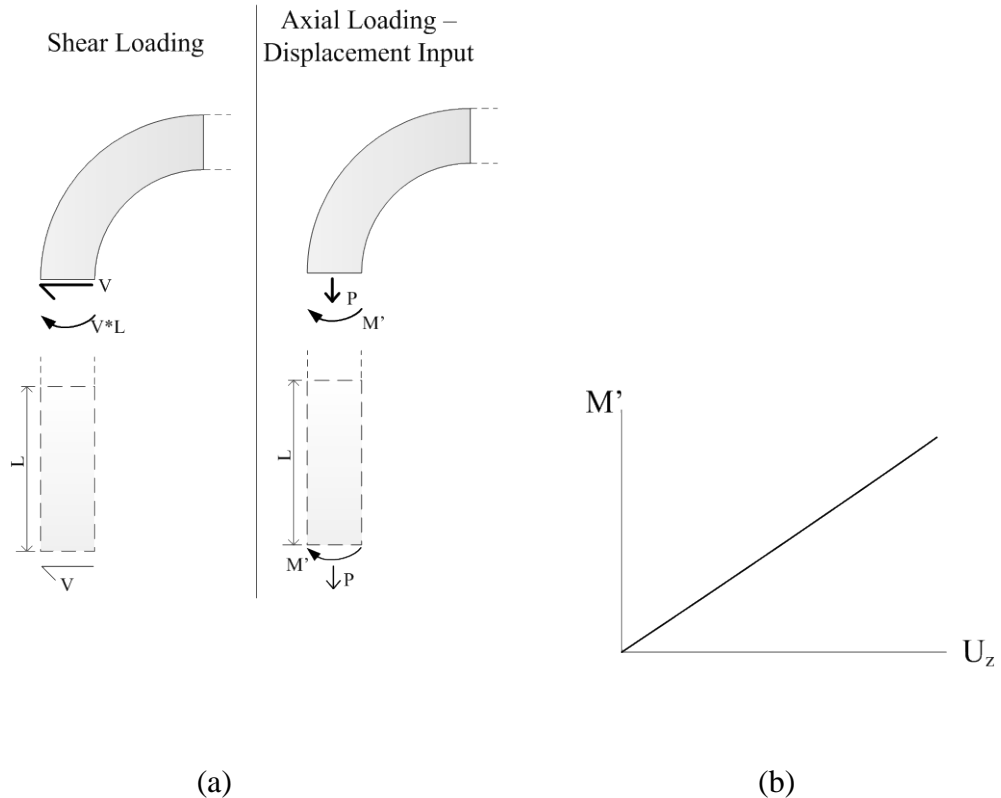
Figure 109 (a) Forces acting on the curved region under shear loading, axial loading with force input and axial loading with displacement input and (b) induced moment, M', as a function of U_z for axial loading case.

Although the induced moment, M', is zero at the beginning of the axial loading, M' linearly develops with the U_z as shown in Figure 109b. It means that the moment is induced according to the type of loading; i.e. whether it is displacement or force. On the other hand, the moment induced by the shear loading does not change as considerable as the axial loading since the moment arm does not substantially vary. The resulting moment will be either an "opening" or "closing" one which defines the

180

sign of the radial stress according to eqn. (10). The positive sing convention of the sectional forces of P and V is intentionally selected to induce opening moment.

(a) (b)
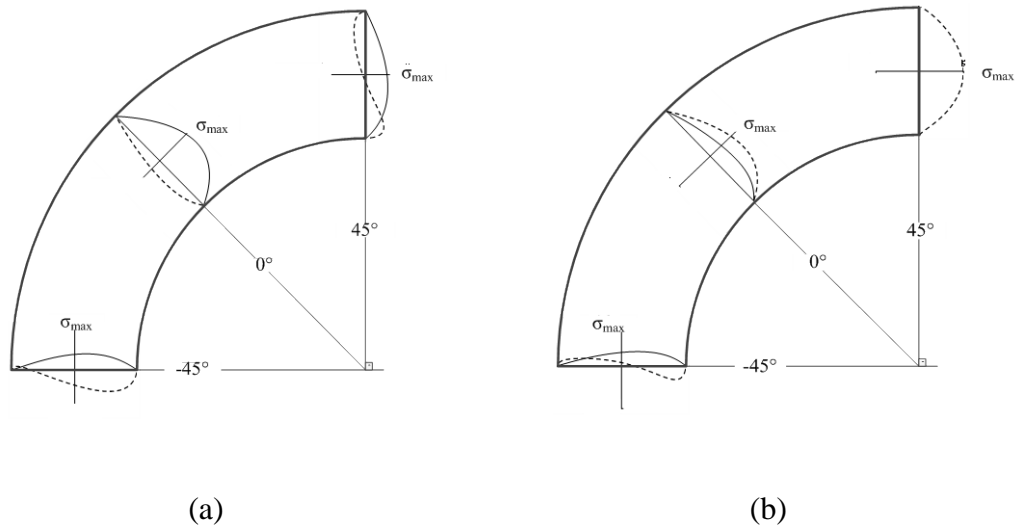
Figure 110 Radial normal (solid line) and radial shear (dash line) distributions for (a) shear and (b) axial loading cases.

Figure 110a and Figure 110b show the radial normal and shear stress distributions of shear and axial loading cases at several sections, respectively. Radial normal and shear stresses are normalized by the maximum stress attained in the curved region and represented by solid and dash lines, respectively. The stress distribution is dominated by the radial opening stresses compared to the shear stresses for the shear loading. The maximum stress is attained at 0° in Figure 110a and closer to the inner radius. A more convoluted stress distribution is achieved in the axial loading as shown in Figure 110b. Initially at -45°, the magnidutes of shear and opening stresses are close to eachother. The shear stress develops to the maximum level at +45° where the normal stress diminishes. The stress distribution in axial loading cases suggests that a crack propagating from the lower arm towards the upper arm is initially exposed to mode-I and mixed-mode in the curved region and then it is exposed to mode-II fracture in the upper arm.
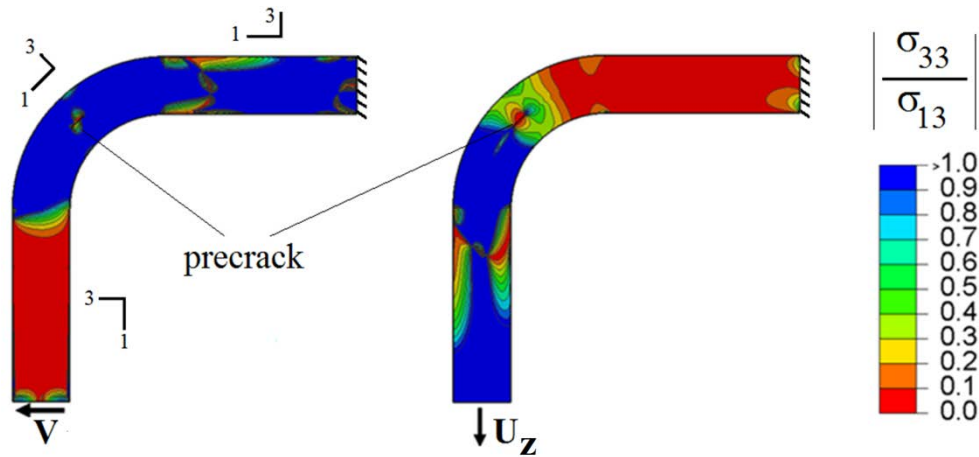
Figure 111 Fringe contours of $|\sigma_{33}/\sigma_{13}|$ in the L-shaped orthotropic material taken from the study of Gozluklu and Coker [88] for shear (left) and axial (right) loadings (1- fiber direction, 3-thickness direction).

Fringe contours of $|\sigma_{33}/\sigma_{13}|$ of an L-shaped orthotropic beam with a centered crack subjected to shear and axial loads are shown in Figure 111. The ratio of the radial normal stress (σ_{33}) to shear stress (σ_{13}) can be considered as a stress based "mode-mixity" parameter. Blue color corresponds to mode-I dominated fracture whereas red color refers to mode-II dominated fracture. From the Figure 111, more complex crack propagation behavior can be expected for the axial loading case since two sides of the crack tip are exposed to different modes. On the other hand, the fracture modes in the shear loading case may be more straight forward as both crack tips are under similar loading conditions. Specifically, mode-I dominated fracture is expected in the curved region whereas mode-II dominated fracture is expected in the arms region for the shear loading case.

Typical load-displacement curves for the fracture of L-shaped composite laminates under axial and shear loads can be summarized in Figure 112 based on the references of [79,83-85,88,94]. A relatively linear loading part is observed in all cases until the failure of the part which is associated with the delamination. During the load drop, snap-back behavior is observed where a load-controlled solution will follow the dash line denoted by "d" whereas a displacement controlled solution or the experiment reveals a vertical load drop as shown by the line "e". Noticeably, the curve "c" can

182

be reached by using arc-length method as discussed in section 3.1. The load-displacement curves with snap-back behavior are generally observed in the models with smaller initial cracks as suggested by Wimmer et al. [83]. Moreover, they are attributed to "unstable fracture" in which instantaneous crack growth takes place. Relatively stable fractures resemble the curves like "a" and "b" in Figure 112. Stable fractures are generally attained with larger initial cracks as suggested by Wimmer et al. [83] or using stitching as mentioned by Cox et al. [65].
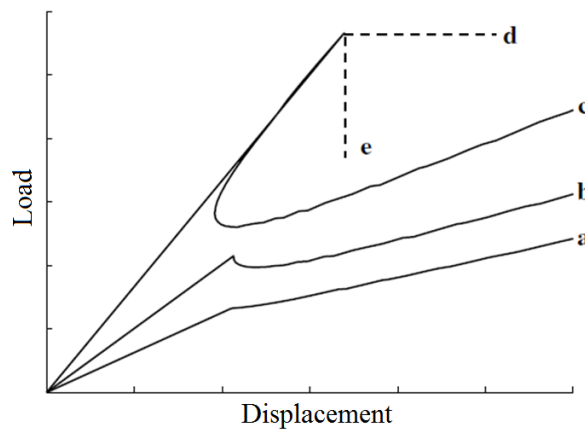
Figure 112 Typical load-displacement curves obtained for the fracture of L-shaped composite laminates [83].

5.2. Recent Experiments on Delamination of L-shaped Composite Laminates

Uyar et al. [231,232] recently conducted experiments on the delamination of L-shaped composite laminates in METU Laboratories. Their experimental fixture was designed to create a displacement loading perpendicular to the horizontal arm as shown in Figure 113a. The load was kept parallel to the Z-direction through the pivot pin bearing system. The specimen was bolted to the pivot pin in favor of fixing the loaded arm with respect to the curved region of the specimen. The vertical arm of the specimen was clamped to the fixture by fasteners. The lower side of the fixture was free to translate along the X-direction through a linear motion bearing system which provided a smooth and precised motion. As a result, no reaction force in the X-axis

183

was induced. The testing machine is a screw-driven displacement controlled tensile-compression machine having 10 kN of loading capacity (Schimadzu Autograph AGS-J). All experiments had been conducted at the cross-head speed of 3 mm/min at room temperature. Photron FASTCAM SA-5 ultra-high-speed camera system was used at 500,000 fps with a resolution of 64x32 pixels to capture the dynamic delamination (Figure 113b). The focus of the camera was aimed at the curved region of the L-shaped laminate which is encircled in Figure 113a.

The experimental specimen is 12 layer cross ply laminate ($[(0°/90°)_6]_s$) made of AS4/8552 plain weave woven fabric plies. The laminate was manufactured by hand-lay up method by lying on a male tool together with caul-plates. The curing was performed at the pressure of 6.9 bar in an autoclave at 180° C. The total thickness of the laminate is 3.36 mm, the length of the upper arm is 9 cm, the length of the lower arm is 15 cm and the inner radius is 1 cm. The specimen was mounted on the fixture 40 mm from the ends of the clamps as shown in Figure 113a. Several specimens were tested in the experiments. However, the results of specimen F1 and specimen F2 are taken for this study since these are the available results for today.
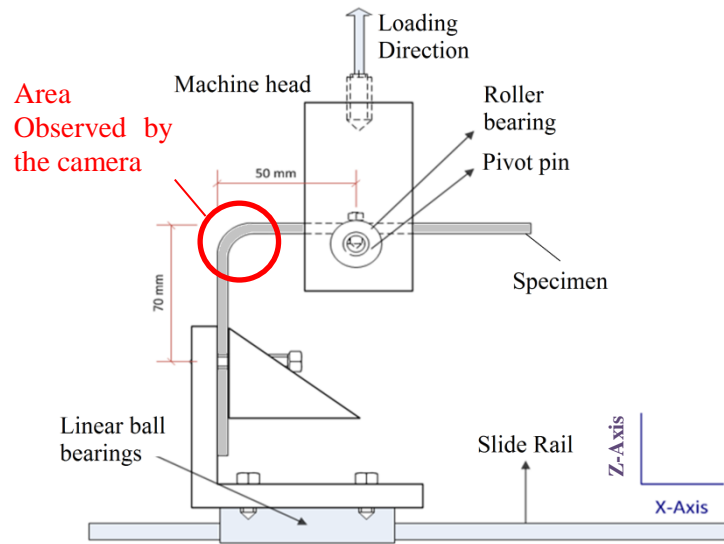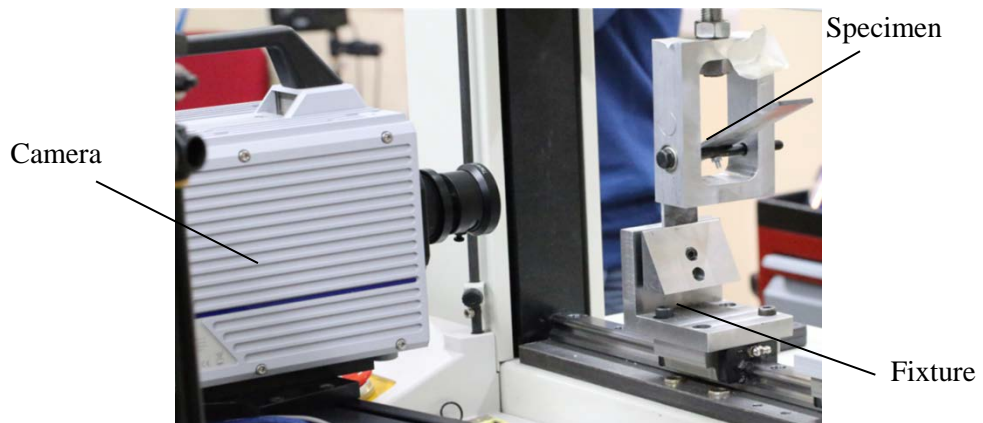
Figure 113 (a) Experimental fixture for the shear loading of L-shaped composite laminates and the area observed by the camera and (b) experimental setup composed of the fixture and the ultra-high speed camera.
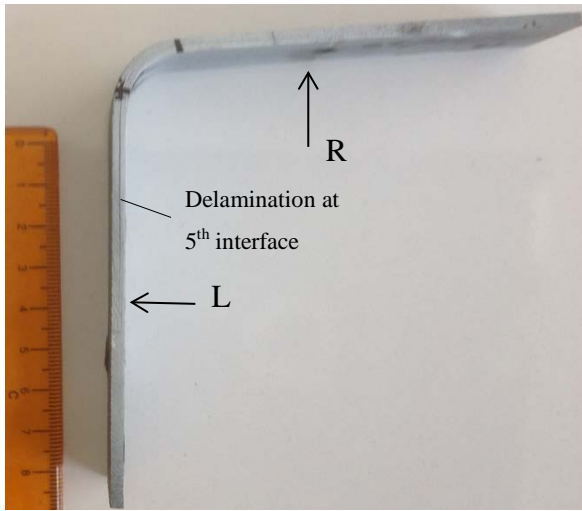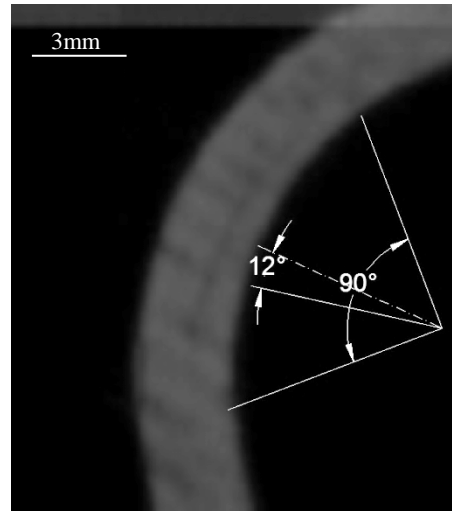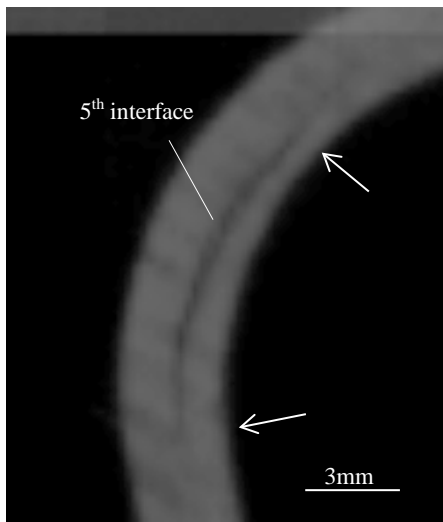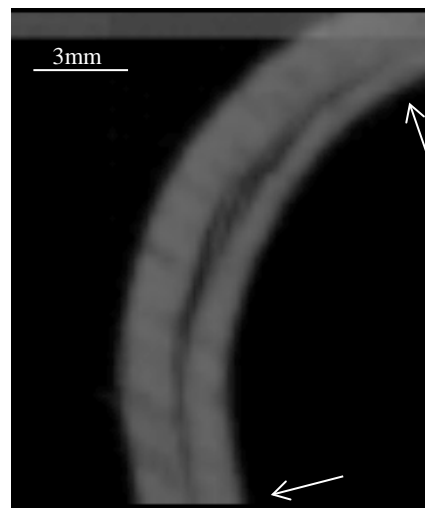
Figure 114 (a) Final view of the failed specimen F2, and (b) snapshot from the ultra-high speed camera captured for experimentally locating the initiation point ($\Delta t = 0$) and during propagation at (c) $\Delta t = 3.8$ μs and (d) $\Delta t = 7.6$ μs for F2 [231,232].

In the experiments, Uyar et al. [231, 232] initially obtained load-displacement curves. Similar to Shikumar et al. [62], a sound of "pop", which was attributed to matrix cracking, was reported by Uyar et al. [231, 232] near the 60-70% of the failure load. Following, the delamination occurs instantaneously with a loud sound of "bang" in parallel to the abrupt load drop in the load-displacement curves. They

observed that a large main delamination at the 5th interface which is between the 5th and 6th plies numbered from the inner radius at the final view (Figure 114a). The main delamination was totally propagated through the specimen until reaching the clamped area where the specimen is mounted. In addition, they reported other small delaminations at the curved region during the load-drop starting at $\Delta t = 570$ μs. The delamination occurred so instantaneously that the process was hardly captured by the camera at 500,000 fps. The crack length and crack tip speeds versus time data were also calculated using the camera recordings where the crack tips are visually located as shown in Figure 114. The crack tip speeds were calculated using forward difference method by $\Delta a/\Delta t$ where Δa is the change of crack length observed from the recordings in Δt of time. For the specimen of F2, the initiation stage was captured by the ultra-high speed camera at the 5th interface with the angular location of 12° from the centerline of the curved region (Figure 114b). The delamination at the 5th interface propagated towards the both ends. The pictures shown in Figure 114b-d are captured at $\Delta t = 0$ (initiation), $\Delta t = 3.8$ μs and $\Delta t = 7.6$ μs, respectively. They recorded a radial motion of the delaminated laminates which vibrates in around 33.3 kHz. After four to five cycles, the vibration is damped. The results of the experiments for the specimens F1 and F2 are provided together with the numerical results in the following sections.

5.3. Modeling of Delamination in L-shaped Composite Laminates under Shear Loading

Modeling of delamination in L-shaped composite laminates under shear loading is studied (Figure 6a). The numerical investigation is motivated from the experimental study of Uyar et al. [231,232].

5.3.1. Locating the cracks tips in the L-shaped laminates

In our simulations of delamination in L-shaped composites, both mode-I and mode-I propagations are observed. As discussed in section 2.2.5.1, the exact location of the crack tip is polemical, especially for the mode-II fracture. Hence, specified crack tip is defined by the point of *partial damage* reaching 60%; i.e. $d = 0.6$. This definition of the crack tip is denoted by $d_{0.6}$. The damage value of $d = 0.6$ is determined by trial-and-error analysis that gives the best crack tip definition for locating the

opening stress concentration region at the specimen arms. On the other hand, mathematical crack tip is denoted by $d_{1.0}$ in which the damage is equal to unity. Representative stress distribution and the definitions of the crack tips for BL and RD CZMs are shown in Figure 115. It is seen that the locations of $d_{1.0}$ and $d_{0.6}$ are close to each other as well as to the experimental crack tip that is defined as the last point of the visible arms for mode-I. On the other hand, $d_{1.0}$ is the closest definition to the experimentally observable crack tip whereas $d_{0.6}$ is considerably far from the experimentally observable crack tip for mode-II condition as illustrated in Figure 115-right. Hence, $d_{1.0}$ is a better approximation for comparison purposes with the experimental observations. However, $d_{1.0}$ does not always stay inside the stress concentration region especially for mode-II delamination such as shown in Figure 101. Namely, neither $d_{0.6}$ nor $d_{1.0}$ would be adequate to explain all delamination process including both mode-I and mode-II conditions. Because of these reasons, both $d_{1.0}$ and $d_{0.6}$ definitions of the crack tip are generally provided in this study. The discussion about $d_{1.0}$ is not applicable to the XN CZM since the traction decay of the XN CZM takes place asymptotically. For XN CZM, the separation of $\delta = 10\delta_0$ is used.
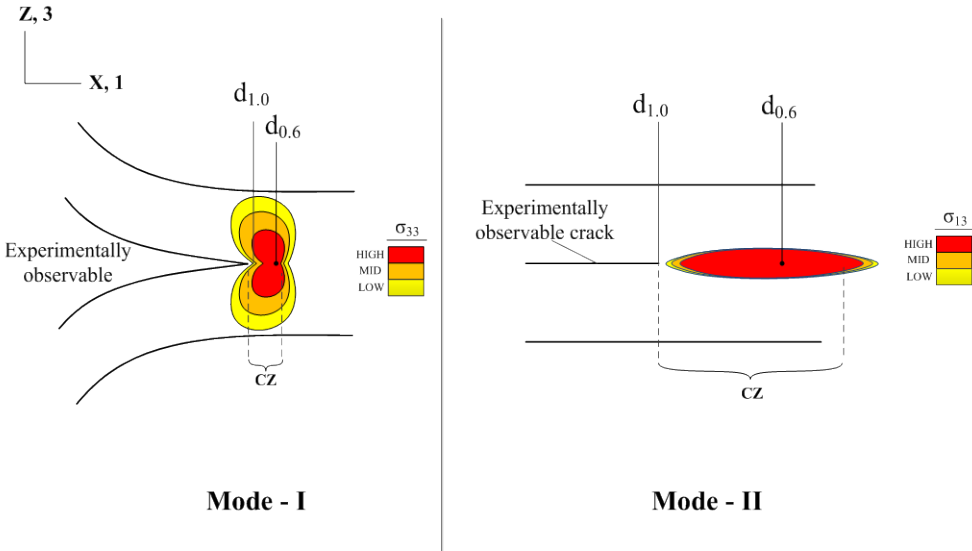
Figure 115 Definitions of crack tips for Mode-I (with normal stress fringe) and Mode-II delamination (with shear stress fringe) for BL and RD CZM.

5.3.2. Numerical Modeling of Intersonic Delamination using BL CZM

Numerical modeling is performed for the experimental specimen mentioned in section 5.2. The deformable region, staying between the clamps, is modeled. Hence, the length of the arms is 40 mm in our model (Figure 117a). The material properties of AS4/8552 are taken from the material specification datasheet [233] which is provided in Table 10. The longitudinal modulus (E_{11}) is the minimum of the average of tension and compression modulus in the datasheet [233]. The reason for taking the minimum value is to have the closest compliance to the experimental specimen where were softer than the nominal data. This can be attributed to environmental factors such as aging. Using the average of compressive and tension modulus is a general attitude in engineering applications for modeling the specimens under bending where both compressive and tensile stresses are equally formed. Interfacial normal and shear strengths are taken as $T_{o,I}$ = 40 MPa and $T_{o,II}$ = 53 MPa, respectively. The interfacial strengths are based on the report of [234] where 4-Point Bending (ASTM D6415 [28]) and Short-Beam Flexure (ASTM D2344 [29]) tests were conducted. On the other hand, G_{Ic} and G_{IIc} were experimentally obtained in METU labs as 375.3 N/m and 1467.1 N/m, respectively, using DCB and Edge Notch Fracture (ENF) tests [235]. Interface and ply numbering are started from the inner radius as indicated in Figure 117a. All of the eleven interfaces are modeled using the implemented zero-thickness cohesive interface elements using BL CZM. The penalty stiffness of the BL CZM is taken as 1×10^{14} N/m^3 in order to minimize the numerical effects of penalty stiffness and minimize the elastic energy stored prior to the softening phenomenon as mentioned in section 2.2.5.4. Higher values of penalty stiffness are avoided in order to not to create numerical problems and not to be too much deviant from XN CZM. The profile of the resulting BL CZM is shown in Figure 116 where the crack tip definitions of $d_{0.6}$ and $d_{1.0}$ are shown. The curve fitting term of the B-K criterion, η, is directly taken from the study of Gozluklu and Coker [88] as η = 2.25. The dilatational wave speed in the ply direction, $C^{\parallel}_d$, is calculated as 6600 m/s and the shear wave speed, C_s, is calculated as 1636 m/s using the eqn.(40). The Rayleigh wave speed, C_R, is calculated as 1572 m/s using the eqn.(42). All the interface and cohesive properties are summarized in Table 11.

Table 10: Material properties of AS4/8552 [233].

E_{11} (GPa)	E_{33} (GPa)	$G_{13} \approx 0.75$ x G_{12} (GPa)	v_{13}	Density (kg/m^3)	Cured ply thickness (mm)
55.7	8.5	3.7	0.30	1570	0.28

Table 11 Interface and cohesive properties of woven fabric CFRP laminate.

G_{Ic} (N/m)	G_{IIc} (N/m)	$T_{o,I}$ (MPa)	$T_{o,II}$ (MPa)	B-K criterion, η	Dilitational wave speed, $C_d^{\parallel}$ (m/s)	Shear wave speed, C_s (m/s)	Rayleigh wave speed, C_R (m/s)
375.3	1467.1	40	53	2.25	6600	1636	1572
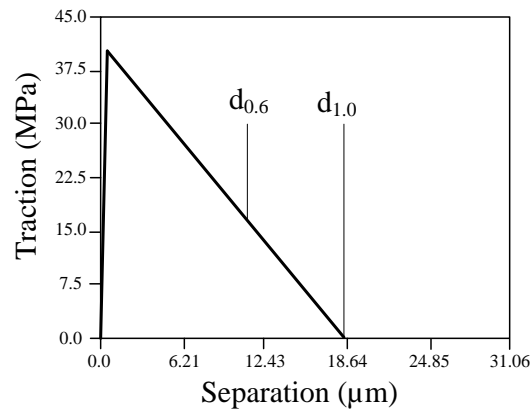
Figure 116 Traction-separation profile of BL CZM together with $d_{1.0}$ and $d_{0.6}$ definitions of the crack tip for mode-I.

The mesh of the finite element model is homogeneous as shown in Figure 117b. The width of the elements is $w_e = 150$ μm at the mid-line. The height of the elements is $h_e = 70$ μm which gives 4 elements in one ply thickness. Noting that, the width of the elements in the curved region becomes 143 μm at the outermost chord whereas it shrinks to 107 μm at the inner chord. The bulk elements are CPE4R, which is a 4-

noded plane strain element with single integration point at the centroid. Noting that, CPE4R is the only quadrilateral plane strain element available in ABAQUS/Explicit [69]. Total number of nodes is 47040, number of CPE4R elements is 37584, number of cohesive interface elements is 8613, and number of degrees of freedom is 141120. The stable time incrementation, Δt, is calculated by ABAQUS as 9.212×10^{-9} s. Solution duration of a single simulation takes 27 hours and 15 minutes by a 64-bit Intel Core i7-2620M CPU 2.70 GHz with 8 GB RAM computer.

Delamination propagation is inhibited from the ends of the arms by "gluing" the nodes of the cohesive elements. The reason is that the experimental fixture shown in Figure 113a grabs the laminate from the ends where the laminate is squeezed. Hence, no propagation may occur due to the compression at the ends. This is taken as a boundary condition in our simulation by stopping the delamination at the latest interface nodes by inhibiting separation of the cohesive elements. The vertical arm is clamped except for translation in the x-direction. The lower right tip of the horizontal arm is displaced by $U_L = 25$ mm in duration of $t_L = 0.025$ s in the Z-direction. A displacement controlled "quasi-static fast loading" is applied, which is discussed in the next section.
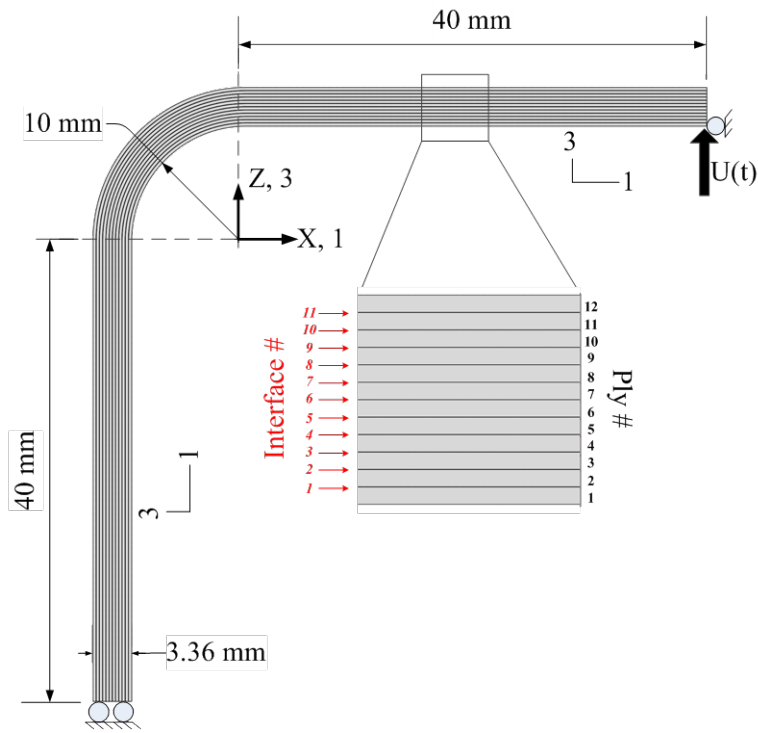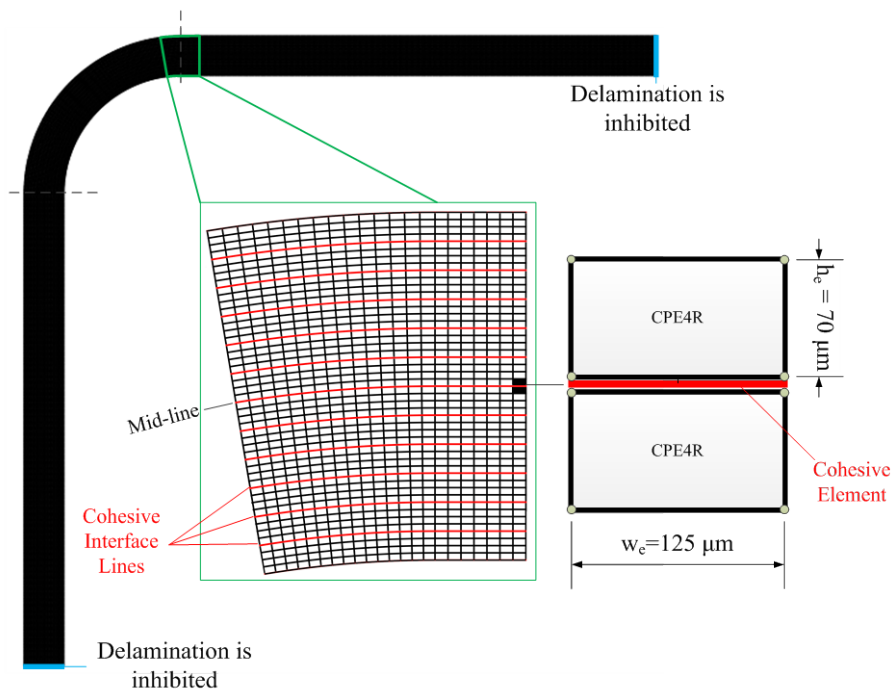
Figure 117 (a) Boundary conditions, geometry and (b) mesh of the L-shaped composite laminate made of twelve woven fabric CFRP plies with eleven interfaces. (1- chord (fiber) direction, 3-thickness direction)

5.3.2.1. Quasi-static fast loading

The main drawback of using explicit FEA in quasi-static loading is the very long durations of solution (or "CPU time"). The total number of increments, Σj, can be defined as $\Sigma j = t_L/\Delta t$, where t_L is the loading duration and Δt is the stable time incrementation. In order to have a quasi-static loading, the loading duration, t_L, should be in the order of seconds, as for our case. On the other hand, the stable time incrementation is extremely small such as in the order of 10^{-7} - 10^{-11} s. As a result, the number of increments becomes so many that CPU time can be unattainably long. As a remedy to the problem, Gozluklu and Coker [88] proposed a sequential method in which the quasi-static loading is solved by implicit FEA as mentioned in sections 3.1 and 3.2. However, the sequential method needs a restart file that has the information of deformation state at the end of the implicit solution. Unfortunately, this is not suitable for the VUEL subroutines due to the program limitations of ABAQUS [69]. Hence, explicit FEA is solely used in this study.

Instead of sequential method, minimization of the loading duration, t_L, helps to reduce the CPU time. However, a fast loading might not be quasi-static, as it may yield dynamic loading. There are two phenomena that may influence the results in case of dynamic loading considering equation of motion. Firstly, viscous effects may become dominant due to high loading speeds. In our simulations, the only viscous phenomenon included in the simulations is the rate-dependency of the RD CZM. The second one is the inertial effects due to high acceleration rates. By minimizing the viscous and inertial effects, fast loading can be achieved without sacrificing the quasi-static assumption.

As discussed in the section 3.2, the loading profile of "smooth step" defined by eqn. (122) is used since it does not induce osscilations in the early stages of loading. From eqn. (122), the speed and the acceleration profiles can be obtained for the smooth step as below [69],

$$V(t) = \frac{dU(t)}{dt} = 30U_L\left[\left(\frac{t}{t_L}\right)^2 - 2\left(\frac{t}{t_L}\right)^3 + \left(\frac{t}{t_L}\right)^4\right] \tag{123}$$

$$A(t) = \frac{dV(t)}{dt} = 60U_L\left[\left(\frac{t}{t_L}\right) - 3\left(\frac{t}{t_L}\right)^2 + 2\left(\frac{t}{t_L}\right)^3\right] \qquad (124)$$

The resulting profiles of loading speed, V(t), and acceleration, A(t), for $U_L = 1$ and t_L = 1 as a function of time and displacement, U(t), are shown in Figure 118a and Figure 118b, respectively. The maximum speed of 1.88 is attained at $t = 0.5t_L$ & U = $0.5U_L$ whereas the maximum acceleration of -5.77 (+5.77) is attained at $t = 0.21t_L$ (t $= 0.79t_L$) and $U = 0.066U_L$ ($U = 0.934U_L$). Figure 118a shows that the specimen is gradually accelerated from zero to a finite value, which inhibits the development of oscillations in the early stages of loading. Hence, the acceleration is dominated by the loading duration, t_L, in the power of three whereas it is linearly dependent to the U_L. Hence, trial-and-error analysis on the loading duration with a fixed value of U_L would reveal the effect of loading speed in the explicit analysis using the smooth step.

(a)   (b)
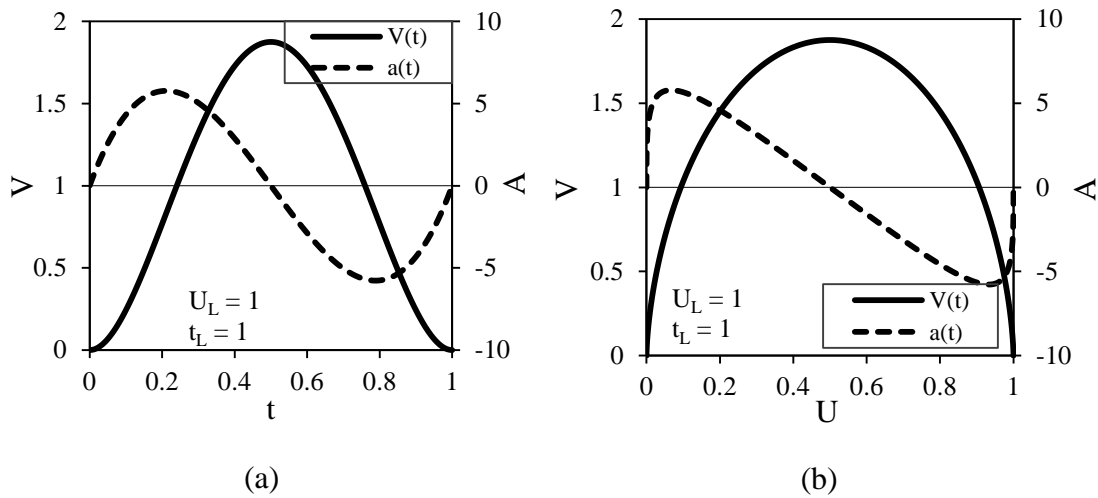
Figure 118 Loading speed (V) and acceleration (A) profiles for $U_L = 1$ mm and $t_L = 1$ s of a smooth step as a function of (a) time and (b) displacement, U.

The simulations at four loading durations of $t_L = 2.5$s, $t_L = 0.25$s, $t_L = 0.025$s, and $t_L = 0.0025$s with $U_L = 25$ mm are performed for L-shaped composite laminate using RD CZM. The reason for using RD CZM is to include viscous effects in the interface. The rate-dependent interface properties are based on the study of Corigliano et al.

[156]; i.e. $G_{Ic,\infty} = 5G_{Ic}$, $G_{IIc,\infty} = 5G_{IIc,}$ $T_{Io,\infty} = 2.5T_{o,I}$, $T_{IIo,\infty} = 2.5T_{o,II}$ and the onset and critical separation velocities of 70 m/s [156]. The load displacement curves of different loading speeds (durations) are shown in Figure 119a. The loading speeds with $t_L = 0.0025$ spawned considerable disturbance in the load-displacement curves that are associated to inertial effects. On the other hand, the load-displacement curves the remaining curves of the remaining speeds sit on each other in Figure 119a. The percentage change of crack tip speeds obtained using $t_L = 0.25s$, $t_L = 0.025s$, and $t_L = 0.0025s$ are calculated with respect to $t_L = 2.5s$ for the left and the right crack tips as shown in Figure 119a and Figure 119b, respectively. For the left crack tip, the fastest loading speed of $t_L = 0.0025s$ reaches 10% of difference whereas the remaining speeds exhibit less than 2.5%. The effect of loading speed is very dramatic for the fastest loading speed of $t_L = 0.0025s$ where the percentage difference reaches 90%. The percentage differences of the remaining loading durations are less than 2%. As a result, the loading speeds in advance of $t_L = 0.0025s$ with $U_L = 25$ mm can be confidently used assuming a quasi-static loading.
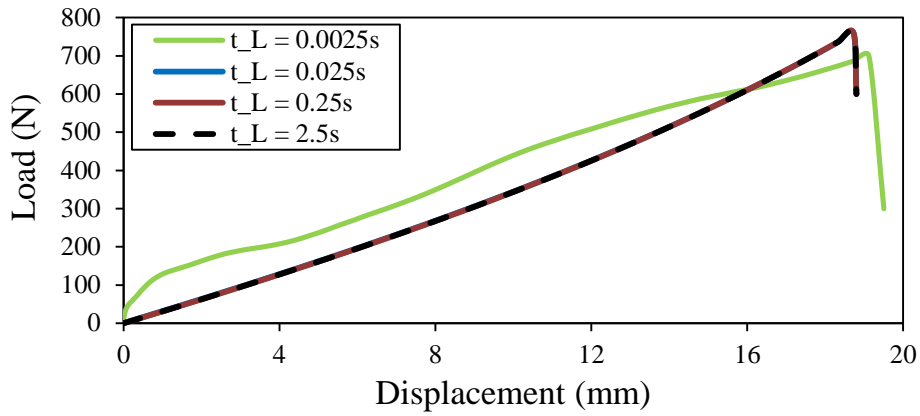
(a)
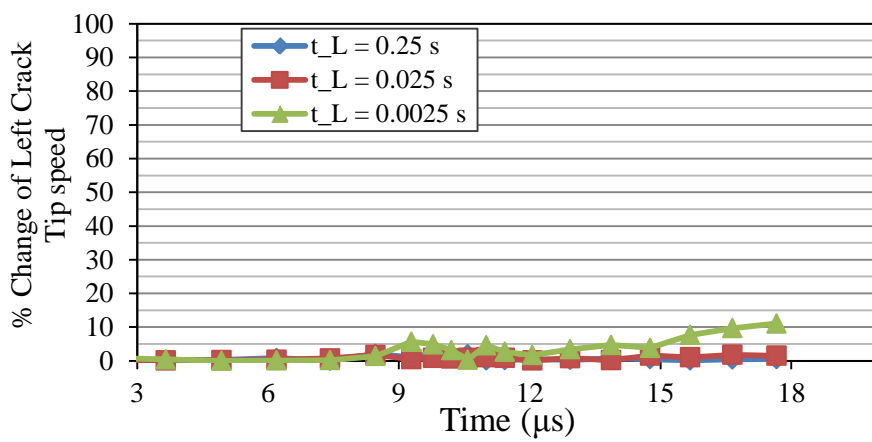
(b)
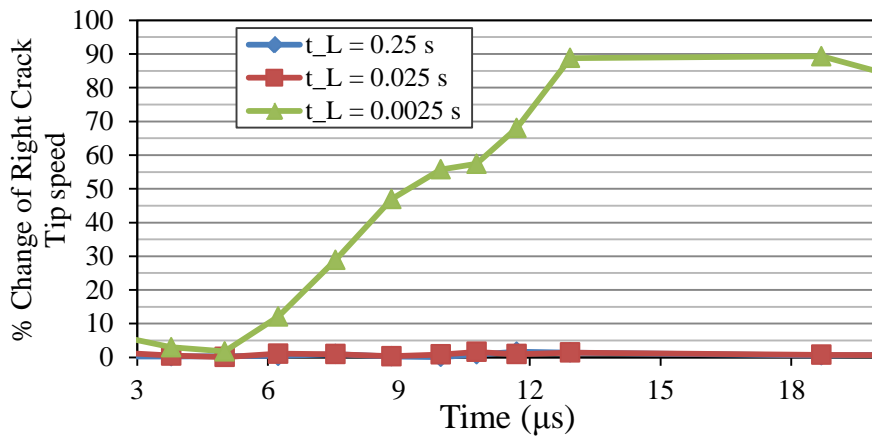
(c)

Figure 119 (a) Load-displacement curves, (b) percentage change with respect to $t_L =$ 2.5s for left crack tip and (c) right crack tip speed versus time curves obtained for t_L = 0.0025s, t_L = 0.025s, t_L = 0.25s, and t_L = 2.5s.

5.3.2.2. Results and Discussion

The simulation using BL CZM is performed in ABAQUS/Explicit [69] with the implemented cohesive interface element. The load-displacement curves of the simulation together with the experimental results of F1 and F2 are shown in Figure 120a. As a general behavior, the load increases almost linearly with the displacement up to a maximum level, so called "failure load". This point can be associated with delamination initiation (point "A"). Afterwards, the load is abruptly dropped which can be associated with the propagation stage. In the experiments, the failure load of specimen F1 is found to be 753 N at U = 19.5 mm shown by light blue dash line in Figure 120a. The load drop of F1 continues until reaching 250 N at U = 19.4 mm. On the other hand, the specimen F2 is failed at the load of 735N when the tip displacement is U = 18.7 mm, shown by the red dash line in Figure 120a. After the minimum load is attained during the load drop, the reloading stage starts with a higher compliance (point "B"). The agreement between the experimental specimens is very good compared to the similar studies on L-shaped composite laminates in references (section 1.4). In the simulations, the failure point is found as 762 N at U = 19.4 mm which is nearly the same with the experimental result of F1 specimen (Figure 120a). Following the failure point, the load is abruptly dropped similar to the experimental results albeit spurious oscillations start as representatively shown by the dash lines in Figure 120b. The frequency of the oscillations for the reaction forces is around 50 kHz. Hence, not all the data is plotted in the figure. Otherwise, it would be filled by a "black area" due to huge amount of oscillating curves. The oscillations are observed to be slightly reduced by increasing displacement and time. The oscillations continue harmonically around the "slope – BL" shown by the straight blue line in Figure 120b. The slope can be extended leftward to U = 19.4 mm in order to capture an approximate point "B" around 140N for the simulation. Delamination propagation continues for several cycles of the reaction force at U = 19.4 mm. In other words, delamination propagation cannot be associated to a single load drop in the simulations.
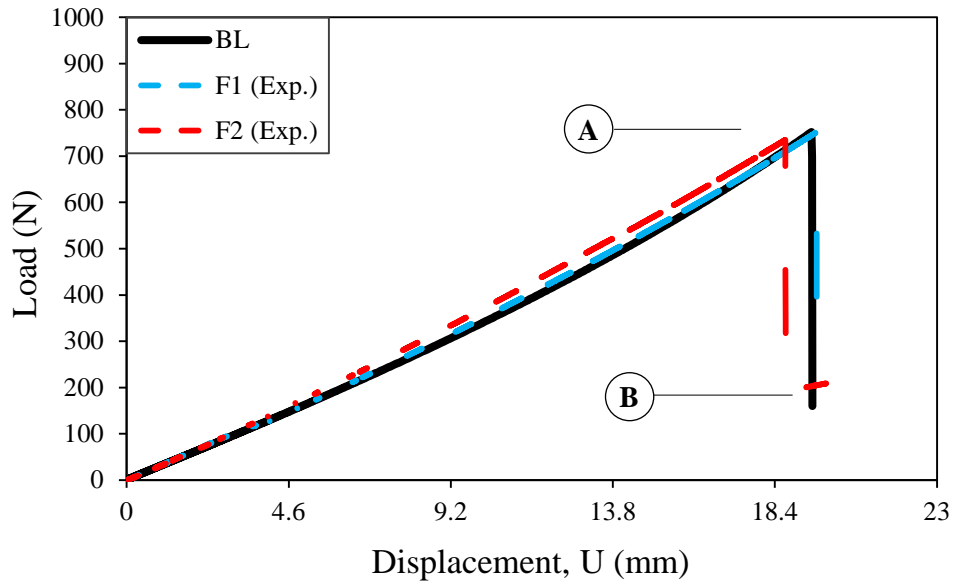
(a)
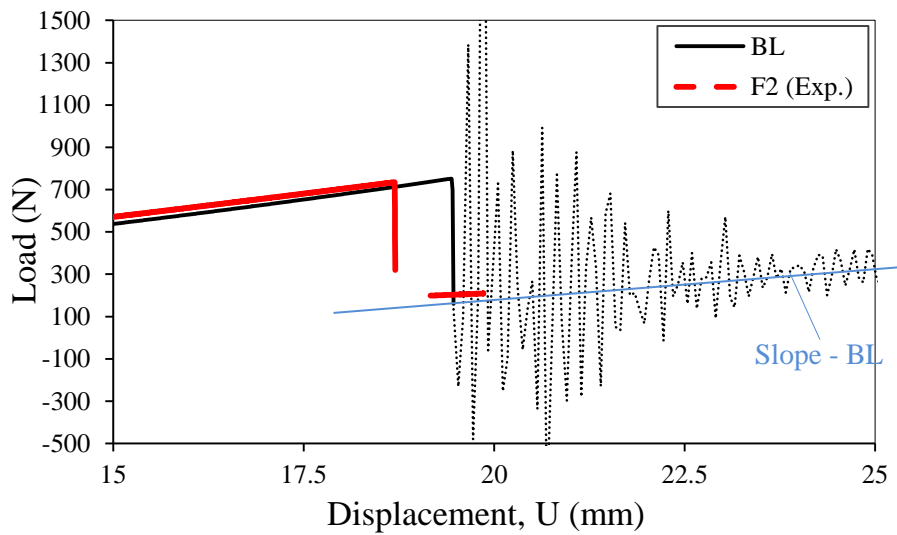
(b)

Figure 120 Load-displacement curves obtained for (a) BL CZM together with the experimental result and (b) slopes of second loading parts of experiments and BL CZM with the severe oscillations (Point "A": Start of initiation, Point "B": End of propagation).

Prior to the delamination initiation, contours of radial opening (σ_{33}), shear (σ_{13}) and longitudinal (σ_{11}) stresses are shown in Figure 121a left, middle and right, respectively. At that instance, no damage has been developed in the specimen. In other words, no material nonlinearity has affected the stress distribution. As a general behavior, the curved region is dominated by opening stresses whereas the arms are dominated by shear stresses together with compressive normal stresses. The maximum opening stress is attained at the curved region around 42% of the thickness with respect to the inner radius. Shear stresses are localized at four points near the corners of the curved region where the maximum shear stress of 42.7 MPa and the minimum of -24.3 MPa are located close to the inner radius (Figure 121a-middle). The longitudinal stresses resemble a typical stress distribution of a beam under bending load. From the Figure 121a, the delamination is expected to initiate under mode-I condition at the curved region by exceeding the interfacial normal strength of $T_{o,I} = 40$ MPa (Table 11). On the other hand, propagation is expected to occur along the arms in mode-II. However, assessments about the fracture modes based on initial stress distribution may not provide real modes since stress states would change during the crack growth. The final view of the delaminated specimen obtained by the simulations is shown in Figure 121b where the opening, shear and longitudinal stress distributions are plotted. It is seen that the delamination crack lies along the 5th interface which is the closest interface to 42% of the thickness at the point of maximum opening stress (Figure 121a-left). The left (L) and right (R) crack tips of the delamination is stopped close to the boundary conditions. The final picture is very similar to the experimental specimen as shown in Figure 114a where the cracks were stopped near the clamps. Unfortunately, small delaminations in the other interfaces of the curved region observed during the experiments are not predicted by the simulations. Besides, there are minor delaminations initiated near the boundary conditions subsequent to the delamination at the 5th interface. These cracks are not discussed because they are small and could be numerical artifacts since they are located near the boundary conditions. Figure 121b-left shows that the normal stresses localize at the curved regions of each delaminated part, resembling the same distribution observed in Figure 121a-left. However, the level of the opening stresses is not adequate to initiate a new crack at the delaminated arms. On the other hand, shear concentration regions are observed in motion while the specimen is under

harmonic vibrations that were initiated by the delamination (Figure 121b-middle). The longitudinal stresses indicate that the delaminated parts are under bending (Figure 121b-right).

Up to now, numerical results that can be obtained using conventional numerical and experimental methods are presented. The progress of the delamination process taking place between Figure 121a and Figure 121b is the critical part which needs non-conventional analysis techniques that is the focus of this study. Contours of radial normal stresses just prior to initiation at t = 19400 μs (t = 19.4 ms) and beginning of the initiation at $t_{in,BL}$ = 19406 μs are shown in Figure 122a and Figure 122b, respectively. Notably, Figure 122a is nothing but a zoomed view of the curved region given in Figure 121a-left. The total angle of the curved region becomes 84° due to the deformation of the specimen. The maximum opening stress of 40 MPa is attained at the angle of 13° counterclockwise from the centerline of the curvature, equal to an arc-length of 2.6 mm (Figure 122a). After 6 μs, initiation of a delamination becomes apparent as local decreases in the normal stress contours as shown in Figure 122b where one cohesive element is totally failed with d = 1. Hence, $t_{in,BL}$ = 19406 μs is assumed as the reference time of initiation for BL CZM. The time of occurrence is generally calculated with respect to the time of initiation, $t_{in,BL}$, using the following notation; Δt_{BL} = t - $t_{in,BL}$. The initiation can not be observed in the shear and longitudinal stress contours which are, therefore, not presented. Finally, it can be stated that the location of the initiation point predicted by BL CZM is very close to the experimental point reported as 12° counterclockwise (Figure 114b).
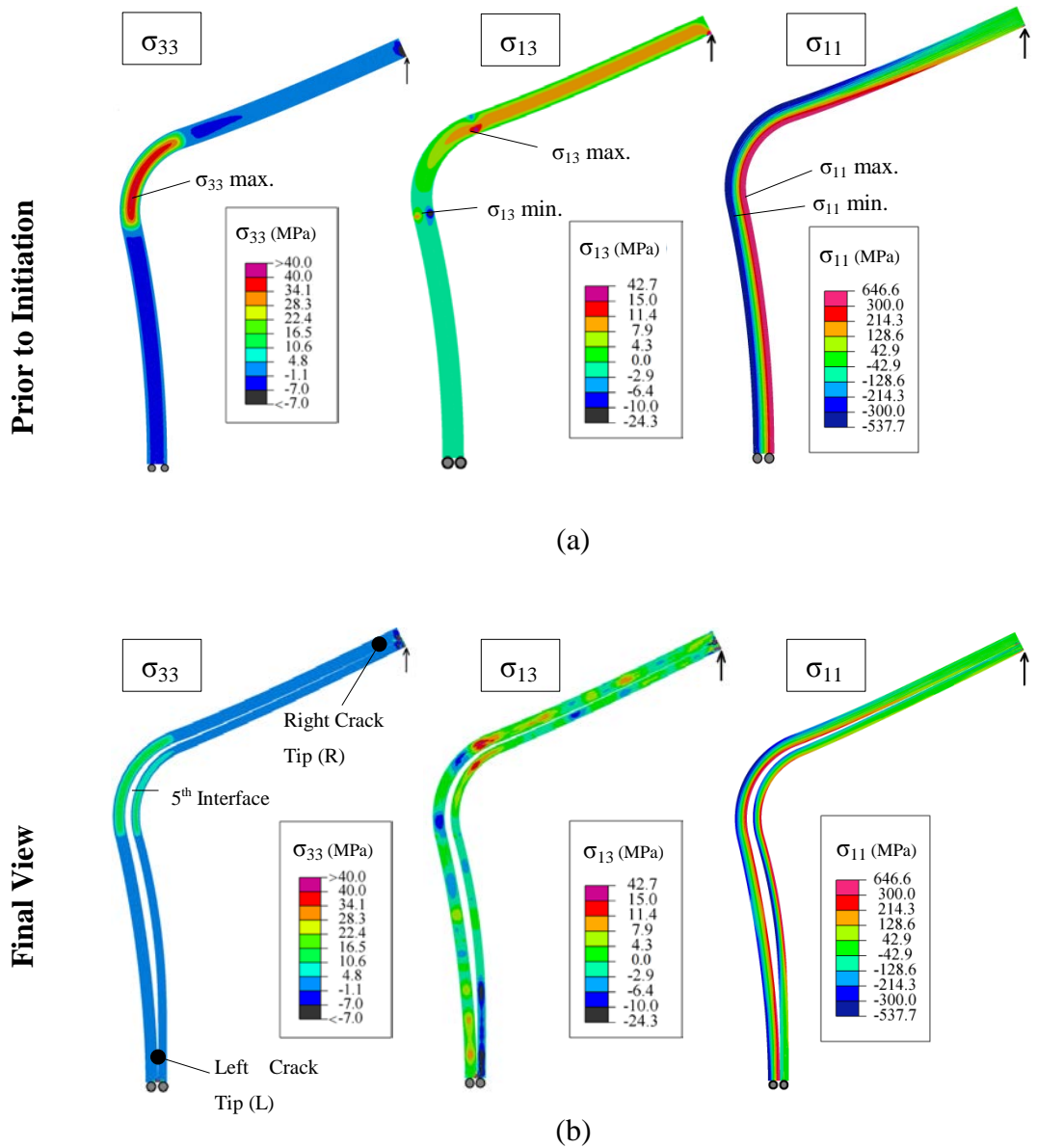
Figure 121 Contours of (a) opening radial (σ_{33}) (left), shear (σ_{13}) (middle) and fiber stress (σ_{11}) (right) prior to delamination initiation and (b) opening radial (σ_{33}) (left), shear stress (σ_{13}) (middle) and fiber stress (σ_{11}) (right) at the final view.

201
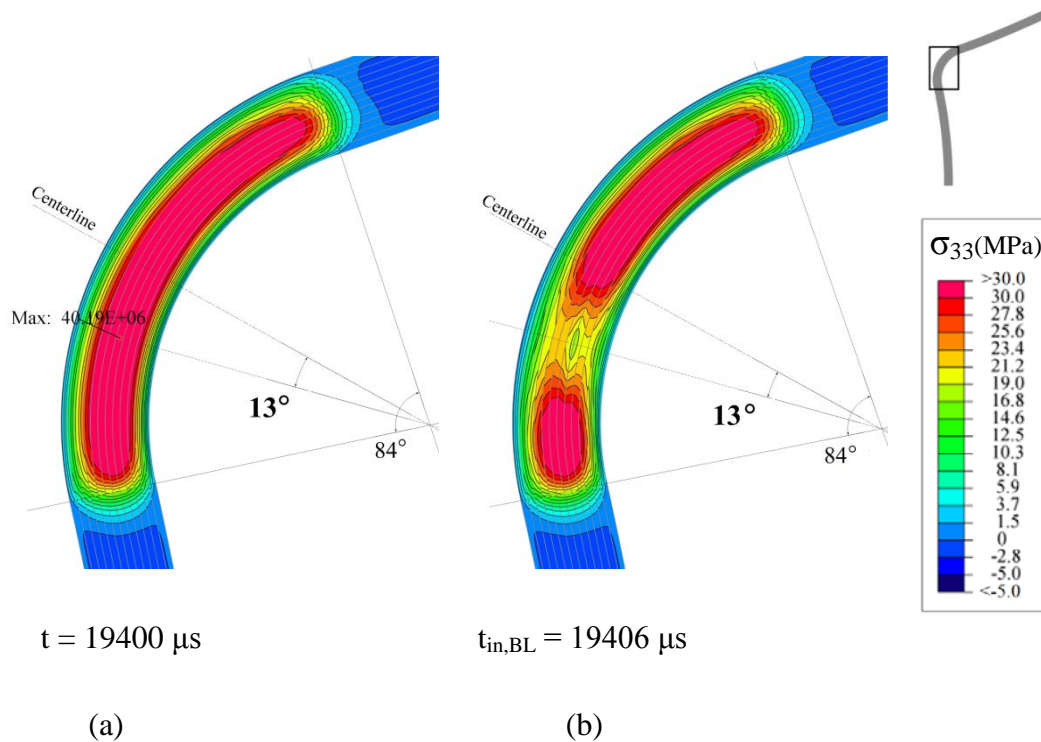
Figure 122 Contours of radial normal stresses (σ_{33}) (a) just before the initiation at t = 19400 μs and (b) during the initiation with one failed cohesive element (d = 1) at $t_{in,BL}$ = 19406 μs for the simulation with BL CZM.

Following the start of initiation, propagation of delamination can be followed from Figure 123 where the boundaries of layers (cohesive interfaces) are drawn as grey lines. The locations of left and right crack tips are labeled by "L" and "R", respectively, for $d_{1.0}$. In addition, partially damaged crack tip locations of $d_{0.6}$ are denoted by small letters; i.e. "ℓ" is for the left crack tip and "r" is for the right crack tip. Contours of constant radial normal (σ_{33}), shear (σ_{13}) and longitudinal (σ_{11}) stresses are presented in top, middle and bottom of the figure, respectively. From left to right, successive stages of delamination propagation can be followed from the stress plots given at the instants of Δt_{BL} = 0.6 μs, Δt_{BL} = 1.6 μs, Δt_{BL} = 2.6 μs, Δt_{BL} = 3.6 μs, and Δt_{BL} = 5.6 μs. In Figure 123-top, the opening radial stresses are concentrated in front of the crack tips as the crack propagates to both sides. The left crack tip just passes the vertical arm at $\Delta t_{BL} \approx 2.5$ μs, whereas the right crack tip stays inside the curved region. At Δt_{BL} = 3.6 μs, the crack tip for $d_{0.6}$ (r,ℓ) accelerates whereas the crack tip for $d_{1.0}$ (R,L) stay below the opening stress concentration. From a different interpretation, the opening stresses in front of the opening stress

202

concentration is reduced by damage segregation that is being followed by the crack tip of $d_{0.6}$ (r,ℓ). In parallel, shear stresses develop from ±15 MPa to ±30 MPa symmetrically at both crack tips. These behaviors favors that mixed-mode crack propagation is taking place at Δt_{BL} = 3.6 μs where mode-II condition gradually dominates. The segregation of the damage zone can be explained by transition from mode-I to mode-II loading zones where the length of the cohesive zone, l_{CZ}, in the mode-II is larger than the length in mode-I ($l_{CZ,I} < l_{CZ,II}$) as discussed in section 2.2.5 (Figure 101). At Δt_{BL} = 5.6 μs, the right crack tip moves to the horizontal arm and the opening stresses are sinked. As a general behavior for the curved region, delamination initiates and propagates under mode-I conditions for couple of microseconds. Afterwards, mixed-mode propagation is followed by mode-II dominated crack propagation as the crack approaches to the arms. It can be seen that the crack tip definition of $d_{1.0}$ is compliant with the opening stress concentration region and therefore provided the best crack tip definition. Figure 123-bottom reveals that the longitudinal stress distribution does not resemble zones of stress concentration at the crack tips as the crack is along the hoop direction. Instead, typical longitudinal stress distribution under bending loading is observed.
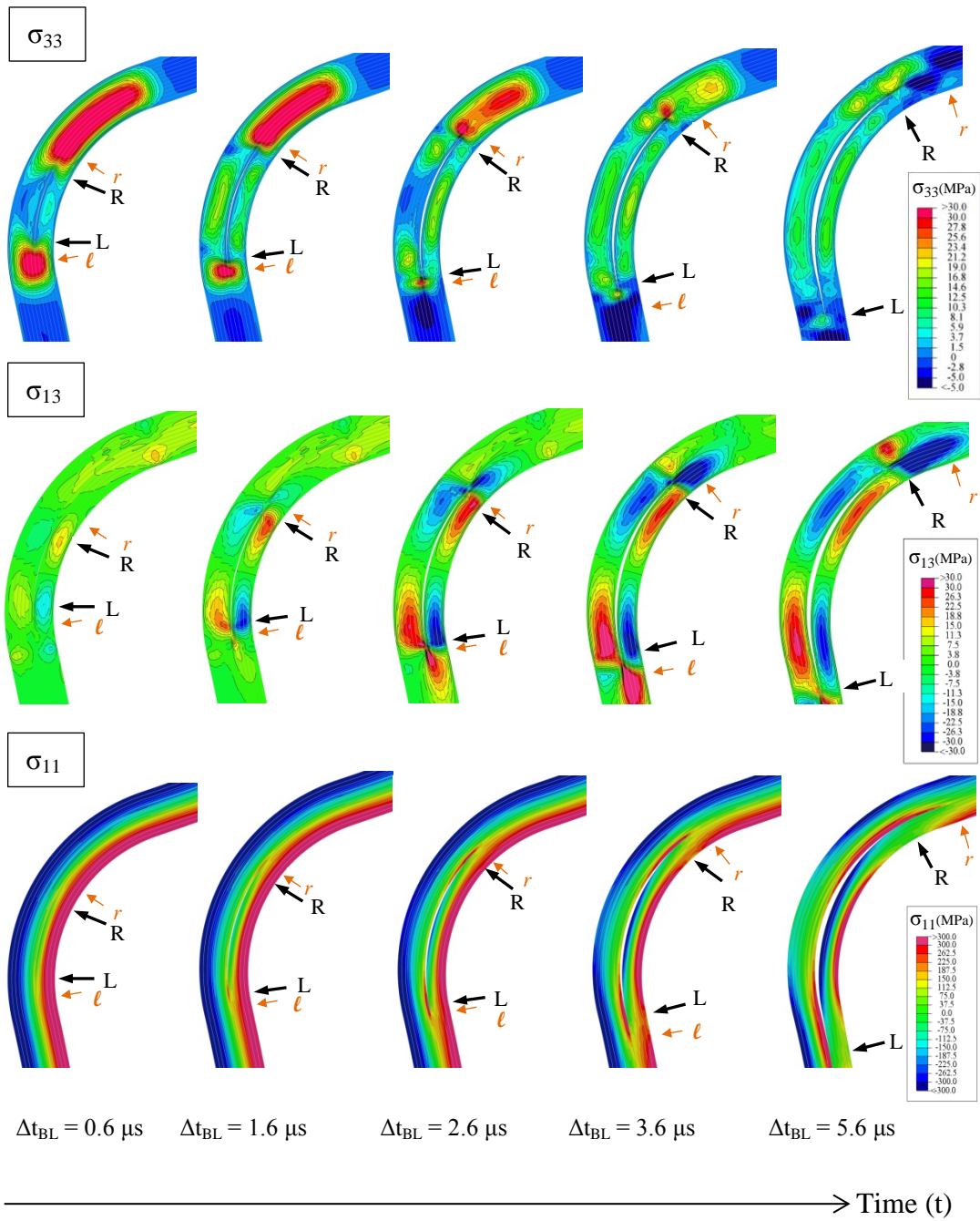
Figure 123 Contours of constant (top) opening (σ_{33}), (middle) shear (σ_{13}) and (bottom) longitudinal stresses (σ_{11}) with respect to time together with locations of fully damaged ($d_{1.0}$) and partially damaged ($d_{0.6}$) left (ℓ,L) and right (r,R) crack tips at the curved region for BL CZM (grey lines represent the interfaces).

Figure 124 shows contours of constant radial opening (top), shear (middle) and longitudinal stresses (bottom) in the horizontal arm with respect to time together with right crack tip locations (r, R). The important observation from the opening stress plots is the formation of oblique opening stress gradients, *stress waves*, at the crack tip for $d_{0.6}$. No observation of stress waves can be made from shear and longitudinal stress contours. In order to show the details of stress waves, a zoomed view of the opening stress plot at $\Delta t_{BL} = 11.6$ μs is shown in Figure 126a. The angle of the stress wave is calculated as 41° from the crack line which is almost kept the same during the propagation in the horizontal arm until $\Delta t_{BL} = 13.6$ μs. After $\Delta t_{BL} = 13.6$ μs, the angle of the stress wave approaches to 90° as it slows down and finally disappears at $\Delta t_{BL} = 15.6$ μs. The wave front is accompanied by other stress waves coming behind the crack tip of $d_{0.6}$. The number of accompanied stress waves is being developed in time which can be seen form Figure 124-top. It can be seen that shear stresses are dominated at the horizontal arm compared to the opening stresses. This suggests that the crack propagation in the horizontal arm takes place under mode-II condition. An important observation is that the crack tip of $d_{1.0}$ does not correctly represent the location of the right crack tip after $\Delta t_{BL} = 7.6$ μs. The crack tip of $d_{1.0}$ is both far away from the stress wave fronts and stress concentration regions. It seems that the crack tip definition using $d_{0.6}$ perfectly represents the location of the crack tip in the horizontal arm where mode-II crack propagation is expected.
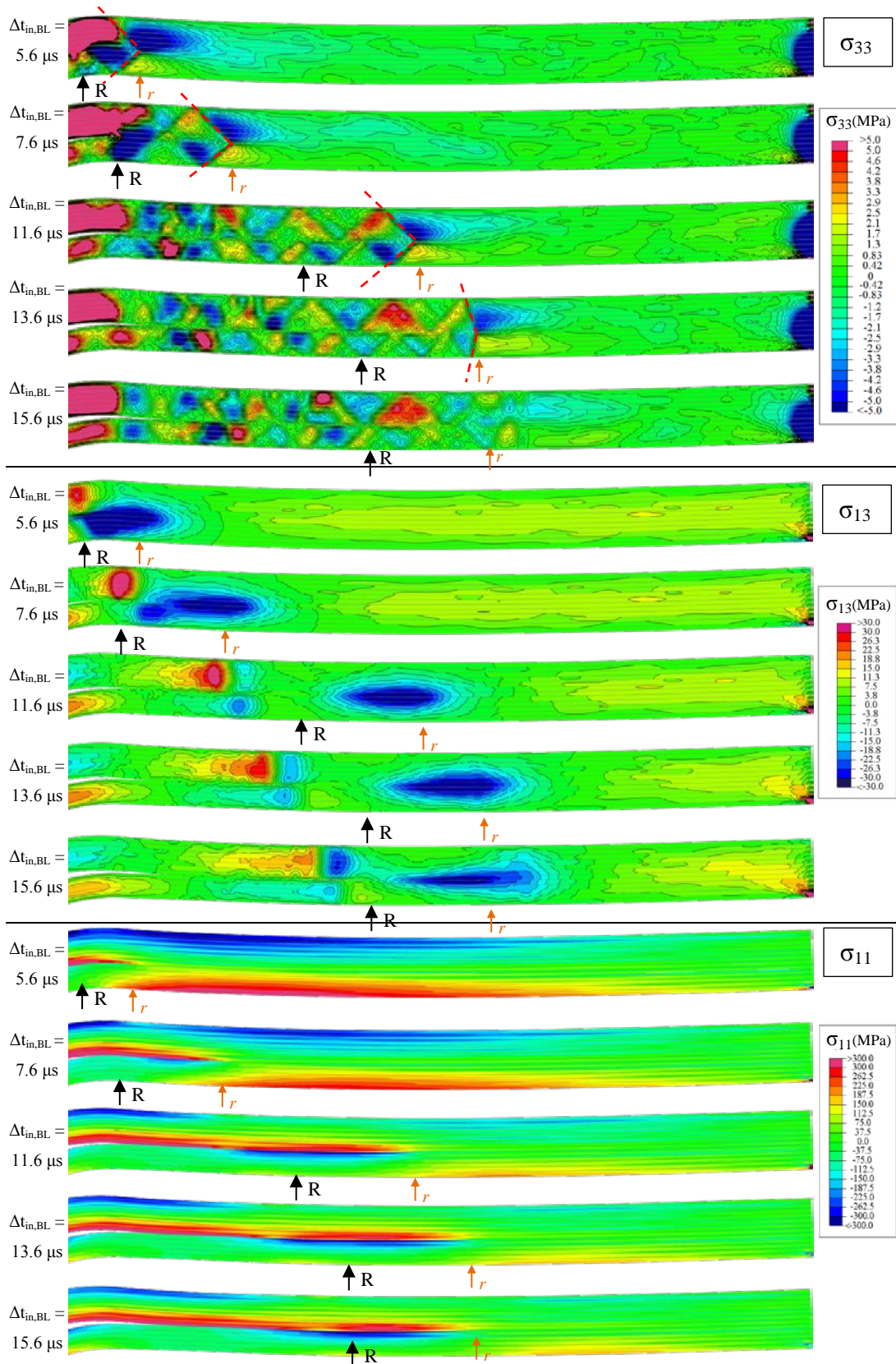
Figure 124 Contours of (top) opening, σ_{33}, (middle) shear, σ_{13}, and (bottom) longitudinal, σ_{11}, stresses at various time intervals for the horizonal arm using BL CZM (r,R $\rightarrow$ d$_{0.6}$, d$_{1.0}$ crack tips, dash lines show shear Mach wave fronts).

206

Contours of constant radial opening (σ_{33}), shear (σ_{13}) and longitudinal stresses (σ_{11}) together with the locations of left crack tips (L,ℓ) for the vertical arm are respectively shown in Figure 125. At Δt_{BL}=5.6 μs, an interesting view of the crack is shown. The left crack tip of $d_{0.6}$ is under pure mode-II condition as the compressive stresses are acting with shear stresses. On the other hand, the left crack tip of $d_{1.0}$ is located at the opening stress concentration region stressing a mode-I dominated condition. Two different definitions for the left crack tip may direct two different loading modes at the same time. Actually, the definition of the left crack tip using $d_{1.0}$ does not reflect the crack tip position after Δt_{BL}=5.6 μs. Similar to the horizontal arm, the crack propagation takes place under mode-II condition along the vertical arm from the stress plots given in Figure 125-left and Figure 125-middle. Opening stress waves trailing the crack tip and following reflecting waves are also observed in the vertical arm. In contrast to the right crack tip, the stress waves are visible throughout the propagation in Figure 125-left. Furthermore, the angle of the stress waves is continuously changing in the figures. The change of angles, which were distinguished from the stress fringes at each microsecond, are measured as 40°, 34°, 30° and 35° at Δt_{BL} = 6.6 μs, Δt_{BL} = 9.6 μs, Δ_{BL} = 12.6 μs and Δt_{BL} = 15.6 μs, respectively (Figure 126b).

Stages of development of a stress wave can be better followed from Figure 127 where the opening stress fringes and the left crack tip locations (ℓ,L) are given at Δt_{BL} = 5 μs, Δt_{BL} = 6 μs, Δt_{BL} = 8 μs, and Δt_{BL} = 9 μs for the vertical arm. At Δt_{BL} = 5, there is no sign of stress wave front where compressive stresses are acting on "ℓ" whereas tensile stresses are applied to "L". One microsecond later, a stress wave front of compressive stress becomes visible above "ℓ". At Δt_{BL} = 8 μs, a second wave is emanated from "L" while the initial wave front moves to the right. Afterwards, the second wave becomes blurry around "L" whereas the initial stress wave moves further to the right. It should be noted that exactly the same patterns are observed at the right crack tip during the given time interval. Therefore, Figure 127 is also applicable to the right crack tip. The morphology and the kinetics of the stress waves reveal signatures of *shear Mach wave* emanated from the crack tip during intersonic crack propagation. Similar to our case, Dwivedi and Espisona [122] reported formations of shear Mach waves only in the normal stress plots during

intersonic crack propagation in composite laminates. It is suggested that the first and the second opening stress waves are emanated from $d_{1.0}$ and $d_{0.6}$ definitions of the crack tips as they successively exceed the shear wave speed of the material. Stress waves will be revisited once the crack tip speed curves are presented in the following paragraphs.
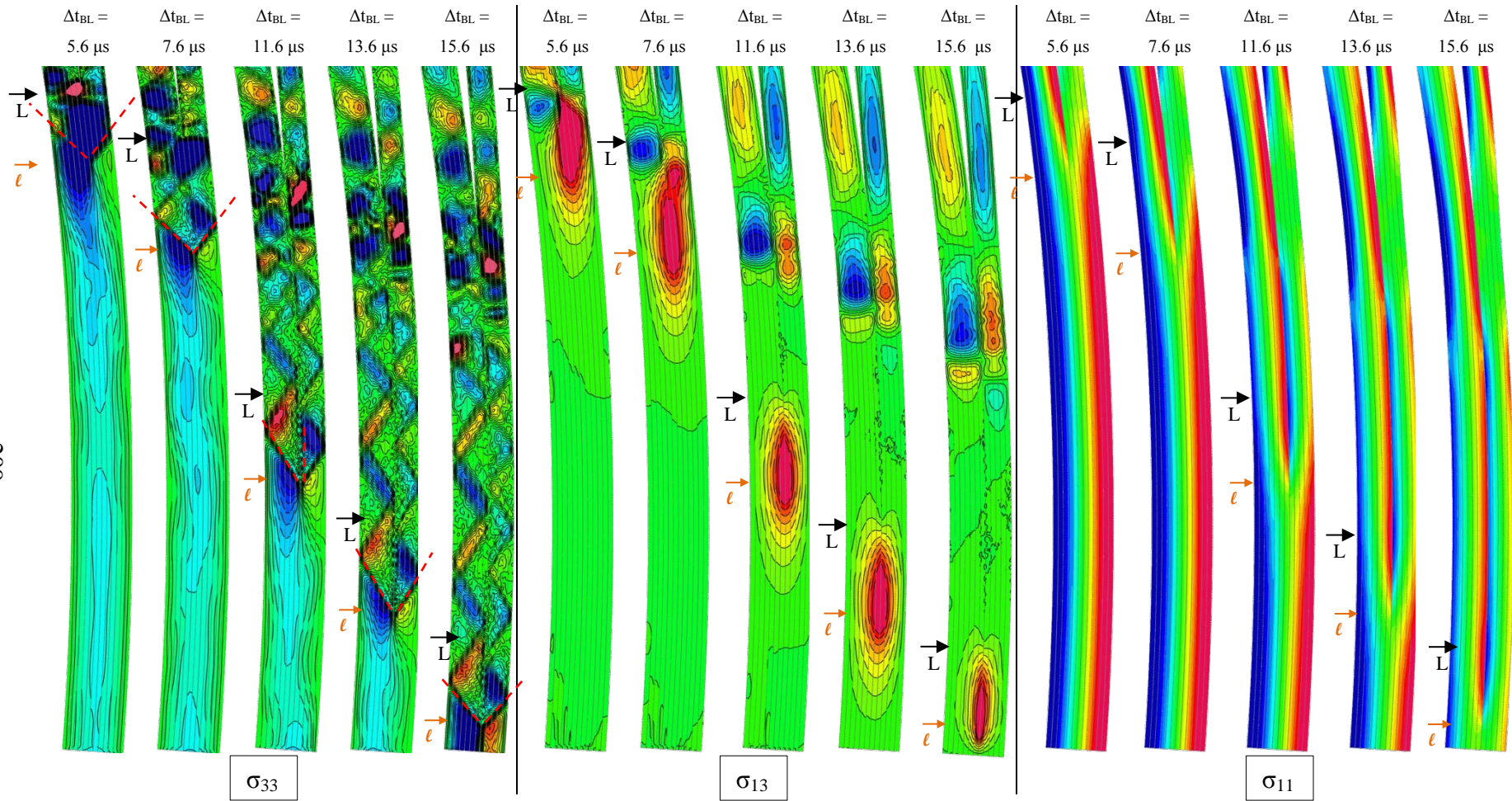
Figure 125 Contours of (top) opening, σ_{33}, (middle) shear, σ_{13}, and (bottom) longitudinal, σ_{11}, stresses at various time intervals for the vertical arm using BL CZM (ℓ,L → $d_{0.6}$, $d_{1.0}$ crack tips, dash lines show shear Mach wave fronts, stress legends are given in Figure 124).
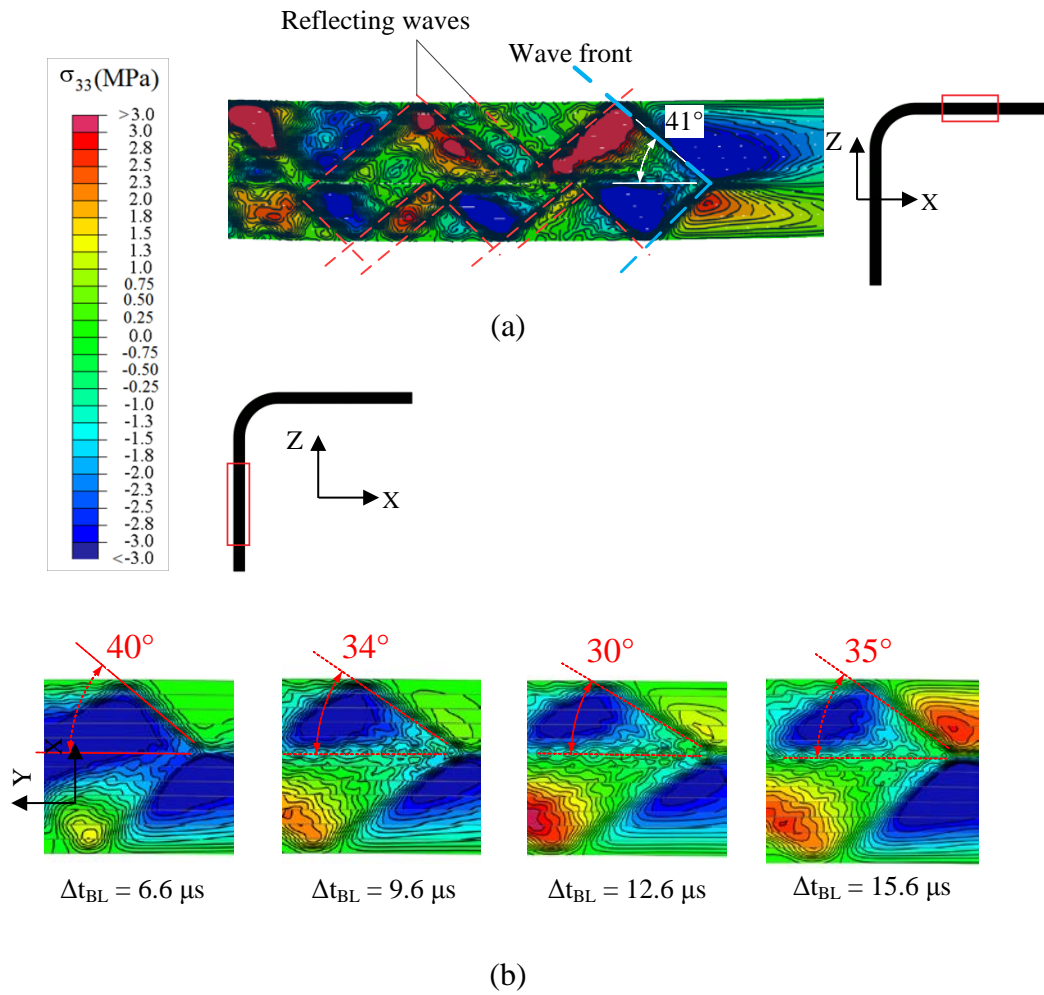
Figure 126 Zoomed views of opening stress contours showing stress wave fronts and reflecting waves for (a) right crack tip (r) in horizontal arm at $\Delta t_{BL} = 13.6$ µs and (b) left crack tip (ℓ) in vertical arm at $\Delta t_{BL} = 6.6$ µs, $\Delta t_{BL} = 9.6$ µs, $\Delta_{BL} = 12.6$ µs and $\Delta t_{BL} = 15.6$ µs.
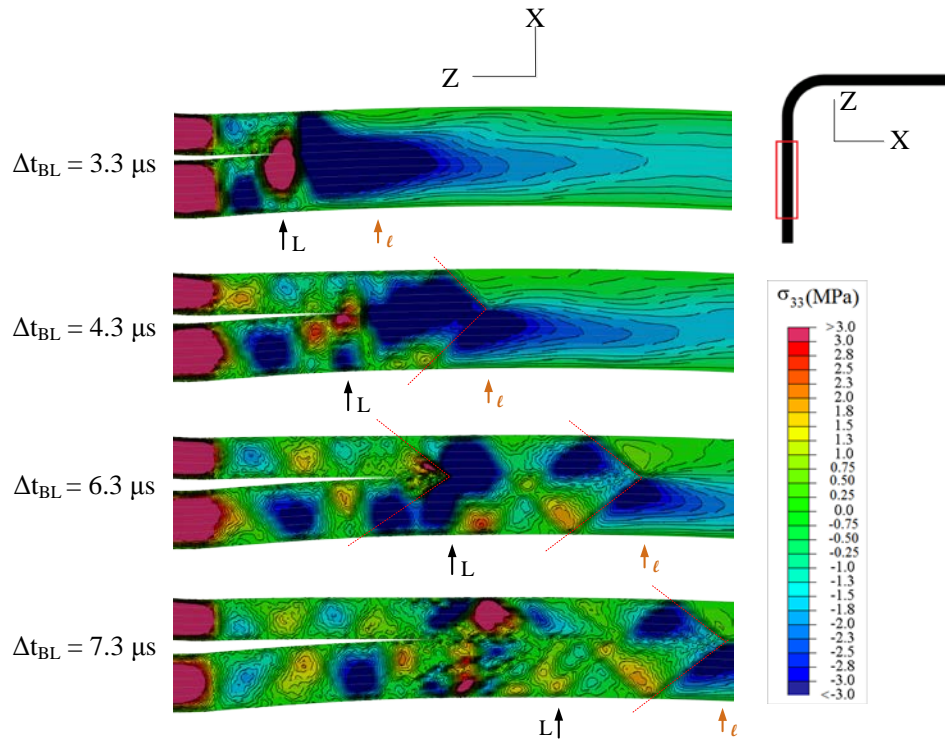
Figure 127 Development of shear Mach wave fronts during the transitioning to the intersonic delamination regime together with opening stress contours.

From the stress plots, it can be stated that fully damaged, $d_{1.0}$, definition of the crack tip represents the crack tip position for mode-I dominated delamination such as for the curved region. On the other hand, partially damaged crack tip of $d_{0.6}$ provided the best representation of the crack tips in the arms where mode-II dominated crack propagation takes place. Neither definition of the crack tips would be adequate to explain the whole process in the L-shaped composite laminate where the delamination involves both mode-I and mode-II regions. As the experimental results are referred in our analysis, the crack tips that were observed in the experiments can be also concerned for selecting one of them. Figure 128 shows experimental and numerical pictures giving an L-shaped composite specimen with similar crack lengths. The experimental crack tip is a black pixel which shows the last black-to-white contrast distinguishable to the naked eye. In other words, the end of "black zone" inside the crack region is considered as "the crack tip". Noting that, no stresses were observed in the experiments. The nearest crack tip definition to that point in the simulations would be $d_{1.0}$ since it corresponds to full separated crack surfaces. Moreover, most of the experimental data are available for the curved region where

$d_{1.0}$ works well. Hence, the crack tip definition of $d_{1.0}$ is selected for the remaining study. Noting that, the results of $d_{0.6}$ are also provided whenever needed.

<center>(a)   (b)</center>
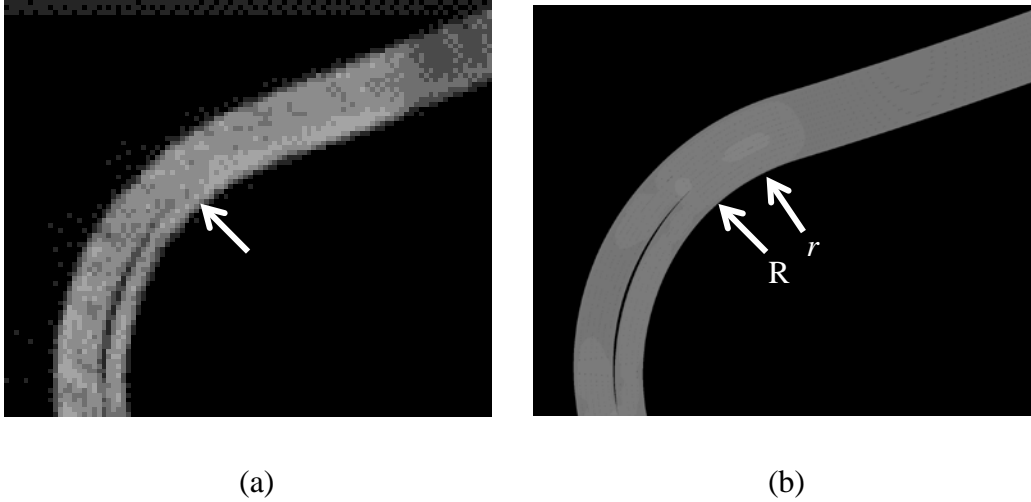
Figure 128 (a) Location of a crack tip observed during the experiments, (b) numerical model with crack tips definitions of r and R for $d_{0.6}$ and $d_{1.0}$, respectively.

Crack length versus time curves for left (L) and right (R) crack tips are shown in Figure 129 where the experimental results for the specimens of F1 and F2 are also provided. The crack lengths corresponding to end of curved regions (EoCR) for left (L) and right (R) crack tips are represented by horizontal lines in the figure. In Figure 129, the experimental results, which mostly cover the curved region, agree well with the numerical predictions. There is a *rapid propagation* regime of crack propagation, which starts from the beginning and continues until $\Delta t_{BL} \approx 18$ μs. This time of interval is covered by the previous stress plots where signatures of shear Mach waves were encountered. In the rapid propagation regime, the left and right crack tips quickly reach ~41 mm and ~27 mm, respectively. Afterwards, the crack propagation continues either discretely or slowly until the crack tips arrive near the boundary conditions. Finally, the left and right crack tip reaches 45 mm and 50 mm of crack lengths, respectively. The whole process takes around 130 μs when the tip displacement is at U = 19.4 mm and the load has been oscillated around seven times. Minor propagations at the 5th interface or initiation of small delamination at other

<center>212</center>

layers around the boundary conditions are observed at the later stages of loading that are not covered by the figure as they are not discussed. This study focuses on that rapid propagation regime which reveals signatures of intersonic crack propagation, experimentally and numerically.
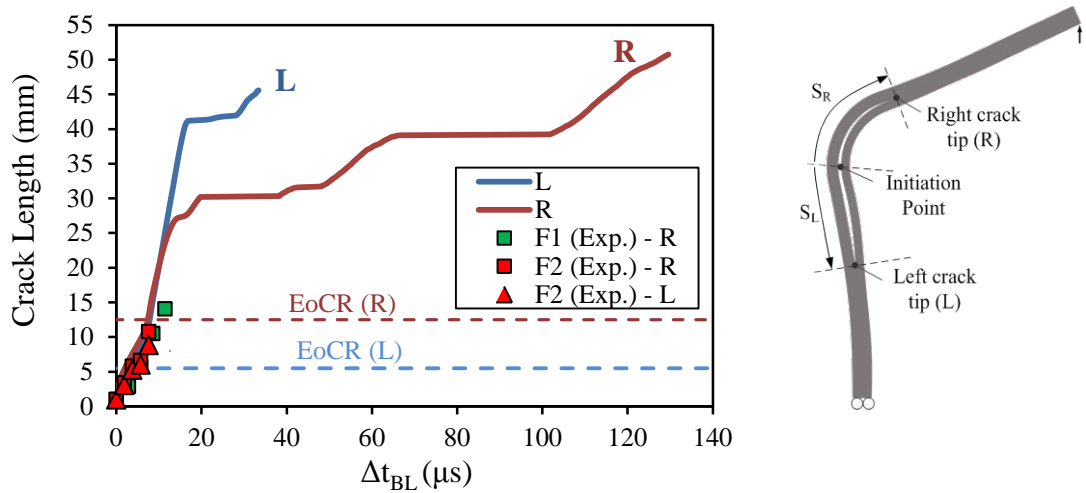
Figure 129 Crack length versus time curves for left (L) and right (R) crack tips for numerical and experimental results (EoCR: End of Curved Region).

The energy release rate for mode-I (GI) and mode-II (GII) for the left and right crack tips are respectively shown in Figure 130a and Figure 130b where the horizontal axis represents the crack tip positions, S_L and S_R. Both crack tips initiate and propagate under pure mode-I condition which stays dominant until the crack tips reach $S_R = S_L \approx 4.0$ mm. Afterwards, the fracture mode is smoothly transitioned to mode-II at $S_R = S_L \approx 12$ mm. The fracture mode can be summarized in Figure 130c in that the crack starts propagation from the curved region under mode-I condition after it smoothly transitions to mode-II through a mixed-mode propagation region. A remarkable symmetry of energy release rate curves between left and right crack tips can be observed in Figure 130 in $S_L, S_R < 27$ mm. It shows that the crack tip propagation takes place under symmetric fracture conditions during the rapid propagation regime although there is no geometrical symmetry. For $S_R > 27$ mm, the right crack tip propagates under complex mixed-mode regimes. Actually, those parts are corresponding to the secondary crack growth stages stated for Figure 129 in the previous paragraph.
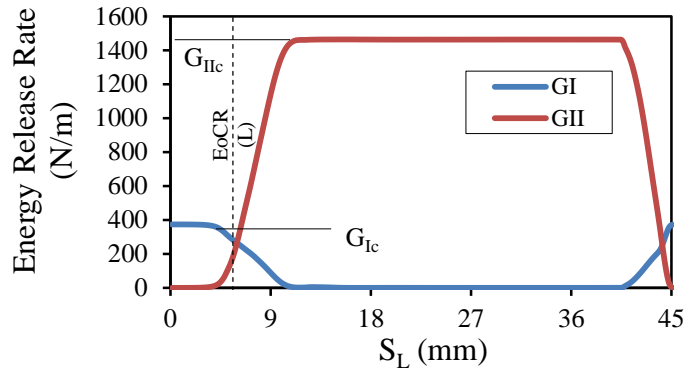
(a)
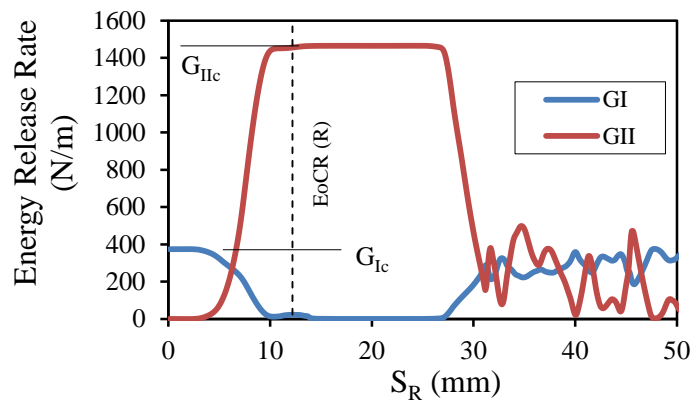
(b)
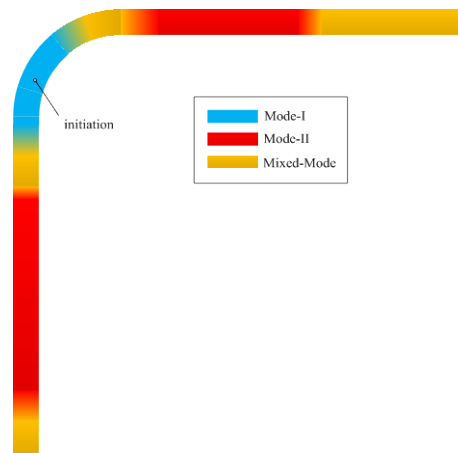
(c)

Figure 130 Energy Release rate as a function of crack tip locations (S_L, S_R) for (a) left (L) and (b) right (R) crack tips and (c) representative zoning of the specimen in terms of fracture modes. (EoCR: End of Curved Region)

Left and right crack tip speeds as a function of time obtained using BL CZM and experimental results for specimens F1 and F2 are shown in Figure 131a and Figure 131b, respectively. No speed data for right crack tip of the F2 specimen was available in the experiments. Crack tip speeds are calculated for both $d_{1.0}$ and $d_{0.6}$ definition of the crack tips. Initiation of delamination takes place asymptotically in the speed curves for $d_{1.0}$ because the initial crack almost suddenly occurs in a finite length. Noting that, $d_{0.6}$ definition of the crack tip similarly initiated asymptotically which is out of the time axis of the figure since $d_{0.6}$ initiated at Δt_{BL} = -2.75 μs. It is known that crack tip speeds cannot exceed Rayleigh wave speed under mode-I condition which is the case at the curved region during the initiation. Hence, it is assumed that the delamination initiates around 1.2 μs when the sub-Rayleigh crack propagation starts after the asymptotic regime. It should be noted that the crack initiation with cohesive elements is a polemical subject that is not focused by this study. After the initiation, $d_{1.0}$ definition of left and right crack tips propagate at sub-Rayleigh wave speeds around 1000 - 1200 m/s until $\Delta t_{BL} \approx 6.7$ μs. The crack tip for $d_{0.6}$ develops to intersonic speeds around 3.5 μs whereas $d_{1.0}$ definition of the crack tips transition from sub-Rayleigh to intersonic speeds at Δt_{BL} = 8 μs. The crack tips for $d_{1.0}$ and $d_{0.6}$ sustainably propagate at intersonic speeds of 3500 m/s and 2500 m/s, respectively. In general, left and right crack tips exhibit nearly the same kinetic behavior until reaching the maximum speeds. Afterwards, the left crack tip tends to continue at intersonic speeds whereas right crack tip gradually slows down to sub-Rayleigh wave speeds. Specifically, $d_{0.6}$ definition of the crack tips generally moves slower than the $d_{1.0}$ definition of the crack tips at the intersonic regime before Δt_{BL} < 12 μs for the left and Δt_{BL} < 10 μs for the right crack tips. Afterwards, both definitions of the crack tip slow down to sub-Rayleigh wave speeds together. For the experiments, the left crack tip speed data for the F2 specimen shows that the propagation occurs at sub-Rayleigh speeds around 1250 m/s for Δt_{BL} = 4 μs. After it slows down to 420 m/s at Δt_{BL} = 5.7 μs, intersonic crack tip speed of 2200 m/s at Δt_{BL} = 7.6 μs was recorded in the experiment which is very close to the numerical curve obtained for $d_{1.0}$ definition. For the right crack tip, the speed data of F1 and F2 specimens are marked as squares and triangles, respectively, in Figure 131b. Both specimens revealed that the crack propagates at sub-Rayleigh speeds around 700 – 1200 m/s until reaching Δt_{BL} = 5.7 μs. Specimen F2 reaches very close to Rayleigh

wave speed at Δt_{BL} = 7.6 μs whereas F1 specimen shows that the crack propagation travels at an intersonic speed of 1700 m/s, just above the shear wave speed, at Δt_{BL} = 8.6 μs. Afterwards, F1 specimen slows down to sub-Rayleigh wave speed of 1250 m/s at Δt_{BL} = 11.5 μs. In general, experimental results agree with the crack tip speeds obtained for $d_{1.0}$ definition of the crack tip using BL CZM even after considering 2.8 μs of time difference between the two definitions. This supports the proposal that $d_{1.0}$ definition of the crack tip is a good approximation for the experimental crack tips that can be followed from the camera recording by naked eye. Especially, right crack tip speeds obtained experimentally agree well with the numerical results except for the speed data near t = 8 μs where BL CZM reaches to critical speed. Although the experimental speeds of F1 are not very close to the numerical results, the crack tip behavior of F1 characterized by increasing from sub-Rayleigh to intersonic speeds and then dropping down to sub-Rayleigh speed is in compliant with the numerical crack tip behavior.

It is suggested that the stress waves that were observed in the arms were actually *shear Mach waves* emanated from the crack tip since the crack tip speed curves revealed intersonic speeds. The propagation speed of crack tips for $d_{0.6}$ at intersonic regime can be calculated from the angle of the wave front, θ, using the equation of V = C_s/sin(θ) (section 2.2.3.1) where C_s = 1636 m/s (Table 11). The angle of the shear Mach wave is measured as 41° for the horizontal arm at Δt_{BL} = 5.6 μs, Δt_{BL} = 7.6 μs and Δt_{BL} = 11.7 μs (Figure 126a). The crack tip speed calculated from θ = 41° is 2494 m/s which is indicated by "X" in the Figure 131b. The crack tip speeds calculated from the wave angle sit on the right crack tip speed curve for $d_{0.6}$. For the vertical arm, the crack tip speeds can be estimated from the wave angles shown in Figure 126b as 2545 m/s, 2925 m/s, 3272 m/s, 3272 m/s and 2852 m/s at Δt_{BL} = 6.6 μs, Δt_{BL} = 9.6 μs, Δt_{BL} = 12.6 μs, Δt_{BL} = 13.6 μs and Δt_{BL} = 15.6 μs, respectively. The calculated crack tip speeds from the wave angles are in perfect agreement with the left crack tip speeds for $d_{0.6}$. These results further validate the predictions of the numerical model especially for the formation of shear Mach waves at intersonic speeds.
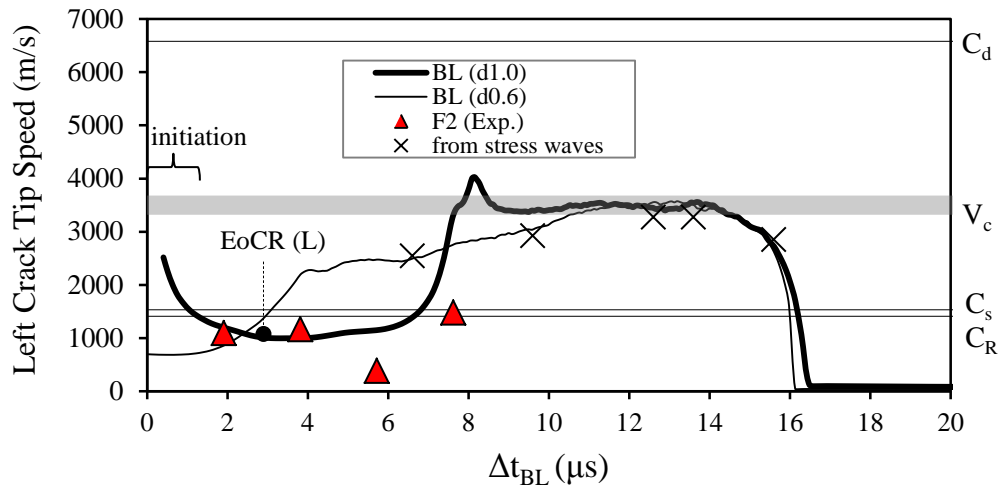
(a)
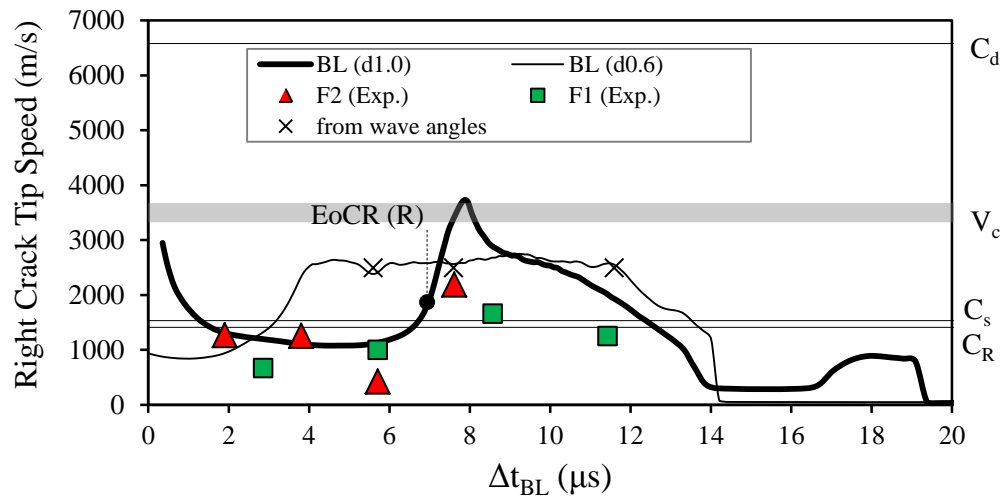
(b)

Figure 131 Crack tip speed as a function of time calculated using FEA in conjunction with BL CZM, experimental specimens for (a) left crack tip and (b) right crack tip (EoCR: End of Curved Region for $d_{1.0}$ definition of the crack tip).

Although exact correspondence between the stress waves and the crack tip speed curves cannot be made due to approximation methods used for the speed data, development of shear Mach waves can be approximately followed from Figure 131. For instance, the development of shear Mach wave emanated from the left crack tip (ℓ) shown in Figure 127 can be explained from Figure 131b. It can be seen that no shear Mach wave front can be observed at $\Delta t_{BL} = 3.3$ μs since the crack tip speeds are below sub-Rayleigh wave speed. At $\Delta t_{BL} = 4.3$ μs, the shear Mach wave is visible at the crack tip of "ℓ" when the crack tip speed is intersonic speed of 2540 m/s. At each step, the angle of the shear Mach wave is gradually decreased that is attributed to the increase of the crack tip speed for $d_{0.6}$. It should be noted that although the formation of secondary shear Mach wave emanated from the crack tip of "L" at $\Delta t_{BL} = 6.3$ μs can be explained by the corresponding intersonic speed in Figure 131b, the disappearance of the Mach wave cannot be explained from the speed curves. The formation of the secondary shear Mach wave is similar to the slip-stick friction behavior as shown in Figure 86d where the resulting formation is so called "train of pulses" [217].

Two observations can be made for the general behavior of the crack propagation using BL CZM. At first, an asymptotical intersonic initiation stage is continued by sub-Rayleigh propagation inside the curved region. Second is that the crack tips suddenly reach intersonic crack tip speeds near the arms. As discussed in section 2.2.3.2, increase of crack tip speeds can be attributed to the mode of fracture. It is recalled that the mode-II propagation tends to travel at intersonic speeds whereas mode-I crack growth is limited below the Rayleigh wave speed of the material (Figure 52a). In addition to the stress plots, phase angles, $\Psi(t)$, as a function of time is a better tool to analyze the mode-mixity which are shown in Figure 132a and Figure 132b, respectively. It can be seen that both phase angle figures start from the zero and stay $\Psi < 10°$ which suggests that the initiation takes place under pure mode-I condition that is maintained for about 3.5 μs. This result is in compliant with the crack tip speeds which are below Rayleigh wave speed during the first couple of microseconds after the initiation stage. Afterwards, the phase angles gradually converge to ninety degree meaning that the propagation takes place under mixed-

mode condition during the transition. After $\Delta t_{BL} > 8$ μs, the propagation continues under almost pure mode-II condition. Comparison of Figure 131 and Figure 132 suggests that both crack tips propagate in sub-Rayleigh wave speed for $\Psi < 80°$ after when it speeds up to intersonic speeds ($\Psi > 80°$). Namely, the transition from sub-Rayleigh to intersonic speeds is in parallel with the mode transition from mode-I to mode-II. However, the phase angles cannot explain the decrease in the right crack tip speed between 8 μs $< \Delta t_{BL} < 14$ μs in Figure 131b as the phase angle of $\Psi \approx 90°$ directs a mode-II crack propagation. The reduction in the speeds can be attributed to the depletion of the available energy for fracture. Interestingly, the similarity between the phase angles of left and right crack tips are dramatically the same for $\Delta t_{BL} < 16$ μs. The symmetry in the kinetics of the crack growth conflicts with asymmetry in the initial stress distributions as shown in Figure 121a. It is suggested that the symmetry in the kinetics of the propagation can be explained that the crack propagation is driven by the release of strain energy stored by the quasi-static loading not by the external stresses.

(a)

(b)
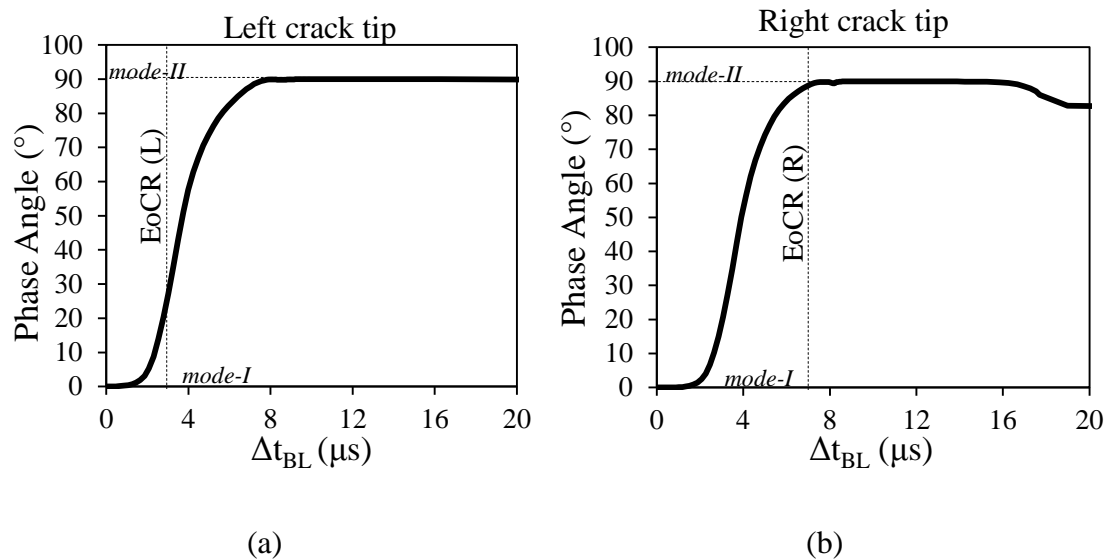
Figure 132 Phase Angle, Ψ, as a function of time for (a) left and (b) right crack tips (EoCR: End of curved region).

The energy balance in the specimen as a function of time is shown in Figure 133a after t = 10 ms where total work done, strain, fracture and kinetic energies are

219

presented. In addition, there are *artifical strain* and *viscous dissipation energies* because of using slight hourglass control and quadratic damping in the bulk elements (CPE4R) [69]. These artificial phenomena are inherently involved by ABAQUS/Explicit as a default property [69]. In this study, the total fraction of the artificial energies never exceeds 5% of the total work which is suggested by the ABAQUS [69]. In Figure 133a, the external work done has been totally transformed into strain energy before the load is gradually increased to the failure load. When strain energy and external work reach 6.7 J at t = 19.4 ms, the strain energy suddenly drops down to 2.6J whereas external energy does not change. In parallel, fracture energy rapidly jumps to 2.6 J and the kinetic energy develops to 1.5J at the rapid propagation region. This behavior dictates that the strain energy is transformed not only to fracture energy but also to kinetic energy at the rapid propagation region (Figure 133a). Development of kinetic and the fracture energies as a result of increase of specimen compliance while decreasing the strain energy can be explained by eqn. (45). The remarkable point is that kinetic energy reaches considerably high values under quasi-static loading and it is only initiated by the delamination reaching intersonic speeds. To the best of author's knowlegde, such a behavior has not been shown before for composite engineering parts. After the rapid propagation phase, strain and kinetic energies are harmonically transformed to eachother with an amplitude and frequency of ~1.6J and ~500 Hz, respectively. It means that the initial jump of the kinetic energy was an overshoot of the component disturbed the equilibrium of the specimen and eventually leading to vibrations.

The intersonic delamination takes place at the rapid propagation region where the majority of the energy transformation occurs. After the rapid transformation, there are minor increases of fracture energy as a result of small or discrete crack growths at slow speeds and other minor crack initiation regions near the boundary conditions as mentioned before. Figure 133b gives a zoomed view of the Figure 133a at the rapid transformation region. The majority of the energy transformation occurs around 20 μs. In detail, the fracture energy is dissipated slightly before $\Delta t_{BL} = 0$ since the damage starts to develop prior to the initiation that was assumed to be the instant when an element attains d = 1. A second phase of vibration is observed at the frequency of 50 kHz which is seen from the harmonic transformations of strain and kinetic energies. The high frequency vibrations can be linked to the supirious

osscilations in the load displacement curves as they have the same frequency around 50 kHz (Figure 120b). Noting that high frequency vibrations of 33.3 kHz were reported by the high speed camera recordings in the experiments. The vibrations in the simulations are very close to the expermental results. The vibrations were damped after several cycles in the experiments.
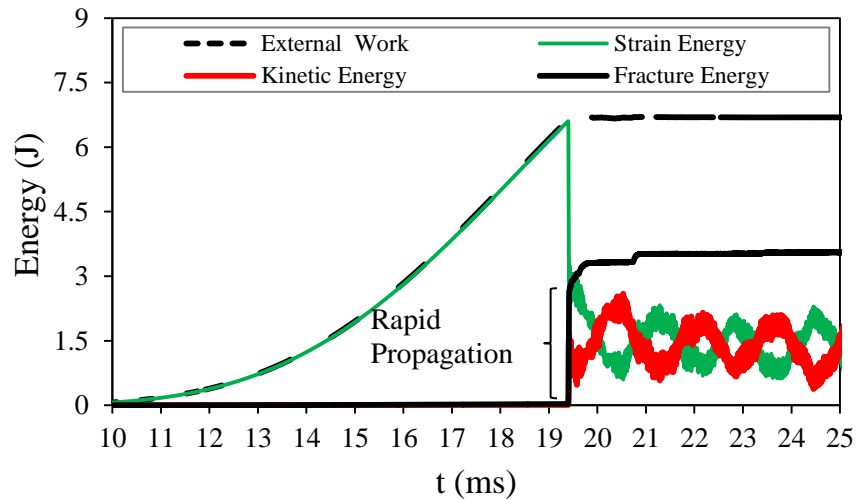
(a)
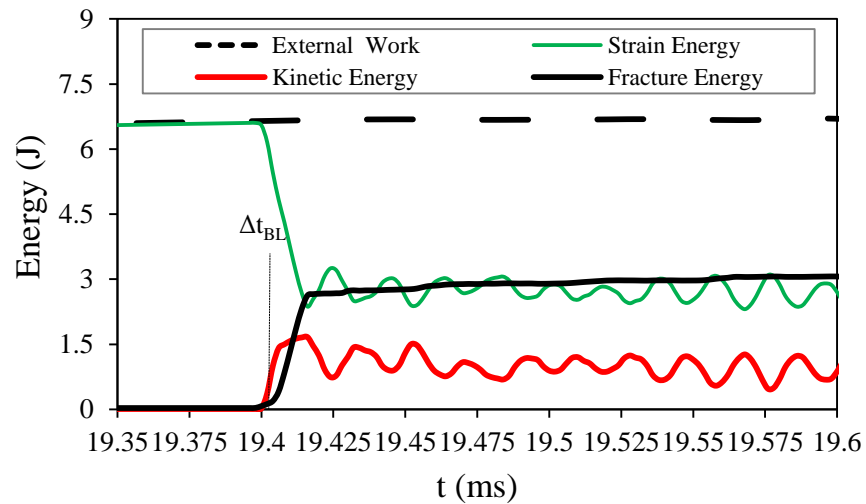
(b)

Figure 133 (a) Energy balance (external work done, strain, and kinetic and fracture energies) for BL CZM after t = 10 ms and (b) energy balance focused on the rapid transformation region as a function of time.
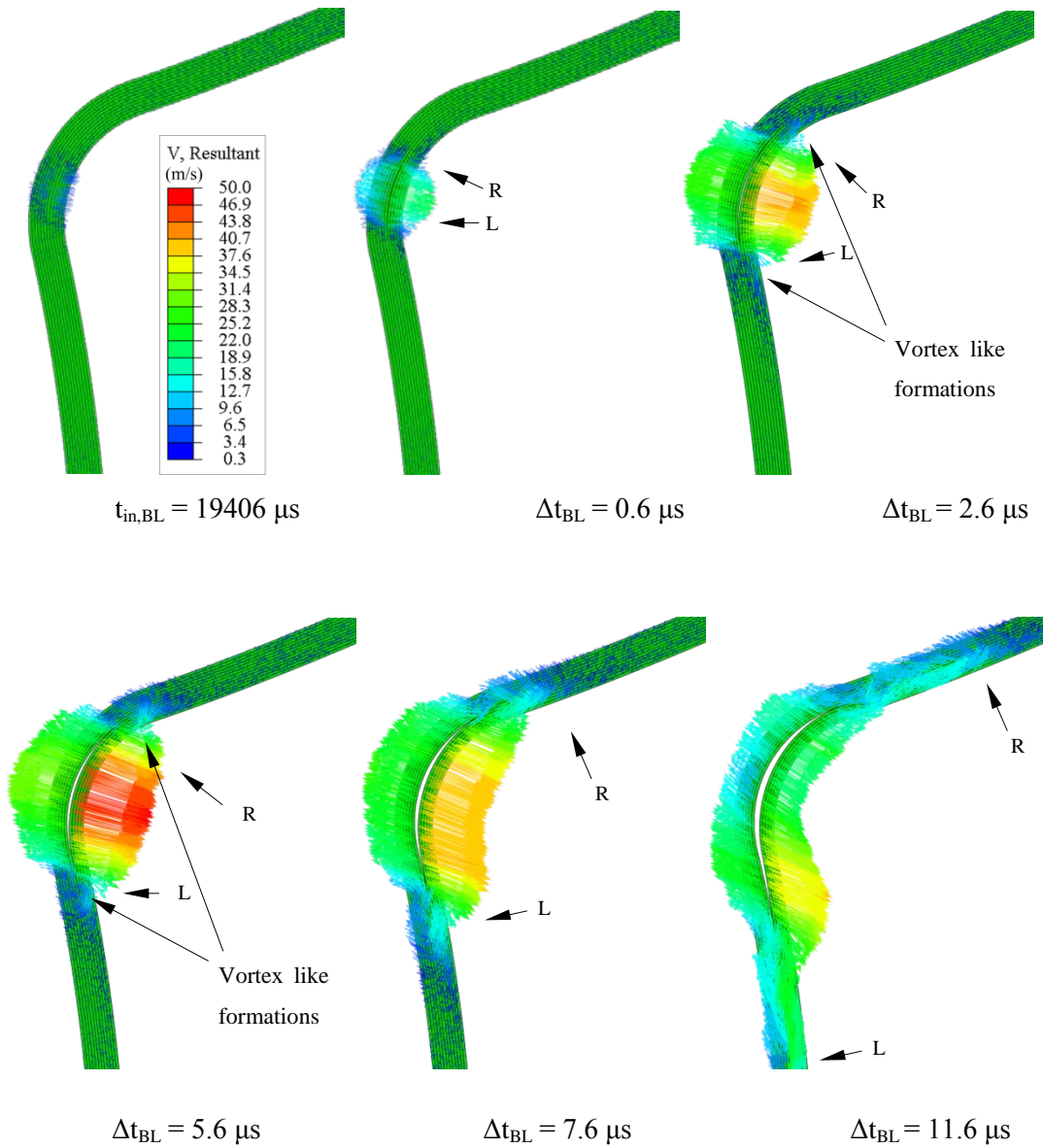
Figure 134 Vector plots of resultant velocity during initiation ($t_{in,BL}$ = 19406 µs) and stages of propagation at Δt_{BL} = 0.6 µs, Δt_{BL} = 2.6 µs, Δt_{BL} = 5.6 µs, Δt_{BL} = 7.6 µs, and Δt_{BL} = 11.6 µs (Left and right crack tips are shown as "L" and "R", respectively).

Initiation of the delamination triggers the motion of the L-shaped composite specimen. Vector plots of resultant velocity during the initiation at $\Delta t_{BL} = 0$ and stages of propagation at $\Delta t_{BL} = 0.6$ µs, $\Delta t_{BL} = 2.6$ µs, $\Delta t_{BL} = 5.6$ µs, $\Delta t_{BL} = 7.6$ µs, and $\Delta t_{BL} = 11.6$ µs are shown in Figure 134. The adjacent parts of laminate separated from the 5th interface at the delamination site start to radially translate to the opposite sides by the initiation. At $\Delta t_{BL} = 0.6$ µs, the radial separation of the parts accelerates to ~25 m/s. The magnitude of the radial separation velocity further develops to 50 m/s at $\Delta t_{BL} = 5.6$ µs. Afterwards, the separation velocity spreads to both directions following the crack tips ("L" and "R"). Starting from $\Delta t_{BL} = 2.6$ µs, the vortex like velocity vectors appear in the vicinity of the crack tips. The velocity vectors at the arms are so complex that velocity vectors resembles a longitudinal separation indicating shear deformation and vortex like formations. The velocity field loses its symmetry when the crack reaches the half of the arms at $\Delta t_{BL} = 11.6$ µs. The velocity vectors at the arms become more significant even reaching to 20 m/s in the arm direction at $\Delta t_{BL} = 11.6$ µs.
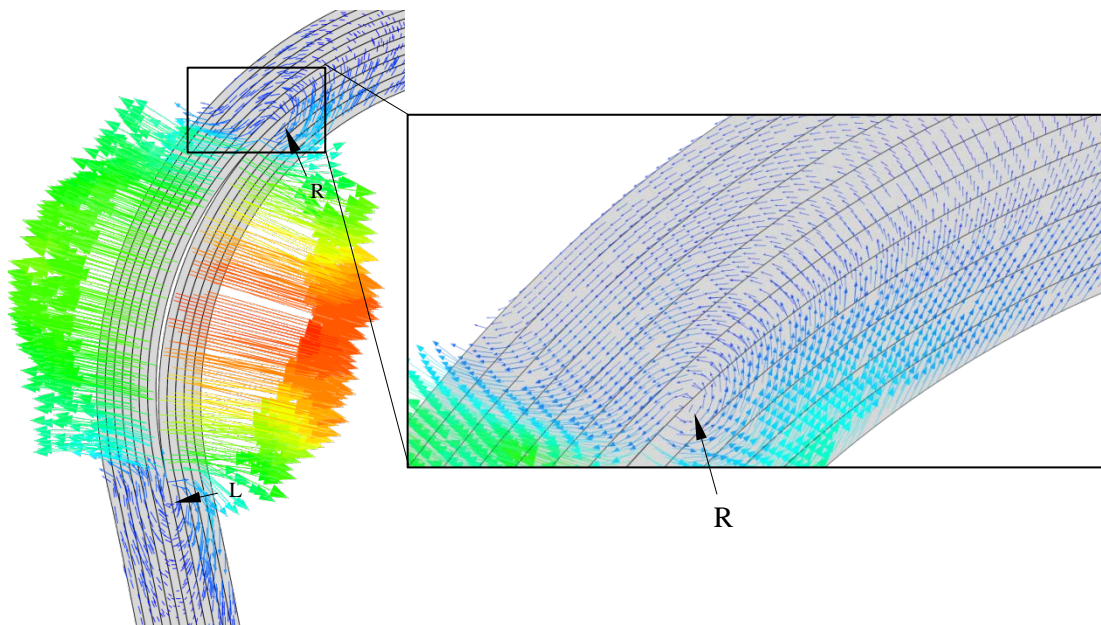
Figure 135 Particle velocity vector plot at $\Delta t_{BL} = 5.6$ µs and a zoomed view of a vortex like formation above the right crack tip (R) (Velocity legend is given in Figure 134).

Several interesting observations can be made from Figure 134. First of all, the velocity fields somehow resemble the same characteristic of mode-mixity seen in the phase angles. For instance, the mode-I dominated zone at the curved region shows opening velocities whereas separation velocities are observed at the arms where the mode-II fracture is dominated. The second remarkable observation is the formations of vortex like hot spots at the velocity plots. A zoomed view of the vortex like formations is shown in Figure 135 at $\Delta t_{BL} = 5.6$ μs. The zoomed view shown on the right side of Figure 135 presents a rather smooth velocity distribution making whirl motion during the crack propagation. Such formations are generally observed at the mixed-mode fracture regions in the vicinity of the $d_{1.0}$ definition of the crack tip.

5.3.2.3. Parametric Study

The prediction of the numerical analysis using BL CZM presented in the previous section is based on material and interface properties as well as the numerical parameters such as mesh density and number of cohesive interfaces. The material and interface properties are actually "fixed values" that are obtained from experiments. On the other hand, the numerical parameters of mesh density and the number of cohesive interfaces can be changed. The objective of this section is to investigate the effects of such numerical parameters. Load-displacement curves, fracture pattern, stress distributions and crack-tip speed curves are studied.

5.3.2.3.1. Mesh Sensitivity Study

The height of the elements is applicable to the bulk elements since the cohesive elements do not have height. On the other hand, the width of the elements is determined by the minimum number of cohesive elements used in a cohesive zone (l_{CZ}) as discussed in section 2.2.5.4 where two cohesive elements are suggested for implicit solvers. However, there is no such a solid suggestion for the explicit FEA. Initially, the simulations with the element widths of $w_e = 1000$ μm, 500 μm, 250 μm, 125 μm, and 62.5 μm are repeated. The height of the body elements is 132 μm, except for the finest mesh ($w_e = 62.5$ μm) where $h_e = 90$ μm. Figure 136 shows failure load and failure displacement normalized by the values obtained using the finest mesh model with $w_e = 62.5$ μm and $h_e = 90$ μm as a function of mesh density characterized by the number of cohesive elements per cohesive zone (l_{CZ}). The length of the cohesive zone is 1.76 mm which is calculated for mode-I. In Figure

136, both the failure loads and the failure displacements converge to unity by $w_e =$ 125 μm corresponding to 8 elements in a cohesive zone. It should be noted that severe oscillations in the load-displacement curves just after the failure point are observed no matter which of the mesh size was used.
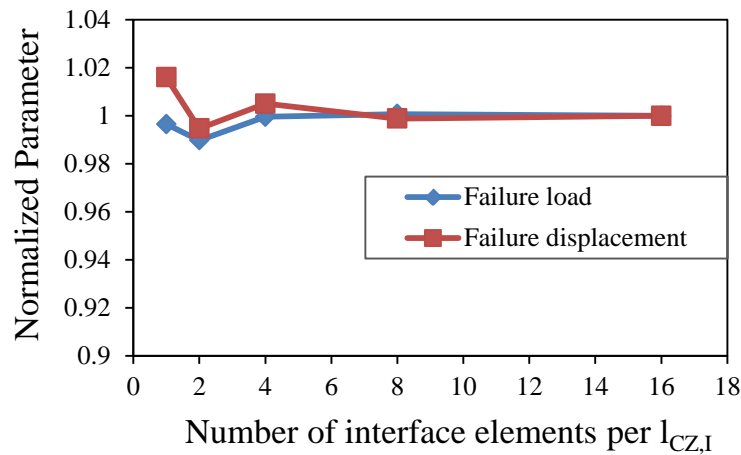
Figure 136 Normalized parameters of failure loads and failure displacements as a function of mesh density characterized by the number of cohesive elements modeled per cohesive zone ($l_{CZ,I} / w_e$) for $w_e = 1000$ μm, 500 μm, 250 μm, 125 μm , 62.5 μm and $l_{CZ,I} = 1.76$ mm.

For the above widths of the interface elements, the curves of left and right crack tip speeds for a certain interval of time (1 μs < t < 10 μs) are plotted in Figure 137a and Figure 137b, respectively. In Figure 137a, the influence of the mesh size is observed to be small for the left crack tip except for the coarsest mesh size of $w_e = 1000$ μm. The right crack tip speeds are in good agreement with each other for $w_e = 250$ μm, 125 μm and 62.5 μm (Figure 137b). However, the mesh sizes of $w_e = 1000$ μm and 500 μm diverge from the crack tip speed curve. Hence, there is no considerable difference in the crack tip speed data for $w_e \leq 250$ μm. This conclusion supports using $w_e = 125$ μm in our simulations.
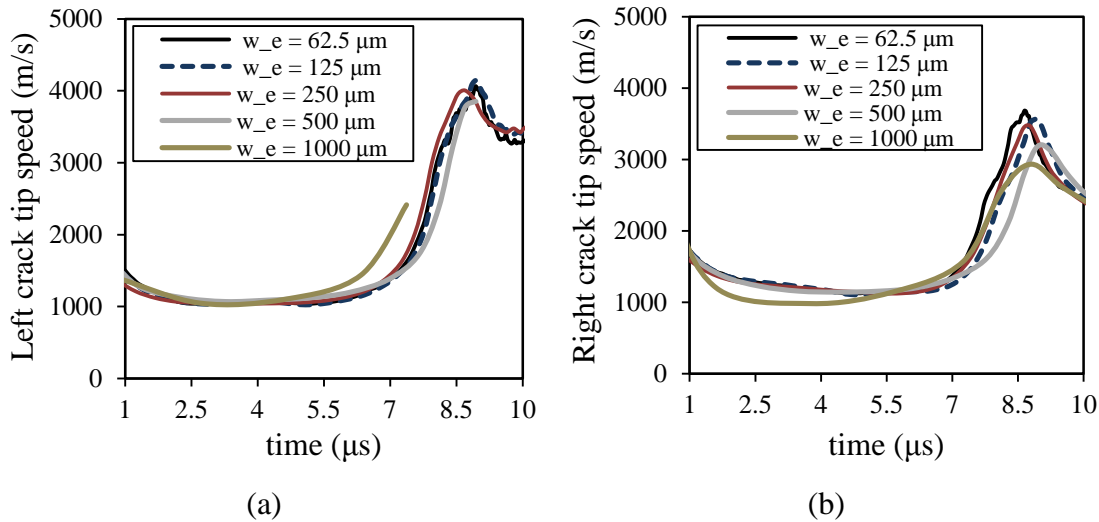
Figure 137 Crack tip speed as a function of time for (a) left and (b) right crack tips for the mesh sizes of $w_e = 1000$ μm, 500 μm, 250 μm, 125 μm and 62.5 μm.

The mesh density also affects the fracture pattern characterized by the number and locations of delaminations. In the trial simulations, the major influencing parameter is the number of elements modeled through the thickness or the height of the elements, h_e. The number of elements in the thickness direction between the each interface, N_e, is defined by $N_e = 280mm/h_e$ where 280 μm is one ply thickness (Figure 117). The models with $N_e = 1$, 2 and 3 are investigated by comparing to the finest mesh model, $w_e = 62.5$ μm with $N_e = 6$ elements (Figure 138a). The results show that the models having $N_e = 2$, 3 and 6 predict the delamination at the 5th interface as presented in 5.3.2.2. On the other hand, the model having $N_e = 1$ (Figure 138b) predicts a different fracture pattern with a new delamination at the 6th interface during the load-drop. Hence, using single element in one ply thickness wrongly predicts the fracture pattern.
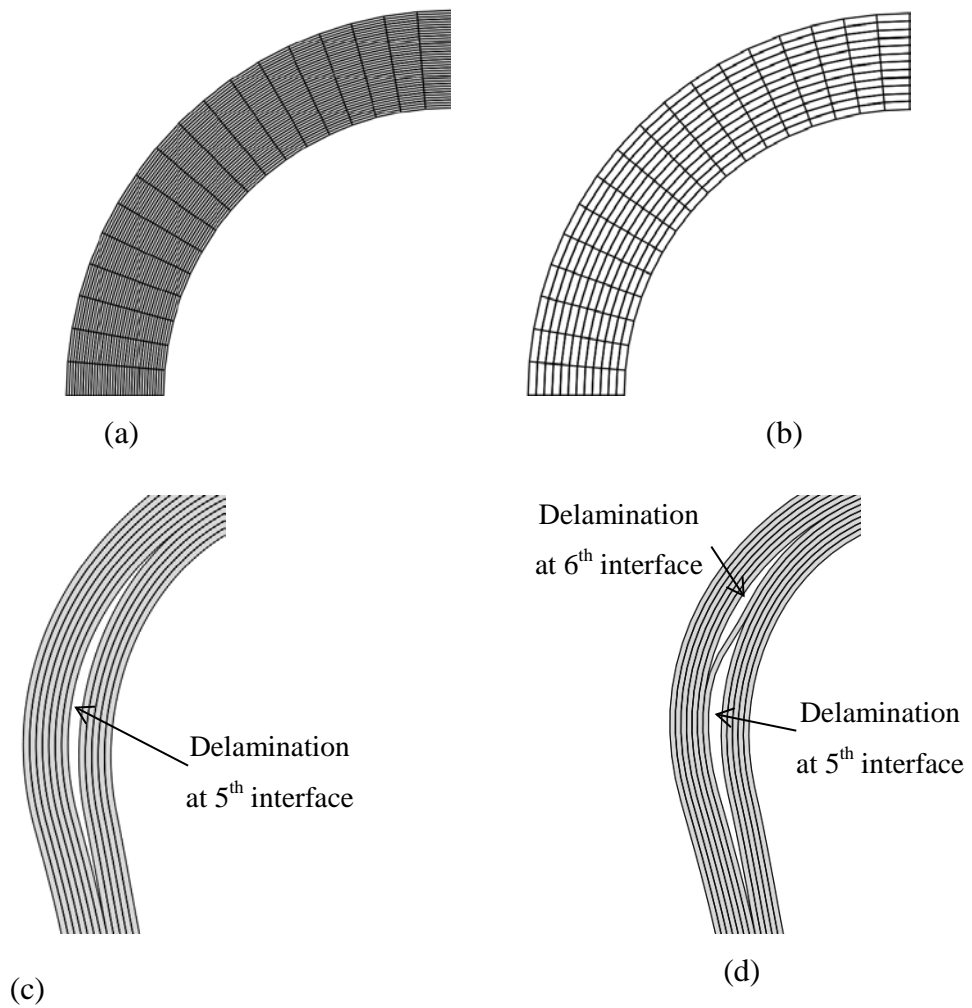
Figure 138 Curved region of the finite element modelgiven for (a) $N_e = 6$, (b) $N_e = 1$ and locations of delaminations predicted by the models having (c) $N_e = 2$, 3, 6 and (d) $N_e = 1$ elements during the load-drop (ply boundaries are shown by straight lines).

5.3.2.3.2. Number of Cohesive Interface Lines and Penalty Stiffness

Numerical modeling of a laminate composed of multiple plies can be associated with modeling all the interfaces. As mentioned in section 2.2.5.4, the compliance of the model could be artificially increased due to introduction of cohesive compliance into the system if there are too many cohesive elements in the system.
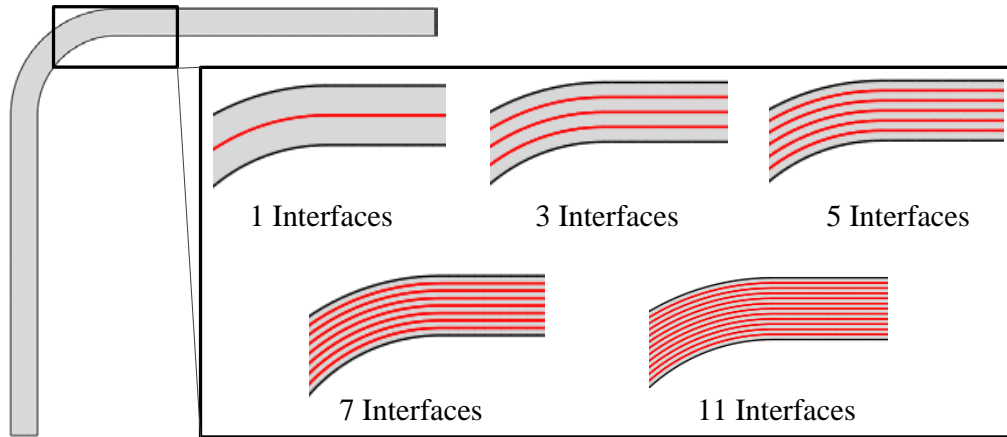
Figure 139 L-shaped composite laminate specimen with 1, 3, 5, 7 and 11 lines of cohesive interfaces shown by red lines.

Five different number of cohesive interfaces; 1, 3, 5, 7 and 11 are studied as shown in Figure 139. In the models, the cohesive lines are equally spaced through thickness. The compliance of the specimen is specified as the average of the inverse slope of the load-displacement curves up to the failure point. The change of compliance with respect to number of cohesive interfaces is shown in Figure 140a for the penalty stiffness of $4x10^{13}$ N/m^3, $2x10^{13}$ N/m^3, and $1x10^{13}$ N/m^3. It can be seen that the specimen compliance linearly increases with the number of cohesive interfaces. Moreover, the penalty stiffness strongly decreases the compliance of the specimen. The effect of the penalty stiffness is isolated for the models using 1 and 7 cohesive interfaces as shown in Figure 140b. It is important to notice that the influence of the penalty stiffness is much more dramatic. The percentage difference of the compliance is calculated with respect to the specimen compliance without cohesive interface. Figure 140c shows the percentage difference of the compliance as a function of number of cohesive interface lines. The maximum increase of the compliance is about 4% for the model with 11 cohesive interfaces having the softest penalty stiffness of $1x10^{13}$ N/m^3. On the other hand, the model using the penalty stiffness of $1x10^{14}$ N/m^3 gives only 0.55% of difference. The effect of penalty stiffness is much more pronounced as seen in Figure 140d, where any reduction in the penalty stiffness exponentially increases the compliance of the specimen. In

228

conclusion, the value of the penalty stiffness dominates the compliance effect compared to the number of cohesive lines.

The numerical analyses are repeated using the softest (compliant) penalty stiffness of $1x10^{13}$ N/m^3 corresponding to 1/10 of the original model ($1x10^{14}$ N/m^3). Figure 141a, Figure 141b and Figure 141c respectively shows the resulting load-displacement, left and right crack tip speed curves for $d_{1.0}$ definition using BL CZM with the original penalty stiffness (BL) and the compliant BL CZM (BL (Compliant)) using the softest penalty stiffness. Although the failure load is slightly increased by 10 N, the failure displacement is considerably increased by 1 mm for the compliant BL CZM (Figure 141a). Hence, the compliance of the specimen is increased by 4% for the BL (Compliant). The crack tip speed curves exhibit the same profile; however, it shifts towards the right by 0.7 μs prior to the transition region (Figure 141b-c). It means that the crack propagation in sub-Rayleigh speeds, where mode-I dominated crack propagation occurs, takes longer time by the compliant BL CZM.

Influences of using multiple cohesive interfaces are not limited to increase of compliance. Cohesive interfaces also cause discontinuities of stress contours at the interfaces. Figure 142 shows two example contour plots of opening stress (σ_{33}) obtained using a fine mesh (left) and a coarse mesh (right) in the thickness direction for a model with 11 cohesive layers. In Figure 142, there is no damage developed in the cohesive elements and no relative displacements between the interfacial nodes. The former mesh has N_e =55 elements, whereas the latter has N_e =22 elements in the thickness direction, where w_e = 250 μm for both. It can be seen that the stress contours are discrete between the interfaces for the coarse mesh model (N_e =22). On the other hand, the mesh with N_e =55 shows rather smooth stress distribution with continuous contour lines. The reason for the stress discontinuities can be attributed to the mismatch of the integration points between the cohesive and the bulk elements. The integration points of the cohesive elements are located at the nodes whereas the bulk elements, CPE4R, have a single integration point at the centroid. Using large number of elements in the thickness direction reduces the effect of the mismatch of the integration schemes as the number of data points for extrapolating the stresses is increased.
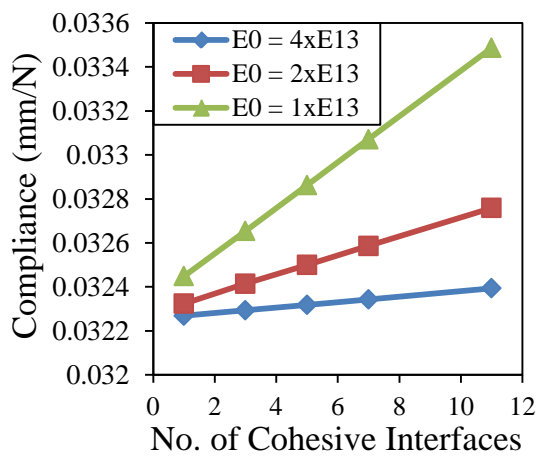
(a)
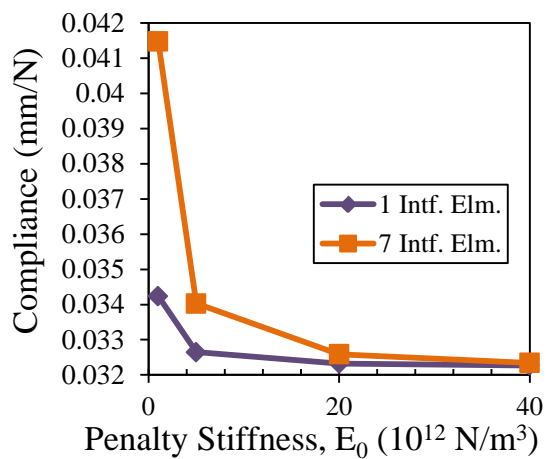
(b)
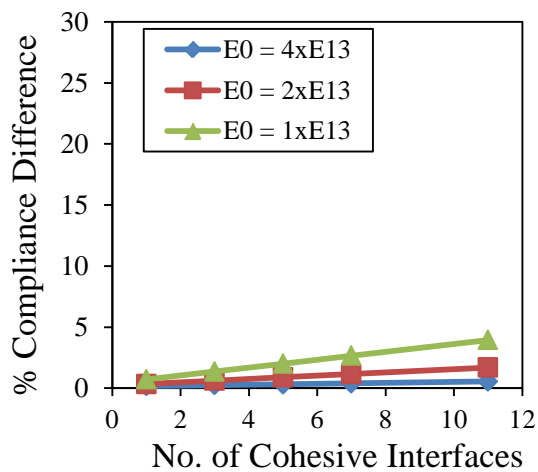
(c)
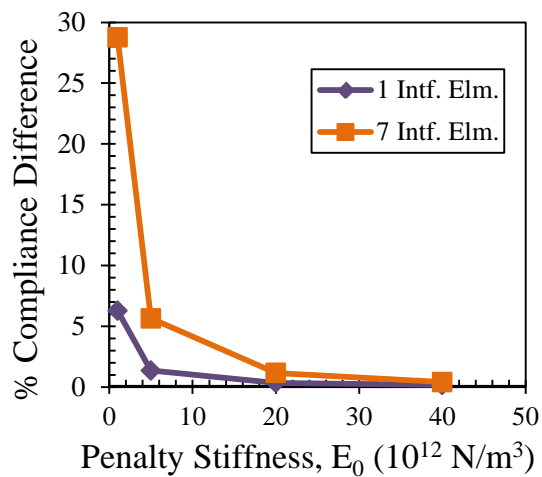
(d)

Figure 140 (a) Compliance of the specimen versus number of cohesive interfaces, (b) compliance versus penalty stiffness and difference of compliance change with respect to number of cohesive interfaces as a function of (c) number of cohesive interfaces and (d) penalty stiffness, E_0.
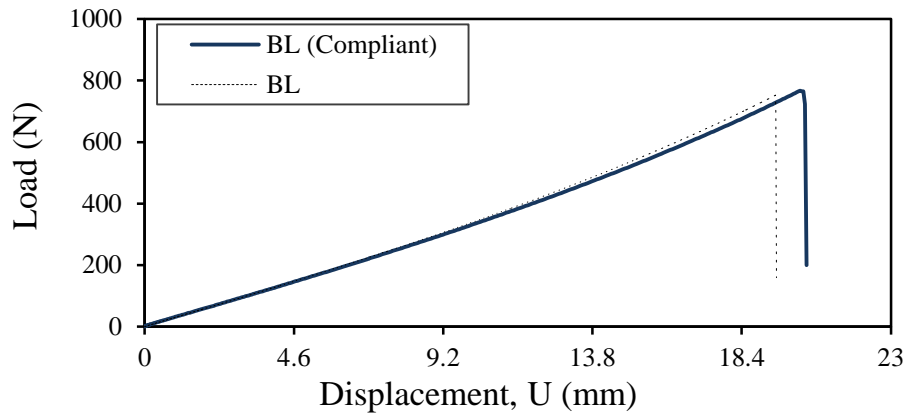
(a)
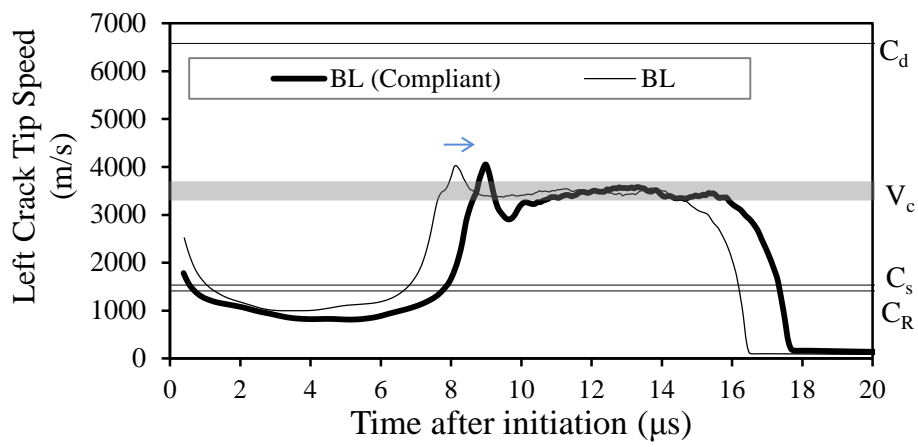
(b)
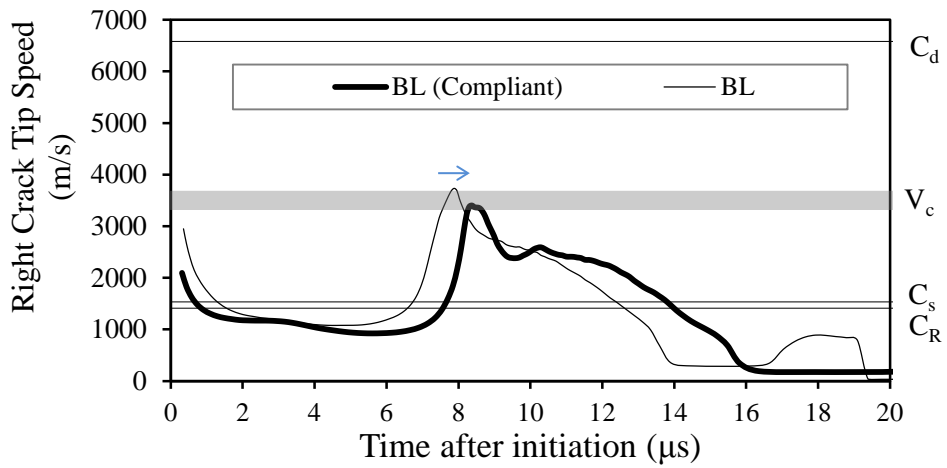
(c)

Figure 141 (a) Load-displacement curves and crack tip speeds as a function of time curves for (b) left and (c) right crack tips for the original BL CZM and the compliant BL CZM (BL (Compliant)).
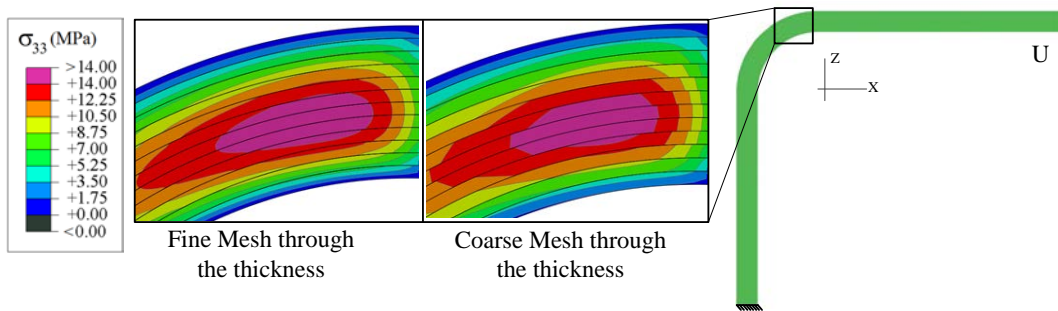
Figure 142 Contours of constant opening stresses (σ_{33}) on the curved region during the shear loading with 11 layers of interface lines (black straight lines) using fine mesh (left) and coarse mesh (right) for the thickness direction.

Slight discontinuities in the stress contours are also reported in the references [112,165,217].   For example, the stress fringes shown in Figure 86 reveal discontinuities at the stress contour lines although the mesh is extremely fine. These types of discontinuities are attributed to *early sliding of the plies* in shear deformation before any softening. The sliding of the plies can be observed from tangential relative displacement of the interface nodes.. The influence of early sliding of plies becomes much evident for multiple interface models and with compliant CZMs. Figure 143a provides the angles of Mach waves for the models with single and multiple interfaces using the original BL CZM with $E_0 = 10^{14}$ N/m^3 and multiple interface model using the compliant BL CZM with $E_0 = 10^{13}$ N/m^3 at an instant of intersonic crack propagation. The angle of the Mach waves are measured as 37° for both single and multiple interface models which are all using the high penalty stiffness of $E_0 = 10^{14}$ N/m^3. On the other hand, the angle of the Mach wave in the upper and lower delaminated parts are reduced to 28° and 30°, respectively, for the compliant BL CZM using $E_0 = 10^{13}$ N/m^3. The reduction in the wave angles is attributed to early sliding of the interfaces for the compliant BL CZM since the crack tip speeds are nearly the same. The difference between the upper and lower delaminated arms is accounted for the number of interfaces in the delaminated parts where the former has the largest number of interfaces revealing more sliding and therefore smaller Mach wave angle. It is suggested that the sliding of plies makes a rigid body motion of the plies that results in a false view of canted stress contour

lines although the angle of stresses inside the plies are correct. Representative stress contour lines for sliding (soft CZM) and non-sliding cases (stiff CZM) together with the ply stress contour lines are shown in Figure 143b. It can be seen that although the stress contour lines inside the plies are parallel with the non-sliding model, sliding of the plies forms an artificial canted stress line forming the shear Mach wave front. This phenomenon will be revisited in section 5.3.3.1 where XN CZM exhibited similar patterns.

As mentioned in section 2.2.5.5.1, the penalty stiffness is required for implicit solvers as the first perturbation requires tangent stiffness matrix. The value of the penalty stiffness in explicit solvers should be taken as high as possible while it should not create numerical problems such as during matrix operations.
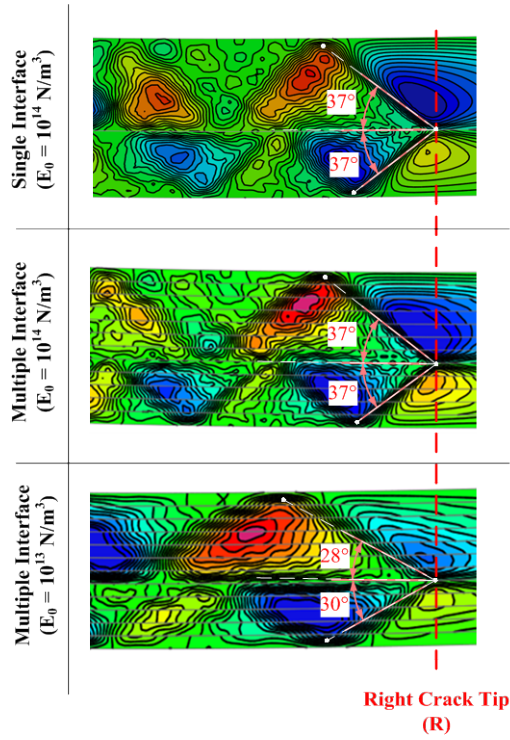
(a)
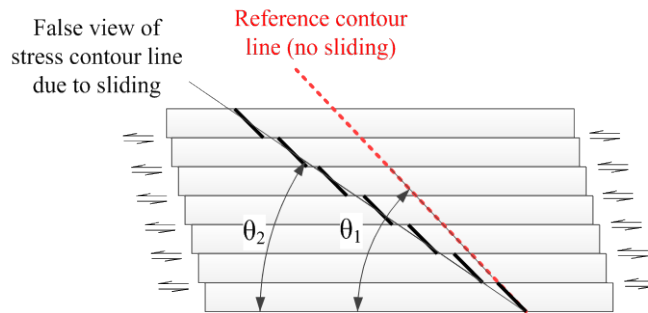
(b)

Figure 143 (a) Angles of Mach wave fronts obtained by single interface with $E_0 = 10^{14}$ N/m^3, multiple interface with $E_0 = 10^{14}$ N/m^3 and $E_0 = 10^{13}$ N/m^3 and (b) representative stress contours lines due to early sliding of plies (straight black line) together with a reference non-sliding stress contour line (red dash line).

234

5.3.3. Numerical Modeling of Intersonic Delamination using XN CZM

Two FE models for the L-shaped specimen presented in section 5.3.2 were solved using XN CZM. The first of the models is the one shown in Figure 117a with all of the parameters are the same except for the CZM where XN CZM is used. The second L-shaped model for the XN CZM is nothing but modeling single interface at the 5th interface where all remaining parameters are the same. The reason for building a second model with single interface is to minimize the effect of using large number of cohesive interfaces to the artificial compliance referring to the discussion in section 5.3.2.3.2. Unfortunately, XN CZM does not have an independent penalty stiffness parameter that can be increased to minimize the artificial increase of the specimen compliance. The penalty stiffness of the XN CZM using Table 11 can be approximately calculated as 1.3_x10^{13} N/m^3 using the eqn. (81) and eqn. (83). It means that the initial stiffness of XN CZM is very close to the penalty stiffness of the compliant BL CZM that exhibited early sliding of the plies in section 5.3.2.3.2. Hence, a single interface model is needed to find out possible complications. The main objective of this section is to make a comparison between XN CZM with BL CZM using the model with 11 interfaces. Hence, "XN CZM" in the following paragraphs directly corresponds to the model with 11 interfaces otherwise the single model is indicated as "XN CZM (Single Int.)" or "XN CZM with single interface". Secondly, the influences of using multiple interfaces with XN CZM are revealed wherever the differences are evident.

Traction-separation profile of XN CZM together with the BL CZM using Table 11 properties are shown in Figure 144. The onset separations for mode-I and mode-II are calculated as $\delta_{o,I} = 3.5$ μm and $\delta_{o,II} = 23.7$ μm, respectively which are greater than the onset separations of BL CZM. The location of the crack tip is calculated using $6\delta_{o,i}$ whenever mode-I and mode-II separations (i = I, II) are attained first which was also used by Xu and Needleman. As the XN CZM is an exponential function, using the separation value for zero traction as a crack tip is not convenient. Hence, the value corresponding to $d_{1.0}$ of BL CZM is assumed as $6\delta_{o,I}$ for XN CZM. No discussion is made for any other crack tip for the sake of simplicity and the reasons mentioned in section 5.3.2.2.
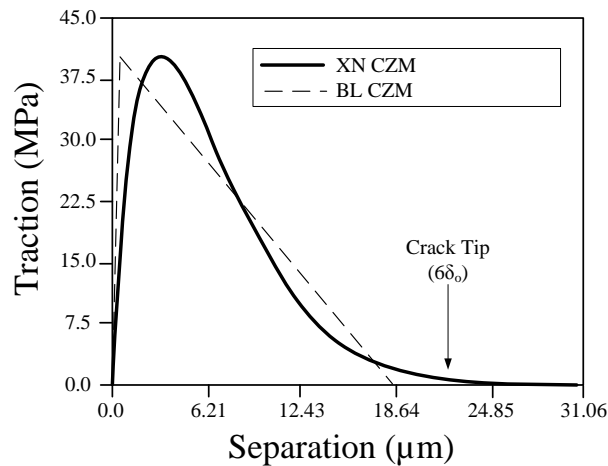
Figure 144 Traction-separation profile of XN CZM together with the BL CZM for mode-I.

5.3.3.1. Results and Discussion

The simulation using XN CZM is performed in ABAQUS/Explicit [69] with the implemented interface element via VUEL user-subroutine. The load-displacement curve of the numerical analysis using XN CZM is shown in Figure 145a together with the BL CZM and the experimental results. The failure point of the XN CZM curve is found to be 791 N with U = 20.6 mm when initiation of delamination takes place. Just after the load drop, severe oscillations are observed for the XN CZM accompanied with the propagation of delamination very similar to the BL CZM. Hence, no effect of using high order CZM is observed for reducing the oscillations or changing the load-displacement behavior. The load level at the reloading stage is calculated around 150 N using the same procedure in BL CZM for getting rid of oscillations. Although the model of XN CZM overshoots the failure load of the experiments by 5.5%, the failure is predicted very well. The vital observation is that the compliance of the XN CZM is slightly greater than the compliance of the model using BL CZM.
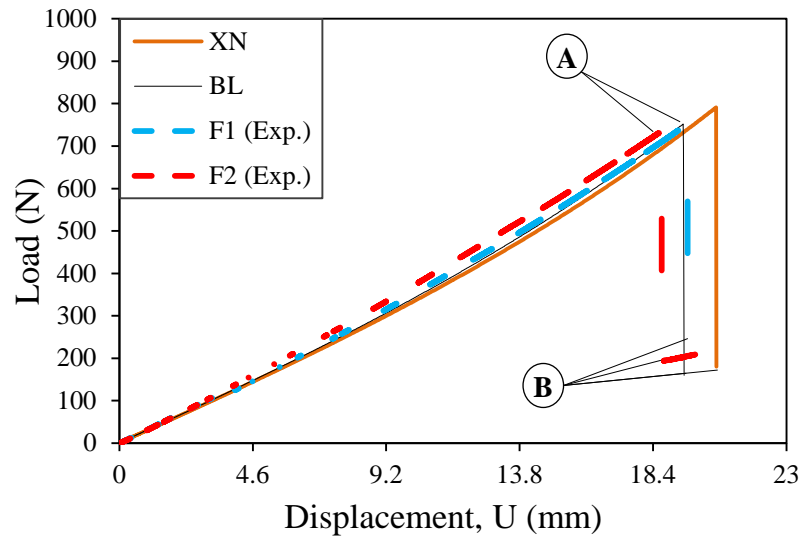
(a)
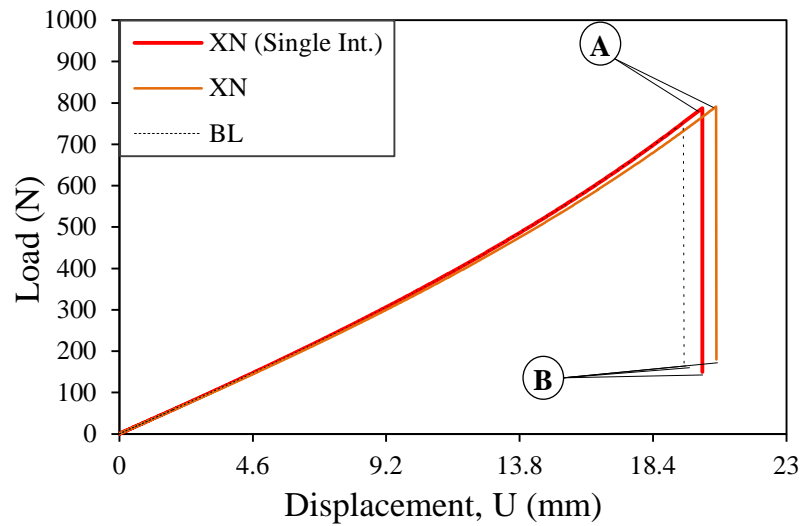
Figure 145 (a) Load-displacement curves of XN CZM, BL CZM and the experimental results and (b) with the curve obtained for single interface model (XN CZM (Single Int.)).

The load-displacement curve obtained using XN CZM with single interface (XN CZM (Single Int.)) is shown in Figure 145b together with the curves of BL CZM and XN CZM. It can be seen that the failure load of XN CZM with single interface is still the same with XN CZM albeit the displacement, U, reduces to 20.1 mm. The XN CZM has the highest compliance whereas XN CZM with single interface has the same compliance with the BL CZM. This result dictates that the effect of using large number of cohesive interfaces is more evident for the XN CZM.

The fracture pattern obtained from XN CZM is the same with BL CZM which is the delamination at the 5th interface reaching the ends of the specimen. Moreover, the stress plots given in Figure 121 are the same for the XN CZM. The fracture pattern obtained from XN CZM with single interface is also the same. However, the figures of initiation are not the same compared to Figure 122. Figure 146a and Figure 146b shows contours of radial normal stresses (σ_{33}) prior to initiation at t = 21393 μs and during the initation at $t_{in,XN}$ = 21397 μs for the model with XN CZM, respectively. During the initiation, the angle of the curved region is 83° which is slightly smaller than the angle obtained by BL CZM due to the larger crack tip displacement, U, in XN CZM. The maximum opening radial stress is attained at 23° towards the vertical arm. Interestingly, the angular location of the initiation point is 20° (Figure 146b) which is not the same location of the maximum stress (Figure 146a). Recalling that, the delamination was initiated at the point where the maximum stress had been attained for the BL CZM (Figure 122). The stress contours prior to the initiation and at the instant of initiation obtained by the XN CZM with single interface are presented in Figure 146c and Figure 146d, respectively. The time of initiation in the single interface model, t_{in,XN_1} = 20555 μs, is earlier than the XN CZM. Such a difference can be expected as the failure tip displacement of the single interface model is smaller than the XN CZM model. An interesting observation is that the angular location of the maximum stress and the initiation points are not equal to the model with 11 cohesive interfaces even though the angle of the curved region is same. Moreover, the angular locations of the initation parameters, maximum stress and initiation points, are closer to the BL CZM for the XN CZM with single interface. This suggests that the number of cohesive interfaces may also affect the location of the initiation point.

Figure 146 Contours of radial normal stresses (σ_{33}) (a) just before the initiation at t = 21393 μs of XN CZM and (b) during the initation at t = 21397 μs of XN CZM and (c) prior to initiation at t = 20550 μs of XN CZM with single interface and (d) during the initation with at t = 20555 μs of the simulation using XN CZM with single interface.
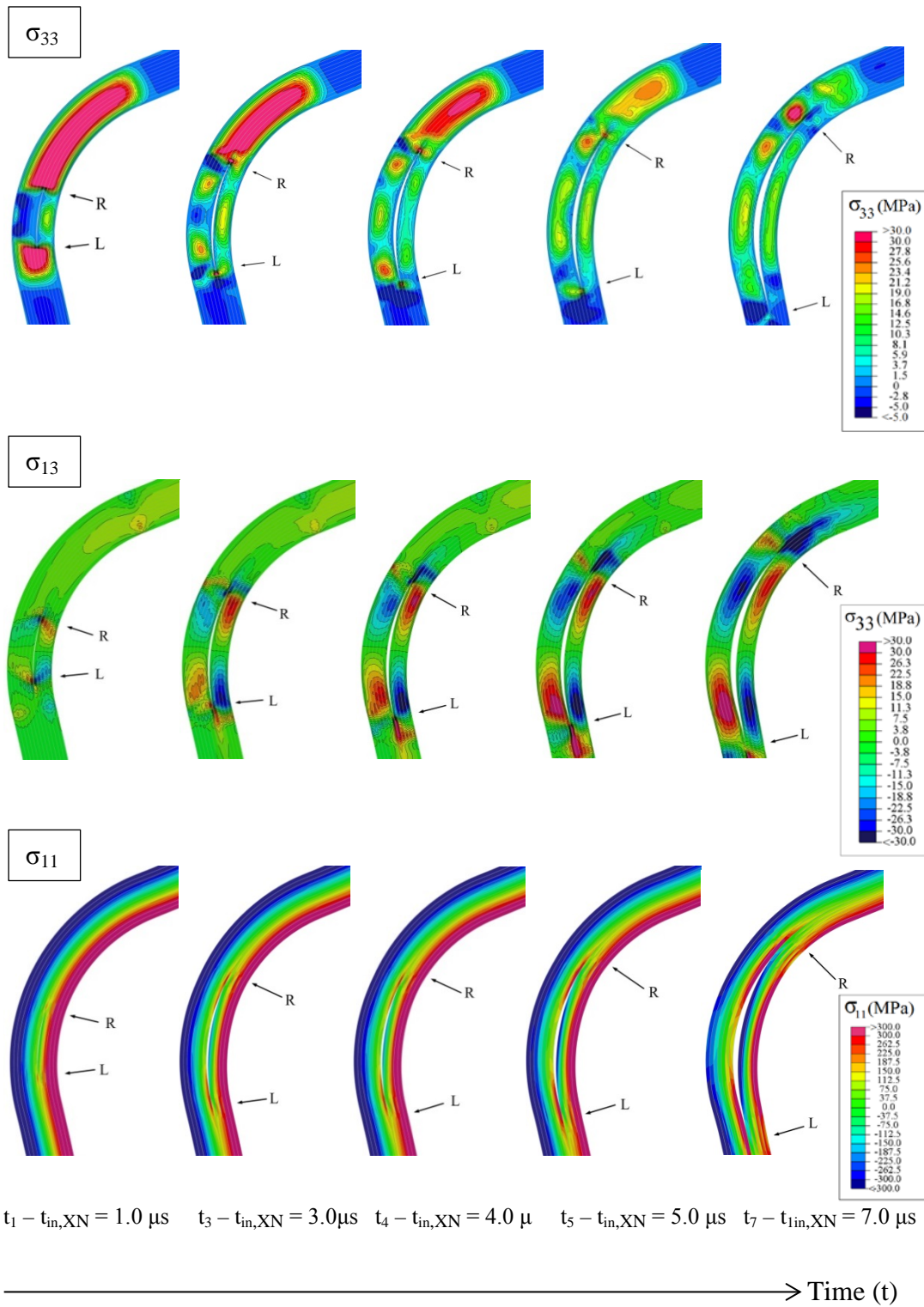
Figure 147 Contours of constant (top) opening (σ_{33}), (middle) shear (σ_{13}) and (bottom) longitudinal stresses (σ_{11}) with respect to time together with locations of fully damaged ($d_{1.0}$) and partially damaged ($d_{0.6}$) left (ℓ,L) and right (r,R) crack tips at the curved region for XN CZM (grey lines represent the interfaces).

Contours of constant radial opening (σ_{33}), shear (σ_{13}) and longitudinal stresses (σ_{11}) with respect to time together with the locations of left (L) and right (R) crack tips at the curved region for the model using XN CZM are shown in Figure 147-top, Figure 147-middle and Figure 147-bottom, respectively. From the opening stress contours, it can be seen that the opening stresses reduce as the left and right crack tips propagate towards the arms. The stress contours are very similar to the results of BL CZM shown in Figure 123. However, the stress plot reveals formations of circular stress contours at each ply. An example of shear stress distributions with circular patterns is shown in Figure 148a which is the zoomed view of the picture $\Delta t_{XN} = 3.0$ μs in Figure 147-middle. The corresponding stress plot obtained using XN CZM with single interface is also provided in Figure 148b where smoother stress distribution without any circular formations can be seen. It is sugguested that the interfaces in the XN CZM exhibit soft mechanical response that reduces strain compatability in the thickness direction. As a result, shear stresses individually develop inside the plies while weakly sustains the total stress distribution. It should be noted that similar patterns are observed for the multi-interface model for compliant BL CZM discussed in section 5.3.2.3.2.

(a)   (b)
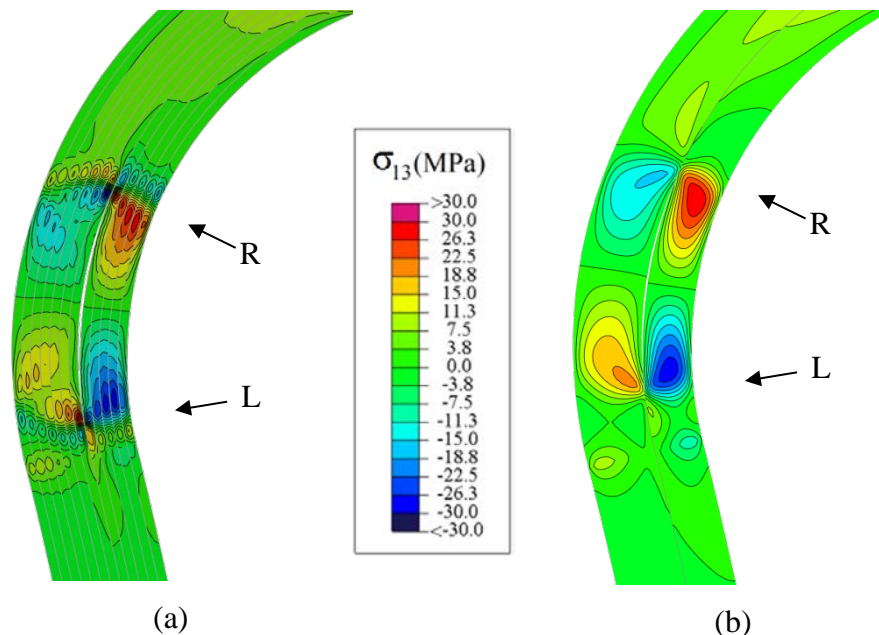
Figure 148 Contours of shear stresses at $\Delta t_{XN} = 3.0$ μs for (a) XN CZM and (b) XN CZM (Single Int.)
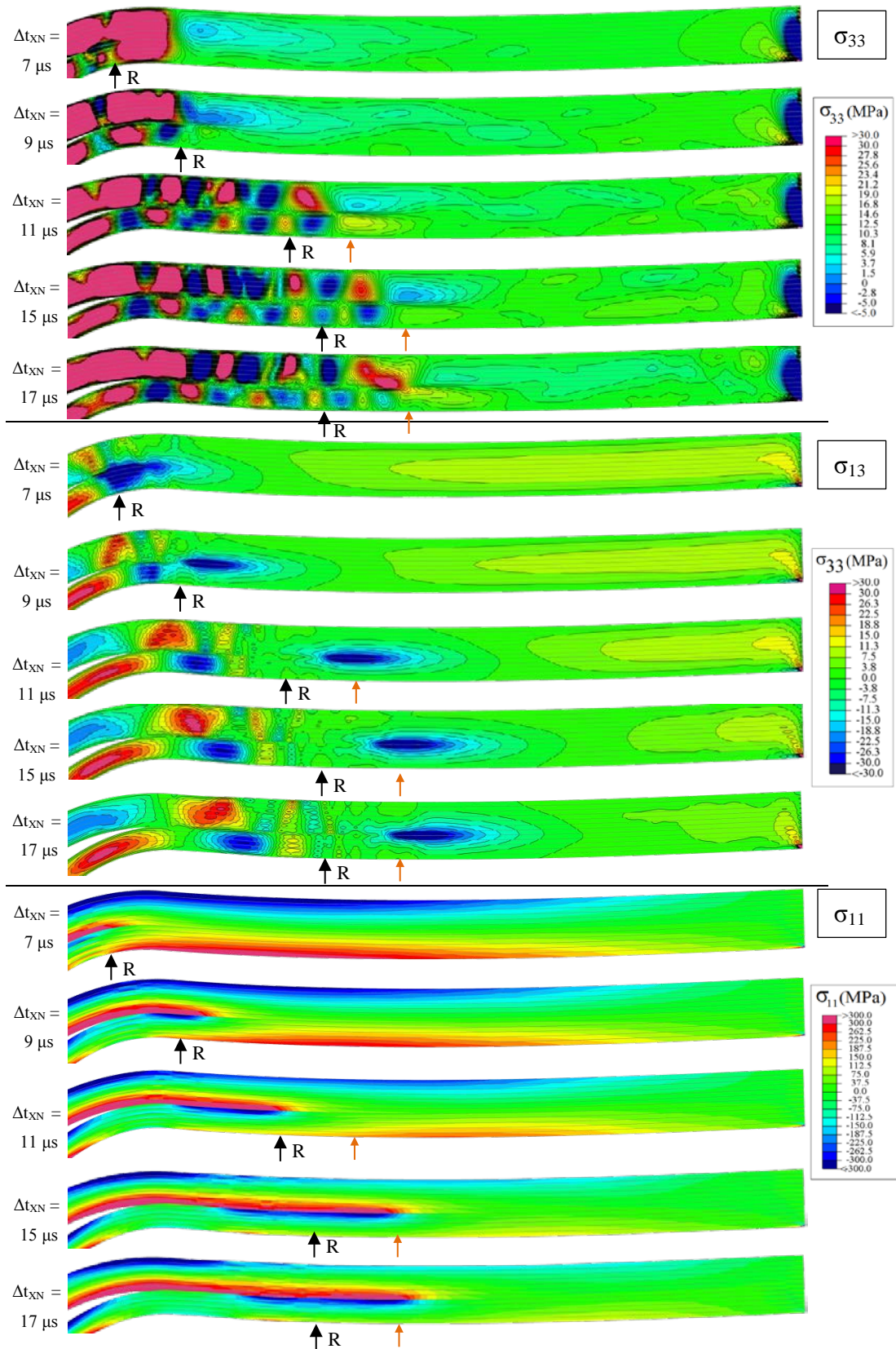
Figure 149 Contours of (top) opening, σ_{33}, (middle) shear, σ_{13}, and (bottom) longitudinal, σ_{11}, stresses at various time intervals in horizontal arm for XN CZM (R $\rightarrow$ $6\delta_{o,I}$ definition of crack tip, orange arrow follows opening stress concentration).
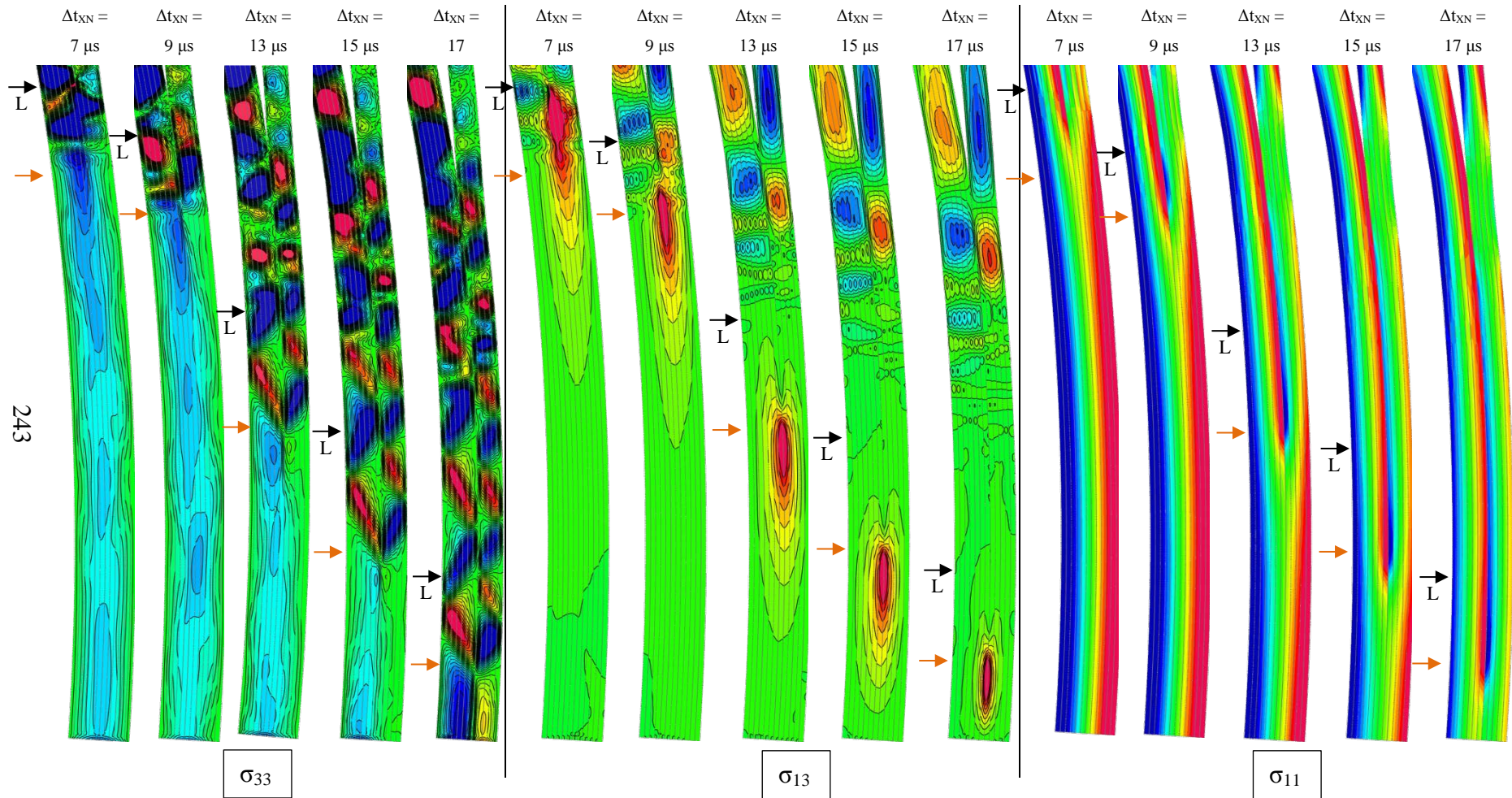
Figure 150 Contours of (top) opening, σ_{33}, (middle) shear, σ_{13}, and (bottom) longitudinal, σ_{11}, stresses at various time intervals in vertical arm for XN CZM (L $\rightarrow$ $6\delta_{o,I}$ definition of crack tip, orange arrow follows opening stress concentration, legends are given in the previous figure).

Figure 149-top, Figure 149-middle, and Figure 149-bottom respectively show contours of constant radial opening (σ_{33}), shear (σ_{13}) and longitudinal stresses (σ_{11}) at the horizontal arm for XN CZM. The small-orange arrows follow the tip of the opening stress distributions. The stress gradients at the right crack tip are oblique but not as sharp as the BL CZM shown in Figure 124. Other the other hand, no oblique stress gradients that could be the reflecting waves are not observed in the simulations of XN CZM in the horizontal arm. The fringes of shear and longitudinal stresses (Figure 149-middle, and Figure 149-bottom, respectively) exhibit very similar stress contours compared to the results of BL CZM shown in Figure 124-middle and Figure 124-bottom, respectively. There are minor differences such as formations of circular shear stresses concentrating at the middle of the plies of the XN CZM simulations.

For the vertical arm, the contours of opening, shear and longitudinal stresses at various time intervals are respectively shown in Figure 150-left, Figure 150-middle and Figure 150-right for the XN CZM. An arrow for locating the left crack tip (L) and a small-orange arrow following the tip of the opening stress distributions are shown in the figures. The opening stresses form clear formations of oblique gradients during the propagation of the left crack tip. The oblique formations are visible for the reflecting stress waves. Although the gradients are not as clear as BL CZM seen in Figure 125-left, the stress waves are expected to be shear Mach waves in the vertical arm. Shear and longitudinal stresses are very similar to the stress contours of BL CZM except for the formations of circular shear stresses concentrating inside the plies.
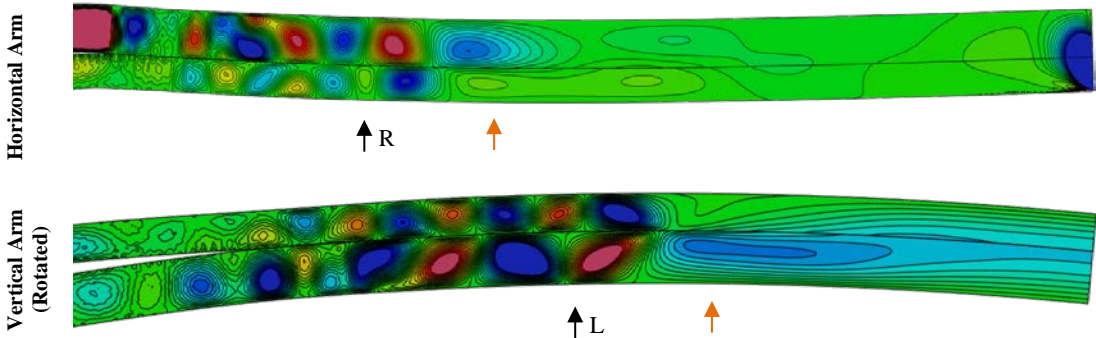
Figure 151 Contours of constant opening stresses (σ_{33}) for horizontal and vertical arms obtained using XN CZM with single interface at Δt_{XN_1} = 13 μs (The legend is given in Figure 150).

Example plots for constant opening stress contours are presented in Figure 151 for horizontal and vertical arms at $\Delta t_{XN\_1} = 13$ µs using XN CZM with single interface. At first glance, the stress distribution at the horizontal arm is somehow similar to the one given in Figure 149-top in terms of stress concentrations of tensile/compressive regions and remaining stress patterns moving with the crack tip. However, the morphology is not exactly the same. For example, the oblique stress gradient at the crack tip obtained by XN CZM with multiple interfaces is elongated than the gradient found for the single interface model. Moreover, the magnitudes of the moving stress concentrations behind the crack tip are smaller in the single interface model. Similarly, the stress contours at the vertical arm in the single interface model seems similar to the result obtained by the multiple interface model (Figure 150-left). Yet, the stress concentration in the single interface model is smoother and more circular shape compared to the fringes given in Figure 150-left. For instance, the tensile and compressive stress concentration fields obtained using multiple interfaces in Figure 150-left resemble more tilted morphology like a canted "water drop" with the sharp end looking downward. In addition to the morphology of the stress fields, the magnitudes of the stress concentrations in the delaminated arms are smaller in the single interface model. Actually, the morphology of the stress gradients in the multiple interface models can be attributed to early sliding of the XN CZM model. The opening stress concentration region in front of the left crack tip at $\Delta t_{XN\_1} = 13$ µs obtained using the models with multiple interfaces and single interface are shown in Figure 152a and Figure 152b, respectively. It can be seen that the contour lines are "translated" towards the right between each ply in Figure 152a if they are followed from bottom to the up. On the other hand, the stress contours are rather smooth in Figure 152b where no interface was modeled at the portion of the laminate shown in the picture. It is suggested that the sliding motion of the plies causes an artificial effect to the morphology of the stress contours of the XN CZM model in such a way that the contour lines eventually resemble a more canted view. The sliding phenomenon discussed in section 5.3.2.3.2 disturbs the stress morphology in XN CZM simulations even for the non-damaged regions.

<center>(a)</center> <center>(b)</center>
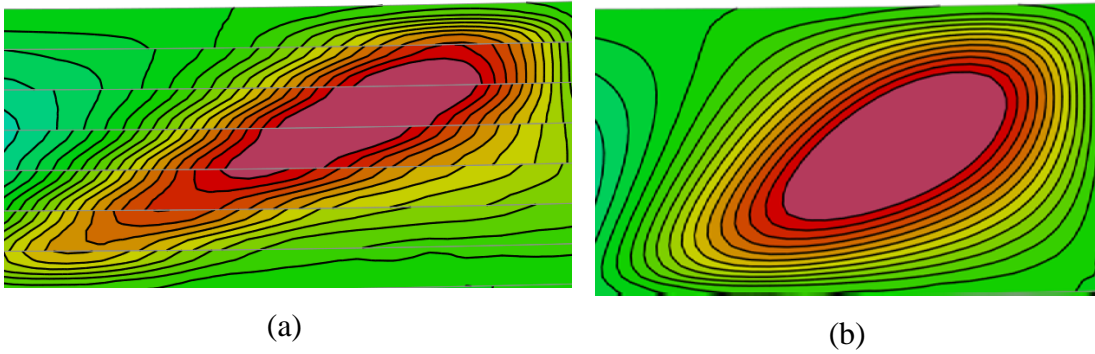
Figure 152 The opening stress concentration region in front of the left crack tip at $\Delta t_{XN\_1} = 13$ μs obtained using (a) multiple interfaces and (b) single interface model.

The left and right crack tip speeds as a function of time using XN CZM and XN CZM with single interface models together with the BL CZM and experimental results are shown in Figure 153a and Figure 153b, respectively. For the left crack tip, the predictions of the models with single and multiple lines of XN CZMs are very well agreed with each other. The left crack tip speeds propagate at sub-Rayleigh wave speeds until $\Delta t_{XN} = 11$ μs when they suddenly jump to 4200 m/s. Just after reaching the top speed, they continue the propagation at critical speed of V_c for more than 4 μs. Afterwards, they start to decelerate. The behavior of the XN CZM is very similar to the BL CZM except the time of the speed jump to intersonic speeds 4.5μs later than BL CZM for the left crack tip. The behavior of the left crack tip is supported by the stress contours shown in Figure 150-left where the formations of Mach waves emerge at $\Delta t_{XN} = 13$ μs. Similar to the left crack tip, XN CZM and XN CZM with single interface are in agreement with each other for the right crack tip. XN CZM exhibits a low profile of propagation speeds which is dominated by sub-Rayleigh wave speeds. The right crack tip accelerates to intersonic speeds around 1800 m/s when the crack tip approaches to EoCR at t = 11.3 μs. The predictions of XN CZM are only in agreement with BL CZM for the first 6 μs. After that time, the speed curves of both models exhibit different behaviors. In general, experimental data is predicted with adequate accuracy by XN CZM for the right crack tip. Lack of Mach wave formations for the opening stresses at the horizontal arm (Figure 149-top) can be explained from Figure 153b which shows slower crack tip speeds.

<center>246</center>
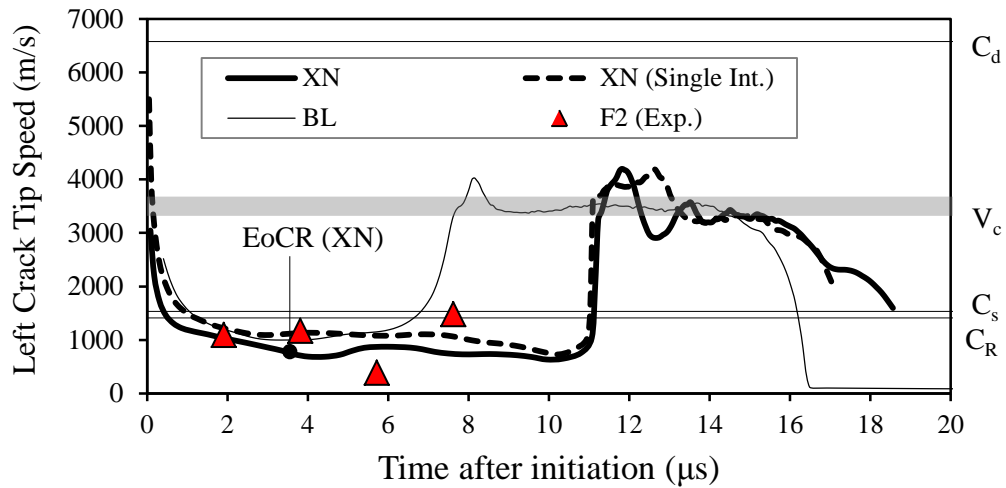
(a)
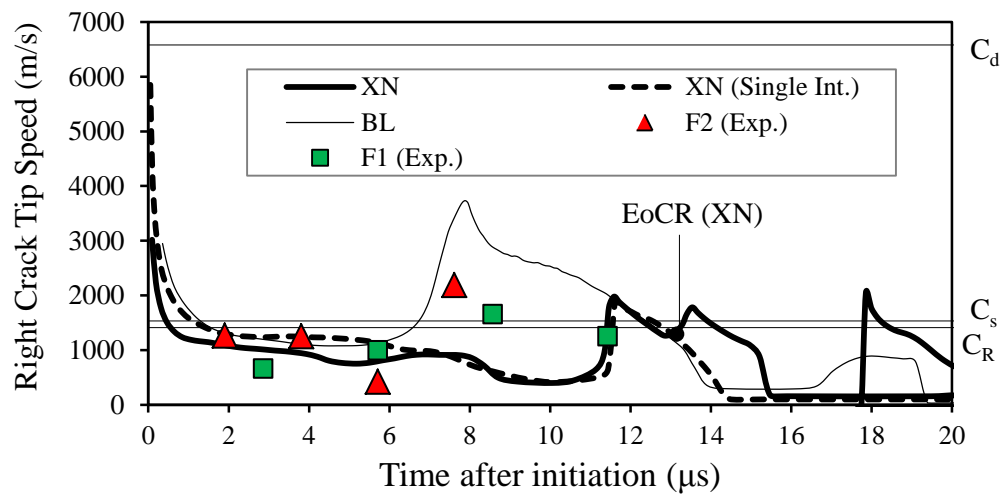
(b)

Figure 153 Crack tip speed as a function of time graphs of XN CZM, XN CZM with
single interface and BL CZM for (a) left and (b) right crack tips

The energy balance obtained for XN CZM is shown in Figure 154a where external
work, strain, kinetic and fracture energies are plotted. The delamination occurs at t ≈
21.4 ms when the external work of 7.4 J is reached. Afterwards, kinetic energy
rapidly develops to 1.8 J while strain energy decreases to 2.8J and the fracture energy
reaches 2.9J. Similarly, the strain energy and the kinetic energy transform to each
other in a frequency of 50 kHz which is equal to the frequency obtained for the BL

247

CZM. A vital observation is the small osscilations observed in the fracture energy. In theory, as the fracture process is irreversible, there could be no decrease in the fracture energy unless the crack is "healed". The osscilations in the XN CZM show decreases of fracture energy although they are small. This happens due to the fact that XN CZM is a reversible model before reaching the fracture toughness. Hence, the small osscilations create "negative" separations that artificially heal the crack. Hopefully, the decreases of the fractue energy is negligibly small. However, this is a very important observation that should be concerned for modeling XN CZM with unloading scenarios.

The kinetic energy graphs of XN and BL CZMs are shown in Figure 154b as a function of time after initiation. It can be seen that the kinetic energy of XN CZM is slightly greater than BL CZM. The reason is that XN CZM has higher strain energy stored at the failure point since it fails at higher load and displacement (Figure 145a). Therefore, more strain energy is available for kinetic energy. No considerable difference is observed in the kinetic energy of the XN CZM with single interface model which is therefore not presented in the figure. Figure 154c shows the fracture energies released during the delamination propagation for the simulations of XN CZM, BL CZM and XN CZM with single interface. An important obsrvation from the XN CZM is that the fracture energy starts from 0.32 J, not from the zero, at the time of initiation. The difference of 0.32 J is sustained between the fracture energies of BL and the XN CZMs in the remaining part of the figure. The difference of 0.32 J is also observed in the total work done. On the other hand, the model using XN CZM with single interface starts from zero and develops to the same level of BL CZM that is around 2.6 J. These results suggest that early sliding of all the interfaces, not limited to the 5th interface, released "unmature fracture energy" before the failure point since the soft interfaces in the XN CZM spawn considerable separation at the cohesive elements forming an unreal fracture energy. This is one of the complications rised by the compliant initial slope of XN CZM.
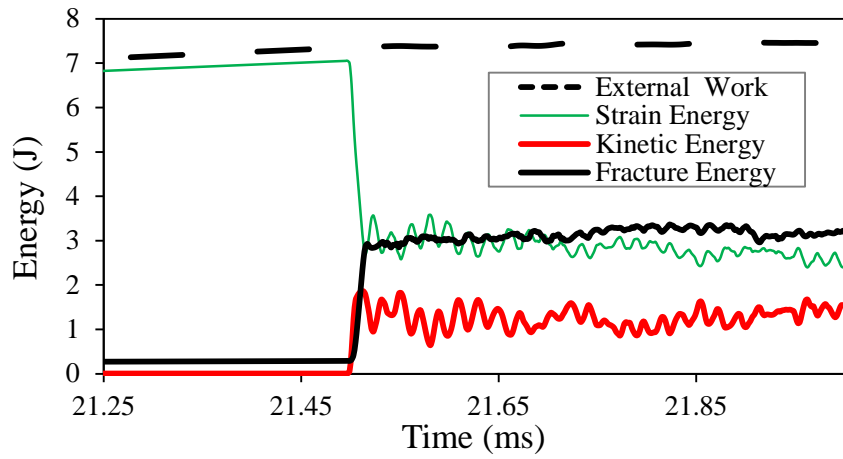
(a)
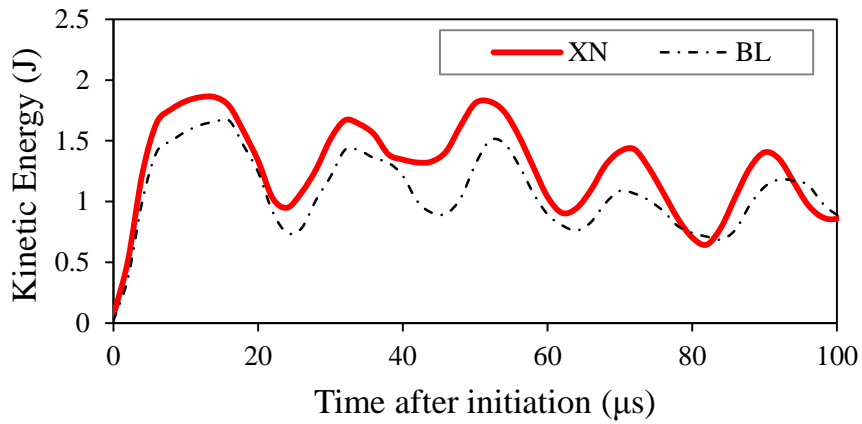
(b)
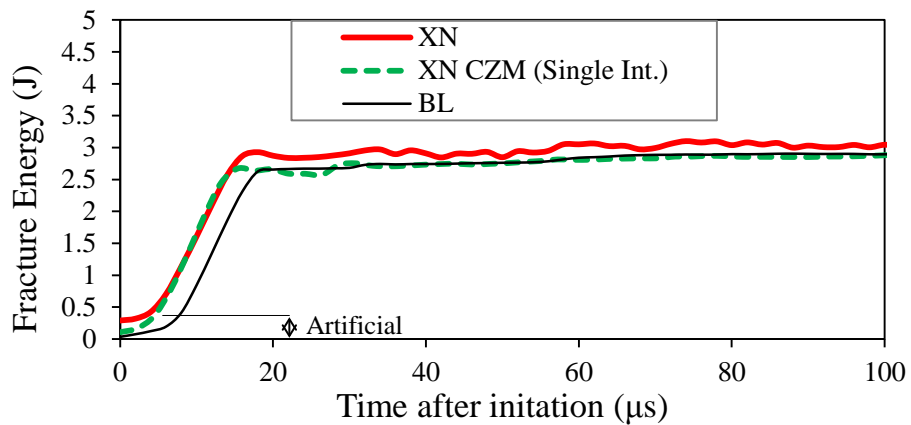
(c)

Figure 154 (a) Energy balance obtained by XN CZM, (b) kinetic energy curves for
XN CZM and BL CZM and (c) fracture energies for BL CZM, XN CZM and XN
CZM with single interface.

5.3.4. Numerical Modeling of Intersonic Delamination using RD CZM

The L-shaped composite laminate and the finite element model presented in section 5.3.2 was solved using RD CZM. Traction-separation profile of RD CZM using the properties of Table 11 is shown in Figure 155 for mode-I case. The rate-dependent interface properties are referred to the study of Corigliano et al. [156]; i.e. $G_{Ic,\infty} = 5G_{Ic}$, $G_{IIc,\infty} = 5G_{IIc}$, $T_{Io,\infty} = 2.5T_{o,I}$, $T_{IIo,\infty} = 2.5T_{o,II}$ and the onset and critical separation velocities are taken as 70 m/s since they were provided for delamination of CFRP laminates [156]. The constitutive law of RD CZM at zero separation speed is equivalent to BL CZM. The crack tip definition in RD CZM is $d_{1.0}$ where fully damaged element (d = 1.0) is considered as the crack tip.
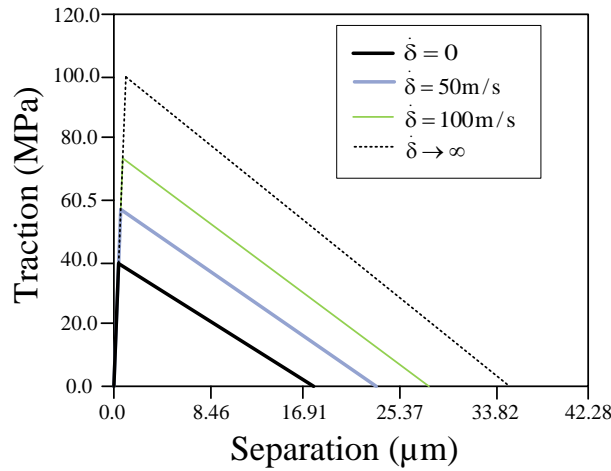
Figure 155 Traction-separation profile of RD CZM for various separation speeds at $\dot{\delta}$ = 0, 50 m/s, 100 m/s and infinite speed.

5.3.4.1. Results and Discussion

The simulation using RD CZM is performed in ABAQUS/Explicit [69] with the VUEL user-subroutine. The resulting load-displacement curve obtained from the numerical simulation of L-shaped composite laminate is shown in Figure 156 together with the experimental results of F1 and F2 specimens and BL CZM. The load-displacement curves of RD and BL CZMs are indistinguishably the same. Actually, the rate-dependency in the interface does not affect the load-displacement curve including the spurious oscillations that still exist as severe as original.

250
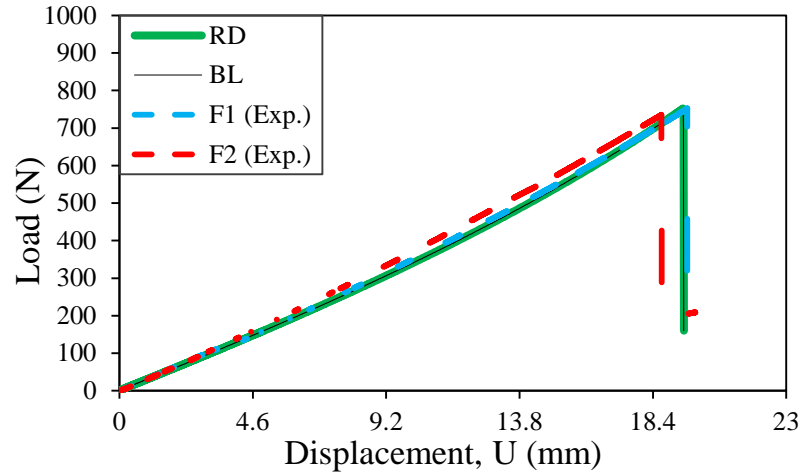
Figure 156 Load-displacement curves of RD CZM, BL CZM and the experimental results.

The delamination occurs at the 5th interface similar to the other CZMs. The final and initial stress distributions are indistinguishably same with the results of BL CZM shown in Figure 121. The constant stress contours of opening radial stresses prior to initiation and the start of initiation are shown in Figure 157a and Figure 157b, respectively, where the angle of the curved region, the angular location of the maximum stress and the initiation point are indicated. The angle of the curved region is equal to 84°, the same with BL CZM, which is expected from the load-displacement curves. The angular location of the maximum stress and the initiation location are attained at 13° from the centerline. The locations of the initiation parameters are the same with the prediction of the BL CZM. Even the time of initiation is found as $t_{in,RD} = 19402$ µs which is only 4 µs earlier than $t_{in,BL}$.

σ_{33}(MPa)

>30.0
30.0
27.8
25.6
23.4
21.2
19.0
16.8
14.6
12.5
10.3
8.1
5.9
3.7
1.5
0
-2.8
-5.0
<-5.0

t = 19396 μs
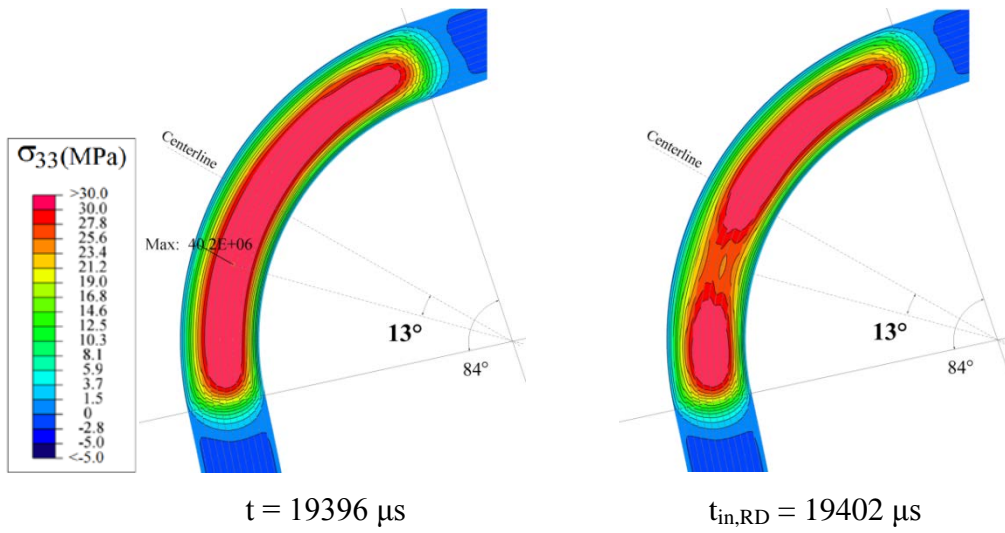
$t_{in,RD}$ = 19402 μs
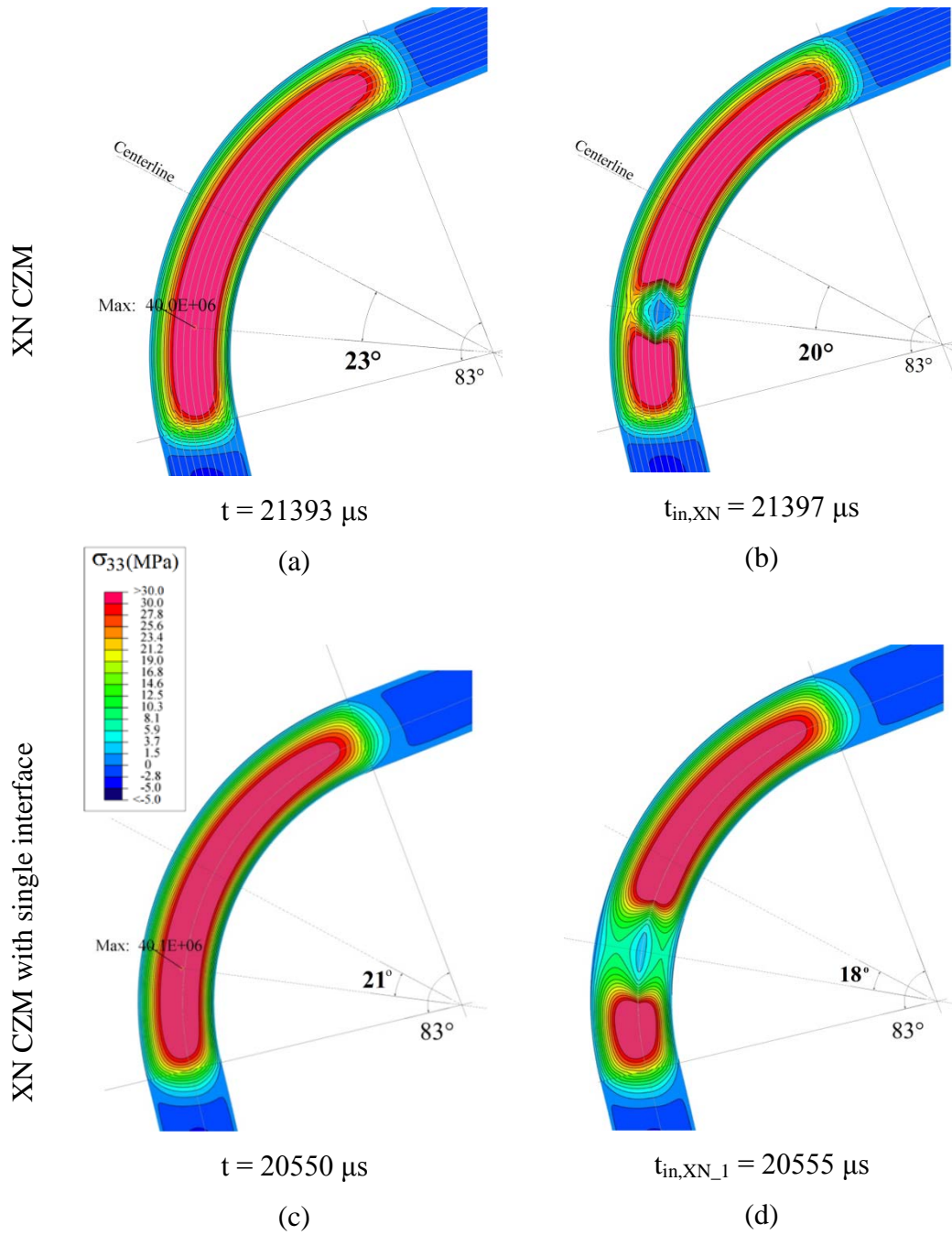
Figure 157 Contours of radial normal stresses (σ_{33}) (a) just before the initiation at t = 19396 μs and (b) during the initation at $t_{in,RD}$ = 19402 μs of the model using RD CZM.

252
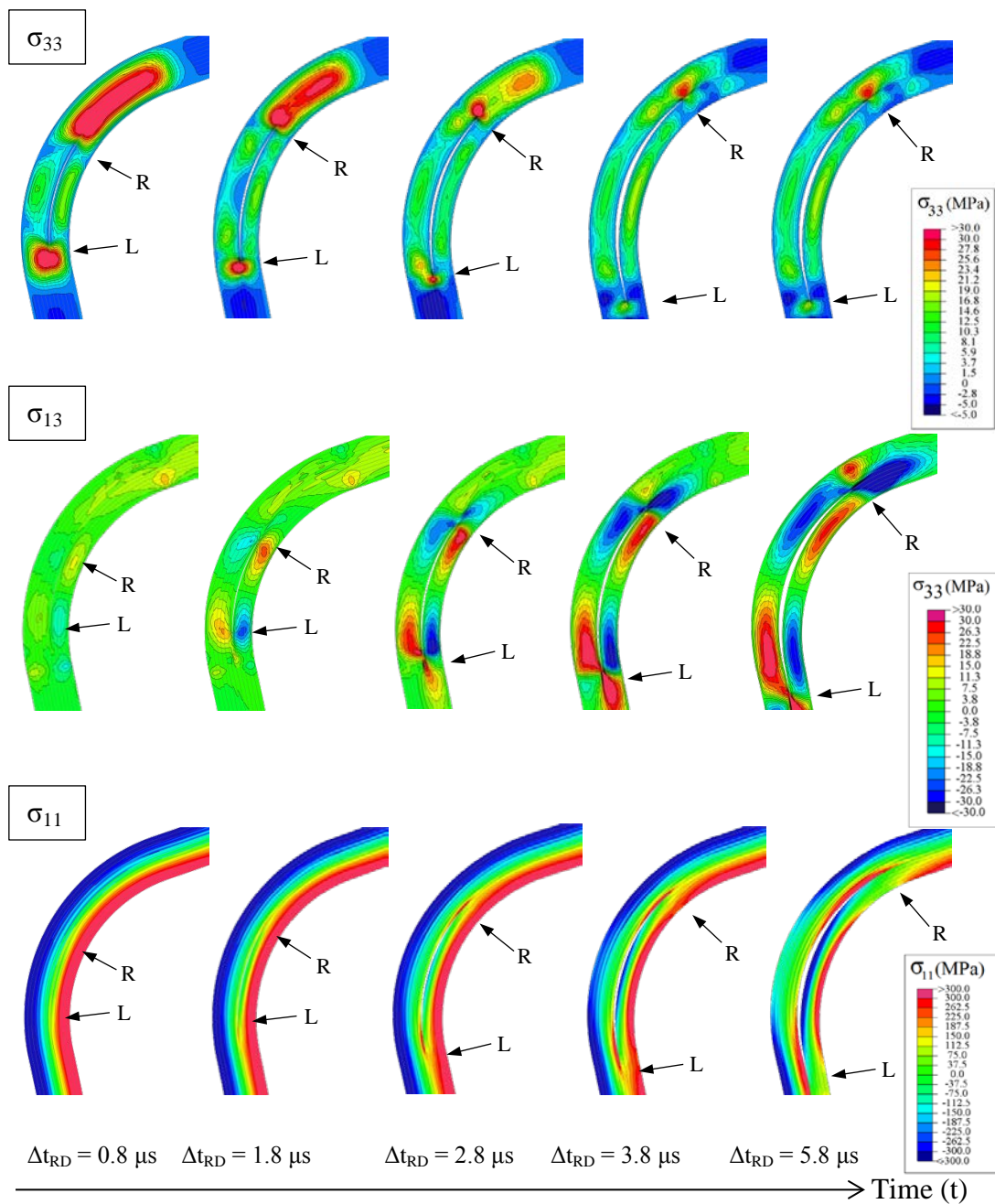
Figure 158 Contours of constant (top) opening (σ_{33}), (middle) shear (σ_{13}) and (bottom) longitudinal stresses (σ_{11}) with respect to time together with locations of fully damaged ($d_{1.0}$) and partially damaged ($d_{0.6}$) left (L) and right (R) crack tips at the curved region for RD CZM (grey lines represent the interfaces).
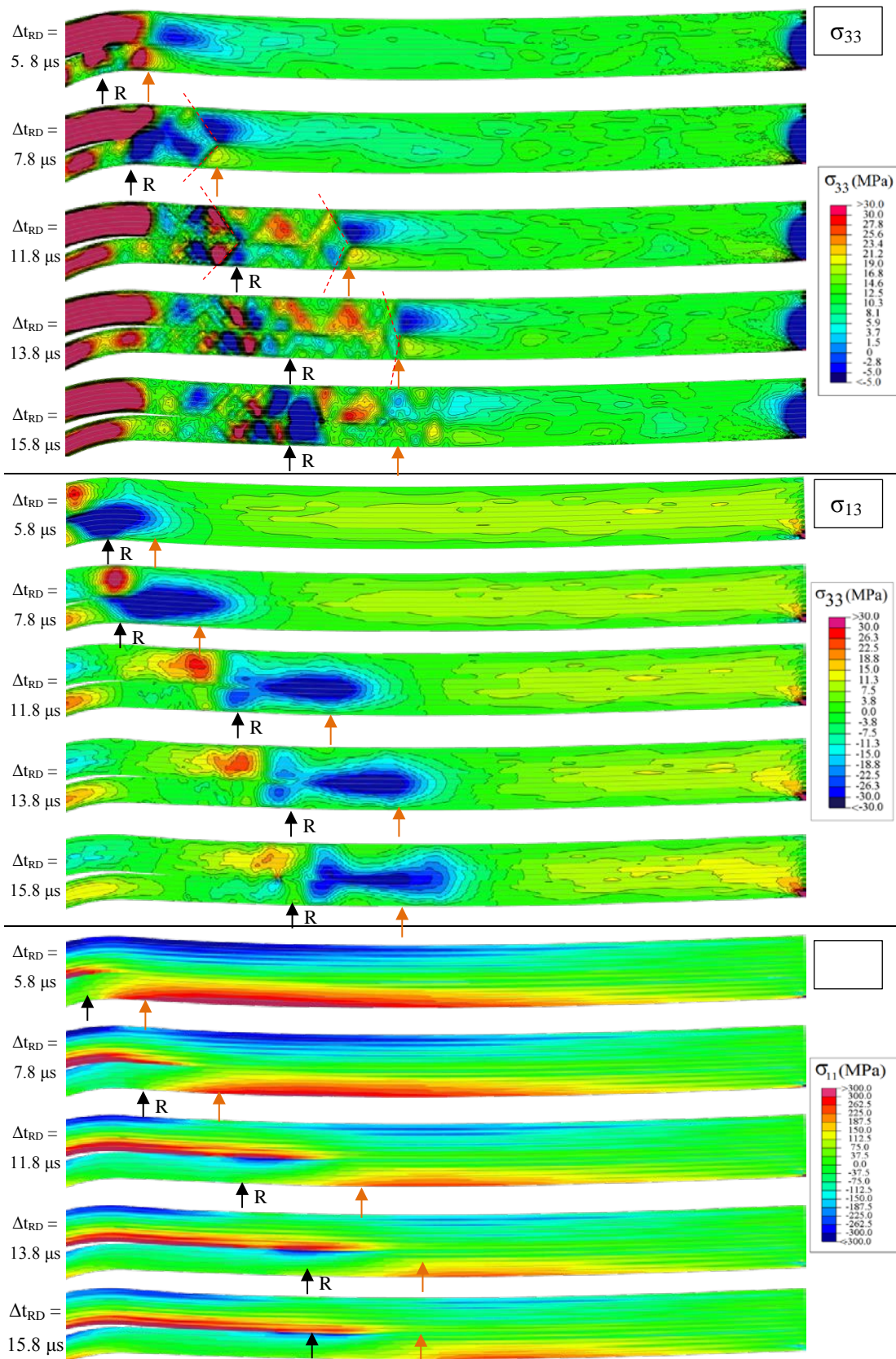
Figure 159 Contours of (top) opening, σ_{33}, (middle) shear, σ_{13}, and (bottom) longitudinal, σ_{11}, stresses at various time intervals in horizonal arm for RD CZM (R $\rightarrow$ 6$\delta_{o,I}$ definition of crack tip, orange arrow follows opening stress concentration).

254

Figure 160 Contours of (top) opening, σ_{33}, (middle) shear, σ_{13}, and (bottom) longitudinal, σ_{11}, stresses at various time intervals in vertical arm for RD CZM (L $\rightarrow$ 6$\delta_{o,I}$ definition of crack tip, orange arrow follows opening stress concentration, legends are given in the previous figure).

In the curved region, contours of constant opening, shear and longitudinal stresses obtained using RD CZM are shown in Figure 158-top, Figure 158-middle, and Figure 158-bottom, respectively. The opening stress contours for the RD CZM are very similar to the contours in Figure 123-top. A slight difference can be seen at Δt_{RD} = 3.8 µs and Δt_{RD} = 5.8 µs in Figure 158-top where the magnitude of the stress concentration at the right crack tip is greater than the stresses in the corresponding pictures of BL CZM (Figure 123-top). The shear and longitudinal stresses of RD CZM are indistinguishably the same with the BL CZM at the curved region.

The constant contours of opening, shear and longitudinal stresses are shown in Figure 159 for the horizontal arm. Similarly, the location of the crack tip and the location of the ends of the opening stress gradients are shown by black and orange arrows, respectively. The pictures of opening stresses before Δt_{RD} = 7.8 µs exhibit almost the same stress plots compared to the BL CZM including shear Mach waves and reflecting waves. At Δt_{RD} = 7.8 µs, interestingly, a second oblique stress gradient resembling a shear Mach wave front is observed behind the main wave front at the right crack tip. Moreover, there are many small wave fronts which seem to be reflecting waves appear behind of the second wave front after Δt_{RD} > 7.8 µs. Finally, the last position of the crack tip in the figures is behind the BL CZM which suggests that the crack propagation is slower and stopped slightly earlier than RD CZM. The shear stresses seen in Figure 159-middle are similar to BL CZM. However, the shape of the shear stress concentration is no more in an elliptical shape which was seen in both XN and BL CZMs. Instead, the shape is like a "fish" which has two larger regions in the tips of the concentration region. Finally, the stress distribution in the longitudinal stresses presented in Figure 159-bottom is very similar to the results of BL CZM only with the difference of slower crack propagation.

For the vertical arm, the fringes of opening, shear and longitudinal stresses are presented in Figure 160-left, Figure 160-middle and Figure 160-right, respectively. To be a contrast, the oblique opening stress gradients are very similar to the BL CZM until reaching Δt_{RD} = 13.8 µs. Afterwards, the wave fronts are not the same in the delaminated laminates in which the thicker laminate has more reflecting waves compared to the other one. The final position of the left crack tip, before the temporary crack arrest, is behind the position of BL CZM, which suggests that the

crack propagation at the left crack tip is also slower than the BL CZM. Other than the opening stresses, the shear and the longitudinal stresses are indistinguishably the same with the stress fringes of BL CZM.
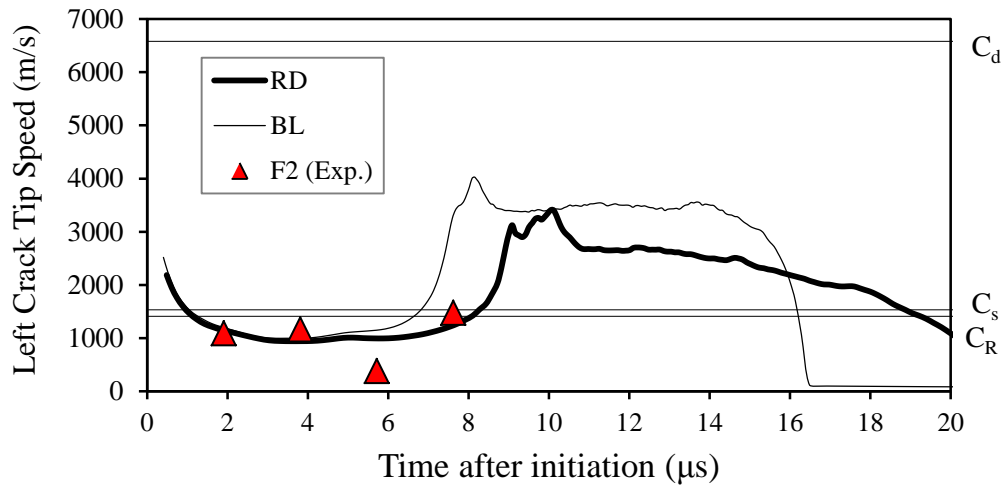
(a)
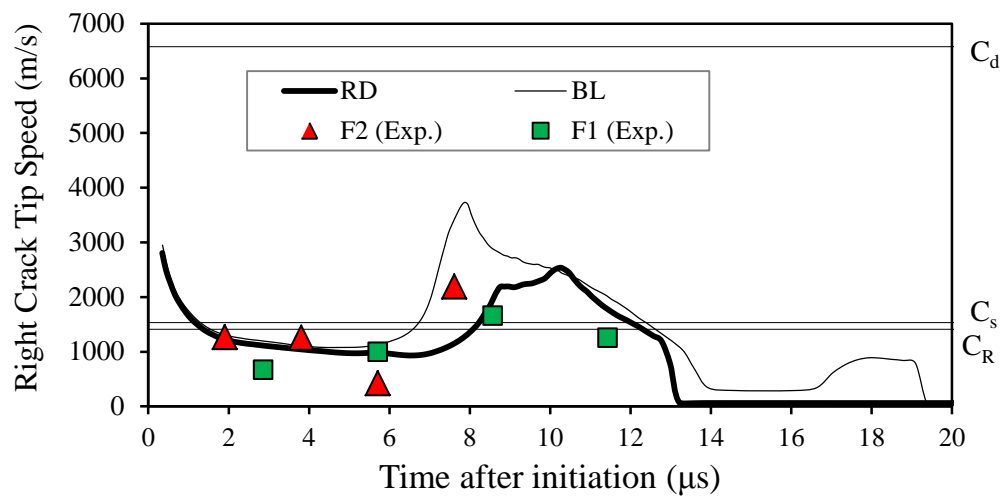
(b)

Figure 161 Crack tip speed as a function of time graphs of RD CZM together with BL CZM and experimental results for (a) left and (b) right crack tips

The crack tip speed as a function of time curves obtained using RD CZM together with BL CZM and experimental results for left and right crack tips are shown in Figure 161a and Figure 161b, respectively. The left crack tip propagates at sub-Rayleigh speeds around 1100 m/s until $\Delta t_{RD} = 8$ μs. Afterwards, the left crack tip speed reaches the critical speed of $V_c = 3500$ m/s around $\Delta t_{RD} = 9$ μs. Following the maximum speed, the left crack tip speed gradually slows down to sub-Rayleigh speed. In general, the RD CZM predicted slower crack propagation speeds. Moreover, RD CZM does not sustain its speed at V_c between $\Delta t_{RD} = 10.5$ μs and $\Delta t_{RD} = 19$ μs as it slows down gradually. Actually, the left crack tip behaves a viscous behavior of the BL CZM which is expected. A remarkable observation is that the experimental data points are best agreed with the RD CZM compared to XN and BL CZM. Especially, the RD CZM can capture the speed point of 1500 m/s at $\Delta t_{RD} = 7.62$ μs as well as the previous experimental points. For the right crack tip, the crack propagation continues at sub-Rayleigh speed until $\Delta t_{RD} = 8$ μs, which is longer than the BL CZM. The right crack tip speed gradually increase to 2500 m/s at $\Delta t_{RD} = 10$ μs. Afterwards, the crack tip slows down to 60 m/s at $\Delta t_{RD} = 13.2$ μs after when the crack propagation continues. Similar to the left crack tip, right crack tip exhibit slower propagation with longer durations of increases and decreases with the lower maximum speeds compared to the BL CZM. RD CZM also excellently predicted the experimental speeds. Especially, the crack tip speeds of F1 specimen are very close to the curve of RD CZM. In general, RD CZM provided the best prediction of the speeds so far. Noting that, the crack tip speeds can be better predicted once the rate-dependent parameters are fine-tuned by experimental results.

The external work done, strain, kinetic and fracture energies obtained using RD CZM are shown in Figure 162a where BL CZM results are also provided for reference. The external work done at the instant of delamination initiation at 19.4 ms is found as 6.7J. It can be seen that the external work done is the same with the BL CZM. However, strain, fracture and kinetic energies are not the same. The strain energy is dropped to 2.4 J whereas the kinetic energy and the fracture energy increase to 1.2 J and 3.2 J, respectively. The transformations of strain and kinetic energies also exist in the same frequency of 50 kHz for RD CZM. However, the kinetic energy of RD CZM is smaller than the kinetic energy obtained by the BL CZM as shown in Figure 162b. The fracture energy obtained using the RD CZM is

about %25 higher than the BL CZM as seen in Figure 162c. The reason of the difference in the energies is that the rate-dependency in the RD CZM increases the fracture toughness at higher separation rates. Hence, it can be roughly stated that global fracture toughness is approximately increased around 25% due to the rate effects. The increase in the fracture energy explains the lower levels of kinetic energies since the strain energy is transformed into more fracture energy due to increase of fracture toughness with high separation rates.
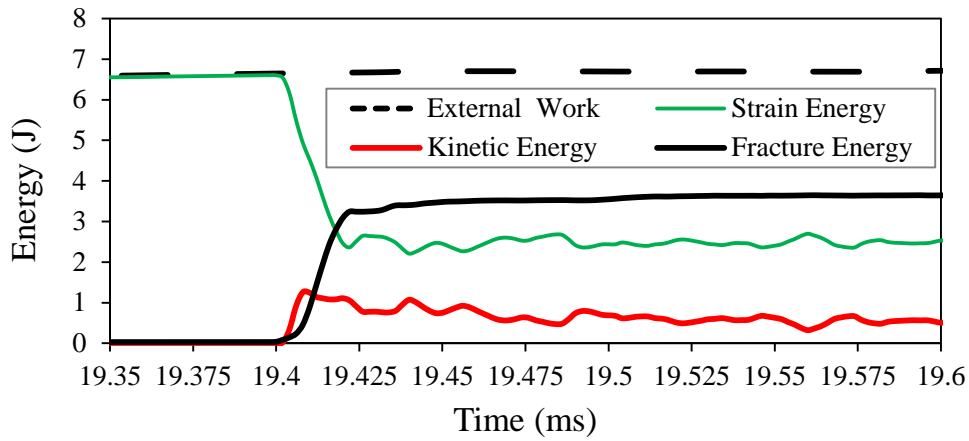
(a)
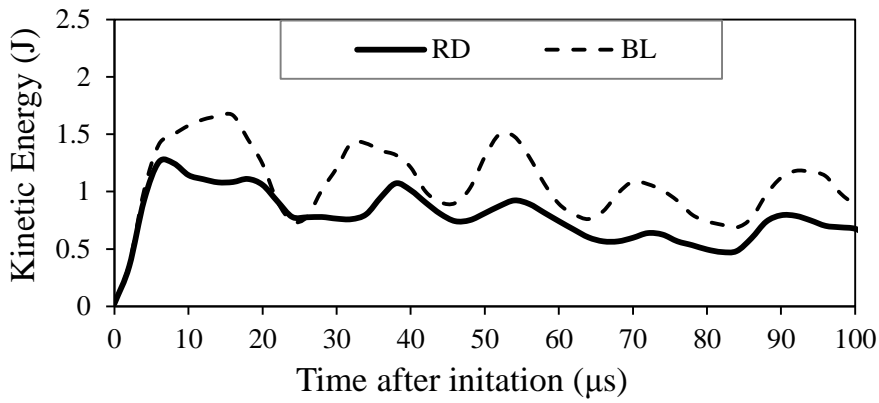
(b)
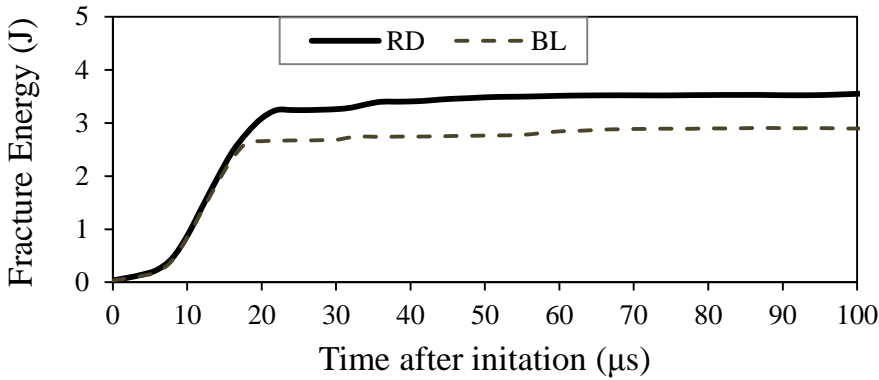
(c)

Figure 162 (a) Energy balance obtained using RD CZM, (b) kinetic energy curves and (c) fracture energies of RD and BL CZMs.

5.4. Final Discussions

One of the topics of discussion is the oscillatory response of the specimen following the initiation of delamination. The oscillations not only affect the load-displacement curves but also the figures of energy balance. The other topic is the definition of the crack tip during the delamination process. It is observed that the definition of the crack tip depends on the fracture mode. In addition, remarkable observations are made for an engineering part of L-shaped composite laminates. First of all is the formation of shear Mach waves emanated from the crack tip under quasi-static loading. The second is the formation of secondary Mach waves that resemble the "train of pulses" that is generally observed in friction simulations. Finally, delamination in L-shaped composite laminate shows a unique feature of transitioning from mode-I to mode-II fracture modes as well as transitioning from sub-Rayleigh to intersonic crack tip speeds.

Oscillatory response in the load-displacement curves has been observed following the delamination of the L-shaped composite laminates for all of the CZMs and mesh sizes. In reference to the section 3.2, spurious oscillations in the load-displacement curves are known to be the phenomena for explicit FEA in conjunction with CZM. Pinho et al. [166] suggested that the oscillatory response can be reduced by using smaller cohesive elements or higher-order ("smoother") CZMs. Considerable reduction in the oscillation is achieved in the DCB simulations as discussed in section 4.1 by reducing the mesh size and using XN CZM. In the simulations of stable crack propagation such as the DCB test, oscillations are attributed to the small disturbances initiated by successive failure of the cohesive elements. However, the oscillatory response observed in the L-shaped laminates cannot be solely explained by this phenomenon. First of all, oscillations are extremely severe in the delamination of L-shaped composite laminates. Secondly, negligible amelioration has been achieved by reducing the mesh size and using XN CZM. Hence, the suggestions made by Pinho et al. [166] did not work for the oscillations observed in the delamination of L-shaped composite laminates.
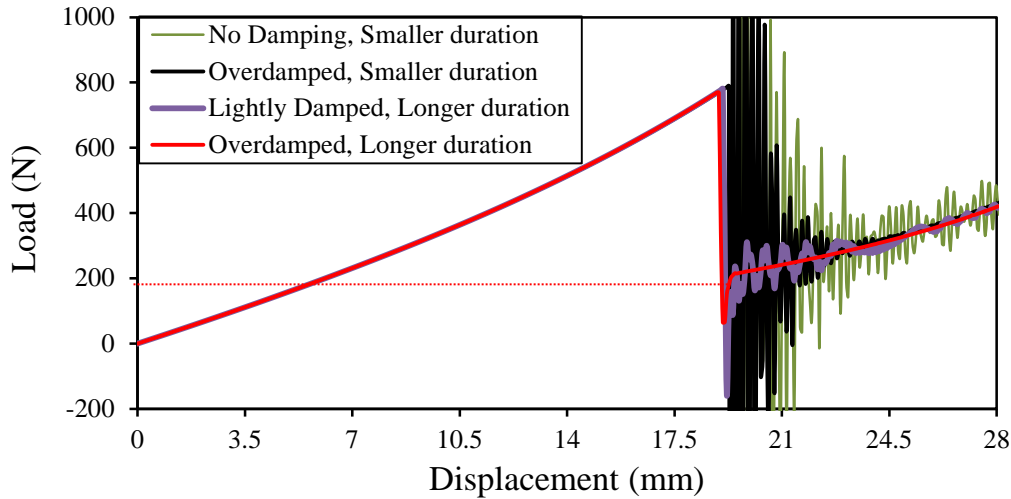
Figure 163 Load-displacement curves obtained using BL CZM in shear loading case for various combinations of damping and loading durations.

The main difference between the crack propagations in a DCB and an L-shaped composite laminate is the stability of the crack. The stability of the delaminations in the L-shaped composite laminates can be explained over the load-displacement curves presented in Figure 112. During the load drop represented by the curve "e", the crack growth takes place. The fracture energy is developed as suggested by the eqn. (20) which further implies that the specimen compliance is also developed together with the fracture energy. Keeping in mind, the load-drop takes place almost instantaneously which was also shown, experimentally. As a result, the stored strain energy dominated by the radial opening stresses is suddenly released at the curved region where the initiation occurs. The resulting motion is the radial translation of the delaminated parts to opposite directions starting from the initiation point. Following, the separating motion becomes a component wise phenomenon. The process develops the kinetic energy so rapidly that the vibrations are triggered. The frequency of the vibrations is the same for all mesh sizes (after a converged value) and CZMs. Even, rate-dependency in the interface has no effect. Actually, Uyar et al. [231,232] reported vibrations of the delaminated plies during their experiments at the frequency of 33.3 kHz which is very close to our prediction of 50 kHz. It is suggested that the harmonic vibrations induce oscillations in the load-displacement curves which is a real phenomenon. Yet, the duration of the oscillations may not be

correct since the experiment showed that the vibration is damped in several cycles. It also indicated that there is strong damping in the real specimen. Moreover, the data acquisition frequency and the sensitivity of the tensile test machine are not as high as the numerical analysis. Hence, it is suggested that the testing machine could not record the oscillations in the loads.
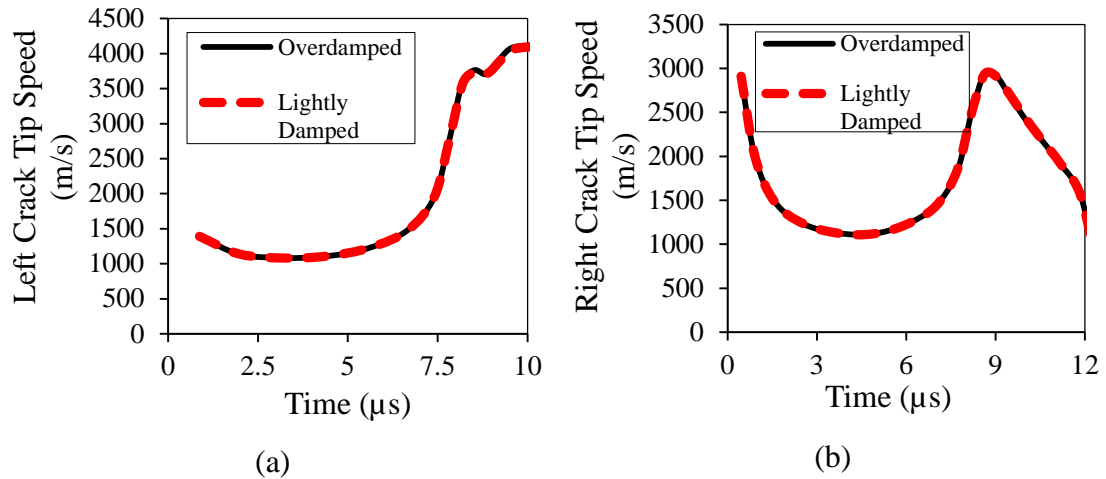
Figure 164 Crack tip speed as a function of time curves of overdamped and lightly damped models for (a) left and (b) right crack tips.

The RD CZM is not effective to damp the oscillations. In the experiments, there are numerous sources of damping such as material damping, damping due to friction between delaminated plies, jig and air. Hence, it is hard to apply a realistic damping into the numerical models, which is not within the scope of this study. By default, a small amount of numerical damping is introduced by ABAQUS/Explicit in the form of bulk viscosity in order to control high frequency oscillations [69]. In addition to the bulk viscosity, Rayleigh viscosity, ζ_i, can be artificially introduced in the form of $\zeta_i = \alpha_R/(2\omega_i) + \beta_R\omega_i/2$ for a given eigenmode-i, where α_R is the mass proportional and β_R is the stiffness proportional damping coefficients [69]. The mass proportional viscosity, α_R, works like "viscous ether" against the flexural vibrations. Therefore, the mass proportional viscosity can be introduced into the system since its effect is more straight-forward and physically predictable. In addition to the viscosity, duration of solution can be increased for damping the system. Figure 163 shows

three load displacement curves obtained using BL CZM for the shear loading case to see the influences of the mass proportional damping and solution time. An undamped system ($\alpha_R = 0$) for a faster loading, characterized by $U_L = 35$ mm and $t_L = 0.35$ s (eqn. (122)), is shown by the thin green line. It can be seen that severe oscillations follow the load drop at $U = 19.4$ mm. The oscillations are slightly reduced before reaching $U = 24.0$ mm. Afterwards, the oscillations continue harmonically at moderate levels in the steady-state condition. Thick blue line represents longer duration of loading by $t_L = 2.8$ s together with a slight damping of $\alpha_R = 0.1$. It can be seen that the oscillations are damped gradually and the reloading curve becomes clearer. The black line represents an overdamped system with $\alpha_R = 10$. for a longer solution duration of $t_L = 2.4$ s. The load-displacement curve slightly undershoots during unloading at $U = 19.4$ mm. Afterwards, it gradually moves to the reloading stage that is expected from an overdamped system. No oscillation is observed for the overdamped system even though the load data is acquired in every 1 µs. The undershooting during the unloading stage can be removed if the frequency of the data acquisition is increased to levels of the test machine. An important observation is that the effect of damping and the loading duration have nearly no effect to the failure point and the point of reloading while diminishing the oscillations in the load-displacement curves. From micromechanical point of view, the curves of crack tip speed versus time data are analyzed for overdamped and lightly damped models (Figure 164) where no effect of the damping can be seen. Hence, the mass-proportional damping can be used in order to remove oscillations in the load-displacement curves without affecting the delamination kinetics and failure point of the delamination fracture in L-shaped composite laminates.

(a)

(b)
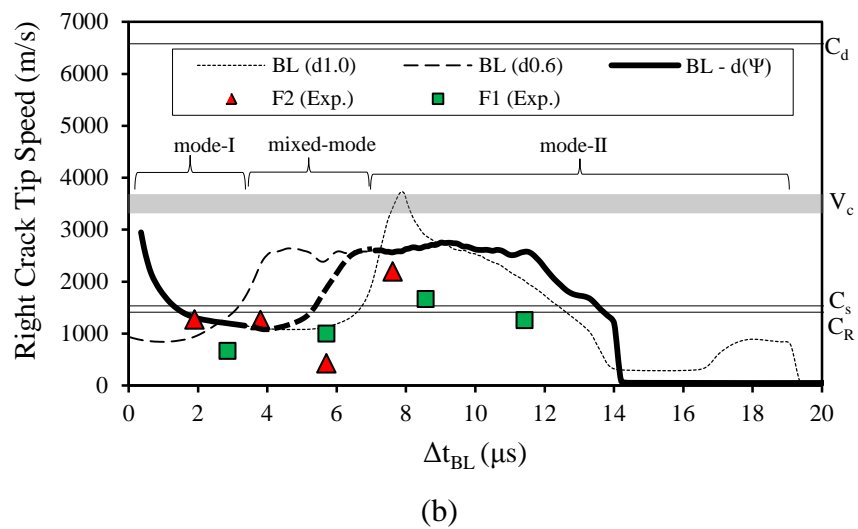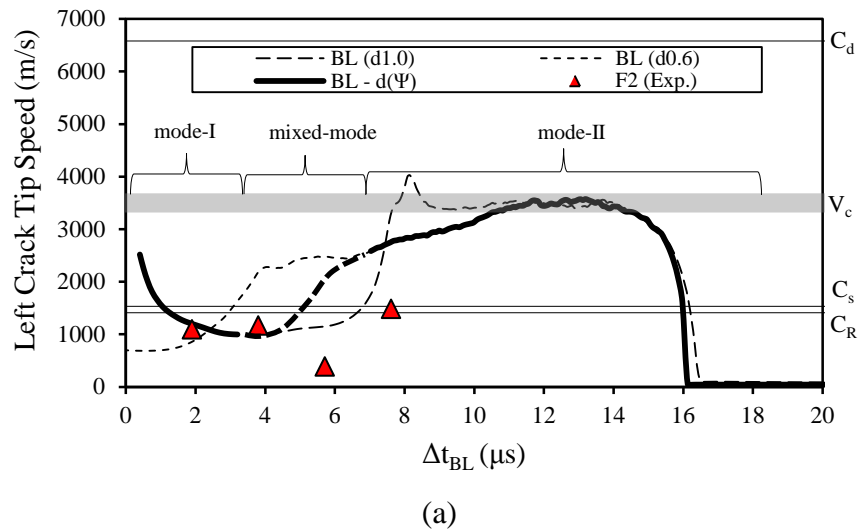
Figure 165 Crack tip speed as a function of time for BL CZM showing a new crack
tip definition of d(Ψ) for (a) left and (b) right crack tips.

The definition of the crack tip based on the damage level affects the results of crack tip kinetics during the delamination of L-shaped composite laminates. It is observed that the fully damaged crack tip location, $d_{1.0}$, is the best fit for representing the crack tip in mode-I condition whereas partially damaged crack tip definition, $d_{0.6}$, is more accurate for locating the mode-II dominated crack tip. In L-shaped composite laminates, the crack propagation occurs in both mode-I and mode-II conditions. Hence, a fixed definition of the crack tip is not adequate to explain the whole fracture. In references, the crack propagation in conjunction with CZM generally occurs in single condition or mixed-mode condition without taking into consideration

of the crack tip position [111,112,136,138,144]. For example, Geubelle and Baylor [175] used $d_{1.0}$ in BL CZM whereas Coker et al. [112] used $5\delta_o$ in the XN CZM which can be considered as a partially damaged crack tip definition. In our results, fully damaged definition of the CZM, $d_{1.0}$, is generally referred since this is to provide the nearest point to the experimentally observable crack tip. However, $d_{1.0}$ cannot be used for locating the shear Mach waves in the arms. Now, we propose a flexible definition of the crack tip which is defined as a function of phase angle, Ψ; i.e. $d(\Psi)$. Specifically, linear interpolation between $d_{1.0}$ and $d_{0.6}$ can be used such as $d(\Psi) = d_{1.0} + \Psi(d_{0.6}-d_{1.0})/90°$. It can be shown that $d(\Psi)$ directs to $d_{0.6}$ for mode-II, $d_{1.0}$ for mode-I and a smooth transition of the damage in mixed-mode condition. The crack tip speeds as a function of time are shown in Figure 165 using the new crack tip definition for the left and right crack tips. It can be seen that $d_{1.0}$ continues in mode-I region until $\Delta t_{BL} = 4$ µs which is followed by mixed-mode definition of the crack tip. Next, the crack tip speed calculated for $d_{0.6}$ continues in the mode-II region. This enables continuous definition of the crack tip to be achieved throughout the propagation. However, the crack tip speeds should be found by following the stress fields using DIC in the experiments.

Numerical models using all CZMs successfully predicted the main delamination at the 5th interface in the experiments. However, the other sites of delamination inside the curved region could not be captured. The simulation using BL CZM is further continued to have other delaminations in the specimen. A second delamination is formed at the 8th interface in $U \approx 38.1$ mm which is followed by a third delamination at the 2nd interface in $U \approx 42.3$ mm (Figure 166). The sequence of the locations of the secondary and the third delaminations are perfectly in agreement with the study of Martin [56]. However, the other sites of delaminations observed in the experiments are not limited to those plies. Moreover, these delaminations were reported during the load drop.
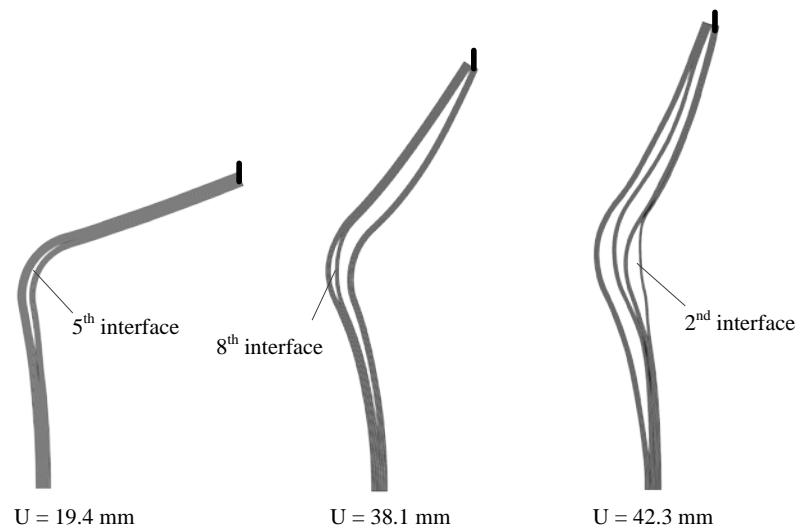
Figure 166 Other delaminations at large displacements for the numerical model of BL CZM.

Shear Mach waves are observed only in the opening (normal) stress contours during our simulations. No wave fronts can be observed in shear and longitudinal stresses. Similarly, Dwivedi and Espinosa [122] obtained shear Mach waves only in the normal stress contours as shown in Figure 167a where longitudinal, maximum shear and opening stress contours are shown from left to right. It can be seen from Figure 167a-right that the shear Mach wave is visible in the normal stress plot whereas there is no sign of shear Mach wave in the other stress fringes. A second example is the formation of "train of pulses" as shown in Figure 167b-left (taken from the opening stress plots of RD CZM at $\Delta t_{RD} = 10.8$ μs). Train of pulses is observed in slip-stick type of sliding simulations dedicated for friction modeling [217] (Figure 167b-right). On the other hand, although no friction is modeled in our simulations, train of pulses can be observed. Hence, the mechanisms can be different albeit the resulting stress patterns are similar.

(a)

(b)
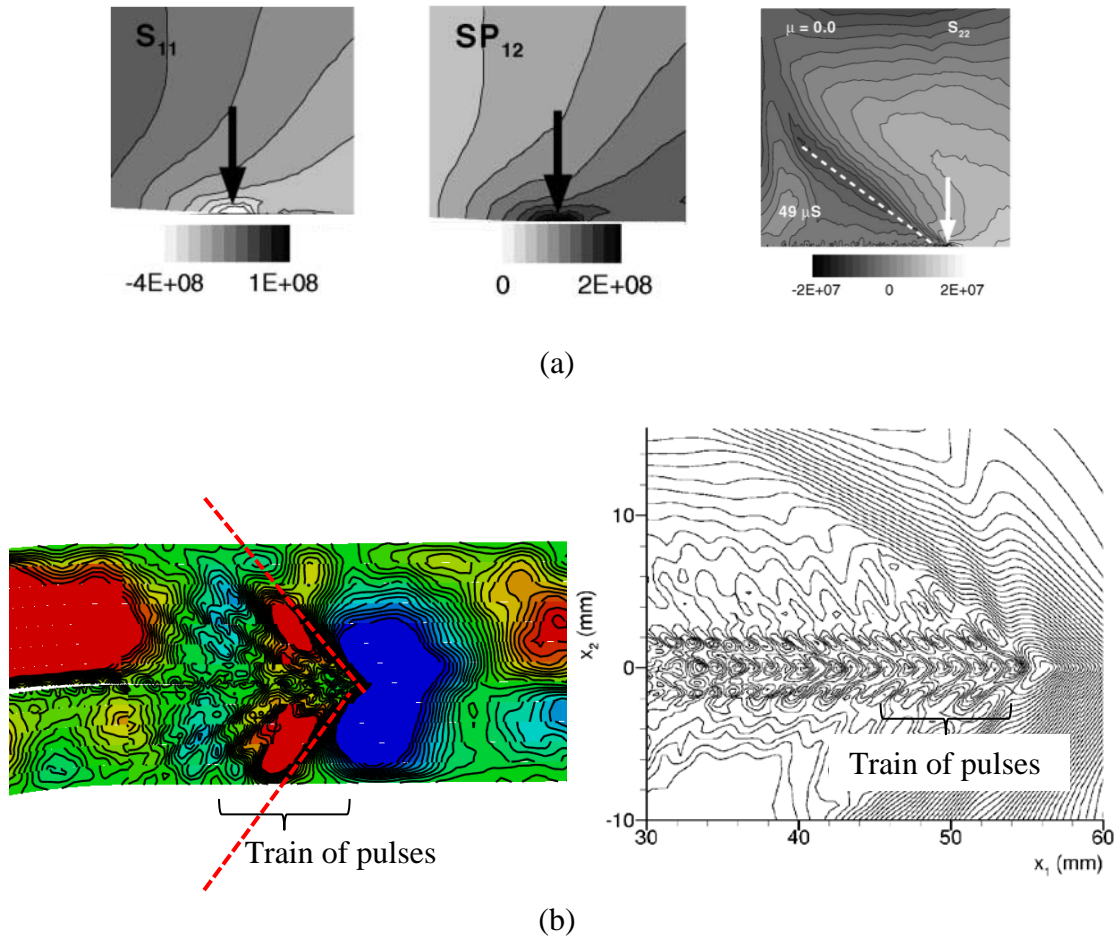
Figure 167 (a) Longitudinal (σ_{11}), maximum shear (principle σ_{12}) and normal stress (S_{22}) fringes obtained by Dwivedi and Espinosa [122] and (b) train of pulses obtained in our analysis and obtained by Coker et al. [217] in friction studies.

The experimental conditions that are used to obtain intersonic crack growth are generally based on "sudden loading". For instance, Rosakis et al. [111] used impact loading to reach intersonic crack growth emanating shear Mach waves as shown in Figure 168a. Rosakis et al. [111] applied high levels of kinetic energy by the impactor for exceeding the threshold to the intersonic regimes. Xia et al. [236] used small explosion at the epicenter of tilted interface under compression for the analysis of super-shear rupture (Figure 168b). On the other hand, the intersonic delamination in L-shaped composite laminates occurred spontaneously under quasi-static loading; without any means of sudden loading. An ordinary tension test machine is adequate to have the intersonic fracture in L-shaped composite laminates. Moreover, the

experiments of super-shear earthquakes and intersonic crack propagation studies in references used "idealized specimens" such as plates. On the other hand, the fracture of L-shaped composite laminates under shear loading occurs in its original shape without taking any precaution for the intersonic delamination. Moreover, a smooth transition from mode-I to mode-II while transitioning from sub-sonic to intersonic speeds is attained by the L-shaped composite laminates. Hence, L-shaped composite laminates may be used as a remarkable tool for investigating intersonic fracture showing both sub-Rayleigh and intersonic delamination under quasi-static loading.

(a)

(b)
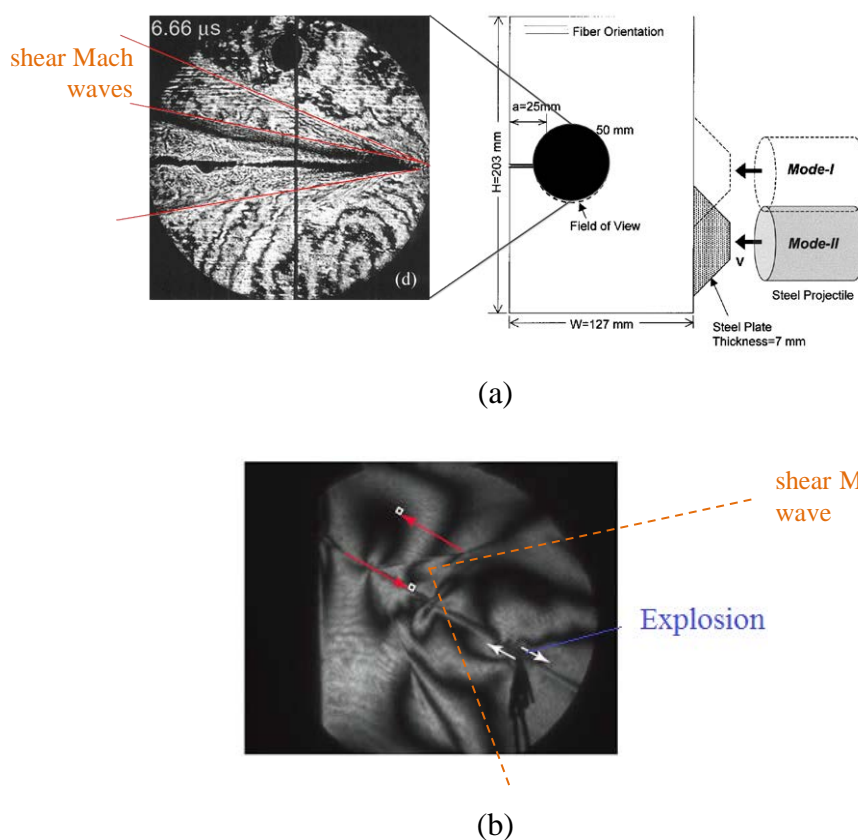
Figure 168 Shear Mach waves obtained using (a) impact loading [111] and (b) explosion devices [236].

One of the remarkable observations of this study is the intersonic delamination occurred under quasi-static loading. Intersonic crack propagation under quasi-static loading is generally seen in earthquakes which is a subject of geophysics. The energy

is stored by the earth crust in thousands of years. In the order of seconds, the crack propagation takes place, which is "instantaneous". The crack propagation speed in the 1999 earthquake of Gölcük, Turkey was shown to be intersonic, so called "super-shear" rupture, exceeding the seismic shear wave speed [237]. Figure 169a shows the fracture of North Anatolian Fault line where shear March wave is emanated from the right crack tip (Eastern) during super-shear rupture [238]. Same behavior is observed in L-shaped composite laminates in terms of intersonic crack propagation, emanation of shear Mach waves in both crack tips under quasi-static loading. A remarkable link between the kilometer scales to milimeter scales might have been established in terms of the same fracture behavior for engineering parts and earth crust by this study.

In addition to the scientific discussions mentioned in the previous paragraphs, there may be a contribution of our study to the aerospace industry in terms of validation of finite element models. Generally, finite element models are validated by experiments where load-displacement curves, the stress/strain data and the resulting failure modes are generally compared. Adequate number of experiments is required to establish a confidence level. These validations are required by the Airworthiness Authorities [10]. It is proposed that the parameters considered for the validation may involve crack tip speeds and the development of fracture pattern. As a result, the confidence level of the FEM can be further established in addition to typical parameters of load-displacement curves and stress/strain data. As an example, although BL CZM and RD CZM predicted the same failure load, RD CZM is further in agreement with the experiments in terms of crack tip speeds. Hence, RD CZM further extends the confidence of the reliability of the model compared to the BL CZM. As a result, the number of experiments to establish the confidence can be reduced since there would be more data to be evaluated by the validation experts. However, this approach needs further experimental instruments such as ultra-high speed camera as used in our analysis. Moreover, crack tip speed data cannot be easily obtained.
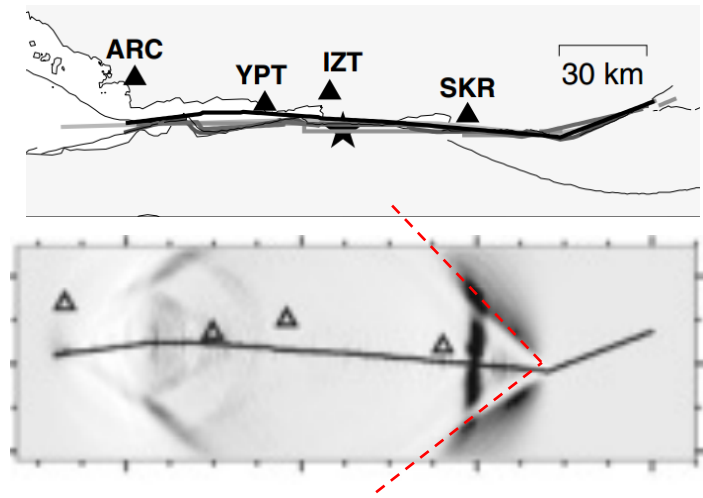
(a)
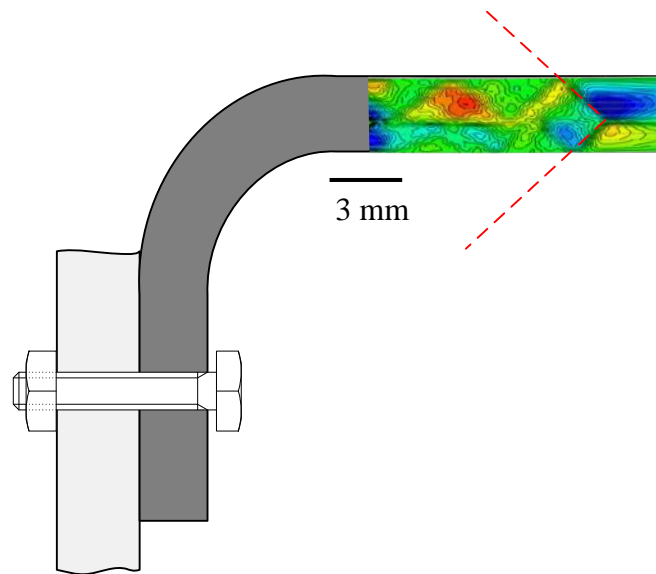
(b)

Figure 169 Shear Mach waves emanated from the crack tip (a) in the Golcuk Earthquake in 1999 [238] in the scales of kilometers and (b) in L-shaped composite laminate in the scales of millimeters (Shear Mach wave fronts are shown in red dash lines).

271

CHAPTER 6

SUMMARY AND CONCLUSIONS

6.1. Summary

In the introductory part, the definition of the problem and the literature survey are presented. It is shown that composite materials are sensitive to interfacial normal, defined as "opening stresses" which promotes mode-I fracture. The interfacial strength in the normal direction and toughness in mode-I are very weak in composite materials. On the other hand, opening stresses are induced in the L-shaped composite laminates due to the curved and thick geometry. Therefore, delamination in L-shaped composite laminates becomes a concrete problem in aerospace and wind energy industries after composite manufacturing technology enabled replacing metallic L-shaped parts with their composite counterparts. Literature about the L-shaped composite laminates generally focuses on the initiation of the delamination where they give consent that delamination is the main failure mode. The delamination in curved and thick composite laminates is reported as unstable. Numerical simulations about the propagation stage are either limited due to lack of propagation data from the experiments or the bad quality of the experimental specimens.

In the second part of the study, theoretical backgrounds including analytical solutions to the delamination problem and fracture mechanics are briefly discussed. CZM and its applications to the finite element analysis are presented. Next, traction-separation constitutive laws of BL and XN CZMs are derived. A new RD CZM based on a rate-dependency theorem presented by Corigliano et al. [155] are proposed using BL CZM formulations. It is shown that the interfacial strength and toughness are rate-dependent properties.

In the third part, the kinematic equations of a 4-noded interface element in compliant with all CZMs are derived. The cohesive interface element is implemented into ABAQUS/Explicit via VUEL user-subroutine. The issues of implicit and explicit FEA in conjunction with CZM are discussed. For the explicit FEA, examples of

oscillations in the load-displacement curves are presented. The reason is attributed to successive failure of the cohesive elements that create small disturbances eventually yielding vibrations. In references, the use of smaller cohesive elements and higher order CZMs to get rid of spurious oscillations are suggested.

In the fourth chapter, the implemented interface elements having the CZM formulations are validated for static mode-I, static mode-II, dynamic mode-I and dynamic mode-II dominated fractures by DCB, ELS, 3-Pt. Bending Impact and Asymmetric Composite-Polymer tests, respectively. The benchmark tests are further studied to reveal the effect of mesh size, crack tip definitions, rate-dependent interface properties and the type of body elements for piloting the simulations of L-shaped composite laminates. It is perceived that DCB is not a good example for studying the rate-dependency behavior of the RD CZM since inertial forces dominates the load-displacement curves before revealing the rate-dependent effects. The spurious oscillations after the start of delamination are observed in the DCB simulation. The oscillations are reduced by using smaller elements or XN CZM as suggested by Pinho et al [166]. ELS is the other example that is inefficient to study the influences of the rate-dependent interfacial properties. The damage distribution in the vicinity of mode-II crack tip is shown over the mode-II stress concentration in the ELS simulation. The length of cohesive zone for mode-II is so large that the fully damaged and partially damaged crack tip definitions are far away from each other. The effect of rate-dependency is investigated by the 3-Pt Bending Impact simulation. The rate dependency ratio of "k" is dominant in the early speeds of loading rate. Moreover, the crack tip speed curves become blunter and slower with the higher "k". In other words, the crack becomes more "viscous" during the propagation by RD CZM. The numerical study of asymmetric composite-polymer impact test manifested that the effect of RD CZM does not affect the critical crack propagation speed. The shear Mach waves are still observed using 4-noded single integration hourglass controlled body elements of CPE4R [69] that is the body element used in the simulations of L-shaped composite laminate. The implemented interface element using BL, XN and RD CZMs are successfully validated by the benchmark tests.

In the fifth part, intersonic delamination of curved and thick composite laminates in an L-shaped form is numerically studied using explicit FEA in conjunction with the

274

three CZMs. The main discussion is based on the modeling of all interfaces in a 12 layer woven fabric CFRP laminate using BL CZM. The specimen geometry and properties are taken from a recent experiment conducted at METU where ultra-high speed camera is utilized for capturing the fracture process and crack tip speeds. All the interfacial and material properties are either determined by independent experiments or taken from the material data sheet. Before presenting the numerical results, a synopsis is presented about shear and axial loading of L-shaped composite laminates. It is shown that moment loading that promotes the opening radial stresses is induced by shear loading. On the other hand, displacement controlled axial loading linearly induces the moment, which is an important analytical observation for stress engineering applications. Next, the experimental method, which is the reference study of our simulations, is briefly discussed. Following, two definitions of the crack tip, fully damaged ($d_{1.0}$) and partially damaged at 60% ($d_{0.6}$), are made. The fully damaged crack tip provides the closest definition to the experimentally observable crack tip albeit it loses the accuracy for following the stress concentration region during mode-II crack propagation. Hence, both definitions of the crack tips are illustrated in the results of BL CZM. In the next section, a loading scheme which is both fast and quasi-static is obtained after trial-and-error analyses in order to reduce the CPU time in our simulations. The fast-quasi-static loading approach is used throughout the study. Finally, the simulations are repeated using XN and RD CZMs.

6.2. Conclusions

Following are the conclusions that can be stated for the simulations of delamination in L-shaped composite laminates using BL CZM;

- Load-displacement curves are successfully predicted by BL CZM in terms of failure point and the compliance compared with the experimental results.
- Failure point in the load-displacement curves is associated with the delamination initiation whereas load-drop is associated with the propagation stage, supported by the experiments.
- Oscillations after the start of the delamination are observed in the load-displacement curves. The frequency of the oscillations is found around 50 kHz which is close to the frequency of vibrations in the experiments which was 33.3 kHz.

- The delamination is initiated at the 5th interface which is the main delamination in the experiments. Angular location of the initiation site and the maximum opening stress are found as 13° counter-clockwise from the centerline. This prediction is very close to the experimental results of specimen F2 which is at the 5th interface and 12° counter-clockwise from the centerline.

- Delamination propagates at the 5th interface that is the closest one to the maximum opening stress calculated by the analytical solution for our specimen geometry and material properties. However, the secondary delamination sites reported at the later stages of loading in the experiments are not captured by the numerical analysis. The delamination at the 5th interface propagates until ends of arms providing a similar picture of the experimental results. The specimen makes couple of cycles as the crack propagation takes place.

- Delamination initiates at intersonic speeds under mode-I condition. Consequently, the crack propagates towards the arms while transitioning from mode-I to mixed-mode condition in the curved region. In addition, the crack tip speeds transition from sub-Rayleigh to intersonic speeds as the fracture mode transitions from mixed-mode to mode-II condition in the arms.

- Fully damaged definition of the crack tip, $d_{1.0}$, provides the best representation of the crack tip in the curved region where mode-I dominates. As the mode transitions from mode-I to mode-II, partially damaged definition of the crack tip, $d_{0.6}$, provides better representation. The distance between the two crack tip definitions increases as the length of the cohesive zone increases by the mode-II condition.

- A shear Mach wave is emanated from the $d_{0.6}$ definition of the crack tip. The shear Mac wave is visible in the opening stress plots when the crack propagates at intersonic speeds in the arms. Similar formations of oblique stress waves, suggested to be reflecting waves of the initial shear Mach wave, are also observed. A second shear Mach wave appears for a short duration emanated from the $d_{1.0}$ definition of the crack tip while revealing "train of pulse" formations.

276

- Fully damaged, $d_{1.0}$, definition of the crack tip is selected for the main discussion since it provides the closest location to the experimentally observable crack tip and best prediction for the experimental crack tip speeds.

- Experimental crack tip speeds are concurring with the numerical predictions.

- All the energy transformation, as well as the main crack propagation process, takes less than 20 μs.

- Kinetic energy develops to considerable levels after it is triggered by initiation of delamination. Before the initiation, kinetic energy is negligibly small.

- The strain energy is harmonically transformed to kinetic energy in two phase vibrations. The first of the phases is high frequency vibration at 50 kHz that is very close to the experimental observation. The other vibration is at 500 Hz in larger amplitude.

- Particle velocity vector plots further supports the fact that the kinetic energy is triggered by the delamination. The motion of separation spreads from the initiation site towards the remaining parts of the specimen in several microseconds. Eventually, the motion of separation becomes specimen wide phenomenon. The separation motion spreads like a "whipping" action that is also observed in the experiments.

- Vortex like particle velocity patterns are observed in motion close to the crack tips. The vortex like particle velocity patterns become apparent at the mixed-mode zones near the curved region.

A parametric study of mesh density, modeling multiple cohesive lines and penalty stiffness is performed using BL CZM. Here are the conclusions drawn;

- Mesh density affects the load-displacement curves,

- Modeling single body element at each ply (thickness) causes incorrect prediction of the delamination pattern.

- Modeling multiple cohesive interfaces linearly increases the compliance of the specimen.

- Modeling soft penalty stiffness exponentially increases the specimen compliance. Hence, high penalty stiffness values are suggested in case of modeling multiple interfaces.

277

- Complaint CZMs spawn early sliding of plies that is defined as considerable relative displacement at adjacent interface nodes. This phenomenon yields tilted views of stress plots due to rigid body translation of stress contour lines.

- Using large number of body elements in the thickness reduces the stress discontinuities between the interfaces which is attributed to the incompatibility of the integration points between the body and interface elements.

- No considerable difference is observed between the predictions of multiple and single interface models using stiff penalty stiffness in BL CZM.

- Mesh density, penalty stiffness and multiple interface modeling are validated for BL and RD CZMs using appropriate penalty stiffness value.

- The modeling parameters used in the simulation of L-shaped composite laminates are validated.

The simulation is repeated with XN CZM using two different FE models. XN CZM does not have independent penalty stiffness value that can be adjusted for getting rid of the numerical artifacts discussed in the parametric study of BL CZM. Moreover, the approximate penalty stiffness, initial slope, of XN CZM is very close to the penalty stiffness of the compliant BL CZM used in the parametric study. Hence, the first model has all interfaces modeled whereas the second model has single interface at the 5th interface. The main discussion is made over the comparison to BL CZM and the influences of using multiple interfaces in XN CZM. The conclusions are;

- XN CZM slightly overshoots the failure point in the load-displacement curves around 5.5% compared to experimental results. The XN CZM model with multiple interfaces shows higher compliance during the loading stage. The delamination pattern is the same with the BL CZM.

- Angular location of the maximum stress and the initiation points are predicted as 21° and 18°, respectively. Namely, the delamination is not initiated where the maximum stress is attained. The location of the initiation is more deviant from the experimental result compared to the BL CZM.

- XN CZM exhibits early slippage of the plies for the multiple interface model. The problem of early slippage of plies is not observed in the single interface model.

278

- Shear stress contours reveal circular patterns of stress concentrations inside each ply. This is attributed to the slippage of plies.

- Shear Mach waves are not as clear as in BL CZM for both single and multiple interface models.

- The crack tip speeds are in fair agreement with the experimental results and slower than BL CZM.

- Intersonic crack tip speeds are attained only in the vertical arm.

- Early slippage of the plies artificially dissipates considerable fracture energy before released by the delamination for the multiple interface model.

- Minor healing of cracks are observed in terms of small reductions in the fracture energy curves that is attributed to the reversible formulation of XN CZM.

- Angular location of the failure point and crack tip speed profiles of XN CZM cannot be attained using BL CZM by varying the penalty stiffness value. Hence, the studies on XN and BL CZMs revealed that influences of CZM profiles are prominent in L-shaped composite laminates.

The third model of RD CZM is used to simulate the same problem. The following conclusions are made;

- Load-displacement curves are exactly the same with the BL CZM. Spurious oscillations in the load-displacement curves still exist for RD CZM.

- Similar stress contours observed in the BL CZM are acquired. Train of pulses in the opening stress contours is apparent in the simulations of RD CZM.

- Crack tip speeds calculated by RD CZM are generally between BL CZM and XN CZM. RD CZM provides the best prediction among the all CZMs compared to the experimental results.

- The kinetic energy is smaller for the RD CZM simulation whereas the fracture energy is increased about 25% due to toughening of the interface by rate-effects. The decrease in the kinetic energy is attributed to the less available energy in the external work due to higher dissipated fracture energy.

Three observations from the simulations are revisited after the simulations of the CZMs. Firstly, neither changing the mesh size nor using XN CZM ameliorates

oscillatory response of the L-shaped composite laminates after the initiation. Hence, the oscillations in the L-shaped composite laminates are suggested to be associated with the unstable crack propagation. The oscillations in the load-displacement curves are diminished by introduction of mass proportional damping into the system. It is shown that load-displacement and crack tip speed curves are negligibly affected by the damping. The specimen was able to be damped after several cycles in the experiments. Hence, the experimental evidence supported the proposal of using high levels of damping. Following the discussion about damping, a new definition of the crack tip as a function of phase angle is proposed. The new crack tip definition covers all fracture modes as well as it continuously follows the stress concentration region throughout the propagation. Finally, the other delamination sites are attained at larger displacements of loading where the order of delamination initiations is in perfect agreement with the study of Martin [56]. In aerospace industry, crack tip speeds and development of fracture pattern can be included as new parameters for the validation of FEMs. The confidence level of the FEM can be further established in addition to load-displacement curves and stress/strain data. As a result, the number of validation tests can be reduced.

Shear Mach waves and train of pulses were reported in literature. Train of pulses is generally encountered in sliding experiments where the friction is studied. Although no friction is modeled in our simulations, the train of pulses can be observed in L-shaped composite laminates. Shear Mach waves were reported in the simulations of fracture under impact loading or explosively triggered fractures as a subject of geophysics. In our study, shear Mach waves are observed under quasi-static loading. To the best of author's knowledge, it is the first time that an engineering specimen exhibits intersonic delamination which is induced by quasi-static loading. Moreover, the delamination in our case smoothly transitions from mode-I to mode-II as the crack tip gradually transitions from sub-Rayleigh to intersonic speeds. In literature, intersonic delamination is generally studied using specific experimental setups which guarantee the dynamic fracture. On the other hand, the dynamic fracture in this study can be studied by using simple tension test machine. Therefore, L-shaped composite laminate might be an effective tool for studying intersonic cracks in wide variety

of applications including super-shear rupture in earth fault lines and catastrophic failure in aerospace structures.

6.3. Future Work

In the future, the numerical modeling approach can be further extended. Firstly, 3D modeling of the delamination can be used. This would enable simulating more complicated geometries as well as studying free-edge-effects in the composite laminates. Modeling the problem by 3D elements would enable studying mode-III fracture.

Modeling mechanisms for kinking of delamination can be introduced to the model as kinking has been frequently observed in most of the experiments. The simplest method for utilization of kinking can be modeling of inplane damage in the plies, such as matrix cracking, fiber cracking. Damaged plies may allow the delamination to branch towards the adjacent interfaces which would be a kinking. However, modeling of kinking through inplane damages does not reflect the correct behavior from fracture mechanics point of view. A more complicated and robust modeling technique of XFEM can be used. XFEM can be coupled with cohesive elements for modeling both kinking and delamination in a single model that would rely on fracture mechanics. Instead of XFEM, cohesive elements can be located between all the triangular body elements where two different types of cohesive elements would exist. In this case, very high penalty stiffness or rigid-linear CZMs can be used. Moreover, VUEL subroutine will be enhanced to work with sequential analysis method [88]. As a result, the solution duration of the numerical analyses will be considerably reduced.

In addition to the numerical methodology, the observations of this study should be further investigated. Firstly, other delamination sites at the curved region observed in the experiments were not captured by our simulations. It can be observed that the delaminated parts cannot reach to the interfacial strength of the laminate. Introduction of viscoelasticity to the laminate bulk may increase the stiffness of the plies. The stresses may increase due to the introduction of viscoelasticity and they may reach to interfacial strength under high strain rates attained during dynamic fracture. This may enable predicting the other delaminations during the same load drop. Hence, the simulations should be repeated by introducing viscoelasticity in the

composite bulk. In addition to prediction of other delamination sites, the transition of sub-Rayleigh to intersonic crack tip speeds suggests that there should be a mother-daughter crack mechanism during the transition. Unfortunately, mother-daughter crack mechanism has not been observed in our study. Similarly, the formation of train of pulses should be investigated in more detail. Actually, mechanism of the transition is an important subject to further work on.

REFERENCES

1. Bruhn EF. Analysis and Design of Flight Vehicle Structures. 2nd Ed. 1973. (ISBN-10: 0961523409)

2. Niu MCY. Airframe Structural Design. 2nd Edition. Hong Kong Conmilit Press Ltd, 2002, ISBN 962-7128-09-0. Print.

3. Sørensen BF, Jørgensen E, Debel CP, Jensen FM, Jensen HM, Jacobsen TK, Halling KM. Improved design of large wind turbine blade of fibre composites based on studies of scale effects (Phase 1) - Summary Report. Risø National Laboratory Denmark, 2004, Risø-R-1390(EN).

4. Ultra-Lightweight materials for Aerospace – An AIAA Information Page, American Institute of Aeronautics and Astronautics (2013). Retrieved October 15, 2013, from

   http://www.aiaa.org/uploadedFiles/Issues_and_Advocacy/Aeronautics.

5. Jones RM. Mechanics of Composite Materials. 2nd Edition. Taylor and Francis, Philadelphia, Pa, USA, 1999. Print.

6. Facts & Figures: A350 XWB Eco-Efficiency, Airbus S.A.S. Press Center (2013), Retrieved October 15, 2013 from

   http://www.airbus.com/presscentre/presskits/?eID=dam_frontend_push&docID=27412.

7. 787 Dreamliner Fact Sheet, Boeing Company (2009), Retrieved October 15, 2013 from

   http://www.boeing.com/boeing/commercial/787family/programfacts.page.

8. Naji MI and Hoa SV. Curing of thick angle-bend thermoset composite part: Curing cycle effect on thickness variation and fiber volume fraction. Journal of Reinforced Plastics and Composites 1999;18:702-723.

9. Personal Communication, Composite Manufacturing Department of Turkish Aerospace Industries (TAI), 2013.

10. Certification Specifications – Large Aero planes - CS25. Amendment 3. European Aviation Safety Agency (EASA) December 11, 2012. Print.

11. Yang Q, Cox B. Cohesive Models for Damage Evolution in Laminated Composites. Rockwell Scientific Co., LLC, 1049 Camino Dos Rios, Thousand Oaks, CA 91360, USA, 2005.

12. Bolotin VV. Delaminations in composite structures: its origin, buckling, growth and stability. Composites: Part B 1996;27B:129-145.

13. Tsai SW. Strength Theories of Filamentary Structures. Fundamental Aspects of Fiber Reinforced Plastic Composites, RT Schwartz and HS Schwartz, Eds. Wiley Interscience New York, 1968;3-11.

14. Dahlen C and Springer GS. Delamination growth in composites under cyclic loads. Journal of Composite Materials 1994;28:732-781.

15. Sridharan S. Delamination behaviour of composites. CRC Press LLC, 2008. Print.

16. Sharma AV. Low-velocity impact tests on fibrous composite sandwich structures. In: Test Methods and Design Allowable for Fibrous Composites, ASTM STP 734, 1981:54-70.

17. Abrate S. Impact on laminated composite materials. Applied Mechanics Review 1991;44:155-190.

18. O'Brien TK. Mixed mode strain energy release rate effects on edge delamination of composites. Effects of Defects in Composite Materials ASTM STP 836. DJ Wilkins ed. American Society for Testing and Materials, Philadelphia PA, 1984;125-142.

19. Curry JM, Johnson ER, Starnes JH. Effect of dropped plies on the strength of graphite-epoxy laminates. Paper no. AIAA 87-0874. In Proc. AIAA/ASME/ACE/AHS 28th Structures, Structural Dynamics and Materials Conf., Monterey, 1987;737-747.

20. Chang F and Springer GS. The strength of fiber reinforced composite bends. Journal of composite materials 1986;20:30-45.

21. Hill R. A theory of yielding and plastic flow of anisotropic metals. Proceedings of the Royal Society, London, 1948 Series A;193:281-297.

22. Tong L and Steven G. Analysis and design of structural bonded joints. Dordrecht: Kluwer; 1999.

23. Kim R and Soni SR. Experimental and analytical studies on the onset of delamination in laminated composites. Journal of Composite Materials 1984(18);4:70–80.

24. Ye L. Role of Matrix Resin in Delamination Onset and Growth in Composite Laminates. Composites Science and Technology 1988;33:257-277.

25. Brewer JC and Lagace PA. Quadratic Stress Criterion for Initiation of Delamination. Journal of Composite Materials, 1988(22);12:1141-1155.

26. Puck A and Schurmann H. Failure Analysis of FRP Laminates by Means of Physically Based Phenomenological Models. Composites Science and Technology, 2002;62:1633-1662.

27. O'Brien T K. Composite Interlaminar Shear Fracture Toughness, G_{IIc}: Shear Measurement of Sheer Myth?. ASTM-STP 1330, American Society for Testing and Materials, 1998:3-18.

28. ASTM Standard D6415/D6415M, 2006. Standard test method for measuring the curved beam strength of a fiber–reinforced polymer–matrix composite. ASTM International, West Conshohocken PA, 2006, DOI: 10.1520/D6415_D6415M, www.astm.org.

29. ASTM Standard D2344, 2006. Standard Test Method for Short-Beam Strength of Polymer Matrix Composite Materials and Their Laminates. ASTM International, West Conshohocken PA, 2006, DOI: 10.1520/D2344_D2344M, www.astm.org.

30. Griffith AA. The phenomena of rupture and flow in solids. Philosophical Transactions of the Royal Society of London 1921;A221:163–198.

31. Anderson TL. Fracture Mechanics: Fundamentals and Applications. 2nd Ed. CRC Press LLC 1995. Press.

32. ASTM Standard D5528, 2007. Standard Test Method for Mode I Interlaminar Fracture Toughness of Unidirectional Fiber-Reinforced Polymer Matrix Composites. ASTM International, West Conshohocken PA, 2007, DOI: 10.1520/D5528_D5528M, www.astm.org.

33. ASTM Standard WK22949. New Test Method for Determination of the Mode II Interlaminar Fracture Toughness of Unidirectional Fiber-Reinforced Polymer Matrix Composites Using the End-Notched Flexure (ENF) Test. ASTM International, West Conshohocken PA, www.astm.org.

34. Hutchinson JW, Suo Z. Mixed mode cracking in layered materials. Advances in Applied Mechanics 1992;29:63–191.

35. ASTM Standard D6671/D6671M, 2006. Standard Test Method for Mixed Mode I-Mode II Interlaminar Fracture Toughness of Unidirectional Fiber Reinforced Polymer Matrix Composites. ASTM International, West Conshohocken PA, 2007, DOI: 10.1520/ D6671_ D6671M, www.astm.org.

36. Benzeggagh ML, Kenane M. Measurement of Mixed-Mode Delamination Fracture Toughness of Unidirectional Glass/Epoxy Composites with Mixed-Mode Bending Apparatus. Composites Science and Technology 1996;56:439–449.

37. Reeder JR. 3D Mixed-Mode Delamination Fracture Criteria–An Experimentalist's Perspective. Proceedings of the 21st American Society for Composites Technical Conference, Dearborn, MI, 2006.

38. Wu EM and Reuter RC Jr. Crack Extension in Fiberglass Reinforced Plastics. T&AM Report No. 275, Department of Theoretical and Applied Mechanics, University of Illinois, Urbana, IL, February 1965.

39. New Cracks Found in the Wings of Some Airbus Planes, The New York Times, 20.01.2012. Retrieved February 22, 2012 from: http://www.nytimes.com/2012/01/20/business/global/a380-jets-may-get-closer-inspections.html?_r=1&adxnnl=1&adxnnlx=1330264957-YWtr4fefgIvKExc6rrqAtA

40. Timoshenko S and Goodier JN. Theory of Elasticity. McGraw-Hill Book Company, 1951. Print.

41. Lekhnitskii SG. Theory of elasticity of an anisotropic body. Mir Publishers. Moscow. 1981. Print.

42. Jimenez MA and Miravete A. Application of the Finite-Element Method to Predict the Onset of Delamination Growth. Journal of Composite Materials 2004;38:1309-1335.

43. Pagano NJ. Exact solutions for composite laminates in cylindrical bending. Journal of Composite Materials 1969;3:398-411.

44. Sun CT and Kelly SR. Failure Analysis of Composite Angle Structures. Developments in the Science and Technology of Composite Materials,

286

Proceedings of First European Conference on Composite Materials and Exhibition, Bordeux, France 1985:277-284.

45. Sun CT and Kelly SR. Failure in Composite Angle Structures Part I: Initial Failure. Journal of Reinforced Plastics and Composites 1988 7:220-232.

46. Sun CT and Kelly SR. Failure in Composite Angle Structures Part II: Onsetof Delamination. Journal of Reinforced Plastics and Composites 1988 7:233-244.

47. Krueger R. The Virtual Crack Closure Technique: History, Approach and Applications. NASA Icase Report 2002;10.

48. Kedward KT, Wilson RS, McLean SK. Flexure of Simply Curved Composite Shapes. Composites 1989.20;6:527-536.

49. Kardomateas GA. Bending of a cylindrically orthotropic curved beam with linearly varying elastic constants. The Quarterly Journal of Mechanics and Applied Mathematics 1990;43(1):43-55.

50. Kardomateas GA. End force loading of generally anisotropic curved beams with linearly varying elastic constants. International Journal of Solids and Structures 1991;21:59-71.

51. Ko WL and Jackson HJ. Multilayer Theory for delamination analysis of a composite curved bar subjected to end forces and end moments. NASA Technical Memorandum 4139, 1989.

52. Tolf G. Stresses in a curved laminated beam. Fiber Science and Technology 1983;19(4):243-267.

53. Ko WL and Jackson HJ. Open-mode delamination stress concentrations in horseshoe and elliptic composite curved bars subjected to end forces. NASA Technical Memorandum 4164, 1990.

54. Hiel CC, Sumich M, Chappel DP. A Curved Beam test Specimen for Determining the Interlaminar Strength of a Laminated Composite. Journal of Composite Materials 1991;25:854-868.

55. O'Brien TK and Salpekar SA. Scale Effects on the Transverse Tensile Strength of Graphite Epoxy Composites. NASA TM107637, June 1991.

56. Martin RH. Delamination failure in a unidirectional curved composite laminate. Composite Materials Testing 1992;10:365–83.

57. NASTRAN User's Manual, Version 65, Document No. MSR-39, MacNeal-Schwendler Corporation, November 1985. Print.

58. Martin RH and Jackson WC. Damage prediction in cross-plied curved composite laminates. Composite materials: Fatigue and Fracture, ASTM STP 1156, W. W. Stinchcomb and N. E. Ashbaugh, Eds., American Society for Testing and Materials, Phledelphia, 1993;4:105 – 126.

59. Qatu MS. Theories and analyses of thin and moderately thick laminated composite curved beams. International Journal of Solids and Structures 1993;30(20):2743–2756.

60. Lu TJ, Xia ZC, Hutchinson JW. Delaminations of beams under transverse shear and bending. Materials Science and Engineering 1994;A188:103-112.

61. Rice JR. A Path Independent Integral and the Approximate Analysis of Strain Concentration by Notches and Cracks. Journal of Applied Mechanics, 1968:379-386.

62. Shivakumar KN, Allen HG, Avva VS. Interlaminar Tension Strength of Graphite/Epoxy Composite Laminates. AIAA Journal 1994;32(7):1478-1484.

63. Wisnom MR and Jones MI. Delamination due to interaction between curvature induced interlaminar tension and stresses at terminating plies. Composite Structures 1995:32;615-620.

64. Cui W, Liu T, Len J, Ruo R. Interlaminar tensile strength (ILTS) measurement of woven glass/polyester laminates using four-point bending curved beam specimen. Composites Part A 1996;27A:1097-1105.

65. Cox BN, Massabo R, Kedward KT. Suppression of delaminations in curved structures by stitching. Composites Part A 1996;27A:1133-1138.

66. Lu TJ and Hutchinson JW. Role of fibre stitching in eliminating transverse fracture in cross-ply ceramic composites. Journal of American Ceramic Society 1995;78(1):251-253.

67. Fraternali F and Bilotti G. Nonlinear Elastic Stress Analysis in Curved Composite Beams. Computers and Structures 1997;62(5):837-859.

68. Kaczmarek K, Wisnom MR, Jones MI. Edge Delamination in Curved $(0_4/\pm45_6)$s Glass-Fibre/Epoxy Beams Loaded in Bending. Composites Science and Technology 1998;58:155-161.

69. ABAQUS User Manual. Pawtucket (RI); Hibbitt, Karlsson& Sorensen Inc.; 2009. Print.

70. Naji MI and Hoa SV. Curing of thick angle-bend thermoset composite part: Curing cycle effect on thickness variation and fiber volume fraction. Journal of Reinforced Plastics and Composites 1999;18:702:723.

71. RA and Wang W. Through-thickness stresses in curved composite laminates and sandwich beams. Composites Science and Technology 2001;61:1501–1512.

72. Münch A and Ousset Y. Numerical simulation of delamination growth in curved interfaces. Computer Methods in Applied Mechanics and Engineering. 2002;191:2045-2067.

73. Figiel L, Kaminski M. Mechanical and thermal fatigue delamination of curved layered composites. Computers and Structures, 2003;81:1865–1873.

74. User's Manual, ANSYS v.5.5.3, 1999.

75. Figiel L, Zafeiropoulos NE, Lauke B. Numerical analysis of the elastic constants' effect on the delamination propagation in a curved layered composite beam under cyclic shear loading. Composites: Part A 2005;36:153–162.

76. Feih S. Shercliff HR. Composite failure prediction of single-L joint structures under bending, Composites: Part A 2005;36:381–395.

77. Wisnom M. 3D finite element analysis of curved beams in bending. J Comp Mater 1996;30:1178–1190.

78. Ecsedi I, Dluhi K. A linear model for the static and dynamic analysis of non-homogeneous curved beams. Applied Mathematical Modeling 2005;29:1211–1231.

79. Wimmer G, Schuecker C, Pettermann HE. Numerical simulation of delamination onset and growth in laminated composites. The e-Journal of Nondestructive Testing 11 (12) – special issue "Online proceedings of the CDCM 2006 – Conference on Damage in Composite Materials", 2006.

80. Ross R, Kress G, Barbezat M, Ermanni P. Enhanced model for interlaminar normal atress in singly curved laminates. Composite Structures 2007;80:327-333.

81. Vanttinen A. Strength Prediction of Composite Rib Foot Corner. MSc Thesis, Helsinki University of Technology, 2008.

82. ESDU 84039. Strength of Angles and Club-Foot Fittings, Amendment A. London, Great Britain: Engineering Science Data Unit, 1984, ISBN 978 0 85679 503 9.

83. Wimmer G and Pettermann HE. A semi-analytical model for the simulation of delamination in laminated composites. Composites Science and Technology 2008;68:2332-2339

84. Wimmer G, Kitzmüller W, Pinter G, Wettemann T, Pettermann HE. Computational and Experimental Investigation of Delamination in L-shaped Laminated Composite Components. Engineering Fracture Mechanics 2009;76:2810-2820.

85. Wimmer G, Pettermann HE. Prediction of delamination growth in laminated structures loaded by quasi-static and cyclic loads. Journal of Composite Materials 2009;43:3303-3324.

86. Avalon SC and Donaldson SL. Strength of Composite Angle Brackets with Multiple Geometries and Nano fiber-Enhanced Resins. Journal of Composite Materials 2010;45(9):1017-1030.

87. Hao W, Ge D, Ma Y, Yao X, Shi Y. Experimental Investigation on Deformation and Strength of Carbon/Epoxy Laminated Curved Beams, Polymer Testing 2012;31: 520–526.

88. Gozluklu B and Coker D. Modeling of the dynamic delamination of L-shaped unidirectional laminated composites. Composite Structures 2012;94:1430–1442.

89. Gozluklu B and Coker D .Modeling of Dynamic Delamination in L-Shaped Composite Brackets. Proc. of International Mechanical Engineering Congress and Exposition (IMECE 2013), IMECE2012-87831, Houston, USA, 2012.

90. Gozluklu B, Coker D. Modeling of Dynamic Delamination in L-shaped Composite Brackets. Proceedings of 6th European Congress on Computational Methods in Applied Sciences and Engineering (ECCOMAS 2012) Vienna, Austria, September 10-14, 2012.

91. Ravi-Chandar K. Dynamic fracture. 2004, Elsevier, Oxford, UK. ISBN: 0-08-044352-4. Print.

92. Gozluklu B, Yavas D, Coker D. Effect of Thickness and Pre-Crack Length on Delamination of Unidirectional L-Shaped Laminated Composites. Proceedings

of 6th European Congress on Computational Methods in Applied Sciences and Engineering (ECCOMAS 2012) Vienna, Austria, September 10-14, 2012.

93. Yavas D, Gozluklu B, and Coker, D. Investigation of Crack Growth Along Curved Interfaces in L-shaped Composite and Polymers. J. Carroll (ed.) Fracture and Fatigue 2014;7:45-50.

94. Yavas D. Experimental and Computational Investigation of Crack Growth along Curved Interfaces. MSc Thesis, Middle East Technical University, 2013.

95. Fraternali F, Spadea S, Ascione L. Buckling behavior of curved composite beams with different elastic response in tension and compression. Composite Structures 2013;100:280–289.

96. Krueger R, Citkovich MK, O'Brien TK, Minguet PJ. Testing and Analysis of Composite Skin/Stringer Debonding Under Multiaxial Loading. Journal of Composite Materials 2000;34:1263–1300.

97. Inglis CE. Stresses in a Plate due to the Presence of Cracks and Sharp Corners. Transactions of the Royal Institution of Naval Architects 1931;55:219–241.

98. Orowan E. Energy Criterion of Fracture. Welding Journal 1955;34:1575–1605.

99. Irwin GR. Fracture Dynamics. Fracturing of Metals 1948, 147–166.

100. Westergaard HM. Bearing pressures and cracks. Journal of Applied Mechanics 1939;6:49-53.

101. Williams ML. On the stress distribution at the Base of a Stationary Crack. Journal of Applied Mechanics 1957;24:109-114.

102. Erdogan F. Stress Distribution in Bonded Dissimilar Materials with Cracks. Jnl. Applied Mechanics, Trans. ASME 1965;32:403–410.

103. Raju IS, Crews JH, Aminpour MA.Convergence of Strain Energy Release Rates Components for Edge-delaminated Composite Laminates. Engineering Fracture Mechanics 1988;30:383–396.

104. Irwin GR. Fracture Handbuck der Physik. Berlin, Springer 1958;6:551–590.

105. Rybicki EF and Kanninen MF. A Finite Element Calculation of Stress Intensity Factors by a Modified Crack Closure Integral. Engineering Fracture Mechanics 1977;9:931–938.

106. Allix O, Ladeveze P, Leveque D and Perret L 1997. On the identification of an interface damage model for the prediction of delamination initiation and growth. in Rossmanith (ed) Damage and Failure of Interfaces 1997; 153:160.

291

107. Corigliano A, Allix O. Some aspects of interlaminar degradation in composites. Computational Methods in Applied Mechanics and Engineering 2000;185:203–24.

108. Wells AA. Unstable crack propagation in Metals: Cleavage and Fast Fracture. Proceedings of the Crack Propagation Symposium, Vol. 1, Paper 84, Cranfield, UK, 1961.

109. Freund LB. Dynamic Fracture Mechanics. Cambridge University Press, Cambridge, UK, 1990. Print.

110. Sun CT and Jin Z-T. Fracture Mechanics. Academic Press, Elsevier, 2012. Print.

111. Rosakis AJ, Samudrala O, Coker D. Cracks Faster than the Shear Wave Speed. Science 1999;284(5418):1337-1340.

112. Coker D, Rosakis AJ, Needleman A. Dynamic Crack Growth along Polymer Composite-Homalite Interface. Journal of the Mechanics and Physics of Solid 2003;51:425-460.

113. Broberg KB. The near-tip field at high crack velocities. International Journal of Fracture 1989;39:1-13.

114. Yoffe EH. The moving Griffith crack. Philosophical Magazine 1951;42:739-750.

115. Fineberg J, Gross SP, Marder MHL. Swinney, Physical Review Letters 1991;67:141.

116. Washabaugh PD, Knauss WG. A reconciliation of dynamic crack velocity and Rayleigh wave speed in isotropic brittle solids. International Journal of Fracture 1994;65(2):97-114.

117. Rosakis AJ. High Speed Failure Phenomena in Heterogeneous Material Systems at All Length Scales – A Revival. Experimental Techniques: Trends in Experimental Mechanics 2003, 27:12-14.

118. Coker D and Rosakis AJ. Experimental observations of intersonic crack growth in asymmetrically loaded unidirectional composite plates. Philosophical Magazine A 2001;81(3):571-595

119. Kalthoff JF, Winkler S. Failure mode transition at high rates of shear loading. In: Chiem, C., Kunze, H.-D., Meyer, L.W. (Eds.), Impact Loading and Dynamic Behavior of Materials 1987(1):185–195.

120. Hao S, Liu WK, Klein PA, Rosakis AJ. Modeling and Simulation of intersonic crack growth. International Journal of Solids and Structures 2004;41:1773-1799.

121. Huang Y, Wang W, Liu C, Rosakis AJ. Analysis of intersonic crack growth in unidirectional fiber-reinforced composites. Journal of the Mechanics and Physics of Solids 1999;47:1893-1916.

122. Dwivedi SK and Espinosa HD. Modeling dynamic crack propagation in fiber reinforced composites including frictional effects. Mechanics of Materials 2003;35:481–509.

123. Burridge R. Admissible speeds for plane strain shear cracks with friction but lacking cohesion. Geophysical Journal of the Royal Astronomical Society 1973;35:439–455.

124. Sih GC, Embley GT, Ravera RS. Impact response of a finite crack in plane extension. International Journal of Solids and Structures 1972;8:977-993.

125. Atkinson C and Eshelby JD. The flow of energy into the tip of a moving crack. Int. J. Fract. Mech. 1968;4:3-8.

126. Nakamura T, Shih CF, Freund LB. Computational methods based on an energy integral in dynamic fracture. International Journal of Fracture 1985;27:229-249.

127. Meyers MA. Dynamic Behavior of Materials. Wiley, 1994. Print.

128. Nakamura T, Shih CF, Freund LB. Analysis of a dynamically loaded three-point-bend ductile fracture specimen. Engineering Fracture Mechanics 1986;25:323-339.

129. Dugdale DS. Yielding of Steel Sheets Containing Slits. Journal of Mechanics and Physics of Solids, 1960;8:100-104.

130. Barenblatt GI. Mathematical Theory of Equilibrium Cracks in Brittle Failure. Advances in Applied Mechanics 1962;7.

131. Oxborough RJ and Bowden PB. A general Critical-Strain Criterion for Crazing in Amorphous Glassy Polymers. Philosophical Magazine 1973;28:547-559.

132. Sørensen BF and Jacobsen TK. Determination of cohesive laws by the J integral approach. Engineering Fracture Mechanics 2003;70:1841–1858.

133. Hillerborg A, Modeer M, Petersson PE. Analysis of crack formation and crack growth in concrete by means of fracture and finite elements. Cement and Concrete Research 1976;6:773-781.

134. Lennard-Jones. On the Determination of Molecular Fields. Proceedings of the Royal Society of London 1924;738:463–477

135. Gozluklu B. Delamination Analysis by using Cohesive Interface Elements in Laminated Composites. MSc Thesis. Middle East Technical University 2009.

136. Mohammed I and Liechti KM. Cohesive zone modeling of crack nucleation at bimaterial corners. Journal of the Mechanics and Physics of Solids 2000;48:735-764.

137. Shet C and Chandra N. Analysis of Energy Balance When Using Cohesive Zone Models to Simulate Fracture Processes. Journal of Engineering Materials and Technology 2002: 124;440-450.

138. Xu XP and Needleman A. Numerical simulations of fast crack growth in brittle solids. J Mech Phys Solids 1994;32(9):1397–434.

139. Borg R, Nilsson L, Simonsson K. Simulation of delamination in fiber composites with a discrete cohesive failure model. Composite Science and Technology 2001;61:667–677.

140. Allix O and Ladeveze P. Interlaminar interface modelling for the prediction of delamination. International Journal of Composite Structures 1992;22:235-242.

141. Camacho GT, Ortiz M. Computational Modeling of Impact Damage in Brittle Materials. International Journal of Solids and Structures 1996;33:2899-2938.

142. Kachanov LM. Time of the Rupture Process under Creep Conditions. Izv. Akad. Nauk. USSR, 1958;8:26-31 (in Russian).

143. Lemaitre J and Desmorat R. Engineering Damage Mechanics. Springer, 2005. Print.

144. Alfano G and Crisfield MA. Finite Element Interface Models for the Delamination analysis of Laminated Compostes; Mechanical and Computational Issues. International Journal for Numerical Methods in Engineering 2001;50:1701-1736.

145. Allix O and Corigliano A. Modeling and simulation of crack propagation in mixed-mode interlaminar fracture specimens. International Journal of Fracture 1996;77:111–40.

146. Qiu Y, Crisfield MA, Alfano G. An interface element formulation for the simulation of delamination with buckling. Engineering Fracture Mechanics 2001;68:1755–76.

147. Xu XP and Needleman A. Void nucleation by inclusion debonding in a crystal matrix. Modelling and Simulation in Materials Science and Engineering 1993;1:111-132.

148. Rose JH, Ferrante J, Smith JR. Universal binding energy curves for metals and bimetallic interfaces. Physical review Letters 1981;47:675–8.

149. Rose JH, Smith JR, Ferrante J. Universal features of bonding in metals. Physical Reviews 1983;28:1835–45.

150. Needleman A. A Continuum Model for Void Nucleation by Inclusion Debonding. Journal of Applied Mechanics 1987;54:525-531.

151. Rice JR, Wang. Embrittlement of Interfaces by Solute Segregation. Materials Science and Engineering 1989;107:23–40.

152. Shahwan KW, Waas AM. Non-Self-Similar Decohesion along a Finite Interface of Unilaterally Constrained Delamination. Proceedings: Mathematical, Physical and Engineering Sciences 1958;435:515-550.

153. van den Bosch MJ, Schreurs PJG, Geers MGD. An improved description of the exponential Xu and Needleman cohesive zone law for mixed-mode decohesion. Engineering Fracture Mechanics 2006;73:1220–1234.

154. Davies GAO, Hitchings D, Ankersen J. Predicting delamination and debonding in modern aerospace composite structures. Composites Science and Technology 2006;66:846–854

155. Corigliano A, Mariani S, Pandolfi A. Numerical modeling of rate-dependent debonding processes in composites. Composite Structures 2003;61:39-50.

156. Corigliano A, Mariani S, Pandolfi A. Numerical analysis of rate-dependent dynamic composite delamination. Composites Science and Technology 2006;66:766-775.

157. Needleman A and Rosakis AJ. The effect of bond strength and loading rate on the conditions governing the attainment of intersonic crack growth along an interface. Journal of the Mechanics and Physics of Solids 1999;47:2411–49.

158. Wisnom MR and Chang F-K. Modelling of splitting and delamination in notched cross-ply laminates. Composites Science and Technology 2000;60:2849-2856.

159. Tvergaard V, Hutchinson JW. The Relation between Crack Growth Resistance and Fracture Process Parameters in Elastic-Plastic Solids. Journal of the Mechanics and Physics of Solids 1992;40:1377–1397.

160. Yang QD, Thouless MD. Mixed-Mode Fracture Analyses of Plastically-Deforming Adhesive Joints. International Journal of Fracture 2001;110: 175-18.

161. Gustafson PA, Waas AM. The influence of adhesive constitutive parameters in cohesive zone finite element models of adhesively bonded joints. International Journal of Solids and Structures 2009;46:2201-2215.

162. Scheider I. Simulation of cup–cone fracture in round bars using the cohesive zone model. In: First MIT Conference on Computational Fluid and Solid Mechanics, vol. 1. Amsterdam: Elsevier; 2001. p. 460–2.

163. Talreja R, Lecture Notes, Damage Mechanics of Composite Materials Lectures in IIMEC 2012 Summer School on Advanced Composite Materials Technical Educational Institute, Serres, Greece 2012.

164. Tvergaard V. Effect of fibre debonding in a Whisker-reinforced metal. Materials Science and Engineering A 1990;125:203–13.

165. Espinosa HD, Zavattieri PD, Dwivedi SK. A Finite Deformation Continuum/Discrete model for the Description of Fragmentation and Damage in Brittle Materials. Journal of the Mechanics and Physics of Solids 1998;46:1909-1942.

166. Pinho ST, Iannucci L, Robinson P. Formulation and implementation of decohesion elements in an explicit finite element code. Composites: Part A 2006;37:778–789.

167. Li S, Thouless MD, Waas AM, Schroeder JA, Zavattieri PD. Use of a cohesive-zone model to analyze the fracture of a fiber-reinforced polymer-matrix composite. Composites Science and Technology 2005;65:537-549.

168. Reinhardt HW, Cornelissen HAW. Post-peak cyclic behaviour of concrete in uniaxial and alternating tensile and compressive loading. Cement and Concrete Research 1984;14:263–70.

169. Planas J, Elices M. Fracture criteria for concrete: Mathematical approximations and experimental validation. Engineering Fracture Mechanics 1990;35:87–94.

170. Ortiz M, Pandolfi A. Finite-Deformation Irreversible Cohesive Elements for Three-Dimansional Crack-Propagation Analysis. International Journal for Numerical Methods in Engineering 1999;44:1267-1287.

171. Repetto EA, Radovitzky R, Ortiz M. Finite element simulation of dynamic fracture and fragmentation of glass rods. Computer Methods in Applied Mechanics and Engineering 2000;183:3-14.

172. Han T-S, Ural A, Chen C-S, Zehnder AT, Ingraffea AR, Billington SL. Delamination buckling and propagation of honeycomb panels using a cohesive element approach. International Journal of Fracture 2002;115:101-123.

173. Yu C, Pandolfi A, Ortiz M, Coker D, Rosakis AJ. Three-dimensional modeling of intersonic shear-crack growth in asymmetrically loaded unidirectional composite plates. Internatonal Journal of Solids and Structures 2002:39;6135-6157.

174. Reedy ED, Mello FJ, Guess TR. Modelling the initiation and growth of delaminations in composite structures. J. Compos. Mater. 1997;31:812–831.

175. Geubelle PH and Baylor JS. Impact-induced delamination of composites: a 2D simulation. Composites Part B 1998;29B:589–602.

176. Mi Y, Crisfield MA, Davies GAO, Hellweg HB. Progressive Delamination Using Interface Elements. Journal of Composite Materials 1998;32:1246.

177. Crisfield MA. An Arc-Length Method Including Line Searches and Accelerations. International Journal of Numerical Methods in Engineering 1983;19:1269-1289.

178. Camanho PP, Davila CG, Ambur DR. Numerical Simulation of Delamination Growth in Composite Materials, NASA/TP-2001-211041, 2001.

179. Camanho PP, Davila C. Mixed-Mode Decohesion Finite Elements for the Simulation of Delamination in Composite Materials, NASA/TP-2007-214869, 2002.

180. Davila C, Camanho PP, Turon A. Cohesive Elements for Shells. NASA/TP-2007-214869 2007.

181. Chen J. Predicting Progressive Delamination of Stiffened Fiber-Composite Panel and Repaired Sandwich Panel by Decohesion Models. Journal of Thermoplastic Composite Materials 2002;15:429-442.

182. Chen J, Ravey E, Hallett S, Wisnom M, Grassi M. Prediction of delamination in braided composite T-piece specimens. Composites Science and Technology 2009;69:2363–2367.

183. de Moura MF, Gonçalves PM, Marques AT, De Castro PMS. Prediction of Compressive Strength of Carbon-Epoxy Laminates Containing Delamination by Using a Mixed-Mode Damage Model. Composite Structures 2000;50:151-157.

184. Aoki Y, Suemasu H, Ishikawa T. Damage Propagation in CFRP Laminates Subjected to Low Velocity Impact and Static Indentation. Advanced Composite Materials 2007;16:45–61.

185. Robinson P, Galvanetto U, Galvanetto D, Bellucci G, Violeau D. Numerical Simulation of Fatigue-Driven Delamination Using Interface Elements. International Journal for Numerical Methods in Engineering. 2005;63:1824–1848.

186. Warrior NA, Pickett AK, Lourenco NSF. Mixed-Mode Delamination – Experimental and Numerical Studies. Strain 2003:39;153–159.

187. Hu N, Zemba Y, Okabe T, Yan C, Fukunaga H, Elmarakbi AM. A new cohesive model for simulating delamination propagation in composite laminates under transverse loads. Mechanics of Materials 2008;40:920-935.

188. Corigliano A, Ricci M. Rate-dependent Interface Models: Formulation and Numerical Applications. Internatonal Journal of Solids and Structures 2001;38:547-576.

189. Espinosa HD, Dwivedi S, Lu H-C. Modeling impact induced delamination of woven fiber reinforced composites with contact/cohesive laws. Computer Methods in Applied Mechanics and Engineering 1999;183:259–290.

190. Williams JG, Hadavinia H. Analytical solutions for cohesive zone models. Journal of the Mechanics and Physics of Solids 2002;50:809–25.

191. Falk ML, Needleman A, Rice JR. A Critical Evaluation of Dynamic Simulations using Cohesive Surfaces. Journal de Physique IV, 2001.

192. Turon A, Davila CG, Camanho PP, Costa J. An Engineering Solution for Mesh Size Effects in the Simulation of Delamination Using Cohesive Zone Models. Engineering Fracture Mechanics 2007;74:1665–1682.

193. Harper PW, Hallet SR. Cohesive Zone Length in Numerical Simulations in Composite Delamination. Engineering Fracture Mechanics 2008;75:4774–4792.

194. Hui CY, Jagota A, Bennison SJ, Londono JD. Crack blunting and the strength of soft elastic solids. Proceedings of the Royal Society A 2003;459:1489–516.

195. Irwin GR. Plastic zone near a crack and fracture toughness. Proceedings of the seventh Sagamore Ordnance materials conference, vol. IV. New York: Syracuse University; 1960. p. 63–78.

196. Corigliano A, Ricci M. Rate-dependent interface models: formulation and numerical applications. International Journal of Solids and Structures 2001;38:547–76.

197. De Xie A, Waas M. Discrete Cohesive Zone Model for Mixed-Mode Fracture Using Finite Element Analysis. Engineering Fracture Mechanics 2006;73:1783–1796.

198. Sprenger W, Gruttman F, Wagner W. Delamination growth analysis in laminated structures with continuum-based 3D-shell elements and a visco-plastic softening model. Computer Methods in Applied Mechanics and Engineering 2000;185:123–139.

199. El-Sayed S, Sridharan S. Predicting and tracking interlaminar crack growth in composites using a cohesive layer model. Composites: Part B 2001;32:545–553.

200. El-Sayed S, Sridharan S. Cohesive layer models for predicting delamination growth and crack kinking in sandwich structures. International Journal of Fracture 2002;117: 63–84.

201. Turon A, Pedro P, Camanho PP, Costa J, Davila CG. An Interface Damage Model for the Simulation of Delamination under Variable-Mode Ratio in Composite Materials. NASA/TM-2004-213277, 2004.

202. de Borst R. Numerical Aspects of Cohesive-Zone Models. Engineering Fracture Mechanics 2003;70:1743–1757.

203. de Borst R, Remmers JJC, Needleman A. Mesh-independent discrete numerical representation of cohesive-zone models. Engineering Fracture Mechanics 2006;73:160-177.

204. Schellekens J, de Borst R. On the Numerical Integration of Interface Elements. International Journal for Numerical Methods in Engineering 1993;36:43-66.

205. Frassine R, Pawan A. Viscoelastic effects on the interlaminar fracture behavior of thermoplastic matrix composites: I. Rate and temperature dependence on unidirectional PEI/Carbon-fibre laminates. Composites Science and Technology 1995;54:193-200.

206. Corigliano A, Frassine R, Ricci M. Rate-dependent fracture properties in the delamination of polymer-matrix composites, in: Proceedings of the WCCM-4, 29 June-2 July, Buenos Aires, 1998.

207. Rahul-Kumar P, Jagota A, Bennison SJ, Saigal S, Muralidhar S. Polymer Interfacial Fracture Simulations using Cohesive Elements. Acta Materiala 1999;47:4161-4169.

208. Landis CM, Pardoen T, Hutchinson JW. Crack velocity dependent toughness in rate dependent materials. Mechanics of Materials 2000;32:663–78.

209. Corigliano A, Mariani S. Parameter identification of a time dependent elastic-damage interface model for the simulation of debonding in composites. Composites Science of Technology 2001;61:191–203.

210. Corigliano A, Mariani S. Identification of a constitutive model for the simulation of time-dependent interlaminar debonding processes in composites. Computer Methods in Applied Mechanics and Engineering 2002;191:1861–94.

211. Samudrala O, Huang Y, Rosakis AJ. Subsonic and intersonic mode II crack propagation with a rate dependent cohesive zone. Journal of the Mechanics and Physics of Solids 2002;50:1231–68.

212. Rosakis AJ, Samudrala O. Coker D. Intersonic shear crack growth along weak planes. Materials Research Innovations 2000;3(4):236–243.

213. Kubair DV, Geubelle PH, Huang YY. Analysis of a rate-dependent cohesive model for dynamic crack propagation. Engineering Fracture Mechanics 2003;70:685–704.

214. Anvari M, Scheider I, Thaulow C. Simulation of dynamic ductile crack growth using strain-rate and triaxiality-dependent cohesive elements. Engineering Fracture Mechanics 2006;73:2210-2228.

215. Cox BN, Gao H, Gross D, Rittel D. Modern topics and challenges in dynamic fracture. Journal of the Mechanics and Physics of solids 2005;53:565–596.

216. Ranjith K, Rice JR. Slip dynamics at an interface between dissimilar materials. Journal of the Mechanics and Physics of Solids 2001;49:341–361.

217. Coker D, Lykotrafitis G, Needleman A, Rosakis AJ. Frictional sliding modes along an interface between identical elastic plates subject to shear impact loading. Journal of the Mechanics and Physics of Solids 2005;53:884-922.

218. Zheng G, Rice JR. Conditions under which velocity-weakening friction allows a self-healing versus crack like mode of rupture. Bulletin of the Seismological Society of America 1998;88:1466–1483.

219. Adams GG. Self-excited oscillations of two elastic half-spaces sliding with a constant coefficient of friction.Journal of Applied Mechanics 1995;62:867-872.

220. Prakash V. Clifton RJ. Pressure-shear plate impact measurement of dynamic friction for high speed machining applications. Proc. 7th Int. Congress on Exp. Mech., Society of Experimental Mechanics, Bethel, CT, 1993;556-564.

221. Harewood FJ, McHugh PE. Comparison of the implicit and explicit finite element methods using crystal plasticity. Computational Materials Science 2007;39:481-494.

222. Crisfield MA. Non-linear Finite Element Analysis of Solids and Structures. John Wiley & Sons 1994.

223. Riks E. An Incremental Approach to the Solution of Snapping and Buckling Problems. Int. J. of Solids and Structures 1979;15:529-551.

224. Wempner GA. Discrete Approximations Related to Nonlinear Theories of Solids. Int. J. Solids and Structures 1971;7:1581-1599.

225. Ramm E. Strategies for Tracing the Nonlinear Response near Limit Points. Nonlinear Analysis in Structural Mechanics. Springer 1981:68-89.

226. Gao YF, Bower AF. A simple technique for avoiding convergence problems in finite element simulations of crack nucleation and growth on cohesive interfaces. Modelling and Simulation in Materials Science and Engineering 2004;12:453–463.

227. Blackman BRK, Dear JP, Kinloch AJ, MacGillivray H, Wang Y, Williams JG, Yayla P. The failure of fibre composites and adhesively bonded fibre composites under high rates of test. Journal of Materials Science 1996;31:4467-4477.

228. Chen J, Crisfield M, Kinloch AJ, Busso EP, Matthews FL, Qiu Y. Predicting progressive delamination of composite material specimens via interface elements. Mechanics of Composite Materials and Structures 1999;6:301-317.

229. Zhang Z and Paulino GH. Cohesive zone modeling of dynamic failure in homogeneous and functionally graded materials. International Journal of Plasticity 2005;21:1195–1254.

230. Abramowitz M, Stegun IA. Handbook of Mathematical Functions with Formulas, Graphs, and Mathematical Tables. Dover Ninth printing. 1970.

231. Uyar I, Arca MA, Yavas D, Gozluklu B and Coker D. Proceedings of the Conference on Wind Energy Science and Technolog - RUZGEM 2013 October 3-4, 2013, Ankara, TURKEY, 2013.

232. Uyar I and Coker D. Experimental investigation of delamination in L-shaped composite brackets, 2014, In preparation.

233. Marlett K. Hexcel 8552S AS4 Plain Weave Fabric Prepreg 193 gsm & 38% RC Qualification Material Property Data report. National Institute for Aviation Research, Wichita State University, CAM-RP-20110-006 April 14, 2011.

234. Internal Report, Turkish Aerospace Industries (TAI), 2013.

235. Arca M. Experimental and Numerical Investigation of Crack Growth in Straight and Curved Interfaces in Composites. MSc Thesis. Middle East Technical University, 2014 (In preparation).

236. Xia K, Rosakis AJ, Kanamori H. Laboratory Earthquakes: The Sub-Rayleigh-to-Supershear Rupture Transition. Science 2004;303(5665):1859-1861.

237. Bouchon M, Bouin M-P, Karabulut H, Toksöz MN, Dietrich M and Rosakis AJ. How fast is Rupture during an Earthquake? New insights from the 1999 Turkey Earthquakes. Geophysical Research Letters 2001;28(14):2723-2726.

238. Aochi H and Madariaga R. The 1999 Izmit, Turkey, Earthquake: Nonplanar Fault Structure, Dynamic Rupture Process, and Strong Ground Motion. Bulletin of the Seismological Society of America 2003;93(3):1249–1266.

PLANE STRAIN COMPLIANCE MATRIX FOR ORTHOTROPIC MATERIALS

In text books, elastic constants for plane stress assumption are easily found since the plane stress is a part of Classical Lamination Theory [5]. However, plane strain solution is not available. In this chapter, plane strain elastic constants are derived.

The Generalized Hooke's law for the orthotropic materials in Voigt notation is given as follows [5];

$$
\begin{Bmatrix} \varepsilon_{xx} \\ \varepsilon_{yy} \\ \varepsilon_{zz} \\ \varepsilon_{yz} \\ \varepsilon_{zx} \\ \varepsilon_{xy} \end{Bmatrix} = \begin{bmatrix} \dfrac{1}{E_x} & -\dfrac{\nu_{yx}}{E_y} & -\dfrac{\nu_{zx}}{E_z} & 0 & 0 & 0 \\ -\dfrac{\nu_{xy}}{E_x} & \dfrac{1}{E_y} & -\dfrac{\nu_{zy}}{E_z} & 0 & 0 & 0 \\ -\dfrac{\nu_{xz}}{E_x} & -\dfrac{\nu_{yz}}{E_y} & \dfrac{1}{E_z} & 0 & 0 & 0 \\ 0 & 0 & 0 & \dfrac{1}{2G_{yz}} & 0 & 0 \\ 0 & 0 & 0 & 0 & \dfrac{1}{2G_{zx}} & 0 \\ 0 & 0 & 0 & 0 & 0 & \dfrac{1}{2G_{xy}} \end{bmatrix} \begin{Bmatrix} \sigma_{xx} \\ \sigma_{yy} \\ \sigma_{zz} \\ \tau_{yz} \\ \tau_{zx} \\ \tau_{xy} \end{Bmatrix} \tag{125}
$$

where the 6x6 matrix is called *Compliance Matrix*, $\widetilde{C}$. Moreover, symmetry of the compliance matrix spawns that; $\nu_{yx} / E_y = \nu_{xy} / E_x$, $\nu_{yz} / E_y = \nu_{zy} / E_z$ and $\nu_{zx} / E_z = \nu_{xz} / E_x$.

The stresses are calculated by inversing the eqn.(125). Stiffness matrix, $\widetilde{S}$, is the inverse of compliance matrix; i.e. $\widetilde{S} = \widetilde{C}^{-1}$. The stiffness matrix is not explicitly written for the generalized case for the sake of simplicity.

The strains on yz and zx planes are zero for the plane strain assumption; i.e.: $\varepsilon_{zz} = 0$, $\varepsilon_{yz} = 0$ and $\varepsilon_{zx} = 0$. Hence, Hooke's law becomes as follows;

$$\begin{Bmatrix} \sigma_{xx} \\ \sigma_{yy} \\ \sigma_{zz} \\ \tau_{yz} \\ \tau_{zx} \\ \tau_{xy} \end{Bmatrix} = \begin{bmatrix} \dfrac{1}{E_x} & -\dfrac{\nu_{yx}}{E_y} & -\dfrac{\nu_{zx}}{E_z} & 0 & 0 & 0 \\ -\dfrac{\nu_{xy}}{E_x} & \dfrac{1}{E_y} & -\dfrac{\nu_{zy}}{E_z} & 0 & 0 & 0 \\ -\dfrac{\nu_{xz}}{E_x} & -\dfrac{\nu_{yz}}{E_y} & \dfrac{1}{E_z} & 0 & 0 & 0 \\ 0 & 0 & 0 & \dfrac{1}{2G_{yz}} & 0 & 0 \\ 0 & 0 & 0 & 0 & \dfrac{1}{2G_{zx}} & 0 \\ 0 & 0 & 0 & 0 & 0 & \dfrac{1}{2G_{xy}} \end{bmatrix}^{-1} \begin{Bmatrix} \varepsilon_{xx} \\ \varepsilon_{yy} \\ 0 \\ 0 \\ 0 \\ \varepsilon_{xy} \end{Bmatrix} \quad (126)$$

As seen from eqn., $\tau_{yz} = 0$ and $\tau_{zx} = 0$ whereas $\sigma_{zz} \neq 0$. By neglecting the part for σ_{zz}, the plane strain stiffness matrix becomes a square matrix. Hooke's law is therefore reduced by removing 3rd, 4th and 5th columns and rows in eqn. (126) to reach the below 2D stress-strain relation;

$$\begin{Bmatrix} \sigma_{xx} \\ \sigma_{yy} \\ \tau_{xy} \end{Bmatrix} = \Lambda \begin{bmatrix} E_x(1 - \nu_{yz}\nu_{zy}) & -E_x(\nu_{yx} - \nu_{zx}\nu_{yz}) & 0 \\ -E_y(\nu_{xy} - \nu_{xz}\nu_{zy}) & E_y(1 - \nu_{xz}\nu_{zx}) & 0 \\ 0 & 0 & 2G_{xy} \end{bmatrix} \begin{Bmatrix} \varepsilon_{xx} \\ \varepsilon_{yy} \\ \varepsilon_{xy} \end{Bmatrix} \quad (127)$$

where

$$\Lambda = \nu_{xy}\nu_{yx} + \nu_{xz}\nu_{zx} + \nu_{yz}\nu_{zy} + \nu_{xy}\nu_{zx}\nu_{yz} + \nu_{yx}\nu_{xz}\nu_{zy}$$

The plane strain compliance matrix, $\widetilde{C}^{\mathbf{Strn}}$, can be reached by inversing the stiffness matrix in eqn.(127), such that;

$$\widetilde{C}^{\mathbf{Strn}} = \begin{bmatrix} \dfrac{1 - \nu_{xz}\nu_{zx}}{E_x} & -\dfrac{\nu_{yx} - \nu_{zx}\nu_{yz}}{E_y} & 0 \\ -\dfrac{\nu_{xy} - \nu_{xz}\nu_{zy}}{E_x} & \dfrac{1 - \nu_{yz}\nu_{zy}}{E_y} & 0 \\ 0 & 0 & \dfrac{1}{2G_{xy}} \end{bmatrix} \quad (128)$$

APPENDIX B

VUEL USER-SUBROUTINE

The following code is written in the language of Fortran 90. Some of the matrix calculations are written in explicit form in order to optimizite the program efficiency.

CODE:

```
c    user element for truss along the X global axis
     subroutine vuel(
*    nblock,
c        to be defined
*    rhs,amass,dtimeStable,
*    svars,nsvars,
*    energy,
c
*    nnode,ndofel,
*    props,nprops,
*    jprops,njprops,
*    coords,ncrd,
*    u,du,v,a,
*    jtype,jelem,
*    time,period,dtimeCur,dtimePrev,kstep,kinc,lflags,
*    dMassScaleFactor,
*    predef,npredef,
*    jdltyp,adlmag)

     include 'vaba_param.inc'

     parameter ( zero = 0.d0, half = 0.5d0, one = 1.d0, two=2.d0 )
```

```fortran
c    operation code
     parameter ( jMassCalc          = 1,
    *        jIntForceAndDtStable = 2,
    *        jExternForce       = 3)


c    flags
     parameter (iProcedure = 1,
    *        iNlgeom    = 2,
    *        iOpCode    = 3,
    *        nFlags     = 3)


c    time
     parameter (iStepTime  = 1,
    *        iTotalTime = 2,
    *        nTime      = 2)


c    procedure flags
     parameter ( jDynExplicit = 17 )


c    energies
     parameter ( iElPd = 1,
    *        iElCd = 2,
    *        iElIe = 3,
    *        iElTs = 4,
    *        iElDd = 5,
    *        iElBv = 6,
    *        iElDe = 7,
    *        iElHe = 8,
    *        iElKe = 9,
    *        iElTh = 10,
    *        iElDmd = 11,
    *        iElDc = 12,
    *        nElEnergy = 12)
```

306

```
c    predefined variables
     parameter ( iPredValueNew = 1,
     *         iPredValueOld = 2,
     *         nPred      = 2)


c    indexing in a 3-long vector


     parameter (factorStable = 0.99d0)


**----------------------------------
C    A - H and O - Z --> REAL*8
**----------------------------------


     dimension rhs(nblock,ndofel), amass(nblock,ndofel,ndofel),
     *    dtimeStable(nblock),
     *    svars(nblock,nsvars), energy(nblock,nElEnergy),
     *    props(nprops), jprops(njprops),
     *    jelem(nblock), time(nTime), lflags(nFlags),
     *    coords(nblock,nnode,ncrd), u(nblock,ndofel),
     *    du(nblock,ndofel), v(nblock,ndofel), a(nblock, ndofel),
     *    dMassScaleFactor(nblock),
     *    predef(nblock, nnode, npredef, nPred), adlmag(nblock)

     dimension cord_n1(2),cord_n2(2),cord_n3(2),cord_n4(2), cord_mid(2)
     dimension vec_A(2),vec_B(2),vec_mid(2),Trnsfrm(2,2),del_GLOBAL(2)
     dimension del_LOCAL(2),force_GLOBAL(2),force_LOCAL(2), damage(2)
     dimension del_step_GLOBAL(2),del_step_LOCAL(2)
     dimension GI_step(2), GII_step(2), trac_(2,2), del_(2,2)
     dimension vel_GLOBAL(2), vel_LOCAL(2)

     character(20) :: cElmID
     character(50) :: cFileOut
```

```fortran
      if (jtype .eq. 2 .and.
     *   lflags(iProcedure).eq.jDynExplicit) then


      width = props(1)   !The width to be used for multiplying the traction
      E0  = props(2)     !The penalty stiffness matrix or E for the X&N
      trac_Ic = props(3)     !Mode-I ILST
      trac_IIc = props(4)    !Mode-II ILSS
      GIc = props(5)     !Mode-I fracture toughness
      GIIc = props(6)    !Mode-II fracture toughness
      rho = props(7)     !Density used for the integration
      fBK = props(8)     !The factor for BK criterion
      StableTime = props(9)     !Stable integration time
      Delfactor = props(10)     !Deleting  the Xu_needleman CZM at that del_o
      GIc_inf = props(11)       !Infinite GIc
      GIIc_inf = props(12)      !Infinite GIIc
      trac_Ic_inf = props(13)       !Infinite Mode-I ILST
      trac_IIc_inf = props(14)      !Infinite Mode-II ILSS
      vel_Ref_o = props(15)      !Reference Separation vel. onset
      vel_Ref_cr = props(16)       !Reference Separation vel. onset
      jPrintFreq = jprops(1)    !Increment frequency for outputting in file
      jModel = jprops(2)        !The model; 1 for X&N, 2 for modX&N,3 for bi.
      nIP = 2        !The nIP is two rods


c
_____

__
c     xxx The characteristic lengths are found for each model xxxx
            SELECT CASE (jModel)
                CASE (1:2)
c                   Xu  and  Needleman  Model  characteristic  length
parameters
        delo_I =GIc/(trac_Ic*exp(one))                  !@Normal dir.
```

delo_II=GIIc/(trac_IIc*sqrt(exp(one)/two)) !@Tangent dir.

XN_q = GIc/GIIc

XN_r = XN_q

delcr_I = Delfactor*delo_I

delcr_II = Delfactor*delo_II

        CASE *(3)*

c   *Bilinear Model length parameters*

delo_I = trac_Ic / E0

delcr_I = two * GIc / (delo_I * E0)

delo_II = trac_IIc / E0

delcr_II = two * GIIc / (delo_II * E0)

        CASE *(4)*

c   *Rate-Dependent Bilinear Model length parameters*

delo_I = trac_Ic / E0

delcr_I = two * GIc / (delo_I * E0)

delo_II = trac_IIc / E0

delcr_II = two * GIIc / (delo_II * E0)

delo_I_inf = trac_Ic_inf / E0

delcr_I_inf = two * GIc_inf / (delo_I_inf * E0)

delo_II_inf = trac_IIc_inf / E0

delcr_II_inf = two * GIIc_inf / (delo_II_inf * E0)

   END SELECT

c

_____

__

c

_____

__

c   *&&&&& ABAQUS - Mass Matrix Update &&&&&*

   IF *(lflags(iOpCode).eq.jMassCalc)* **THEN**

    DO *kblock = 1, nblock*

c   *The current coordinates of nodes , kblock*

```
        cord_n1(1) = coords(kblock,1,1)+u(kblock,1)
        cord_n2(1) = coords(kblock,2,1)+u(kblock,3)
        cord_n3(1) = coords(kblock,3,1)+u(kblock,5)
        cord_n4(1) = coords(kblock,4,1)+u(kblock,7)
        cord_n1(2) = coords(kblock,1,2)+u(kblock,2)
        cord_n2(2) = coords(kblock,2,2)+u(kblock,4)
        cord_n3(2) = coords(kblock,3,2)+u(kblock,6)
        cord_n4(2) = coords(kblock,4,2)+u(kblock,8)


c        The upward diagonal vector, vec_A, kblock
        vec_A(1) = cord_n4(1) - cord_n1(1)
        vec_A(2) = cord_n4(2) - cord_n1(2)


c        The downward diagonal vector, vec_B, kblock
        vec_B(1) = cord_n3(1) - cord_n2(1)
        vec_B(2) = cord_n3(2) - cord_n2(2)


c        The mid-vector, vec_mid, kblock
        vec_mid(1) = half*(vec_A(1) + vec_B(1))
        vec_mid(2) = half*(vec_A(2) + vec_B(2))


c        The length of the mid-vector, |vec_mid|, kblock
        alen_vec_mid = sqrt(vec_mid(1)*vec_mid(1)+
     *          vec_mid(2)*vec_mid(2))


c        The area to be used for traction, kblock
        half_area = half*alen_vec_mid*width


c        The height of the element is dived into two
        aheigth_1= sqrt((cord_n2(1) - cord_n1(1))**two +
     *        (cord_n2(2) - cord_n1(2))**two)
        aheigth_2= sqrt((cord_n4(1) - cord_n3(1))**two +
     *        (cord_n4(2) - cord_n3(2))**two)
```

```fortran
c         The mass matrix can be updated
          am1   = aheigth_1*(half_area*rho/2) !"/2":Up and down nodes
          am2   = aheigth_2*(half_area*rho/2) !"/2":Up and down nodes

          amass(kblock,1,1) = am1
          amass(kblock,2,2) = am1
          amass(kblock,3,3) = am1
          amass(kblock,4,4) = am1
          amass(kblock,5,5) = am2
          amass(kblock,6,6) = am2
          amass(kblock,7,7) = am2
          amass(kblock,8,8) = am2

      ENDDO
c
_____
__

c
_____
__
c        &&&&& ABAQUS - Force Matrix Update &&&&&
      ELSE IF ( lflags(iOpCode) .eq.
   *        jIntForceAndDtStable) THEN
      DO kblock = 1, nblock

c        PRINT *,   svars(kblock,1)
c        PRINT *,   svars(kblock,2)
c        PRINT *,   svars(kblock,3)
c        PRINT *,   svars(kblock,4)
c        PAUSE
```

```
c          Initializing some terms
           damage(:) = zero
           GI_step(:) = zero
           GII_step(:) = zero
           trac_x = zero
           trac_y = zero



c          The current coordinates of nodes , kblock
           cord_n1(1) = coords(kblock,1,1)+u(kblock,1)
           cord_n2(1) = coords(kblock,2,1)+u(kblock,3)
           cord_n3(1) = coords(kblock,3,1)+u(kblock,5)
           cord_n4(1) = coords(kblock,4,1)+u(kblock,7)
           cord_n1(2) = coords(kblock,1,2)+u(kblock,2)
           cord_n2(2) = coords(kblock,2,2)+u(kblock,4)
           cord_n3(2) = coords(kblock,3,2)+u(kblock,6)
           cord_n4(2) = coords(kblock,4,2)+u(kblock,8)


c          The upward diagonal vector, vec_A, kblock
           vec_A(1) = cord_n4(1) - cord_n1(1)
           vec_A(2) = cord_n4(2) - cord_n1(2)


c          The downward diagonal vector, vec_B, kblock
           vec_B(1) = cord_n3(1) - cord_n2(1)
           vec_B(2) = cord_n3(2) - cord_n2(2)


c          The mid-vector, vec_mid, kblock
           vec_mid(1) = half*(vec_A(1) + vec_B(1))
           vec_mid(2) = half*(vec_A(2) + vec_B(2))


c          The length of the mid-vector, |vec_mid|, kblock
           alen_vec_mid = sqrt(vec_mid(1)*vec_mid(1)+
```

312

```
*                 vec_mid(2)*vec_mid(2))


c           The area to be used for traction, kblock
            half_area = half*alen_vec_mid*width


c           The current rotation, Teta
            Teta = acos(vec_mid(1)/alen_vec_mid)
c            IF (vec_mid(1).lt.zero) Teta = Teta + aPI


c           The transformation matrix, Trnsfrm
            Trnsfrm(1,1) =  cos(Teta)
            Trnsfrm(1,2) =  sin(Teta)
            Trnsfrm(2,1) = -sin(Teta)
            Trnsfrm(2,2) =  cos(Teta)


            DO nRod = 1,nIP


            SELECT CASE(nRod)
             CASE (1)
c               Relative displacement in global coords, ROD = 1
                del_GLOBAL(1) = u(kblock,3) -  u(kblock,1)
                del_GLOBAL(2) = u(kblock,4) -  u(kblock,2)
c               Relative displacement step in global coords, ROD = 1
                del_step_GLOBAL(1) = du(kblock,3) -  du(kblock,1)
                del_step_GLOBAL(2) = du(kblock,4) -  du(kblock,2)
c               Separation speed, ROD = 1
                vel_GLOBAL(1) = v(kblock,3) -  v(kblock,1)
                vel_GLOBAL(2) = v(kblock,4) -  v(kblock,2)
             CASE (2)
c               Relative displacement in global coords, ROD = 2
                del_GLOBAL(1) = u(kblock,7) -  u(kblock,5)
                del_GLOBAL(2) = u(kblock,8) -  u(kblock,6)
c               Relative displacement in global coords, ROD = 2
```

313

```fortran
              del_step_GLOBAL(1) = du(kblock,7) -  du(kblock,5)
              del_step_GLOBAL(2) = du(kblock,8) -  du(kblock,6)
c             Separation speed, ROD = 2
              vel_GLOBAL(1) = v(kblock,7) -  v(kblock,5)
              vel_GLOBAL(2) = v(kblock,8) -  v(kblock,6)
        ENDSELECT
c        Relative displacement in local coords, kblock
         del_LOCAL = MATMUL(Trnsfrm,del_GLOBAL)
c        Relative displacement step in local coords, kblock
         del_step_LOCAL = MATMUL(Trnsfrm,del_step_GLOBAL)
c        Separation speed in local coords, kblock
         vel_LOCAL = MATMUL(Trnsfrm,vel_GLOBAL)


c        Skipping the fully damaged element integration point
         IF (svars(kblock,nRod).eq.one) THEN !Damage = 1
            rhs(kblock,:) = zero
            trac_x = zero
            trac_y = zero
            GI_step(:) = zero
            GII_step(:) = zero
            del_(1,nRod) = del_LOCAL(2)
            del_(2,nRod) = del_LOCAL(1)
            GoTO 999
         ENDIF


c        The relative displacement terms in opening and shearig modes
         del_I = del_LOCAL(2)   !The Y-direction is mode-I
         del_II = del_LOCAL(1)  !The X-direction is mode-II
         del_step_I = del_step_LOCAL(2)
         del_step_II = del_step_LOCAL(1)
         vel_I = vel_LOCAL(2)
         vel_II = vel_LOCAL(1)
```

314

c   The magnitude of the relative displacement

del_I_MC = (del_I + abs(del_I)) / two

del = sqrt(del_I_MC**two + del_II**two)

c   The magnitude of the separation speed

vel = sqrt(vel_I**two + vel_II**two)

c   ------------ CALCULATION OF THE TRACTION - MODEL ------------

SELECT CASE *(jModel)*

C   xxxxxxxxxxxx THE ORIGINAL XU and NEEDLEMAN MODEL (1994)xxxxxxxxxxxx

CASE *(1)*

IF *(XN_r.eq.one)* **THEN**

c   The Normal Traction

trac_y = GIc/delo_I*exp(-del_I/delo_I)*

2   (del_I/delo_I*exp(-(del_II**two)/

3   (delo_II**two)))

c   The Tangential Traction

trac_x = two*GIc/delo_I*(delo_I/delo_II)*

2   del_II/delo_II*(XN_q)*exp(-

del_I/delo_I)*

3   exp(-

(del_II**two)/(delo_II**two))

ELSE

c   The Shear Traction

trac_y= GIc/delo_I*exp(-del_I/delo_I)*

2   (del_I/delo_I*exp(-(del_II**two)/

315

3   *(delo_II**two))+(one-XN_q)/(XN_r-one)*(one-*

4   *exp(-(del_II**two)/(delo_II**two)))**

5   *(XN_r-del_I/delo_I))*

c   *The Tangential Traction*

trac_x = two*GIc/delo_I*(delo_I/delo_II)*

2   *del_II/delo_II*(XN_q+(XN_r-XN_q)/(XN_r-one)*del_I/*

3   *delo_I)*exp(-del_I/delo_I)**

4   *exp(-(del_II**two)/(delo_II**two))*

            ENDIF

c   *Dummy Damage for Xu and Needleman Models*

c   *.. Mode_I ..*

        IF** ((del_I.ne.zero).AND.(del_I.gt.delcr_I))* ***THEN

         damage(nRod) = one

        ENDIF

c   *.. Mode_II ..*

        ***IF** ((del_II.ne.zero).AND.*

2   *(ABS(del_II).gt.delcr_II))****THEN***

         damage(nRod) = one

        ENDIF

c   *xxxxxxxxxxxx THE MODIFIED XU and NEEDLEMAN MODEL by [Bosch (2006)] xxxxxxxxxxxx*

          ***CASE** (2)*

c   *The Normal Traction*

trac_y= GIc/delo_I*(del_I/delo_I)*

316

2   exp(-del_I/delo_I)*exp(-(del_II**two)/
         3   (delo_II**two))

c   The Tangential Traction
                             trac_x = two*GIIc/delo_II*(del_II/delo_II)*
         2   (one+del_I/delo_I)*exp(-(del_II**two)/
     3   (delo_II**two))*exp(-del_I/delo_I)

c   Dummy Damage for Xu and Needleman Models

c   .. Mode_I ..
            IF ((del_I.ne.zero).AND.(del_I.gt.delcr_I)) **THEN**
               damage(nRod) = one
            ENDIF
c   .. Mode_II ..
            IF ((del_II.ne.zero).AND.
     2   (ABS(del_II).gt.delcr_II))**THEN**
               damage(nRod) = one
            ENDIF

c   xxxxxxxxxxxx THE BILINEAR MODEL xxxxxxxxxxxx
          CASE (3)

c   Calculation of the onset displacement
            beta = del_II / del_I
            IF(del_I > 0) **THEN** !Mixed-Mode action
               delo = delo_I*delo_II*sqrt((one + beta**two)/
     *   (delo_II**two + (beta*delo_I)**two))
            ELSE   !No Mode-I, Mode-II active only
               delo = delo_II
            ENDIF

c   *Calculation of the onset displacement*

      IF(del_I > 0) **THEN** *!Mixed-Mode action*

        delcr = two/(delo*E0)*(GIc + (GIIc - GIc)*

    *   (beta**two/(one + beta**two))**fBK)

      ELSE   *!No Mode-I, Mode-II active only*

        delcr = delcr_II

      ENDIF

c   *Damage is taken or assumed*

      IF(del > delo) **THEN**

        damage_cand=((del-delo)/(delcr-delo))*delcr/del

        damage_cand=min(damage_cand, one)

      ELSE

        damage_cand = zero

      ENDIF

      damage(nRod) = max(damage_cand, svars(kblock,nRod))

c   *The traction in x-direction on the rod element*

      trac_x = (one - damage(nRod))*E0*del_II

c   *The traction in x-direction on the rod element*

      trac_y = (one - damage(nRod))*E0*del_I

      IF (del_I<0) trac_y = E0*del_I

c   *xxxxxxxxxxx RATE-DEPT BILINEAR MODEL xxxxxxxxxxxx*

    CASE (4)

c   *Calculation of the onset displacement*

      beta = del_II / del_I

      IF(del_I > 0) **THEN** *!Mixed-Mode action*

        delo_0 = delo_I*delo_II*sqrt((one + beta**two)/

    *   (delo_II**two + (beta*delo_I)**two))

```
          delo_inf = delo_I_inf*delo_II_inf*sqrt
     *          ((one + beta**two)/(delo_II_inf**two
     *            + (beta*delo_I_inf)**two))
        ELSE        !No Mode-I, Mode-II active only
          delo_0 = delo_II
          delo_inf = delo_II_inf
        ENDIF


c              Calculation of the onset displacement
        IF(del_I > 0) THEN !Mixed-Mode action
          delcr_0 = two/(delo_0*E0)*(GIc + (GIIc - GIc)*
     *          (beta**two/(one + beta**two))**fBK)
          delcr_inf = two/(delo_inf*E0)*(GIc_inf +
     *          (GIIc_inf - GIc_inf)*(beta**two/(one +
     *           beta**two))**fBK)
        ELSE        !No Mode-I, Mode-II active only
          delcr_0 = delcr_II
          delcr_inf = delcr_II_inf
        ENDIF


c              Rate dependent values are found
        delo = one/(one/delo_inf+(one/delo_0-one/delo_inf)*
     *          exp(-abs(vel)/vel_Ref_o))
        delcr = one/(one/delcr_inf+(one/delcr_0-one/
     *          delcr_inf)*exp(-abs(vel)/vel_Ref_cr))


c              Damage is taken or assumed
        IF(del > delo) THEN
          damage_cand=((del-delo)/(delcr-delo))*delcr/del
          damage_cand=min(damage_cand, one)
        ELSE
          damage_cand = zero
        ENDIF
```

319

```fortran
            damage(nRod) = max(damage_cand, svars(kblock,nRod))
c           The traction in x-direction on the rod element
            trac_x = (one - damage(nRod))*E0*del_II


c           The traction in x-direction on the rod element
            trac_y = (one - damage(nRod))*E0*del_I
            IF (del_I<0) trac_y = E0*del_I


        END SELECT
c       ------------------------------------------------------------------------


c          Force = traction * force factor in LOCAL system
           force_LOCAL(1) = trac_x * half_area
           force_LOCAL(2) = trac_y * half_area


c          Transformation of force matrix from Local to Global
           force_GLOBAL = MATMUL(TRANSPOSE(Trnsfrm),force_LOCAL)


        SELECT CASE(nRod)
         CASE (1)
c          Assemble internal load in RHS, ROD = 1
           rhs(kblock,1) = -force_GLOBAL(1)
           rhs(kblock,3) =  force_GLOBAL(1)
           rhs(kblock,2) = -force_GLOBAL(2)
           rhs(kblock,4) =  force_GLOBAL(2)
         CASE (2)
c          Assemble internal load in RHS, ROD = 2
           rhs(kblock,5) = -force_GLOBAL(1)
           rhs(kblock,7) =  force_GLOBAL(1)
           rhs(kblock,6) = -force_GLOBAL(2)
           rhs(kblock,8) =  force_GLOBAL(2)
```

320

```
      ENDSELECT


c          Averaging for the element output_____
           del_(2,nRod) = del_II
           del_(1,nRod) = del_I
c          _____
 c          Saving the damage term and dissipation energy
           svars(kblock,nRod) = damage(nRod)


c           writing of the crack tip info
           IF((svars(kblock,1).eq.one).AND.
     *          (svars(kblock,2).eq.one))THEN
c          Averaging the tractions and displacements for the centroid
           del_ave_I =  (del_(1,1)+del_(1,2))/two
           del_ave_II =  (del_(2,1)+del_(2,2))/two


c           Calculatng energy release rate for the element
           GI = (svars(kblock,3) + svars(kblock,4))
     *        /(two* half_area)
           GII =(svars(kblock,5) + svars(kblock,6))
     *        /(two* half_area)
           Gc = GIc + (GIIc-GIc)*((GII/(GI+GII))**fBK)
           open(UNIT=100005,FILE=
     *        "C:\ABAQUS_JOBS\Crack_History.out",
     *             STATUS='UNKNOWN',POSITION='APPEND',
     *              IOSTAT=ierror)


c           The lcoation of the element (mid point)
           cord_mid(1) = (cord_n1(1) + cord_n2(1) + cord_n3(1)
     *          + cord_n4(1))/4.d0
           cord_mid(2) = (cord_n1(2) + cord_n2(2) + cord_n3(2)
     *          + cord_n4(2))/4.d0
```

```
          WRITE(UNIT=100005,FMT='(I20,2X,F20.15,2X,I20,
     *          6(F25.15))')kinc,time(iTotalTime),
     *            jElem(kblock),alen_vec_mid,GI,GII,Gc,
     *              del_ave_I*10**3,del_ave_II*10**3
          CLOSE (100005)
         ENDIF
c         Calculating the steps of new energy release rates
          GI_step(nRod) = del_step_I * trac_y * half_area
          GII_step(nRod) = del_step_II * trac_x * half_area
          svars(kblock,nRod+2)=svars(kblock,nRod+2)+GI_step(nRod)
          svars(kblock,nRod+4)=svars(kblock,nRod+4)+GII_step(nRod)


999       ENDDO


          energy(kblock, iElIe) = zero
          energy(kblock,iElDmd) = GI*two*half_area
          energy(nblock,iElCd) =  GII*two*half_area
          energy(kblock,iElDmd) = (GI+GII)*two*half_area
 c         Dilitational wave speed
          dtimeStable(kblock) = StableTime


        ENDDO !kblock - element by element do ends!
      ELSE IF ( lflags(iOpCode) .eq.
     *        jExternForce) THEN
        IF (jdltyp.eq.123) THEN
          DO kblock = 1, nblock
            rhs(kblock,4) = adlmag(kblock)
          ENDDO
        ENDIF
      ENDIF
    ENDIF
    RETURN
    END
```
322

<div align="center">**CURRICULUM VITAE**</div>

PERNOSAL INFORMATION

Surname, Name: Gözlüklü, Burak

Year and Place of Birth: 1983, Ankara

Email: burak.gozluklu@gmail.com

EDUCATION

Degree	Institution	Year of Graduation	C.GPa
PhD	METU, Aerospace Engineering	2014	3.80
MS	METU, Mechanical Engineering	2009	3.50
BS	METU, Mechanical Engineering	2006	3.18
Minor	METU, Metallurgical and Materials Engineering	2006	2.50

WORK EXPERIENCE

Year	Place	Enrollment	Project, Responsibility
2013-	TUSAŞ-Turkish Aerospace Industries Inc. (TAI)	Technical Specialist – Stress Engineer	Turkish Indigeneous Helicopter Project, Crashworthiness Responsible
2007-2013	TUSAŞ-Turkish Aerospace Industries Inc. (TAI)	Lead Stress Engineer, Stress Engineer	A350 Ailerons, Stress Team Leader B787 Cargo Barrier, Static Stress Analysis A400M, Forward Center Fuselage, F&DT EU 6th FM Programme: ALCAS, Stress Analysis.

Year	Place	Enrollment	Project, Responsibility
2006-2007	Limak Holding	Product Engineer	ALGA – Automated Advanced Fuselage Stress Analysis Program, Program Developer

FOREIGN LANGUAGES

Advanced English (TOEFL 2013 iBT Score: 108/120)

AWARDS & SCHOLARSHIPS

- Best paper in university wide Best Research Study Competition on Applied Mathematics organized by the Society for Industrial and Applied Mathematics (SIAM) at METU. (2012)
- Scholarship by TAI and Turkish Ministry of Science, Industry and Technology for PhD-SANTEZ Program (2011-2013)
- Award of International Publications Encouragement from the Scientific and Technological Research Council of Turkey. (2012)

PATENTS

"Successive Two-Stage Honeycomb/Tube Crash Absorption System" → Applied to National and International Patent Institutes, Status: *pending*. (TPE2013/12568)

PUBLICATIONS

Journal Articles

1. Gozluklu, B. and Coker, D., "Modeling of the delamination of L-shaped unidirectional laminated composites." Composite Structures, 94, 1430-1442, 2012.

2. Gozluklu, B. and Coker, D., "Cohesive Zone Modeling of Dynamic Delamination in Curved Woven Fabric Composite Laminates under Quasi-static Loading", Mechanics of Materials, submitted, 2013.

3. Yavas D, Gozluklu B, and Coker, D., "Investigation of Crack Growth Along Curved Interfaces in L-shaped Composite and Polymers", J. Carroll (ed.), Fracture and Fatigue, Volume 7. DOI 10.1007/978-3-319-00765-6_7, 2014.

Refereed Conference Proceeding Articles (International)

1. Gozluklu B, Oncul G, Koseoglu U, "Design Concept of a CFRP External Trailing Edge for Ailerons", Congress of American Society of Mechanical Engineers (ASME), IMECE2013-66066, San Diego, USA, 2013.

2. Gozluklu B and Coker D, "Modeling of Dynamic Delamination in L-Shaped Composite Brackets", Congress of American Society of Mechanical Engineers (ASME), IMECE2012-87831, Houston, USA, 2012.

3. Yavas D, Gozluklu B, Coker D, "Failure Mode Transition during Delamination of Thick Unidirectional L-shaped Composite Laminates", Congress of American Society of Mechanical Engineers (ASME), IMECE2012-88409, Houston, USA, 2012.

4. Yavas D, Uyar I, Gozluklu B, Coker D, "Experimental and Computational Investigation of Debonding at the Interface of Two L-Shaped PMMA Beams", Congress of American Society of Mechanical Engineers (ASME), IMECE2012-88425, Houston, USA, 2012.

5. Gozluklu B, Yavas D, Coker D, "Effect of Thickness and Pre-Crack Length on Delamination of Unidirectional L-Shaped Laminated Composites", 6th European Congress on Computational Methods in Applied Sciences and Engineering (ECCOMAS 2012) J. Eberhardsteiner et.al. (eds.) Vienna, Austria, September 10-14, 2012.

6. Gozluklu B, Coker D, "Modeling of Dynamic Delamination in L-shaped Composite Brackets", 6th European Congress on Computational Methods in Applied Sciences and Engineering (ECCOMAS 2012) J. Eberhardsteiner et.al. (eds.) Vienna, Austria, September 10-14, 2012.

7. Yavas D, Gozluklu B, Coker D, "Experimental and Computational Investigation of Debonding at the Interface of Two L-Shaped PMMA Beams", XXIII ICTAM, 19-24 August 2012, Beijing, China.

8. Gozluklu B and Coker D, "Modeling of the Dynamic Delamination Behavior of L-Shaped Composite Laminate Beams", 16th International Conference on Composite Structures, Porto, Portugal, 2011.

Refereed Conference Proceeding Articles (National)

1. Gozluklu, B. and Coker, D., "Dynamic Phenomena due to delamination initiation in laminated L-shaped composite beams," 6th Ankara International Aerospace Conference, AIAC, Ankara, Turkey, September 2011.

2. Gozluklu, B. and Coker, D., "Belirli Sonlu Eleman Metodu Çözümü ve Kohezif Bölge Metodu," 3rd UHUK Konferansı, Eskisehir, Türkiye, Sept 2010.

3. Gozluklu, B., Parnas, L., and Coker, D., "Laminat Kompozit Çift Ankastre Kiriş Testindeki Delaminasyon İlerlemesinin Kohezif Arayüz Elemanlarıyla Analizi ve Simülasyonu," 5th SAVTEK Konferansı, Ankara, Türkiye, Haziran 2010.

4. Gozluklu B and Coker D, "Dynamic Phenomena Emerged by Delamination Initiation in Laminated L-shaped Beams", 6th Ankara International Aerospace Conference, Middle East Technical University Ankara, TURKEY, Sept 2011.

5. Oncul G, Tanriverdi B and Gozluklu B, "Weight Management and General Weight Opportunities on Composite Aircraft Components", 6th Ankara International Aerospace Conference, Middle East Technical University Ankara, TURKEY, Sept 2011.

6. Gozluklu B, Inan O, Serdaroglu T, Unlu MU, Kokce M, Aydin E, Akyazi D, Gulasik H and Oncul G, "Structural Analysis of Composites in Flight Control Surfaces", 6th Ankara International Aerospace Conference, Middle East Technical University Ankara, TURKEY, 2011.

Selected Conference Presentations

1. Gozluklu B, Yavas D, Coker D "Effect of Cohesive Zone Models on the Dynamic Delamination of Highly Curved Thick Unidirectional Composite Laminates" Congress of American Society of Mechanical Engineers (ASME), IMECE2013-66411, San Diego, USA, 2013.

2. Coker D, Yavas D, Gozluklu B, Arca M, Uyar I. Effect of Thickness and Crack Size on the Dynamic Delamination of L-shaped Unidirectional Composite

Laminates" Congress of American Society of Mechanical Engineers (ASME), IMECE2013-66597, San Diego, USA, 2013.

3. Gozluklu B, "Modeling of the dynamic delamination of L-shaped unidirectional laminated composites", Society of Industrial Applied Mathematics (SIAM) 2012 annual meeting, Minnessota, US, 2012.

4. Coker D and Gozluklu B, "Dynamic Delamination of L-Shaped Composite Laminate Beams", 48th SES Conference, Northwestern University, Evanston, Illinois, US, 2011.

5. Gozluklu B, Coker D,and Parnas L, "Laminat Kompozit Çift Ankastre Kiriş Testinin Kohezif Bölge Metodu ile Simülasyonu", 6. Savunma Teknolojileri Konferansı, Ankara, Türkiye, 2010.

6. Gozluklu B and Coker D, "Dynamic Delamination of L-Shaped Composite Laminate Beams", 2nd International of Conference of Engineering against Fracture, Mykonos, Greece, 2010.

7. Gozluklu B and Coker D, "Performance Issues of Cohesive laws in Large Finite Element Model Applications", Congress of American Society of Mechanical Engineers (ASME), Vancouver, Canada, 2010.